

# Modelling Hemolysis and Thrombosis in Blood-Wetted Medical Devices

A thesis submitted in partial fulfillment of requirements of McGill University,  
for the award of Doctor of Philosophy

Hristo Valtchanov

Department of Mechanical Engineering

McGill University, Montreal

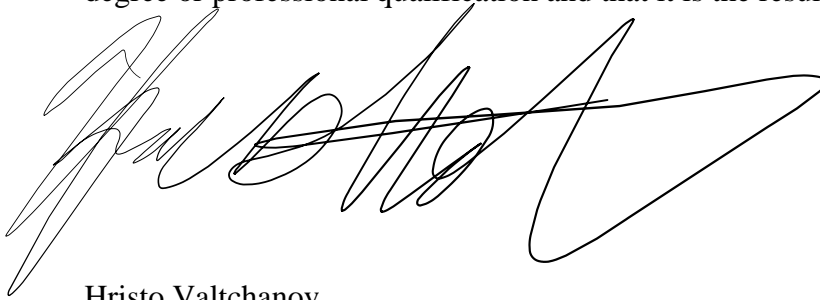
July 2023



## **Declaration**

---

I hereby declare that the work presented in this thesis has not been submitted for any other degree or professional qualification and that it is the result of my independent work.

A handwritten signature in black ink, consisting of several loops and a long horizontal stroke, positioned above the printed name.

Hristo Valtchanov

June 20, 2023

## Abstract

---

Heart failure, broadly characterized by the gradual decline of the ability of the heart to maintain adequate blood flow throughout the body's vascular network of veins and arteries, is one of the leading causes of death worldwide. Due to limited available treatment options for late-stage heart failure, heart transplantation remains one of the few long-term solutions, but is complicated by the limited and declining supply of donor hearts. One of the few available alternative interventions for late-stage heart failure with reduced ejection fraction is Mechanical Circulatory Support (MCS). A blood pump, called a ventricular assist device (VAD), is surgically implanted, and connected to the left (LVAD) and or right (RVAD) heart ventricles to provide additional venous pressure, off-loading some of the work required by the heart to maintain circulation. Modern mechanical circulatory support devices generate non-physiological flow conditions that can lead to the damage and rupture of blood cells (hemolysis), and the formation of blood clots (thrombosis), which pose severe health risks to the patient. It is essential to improve prediction tools for blood damage to reduce the risk of hemolysis and thrombosis.

Constitutive approaches to modelling blood damage are examined and expanded upon by studying the effect of certain key mechanics, namely the effect of red blood cell collisions on sublethal hemolysis, and the interaction between hemolysis and thrombosis. A numerical simulation-based approach is employed to examine these questions. A series of computational experiments are designed to examine the cellular-scale mechanics of sublethal hemolysis and the effect of hemolysis on thrombosis. A fully Eulerian structural method is implemented in ANSYS Fluent to simulate the dynamics of the red blood cell membrane. The effect of the volumetric concentration of red blood cells on the degree of stress and transmembrane diffusion of hemoglobin experienced by red blood cells is examined at various shear rates in a Couette flow. The relationship between shear rate and peak membrane strain is quantified, as is the effect of collisions. Finally, the effect of hematocrit on transmembrane hemoglobin diffusion is examined, finding that RBC collisions have an immense effect on sublethal hemolysis.

A simulation-based approach examines the interaction between hemolysis and thrombosis. Incompressible finite-volume computational fluid dynamics simulations are executed on an open-hub axial flow ventricular assist device. A continuum model of thrombosis and intrinsic coagulation is extended to include the effect of hemolysis. The model accounts for the activation of platelets by shear stress, paracrine signalling, adhesion, and hemoglobin and ADP

released during hemolysis. The effect of hemolysis with thrombosis is modelled by accounting for the hyper-adhesivity of von-Willebrand Factor on extracellular hemoglobin, and the increased rate of platelet activation induced by ADP release. Thrombosis is assessed at varying inflow rates and rotor speeds, and cases are executed where thrombosis is affected by ADP release and Hb-induced hyper-adhesivity. It is found that there is a mild but significant effect from hemolysis on thrombosis across a range of rotor speeds and that both mechanisms play a role. The overall mechanisms of thrombus formation and anti-thrombogenic LVAD design are discussed, and avenues of future research are suggested.

---

L'insuffisance cardiaque, caractérisée par le déclin progressif de la capacité du cœur à maintenir un flux sanguin adéquat dans le réseau vasculaire des veines et des artères de l'organisme, est l'une des principales causes de décès dans le monde. En raison du nombre limité d'options thérapeutiques disponibles pour l'insuffisance cardiaque tardive, la transplantation cardiaque reste l'une des rares solutions à long terme, mais elle est compliquée par le nombre limité et décroissant de cœurs de donneurs. L'assistance circulatoire mécanique (ACM) est l'une des rares interventions alternatives disponibles pour l'insuffisance cardiaque tardive avec fraction d'éjection réduite. Une pompe à sang, appelée dispositif d'assistance ventriculaire (DAV), est implantée chirurgicalement et connectée aux ventricules gauche (DAVG) ou droit (DAVR) pour fournir une pression veineuse supplémentaire, déchargeant ainsi le cœur d'une partie du travail nécessaire au maintien de la circulation. Les dispositifs modernes d'assistance circulatoire mécanique génèrent des conditions d'écoulement non physiologiques qui peuvent entraîner la détérioration et la rupture des cellules sanguines (hémolyse) et la formation de caillots sanguins (thrombose), ce qui présente de graves risques pour la santé du patient. Il est essentiel d'améliorer les outils de prédiction des lésions sanguines afin de réduire le risque d'hémolyse et de thrombose.

Les approches constitutives de la modélisation des lésions sanguines sont examinées et développées en étudiant l'effet de certains mécanismes clés, à savoir l'effet des collisions de globules rouges sur l'hémolyse sublétales et l'interaction entre l'hémolyse et la thrombose. Une approche basée sur la simulation numérique est employée pour examiner ces questions. Une série d'expériences informatiques sont conçues pour examiner la mécanique à l'échelle cellulaire de l'hémolyse sublétales et l'effet de l'hémolyse sur la thrombose. Une méthode structurelle entièrement eulérienne est mise en œuvre dans ANSYS Fluent pour simuler la



dynamique de la membrane des globules rouges. L'effet de la concentration volumétrique de globules rouges sur le degré de contrainte et la diffusion transmembranaire de l'hémoglobine subis par les globules rouges est examiné à différents taux de cisaillement dans un écoulement de Couette. La relation entre le taux de cisaillement et la déformation maximale de la membrane est quantifiée, de même que l'effet des collisions. Enfin, l'effet de l'hématocrite sur la diffusion transmembranaire de l'hémoglobine est examiné, et l'on constate que les collisions entre des GR ont en effet un effet considérable sur l'hémolyse sub létale.

Une approche basée sur la simulation examine l'interaction entre l'hémolyse et la thrombose. Des simulations de dynamique des fluides en volumes finis incompressibles sont exécutées sur un dispositif d'assistance ventriculaire à flux axial à moyeu ouvert. Un modèle continu de thrombose et de coagulation intrinsèque est étendu pour inclure l'effet de l'hémolyse. Le modèle tient compte de l'activation des plaquettes par la contrainte de cisaillement, la signalisation paracrine, l'adhésion, et l'hémolyse. L'effet de l'hémolyse sur la thrombose est modélisé en tenant compte de l'hyper-adhérence du facteur von-Willebrand sur l'hémoglobine extracellulaire et de l'augmentation du taux d'activation des plaquettes induite par la libération d'ADP. La thrombose est évaluée à différents débits d'entrée et vitesses de rotor, et des cas sont exécutés où la thrombose est affectée par la libération d'ADP et l'hyper-adhésivité induite par l'Hb. On constate que l'hémolyse a un effet léger mais significatif sur la thrombose pour toute une gamme de vitesses de rotor, et que les deux mécanismes jouent un rôle. Les mécanismes généraux de la formation de thrombus et de la conception anti-thrombogène des DAVG sont discutés, et des pistes de recherche futures sont proposées.

## **Publications Associated With This Research**

---

**Valtchanov, H.,** Cecere, R., Mongrain, R, (2023) Examining the Effect of Red Blood Cell Collisions on Sublethal Hemolysis and Turbulence. CSME2023, Sherbrooke, Canada, May 28-31, 2023.

**Valtchanov, H.,** Cecere, R., Mongrain, R, (2023) Simulating the effect of hemolysis on device-induced thrombosis in mechanical circulatory support. ICM3DM, Corfu, Greece, June 25-28, 2023.

**Valtchanov, H.,** Cecere, R., Mongrain, R, (2022) Simulation of Red Blood Cell Interaction in a Couette Shear Flow. ESMC2022, Galway, Ireland, July 4-8, 2022.

Rosaire Mongrain, Yinan Bao, **Hristo Valtchanov**, YoungHoon Chung, Renzo Cecere, Optimization of a Hub-less Ventricular Assist Device. (2022), M2D2021, Funchal Portugal, 26-30 June 2022

**Valtchanov, H.,** Cecere, R., Mongrain, R, (2021) In-silico assessment of the Impact of Material on Thrombogenicity in a Left Ventricular Assist Device European Society of Biomaterials. 31<sup>st</sup> Conference of the European Society of Biomaterials, Porto, Portugal, Sept 5-9, 2021.

**Valtchanov, H.,** Cecere, R., Mongrain, R, (2021) Simulation of Red Blood Cell Deformation in a Couette Shear Flow using a Fully Eulerian Membrane Mechanical Model. ESBiomech2021 Milan, Italy, July 11-14, 2021.

## Acknowledgements

---

This work would not have been possible without the support, effort, and contributions of a great many individuals, who have provided guidance, mentorship, moral and academic support, and friendship. My colleagues and friends, Stewart McLennan, Carlos Gil Yanez, and Jorge Gutierrez, who shared many good moments and beverages throughout the process, and my students, namely Yinan Bao, who helped keep me structured through the pandemic and whose optimization work I could build upon. I would like to thank my former boss and mentor, Jean-Sebastien Dick at Pratt and Whitney Canada, who taught me everything I know about multiphase modelling. I would also like to thank the amazing staff in the Mechanical Engineering Department at McGill, Mary Fiorelli, Anne-Marie Pierre, and Greg Ross Doyle, who helped keep me on track, and whose efficiency, professionalism, and dedication made the mechanics of the doctoral process so much easier. Furthermore, I would like to thank my Thesis Supervisory Committee members, Professors Siva Nadarajah, and Professors Laurent Charlin, for their invaluable insights, technical expertise, and guidance during the design of my thesis. I also would like to thank my supervisors, professor Rosaire Mongrain, and Dr. Renzo Cecere, for their stalwart support and encouragement, their succinct and constructive guidance and advisory style, and for their patience with me. Finally I would like to thank my family for their support and inspiration; my mother for her stalwart encouragement to pursue doctoral studies, my brothers for encouraging me to finish on time, and my late friend Patrick Turnbull, whose passing inspired me to enter the biomedical sciences.

## **Contributions to Original Knowledge**

---

All aspects of this thesis including the planning, execution and analysis of the studies, development of the code, and writing of every chapter and section are the original and sole work of the author of the dissertation, Hristo Valtchanov, unless specifically stated otherwise.

The dissertation examines several fundamental aspects of blood damage and provides some key contributions to the existing body of blood damage research at the time of writing and submission. These contributions include the examination of collisions between red blood cells on the strain they experience in simple shear flow and on sublethal hemolysis. Red blood cell collisions were found to have a significant impact on both strain and sublethal hemolysis, which was not previously known. It is also the first time that simulations have been conducted that attempt to compute the effect of red blood cell collisions on sublethal hemolysis, and the first time that small-scale flow disorderliness has been found in simulations and identified as being generated by collisions at cellular length scales.

In addition, the work extends existing thrombosis modelling approaches to incorporate several effects of hemolysis on thrombosis and examines the effect of hemolysis in realistic macroscale flows. To the knowledge of the author, this is the first time that this has been attempted in the context of finite-volume continuum thrombosis simulation. Novel constitutive models for single platelet embolization in a continuum framework are developed and implemented in the thrombosis simulations.

## Table of contents

---

### **Chapter 1: Introduction.....1**

---

1.1	Motivation .....	1
1.1.1	Ventricular Assist Devices as a Case Study on Blood Damage Modelling.....	1
1.1.2	Project Scope and Organization of the Thesis .....	5
1.2	Hypotheses and Objectives .....	5

### **Chapter 2: Literature Review .....7**

---

2.1	Design Considerations for Mechanical Circulatory Support Devices .....	7
2.1.1	Historical Overview of MCS .....	7
2.1.2	Pathology of Complications Associated with Non-Physiological Flow.....	8
2.1.3	Future Perspectives on Non-Physiological Flow Associated Pathologies.....	13
2.2	Fluid Dynamics of Blood Flow .....	14
2.2.1	Dynamics of Blood Cells and Blood Constituents in Flow .....	15
2.2.2	Continuum Modelling of Whole Blood and Blood Flow .....	17
2.3	Mechanical Properties of the Red Blood Cells Membrane .....	22
2.3.1	Resting Shape of the Red Blood Cell .....	23
2.3.2	Deformation of the Red Blood Cell Membrane.....	25
2.3.3	Viscoelastic Modelling of the Red Blood Cell Membrane .....	27
2.4	Modelling and Prediction of Hemolysis.....	29
2.4.1	Measurement of Hemolysis and Index of Hemolysis .....	30
2.4.2	Mechanics and Criteria of Red Blood Cell Lysis .....	30
2.4.3	Predicting Lethal Hemolysis.....	32
2.4.4	Effect of Turbulence on Hemolysis .....	37
2.4.5	Effect of RBC Collisions and Hematocrit on Hemolysis .....	39
2.4.6	Predicting Sublethal Hemolysis .....	40

2.4.7	Lagrangian and Eulerian Implementation of Hemolysis Models in CFD .....	46
2.5	Modelling and Prediction of Thrombosis.....	49
2.5.1	Overview of Thrombosis .....	49
2.5.2	Platelet Anatomy and Function in Thrombosis .....	52
2.5.3	Anticoagulation.....	63
2.5.4	Links Between Hemolysis and Thrombosis .....	65
2.5.5	Simulation of Thrombosis.....	66
2.6	Summary and Overview .....	72
2.6.1	Design Considerations for Mechanical Circulatory Support Devices .....	72
2.6.2	Blood Flow Modelling.....	72
2.6.3	Blood Damage Prediction .....	73
2.7	Key Challenges and Future Perspectives .....	74
<b>Chapter 3: Methodology .....</b>		<b>76</b>
3.1	Overview of the Finite-Volume Method.....	77
3.1.1	Overview of Computational Fluid Dynamics Simulation and Solution .....	77
3.1.2	Numerical Discretization and Solution.....	78
3.2	Microscale Modelling of the Interaction of Red Blood Cells .....	82
3.2.1	Computational Scheme .....	83
3.2.2	Implementation of Deformation Transport Equations in ANSYS Fluent .....	88
3.2.3	Computation of Transmembrane Hemoglobin Diffusion .....	95
3.2.4	Objectives and Executed Test Cases.....	99
3.3	Continuum Modelling of Thrombosis and The Effect of Hemolysis.....	101
3.3.1	Governing Equations of Fluid Flow .....	101
3.3.2	Equations Governing Thrombosis and Implementation in Ansys Fluent.....	103
3.3.3	Platelet Activation and Adhesion.....	105
3.3.4	Platelet Adhesion and Embolization .....	107
3.3.5	Deriving an Alternative Embolization Formulation .....	109

3.3.6	Anticoagulation and Thrombin Production .....	111
3.3.7	Modelling the Effect of Hemolysis on Thrombosis.....	112
3.3.8	Model Assumptions .....	115
3.3.9	Computational Domain and Simulation Setup .....	117
3.3.10	Objectives and Executed Test Cases.....	129
<b>Chapter 4: Results .....</b>		<b>131</b>
4.1	Simulation of Red Blood Cell Membrane Mechanics in Couette Flow.....	131
4.1.1	Verification and Validation of the Computational Method .....	131
4.1.2	Effect of Shear Rate on Strain and Sublethal Hemolysis for Dispersed Cellular Flows	136
4.1.3	Effect of Shear Rate on Red Blood Cell Collisions on Sublethal Hemolysis..	150
4.1.4	Effect of Viscoelasticity .....	155
4.1.5	Effect of Hematocrit on Area strain and Sublethal Hemolysis at Constant Shear Rate	158
4.1.6	Summary of Findings and Contributions .....	162
4.2	Simulation of the Effect of Hemolysis on Thrombosis.....	163
4.2.1	Fitting Embolization Rate from Experiment.....	163
4.2.2	Verification and Validation of Thrombosis Simulations .....	166
4.2.3	Simulation of Hemolysis and Thrombosis.....	171
4.2.4	Designing Blood-Wetted Devices to Minimize Thrombosis.....	181
4.2.5	Summary of Findings and Contributions .....	185
<b>Chapter 5: Discussion.....</b>		<b>187</b>
5.1	Effect of Collisions on Hemolysis .....	187
5.1.1	Dispersed Cellular Mechanics in a Couette Shear Flow .....	187
5.1.2	Effect of Collisions on the Red Blood Cell Membrane and Sublethal Hemolysis 193	
5.1.3	Study Limitations and Validity of the Computational Method .....	201

5.1.4	Future Work .....	203
5.2	Modelling Thrombosis and Effect of Hemolysis on Thrombosis .....	204
5.2.1	Embolization Mechanics and Effect of Shear Rate on Embolization .....	204
5.2.2	Effect of Hemolysis on Thrombosis .....	206
5.2.3	Minimizing Thrombosis in Blood-Wetted Devices and MCS .....	209
5.2.4	Limitations of the Computational Method and Study .....	211
5.2.5	Future Work .....	213
<b>Chapter 6: Conclusions .....</b>		<b>216</b>
<b>References .....</b>		<b>218</b>
<b>Appendix A: Timescale Sensitivity Analysis of Thrombosis Acceleration .....</b>		<b>259</b>
<b>Appendix B: Parameters for Six Best LVADs .....</b>		<b>261</b>

---



## List of Figures

---

Figure 1: Schematic depiction of the various RBC dynamic states at the different shear rates. Adapted from Arora et al <sup>7</sup> .	16
Figure 2: Apparent blood viscosity is shown as a function of shear rate, along with several well known non-Newtonian constitutive viscosity models. Adapted from Robertson <sup>162</sup> .	18
Figure 3: Schematic illustration of the red blood cell membrane and arrangement of proteins that comprise the cytoskeleton. Adapted from Hansen et al <sup>198</sup> .	22
Figure 4: Schematic illustration of the process of stretching a red blood cell using an optical trap using the optical tweezer approach. Adapted from Dao et al <sup>206</sup> .	26
Figure 5: Comparisons of deformation computed from FEA simulations using a) Neo-Hookean model and b) Yeoh model with optical tweezers experiments. Adapted from Mills et al. <sup>207</sup>	27
Figure 6: Surface of Index of Hemolysis as a function of exposure time and shear stress experienced. Adapted from Giersiepen et al. <sup>6</sup>	33
Figure 7: Molecular dynamics simulations of a lipid bilayer membrane reinforced by a 80nm spectrin triangular mesh, showing the variation of a) critical area strain for poration initiation b) ...	43
Figure 8: Self-diffusivity of hemoglobin at varying physiological concentrations.	44
Figure 9: Maximum area strain at different shear rates. Adapted from Sohrabi and Liu. <sup>10</sup>	46
Figure 10: Schematic illustration of the coagulation cascade illustrating the extrinsic and intrinsic ...	51
Figure 11: SEM images of (a) resting discoidal platelets and (b) platelets activated by ADP. Adapted from Zucher and Nachmias <sup>306</sup>	54
Figure 12: Schematic illustration of bonding via vWF, collagen, and fibrinogen, and the corresponding mechanisms of platelet activation. Adapted from Fogelson and Neeves <sup>292</sup>	61
Figure 13: Embolization probability maps of Basmadjian. Shows the probability of embolization based on the shear rate and lesion height. Adapted from Basmadjian <sup>351</sup>	63
Figure 14: Schematic illustration of computational domain used for RBC collision simulations	86
Figure 15: Plot of derivatives of strain energy function for incompressible Yeoh material model developed in Eqn.....	93
Figure 16: Illustration of RBC initialization where red indicates cytoplasmic volume fraction.	94
Figure 17: Illustration of pore density and pore radius over the expected range of distributions.....	99

Figure 18: Probability of embolization vs shear stress given by Goodman et al. <sup>324</sup> .....	109
Figure 19: Schematic illustration of the experimental setup of a thrombus growing downstream from a backward-facing step by Taylor et al. <sup>341</sup> and Yang et al. <sup>383</sup> .....	122
Figure 20: Illustration of the computational domain of the validation case reproducing the test section of Taylor et al. <sup>341</sup> and Yang et al. <sup>383</sup> .....	123
Figure 21: Schematic Illustration of computational LVAD domain in which Thrombosis simulations are executed. The open-hub LVAD design is a novel LVAD developed at McGill.....	124
Figure 22: Final computational grid selected to execute blood clot in the LVAD case (maximum and minimum grid spacing and inflation layer values are 0.75 mm, 0.05 mm, and 5, respectively). .....	127
Figure 23: Comparison of area strain distribution at peak stretch ( $\mathbf{t\gamma} = \mathbf{10}$ ) for the 2 and 3 refinement level cases, where mesh spacing corresponds to 125 nm and 62.5 nm.....	132
Figure 24: Comparison of RBC length at shear rate of $20,000 \text{ s}^{-1}$ using 2 adaptive grid refinement levels adaptive mesh and 3 refinement levels. ....	133
Figure 25: Steady-state parachuting and comparison with Tomaiuolo et al <sup>396</sup> .....	134
Figure 26: Quantitative comparison a) of the length of an RBC stretched by shear in the present simulations at peak stretch (blue dots), with the optical tweezers experiments of Mills et al. <sup>207</sup> .....	135
Figure 27: Dynamics of complex tumbling at $4800 \text{ s}^{-1}$ . The RBC vacillates between successive phases of tumbling and tank treading, being stretched out when aligned with the shear axis, and then contracted when perpendicular to it as the RBC rotates.....	138
Figure 28: Dynamics a RBC during tank treading at $20\,000 \text{ s}^{-1}$ . RBC membranes are coloured by area strain, $\epsilon A$ , scaled by maximum and minimum values. ....	139
Figure 29: Evolution of Shape parameter over time for a single red blood cell in a Couette shear flow in the tumbling and pseudo-tumbling dynamic regime.....	140
Figure 30: Evolution of shape parameter over time for a single red blood cell in a Couette shear flow in the tank-treading dynamic regime.....	141
Figure 31: Time variation of membrane-averaged a) area and b) uni-axial strain at shear rates in the tumbling and pseudo-tumbling regime in a Couette shear flow. ....	142
Figure 32: Time variation of membrane-averaged a) area and b) uni-axial strain at shear rates in the tank-treading regime in a Couette shear flow. ....	143
Figure 33: Time variation of a) membrane-maximum and b) membrane-minimum area strain at shear rates in the tank-treading regime in a Couette shear flow.....	143

Figure 34: (a) Membrane-averaged and membrane-maximum area strain and (b) membrane-averaged strain time averaged at dynamic steady state. ....	144
Figure 35: Distribution of area strain, pore density, and pore diameter at peak stretch at $t\gamma = 20$ at high shear rate, $\gamma = 20\,000\text{ s}^{-1}$ . Peak length of the stretched RBC is $18.3\text{ }\mu\text{m}$ . ....	145
Figure 36: Distribution of area strain, pore density, and pore diameter during tank-treading at $t\gamma = 50$ at high shear rate of $\gamma = 20 \cdot 10^3\text{ s}^{-1}$ . Length of the stretched RBC at peak stretch is $14.3\text{ }\mu\text{m}$ . ....	146
Figure 37: Time-variation of membrane-averaged transmembrane effective diffusion coefficient normalized by self diffusion coefficient for a single RBC in a couette shear flow. ....	147
Figure 38: a) Effective transmembrane hemoglobin diffusion coefficient vs mean area strain...vs membrane-averaged area strain and maximum area strain for b) all cases and c) low shear rate ....	148
Figure 39: Fitting of high shear transmembrane hemoglobin diffusion cases to erf surface of membrane-averaged and membrane-maximum area strain. ....	150
Figure 40: Visualization of collision between two red blood cells in a Couette shear flow at $20\,000\text{ s}^{-1}$ . Red blood cells are in general prevented from tumbling by the collisions, and significant strain is observed in the areas where the collision is occurring. Lubrication forces keep the red blood cells from actually coming into contact, and generally result in a constant minimum spacing. ....	151
Figure 41: Comparison of time and shear rate variation of membrane-averaged area strain between (a) a single cell case b) two cells in a Couette shear flow. ....	152
Figure 42: Time and shear rate variation of a) membrane-minimum and b) membrane-maximum area strain of two cells in a Couette shear flow. ....	153
Figure 43: Membrane-average diffusion coefficient in the a) single and b) multicell case. ....	153
Figure 44: Fitting of effective transmembrane hemoglobin diffusion coefficient with membrane-averaged area strain and membrane-maximum area strain to an erf surface. ....	155
Figure 45: Illustration of glancing collision between red blood cells wherein viscosity inside of the boundary indicator function where the structural model is set to $0.3\text{ }\mu\text{Pa s m}$ . ....	156
Figure 46: Comparison of a) membrane-avreaged area strain and b) the effective transmembrane diffusion coefficient during collisions at $20\,000\text{ s}^{-1}$ in the viscoelastic and non-viscoelastic cases for 2 and 4 cells. ....	158
Figure 47: Comparison of a) membrane-maximum and b) membrane-minimum area strain during collisions at $20\,000\text{ s}^{-1}$ in the viscoelastic and non-viscoelastic cases for 2 and 4 cells. ....	158
Figure 48: Visualization of head on collisions in the 4-cell case ( $\text{Hct} = 12.1\%$ ) causing contraction in length and rotation in the 4-cell case at $20\,000\text{ s}^{-1}$ shear rate. Collision begins at $t\gamma = 16$ . ....	159

Figure 49: Time variation of membrane-averaged area strain and diffusion coefficient with number of cells. Effective hematocrit is between 3 and 36%, .....	161
Figure 50: Time variation of a) membrane-maximum and b) membrane-minimum area strain with between 1 and 12 cells in the domain, which corresponds to effective hematocrit of 3% and 36% ..	162
Figure 51: Fitting of embolization rate and threshold stress in modified-Goodman model using experimental data from Navitsky et al <sup>352</sup> . .....	164
Figure 52: Fitting of embolization rate and threshold stress in power law model using experimental data from Navitsky et al <sup>352</sup> . .....	165
Figure 53: Steady-state wall shear stress distributions in backwards-facing step validation case with fine (top) and coarse (bottom) polyhedral element .....	166
Figure 54: Variation of maximum and wall-averaged wall shear stress and volume maximum and volume averaged hemolysis index with maximum grid spacing, number of inflation layers,.....	167
Figure 55: Top-view of thrombus formed downstream from a backward-facing step in a 10mm diameter tube (modified-Goodman model), visualized as isosurfaces of platelet volume fraction .....	170
Figure 56: Quantitative comparison of thrombus length formed downstream from a backward-facing step with Yang et al. <sup>383</sup> and Taylor et al. <sup>341</sup> . .....	171
Figure 57: Flood plots of velocity magnitude at three characteristic rotor speeds of the open-hub LVAD. Velocity magnitude is scaled with peak global velocity in the domain. Images are extracted from transient simulation data after quasi-steady state is reached (10 s flow-time).....	172
Figure 58: Flood plots of shear stress on the LVAD surfaces, and of von-mises stress on a plane passing through the LVAD central axis, at 15 minutes thrombus time at 3000 RPM. ....	174
Figure 59: Variation of mass-flow averaged Index of hemolysis at the LVAD outlet at various rotor speeds with thrombus time.....	175
Figure 60: Flood plot of hemolysis index at 3000 RPM after 15 minutes of thrombus time. ....	175
Figure 61: Variation of a) Maximum value of hyper-adhesive vWF ( $vWF_{ha}$ ) and b) Maximum platelet hyperadhesion factor in the domain with thrombus time.....	176
Figure 62: Flood plots in a plane bisecting the central axis of the open-hub LVAD at 3000 RPM of (top) hyper-adhesive vWF, (middle-right) platelet volume fraction, and (bottom) axial velocity. ....	177
Figure 63: Flood plots of platelet hemolysis-induced hyperadhesion factor, $k_{Hemo}$ , at 3000 RPM at 15 minutes thrombus time, indicating the spatial distribution of the local effect of hemolysis on LVAD walls. ....	178

Figure 64: Variation of total thrombus volume in the LVAD over the domain at three rotor speeds, without hemolysis modelling (solid), with hemolysis modelling where $k_{\text{Hemo}}$ is set to 1 (dotted), ...	179
Figure 65: Illustration of Thrombus (Isosurfaces of deposited platelet volume fraction, $\phi_{\text{pad}} = 0.1$ ) at three rotor speeds extracted at 15 minutes thrombus time, illustrating the effect of hemolysis). .....	180
Figure 66: Design of experiments illustrating the effect of hemolysis on thrombus growth rate. ....	182
Figure 67: Effect of geometric optimization to reduce thrombogenesis at three rotor speeds at 10 minutes thrombus time. Thrombus regions are indicated in red. ....	183
Figure 68: Comparison of hemolysis index at outlet in the open-hub LVAD where hemolysis equations are sped up by a factor of 25 and 100. Time is given in minutes hemolysis time. ....	259
Figure 69: Comparison of thrombus volume in the open-hub LVAD where hemolysis equations. Time is given in minutes thrombus time. ....	260

## List of Tables

---

Table 1: Power law coefficient sets for hemolysis index (%).....	33
Table 2: Platelet deposition and binding coefficients for various surfaces.....	62
Table 3: Summary of simulations executed to examine the effect of hematocrit on red blood cell stress and sublethal hemolysis .....	100
Table 4: Overview of source terms used for equations in model.....	119
Table 5: Constants and property values used in Thrombosis Model .....	120
Table 6: Boundary conditions used for thrombosis models. $J$ indicates a flux boundary, $C$ indicates a concentration boundary. Subscript W denotes values at the wall boundary.....	124
Table 7: Summary of thrombosis simulations executed .....	130
Table 8: Time and membrane averaged values of area strain and effective transmembrane hemoglobin diffusion coefficients for one and two cells in a Couette shear flow. ....	154
Table 9: Comparison of time and membrane-averaged area strain and effective transmembrane hemoglobin diffusion coefficients with increasing hematocrit.....	161
Table 10: Normalized sensitivity of thrombus growth rate to changes in geometric and operating parameters.....	184

## List of Symbols

---

$\rho$	Density, fluid, pore or otherwise
$\vec{v}$	Fluid velocity vector
$\sigma$	Stress Tensor
$f$	Momentum source term, or momentum density constant
$\mu$	Dynamic Viscosity
$\nu$	Kinematic viscosity
$\psi$	Generic scalar variable
$A$	Area
$\phi_i$	Volume fraction, for species i
$D$	Diffusivity coefficient, or Diameter
$\mathbf{G}_s$	Surface Left Cauchy deformation tensor
$\mathbf{L}_{ij}$	Velocity gradient tensor
$\kappa_r$	Curvature (reference)
$\mathbf{P}_s$	Surface projection matrix, equal to $\mathbf{P}_s = \mathbf{I} - \mathbf{n}\mathbf{n}^T$
$P$	Pressure or Probability
$\tau_s$	Shear stress, or (Bolded) shear stress tensor, subscript s indicates surface projection or surface formulation
$\mathbf{q}_s$	Stress induced by bending moments
$E_s$	Surface elasticity modulus
$I_s$	Surface invariant of Surface Left Cauchy deformation
$II_s$	Second invariant of surface Left Cauchy deformation
$I_v$	First invariant of volumetric Left Cauchy deformation
$II_v$	Second invariant of volumetric Left Cauchy deformation
$W_s$	Surface Material strain energy
$\lambda_1, \lambda_2$	First and second principle stretches
$(\mathbf{P}_s \cdot \nabla) \cdot$	Surface divergence operator
$\vec{m}$	Bending moment vector
$\vec{n}$	Surface normal vector

$E_b$	Bending stiffness
$\kappa$	Surface curvature tensor
$t_m$	Red blood cell surface thickness
$\dot{\gamma}$	Shear rate
$\epsilon_A$	Area or biaxial strain
$\bar{\phantom{x}}$	Overbar - represents averaging
$\epsilon$	Linear or uniaxial strain
$\rho_p$	Pore density
$\mathcal{P}$	Porosity
$\bar{r}_p$	Pore radius
$C_{imb}$	Immersed boundary viscous resistance factor for Brinkman term
$k_{C_j, C_i}$	Rate constant for $C_j$ to influence $C_i$ , $\frac{\partial C_i}{\partial C_j} = k_{C_j, C_i}$
$S_{C_i}$	Source term for thrombus equation $C_i$
$P_{\bar{a}\bar{d}}$	Non-activated non-deposited (i.e. resting) platelets
$P_{a\bar{d}}$	Activated non-deposited platelets
$P_{\bar{a}d}$	Non-activated deposited platelets
$P_{ad}$	Activated deposited platelets
$P_s$	Stabilized platelets
$PT$	Prothrombin
$T$	Thrombin
$AT$	Antithrombin
$ADP$	Adenosine Diphosphate
$TxA_2$	Thromboxane A <sub>2</sub>
$H$	Heparin
$\mathcal{D}$	Hemolytic mechanical dose, directly related to hemolysis index
$vWF$	Von-Willebrand Factor
$vWF_{ha}$	Hyper-adhesive von-Willebrand factor
$k_{apa}$	Agonist platelet activation rate
$k_{spa}$	Shear platelet activation rate
$\Omega$	Normalized agonist blending factor



$t_{act}$	Characteristic activation time
$\lambda_{Ci}$	Release rate of Agonist $C_i$ during platelet activation
$k_{i_{dep,j}}$	Deposition rate of platelet I onto j, where $i \in \{\bar{a}, a\}$ denoting not activated and activated platelets, respectively and $j \in \{W, P\}$ denoting Walls or Platelets, respectively
$k_{i_{dep,j}}^*$	Hemolysis augmented platelet deposition rate
$\phi_{Pd}$	Platelet volume fraction
$k_{hemo}$	Scaling factor for adhesion rate due to hemolysis
$\tau_{emb,i}$	Characteristic Shear Stress of embolization from surface i
$t_{emb}$	Characteristic time of Embolization
$k_{emb,i}$	Embolization rate from surface i
$\kappa_{emb}$	Constant of embolization so that $k_{emb} \sim \kappa_{emb} \dot{\gamma}$
Re	Reynolds Number
$D_{plt}$	Platelet Diameter
$t_{vWF_{ha}}$	Characteristic reaction time scale of hyper-adhesive von—Willebrand factor conversion
$k_{d_{vWF}}$	Dissociation rate of von-Willebrand factor
$k_{d_{vWF_{ha}}}$	Dissociation rate of hyper-adhesive von-Willebrand factor
IH	Index of Hemolysis
$C_{IH}$	Coefficient in hemolysis Power law
$\alpha$	Exponent of shear stress in hemolysis power law
$\beta$	Exponent of exposure time of hemolysis power law
$M$	Molar mass
$J$	Flux (generally into a cell or domain) at a boundary

## List of Acronyms

---

LVAD, RVAD, VAD	Left-, Right-, Ventricular Assist Device
ADP	Adenosine Diphosphate
LDH	Lactase Dehydrogenase
RVF	Right Ventricular Failure
RV	Right Ventricle
LV	Left Ventricle
MCS	Mechanical Circulatory Support
RBC	Red Blood Cell
WBC	White Blood Cell
Plt	Platelet
GI	Gastrointestinal
GW	Giersiepen Wurzinger (equation or power law)
DPD	Dissipative Particle Dynamics
CGMD	Coarse-Grained Molecular Dynamics (simulation)
MD	Molecular Dynamics (simulation)
ADR / UDS	Advection Diffusion Reaction (equation) or User Defined Scalar (equation – ANSYS Terminology)
CFD	Computational Fluid Dynamics (simulation)
FE / FEMM	Finite Element / Finite Element Mechanical Model

## Chapter 1: Introduction

---

### 1.1 Motivation

#### 1.1.1 Ventricular Assist Devices as a Case Study on Blood Damage Modelling

Heart failure (HF) is the 2<sup>nd</sup> leading cause of death in Canada<sup>1</sup>. HF can be defined as the gradual decline of the ability of the heart to maintain adequate blood flow throughout the body's vascular network of veins and arteries. Due to limited available treatment options, heart transplantation remains one of few long-term solutions, but is complicated by the limited and declining supply of donor hearts<sup>1</sup>. Heart failure can be ameliorated by Mechanical Circulatory Support (MCS). A blood pump, called a ventricular assist device (VAD), is surgically implanted, and connected to the left (LVAD) and or right (RVAD) heart ventricles to provide additional venous pressure. This relieves the work required from the heart. Pressure and loading are greater in the left ventricle, and thus LVAD implantation is more common.

Despite decades of research, MCS implantation still results in a variety of adverse health complications to the patient that result in significant risks and severe reduction in the patient's overall quality of life. For example, the absence of pulsatility can cause buildup of collagen in the folds of underutilized valves that are opened by pulses of blood, causing them to fuse permanently. This along with increased shear stress has been linked to deficiencies in quantity and function of von-Willebrand factor (vWF) proteins in the blood, which are necessary for blood clotting, and furthermore, their absence has been linked to gastro-intestinal (GI) bleeding. Flow conditions in VADs greatly exceed physiological levels (called supraphysiological or non-physiological), which can cause blood damage. High hemodynamic stresses can trigger blood clot formation (thrombosis) and blood cell damage (hemolysis). Hemolysis and thrombosis pose significant risks to patient morbidity and death. Lethal levels of hemolysis can lead to multi-organ failure and death. Hemolysis, even at low levels has been linked to formation of an occlusive blood clot (thrombus) in the pump, ultimately leading to death<sup>2</sup>. Small blood clots forming on surfaces can also be embolized and travel into the bloodstream, causing thromboembolic stroke, deep-vein thrombosis and exacerbate the risk of a cardiac event<sup>1</sup>. The prevalence of sublethal or subclinical hemolysis is difficult to ascertain, and it often goes undiagnosed because of its asymptomatic nature. Consequently, sublethal hemolysis and its risks are not well studied, but can cause anemia and kidney failure. Furthermore, although hemolysis is often associated with thrombosis, the exact mechanisms

and magnitude of their interaction are yet unknown<sup>3</sup>. It is a major focus of this work to better understand this interaction, which will help physicians understand and quantify the risk to patients, and device designers to improve the safety of blood-exposed devices. Blood damage is also, in general, a pernicious issue central to the design of many blood-wetted medical devices such as surgical guidewires, extra-corporeal oxygenation, cannula, stents, and VADs. Such devices, like LVADs induce supraphysiological and or non-physiological flow conditions, activate the immune system, introduce foreign substances, and affect homeostasis locally and far downstream.

Hemolysis generally is quantified by the percentage change of extracellular hemoglobin relative to intracellular hemoglobin measured by drawing blood; this is also known as the index of hemolysis (IH). Normalized Index of Hemolysis (NIH) values (IH normalized by hematocrit) lower than 0.1 can be considered subclinical or sublethal (these terms are used interchangeably in this work). More specifically, sublethal hemolysis is hemolysis that arises without full RBC membrane rupture as defined by Leverett<sup>4</sup>. Membrane rupture is indicated by elevated LDH and bilirubin, which is used to diagnose lethal hemolysis. Subclinical hemolysis, which primarily occurs due to the diffusion of hemoglobin through the RBC membrane, does not involve membrane rupture. Thus, short of regular bloodwork and measuring hemoglobin levels, sublethal hemolysis is difficult to detect. Because of this, little is known about the pathological connection between subclinical hemolysis and other pathologies such as stroke and thromboembolism. Subclinical hemolysis has generally been linked to subtle forms of damage to the liver, such as decreased haptoglobin production which is linked with increasing risk of diabetes and atherosclerosis disease<sup>5</sup>, but has also been linked with LVAD thrombosis<sup>3</sup>.

Blood is a remarkably complex suspension of cells in blood plasma. Blood plasma is a solution of proteins, nutrients, hormones, salts and innumerable biochemicals in water that support innumerable body functions. Red blood cells (RBCs) comprise 40-55% of the volume of blood (called the hematocrit value), and account for a large degree of its unique mechanical properties. Blood has non-Newtonian shear-thinning viscosity that is time-dependant (thixotropic) as well as viscoelastic. Red blood cells are highly deformable, which results in the shear rate dependant distribution of blood's cellular constituents. This effect, known as the Farrhaus-Lindquist effect, wherein red blood cells are excluded in near-wall regions, and platelets tend to aggregate in these regions is essential to homeostasis. Because of the complexity of blood, the non-deformable and rough surfaces of biomedical devices interact

with blood in extraordinarily complex ways. For example, metals activate platelets merely by contact and provide ideal media for cells, platelets, and proteins to adhere to. This complexity renders the prediction of hemodynamics and blood damage particularly difficult.

Hemolysis prediction has been approached both empirically and constitutively. The gold standard of hemolysis prediction is the Giersiepen-Wurzinger power law<sup>6</sup>, which fits IH as a power-law of the shear stress and stress exposure. Red blood cell dynamics are complex, and factors such as RBC collisions, and the hyperelastic and viscoelastic properties of the red-blood cell membrane, affect these dynamics and modulate the strain developed on the red blood cell membrane. It can be expected that changing the dynamic conditions such as streamline curvature, the red blood cell volume fraction, and turbulence will have a profound effect on the degree of damage accumulated by the red blood cell. This complexity is the main factor driving the necessity for constitutive modelling because data-driven methods such as the empirical GW equation are always limited to the experimental conditions under which data were collected. Constitutive modelling approaches by Arora,<sup>7</sup> Vitale<sup>8</sup>, and McKean<sup>9</sup> use a bubble analogy for the RBC and parameterize the red blood cell shape as an ellipsoid. Rather than computing strain resulting from stress, deformation is directly accumulated by solving a transport equation where the shear and vorticity tensors impose incremental deformations to the cells each timestep. Multiscale models<sup>10-12</sup> extract loading conditions from computational fluid dynamics simulations (CFD) and apply them to finite-element models of the red blood cell membrane, averaging the result over a finite number of cells.

All such models neglect complex membrane behaviour such as non-ellipsoidal shapes induced by varying stress application rates or complex loading, collisions, and the effect of turbulence. The stress application rate is quite important because shear stress is very localized in complex flows, and impacts turbulence and RBC collisions. Turbulence and collisions are, however, the far more complex and ambiguous problems for which there is a severe scarcity of published studies. Finally, little is known about how the distribution of strain on the RBC membrane, and how it affects sublethal hemolysis. These gaps have naturally arisen because the problems are daunting. The effect of RBC collisions on membrane strain is profoundly difficult to measure, and even simulating RBC collisions is complex. It is understood that the same is true for their effect on transmembrane hemoglobin diffusion.

Blood clotting or thrombosis, induced by non-physiological flow conditions, is the other major form of blood damage. A complex network of biochemical signalling reactions (the coagulation

cascade) results adhesion of platelet cells in blood, which bind together to form blood clots. This process also triggers the polymerization of fibrin gel from fibrinogen in blood plasma that solidifies and stabilizes the clots. Thrombus form in the wake of highly sheared regions of the VAD flow path, regions of stagnant flow where platelet accretion occurs such as in small grooves or wakes, or at inflow and outflow cannula<sup>13</sup>. Heat and chemical agonists can increase the likelihood of thrombosis by accelerating the relevant reactions, and bearings are particularly prone to thrombosis<sup>14</sup>. The connection between thrombosis and hemolysis has long been recognized, and hemolysis is often noted to be an indicator that pump thrombosis has occurred in MCS patients. It is, however, unclear exactly what mechanisms drive the interaction, whether hemolysis precedes thrombosis or vice versa, and the degree of hemolysis necessary to cause thrombosis.

Thrombosis modelling and prediction, unlike hemolysis, has only been attempted and realized in the last decade at a scale useful for designing medical devices. Due to the multi-scale nature of thrombosis, however, such analysis can be very computationally expensive for realistic flows and is therefore challenging to apply to MCS design. With some notable exceptions,<sup>15–18</sup> thrombosis modelling is not attempted in complex flows relevant to most biomedical devices. Furthermore, at the time of writing, although there is a strong connection between hemolysis and thrombosis, no literature has been published that attempts to model both hemolysis and thrombosis in a connected way.

The importance of understanding and predicting blood damage is crucial to improving the safety of any blood-wetted medical device as predicting negative outcomes is essential to the process of designing against them. It is particularly important furthermore, to develop constitutive models of blood damage, which can predict the risk of negative outcomes in conditions for which no experimental data yet exists. The central theme of this work is to answer some key questions pertaining to the prediction of sublethal hemolysis and furthermore to examine the link between hemolysis and thrombosis. In turn, this will help inform modelling efforts and improve upon our ability to model blood damage. The impacts of this research to patients are both immediate, and long term. A better understanding of the connection between hemolysis and thrombosis will provide clinical insight into management of pump thrombosis, give a better understanding of a tolerable level of hemolysis, and can help determine if anticoagulation regimes are effective in reducing the risks of thrombosis to patients. It will also provide the means to develop devices with reduced risk of thromboembolism. In turn, the risk to patients of thromboembolic complications with MCS may be reduced. Better management

of anticoagulation will help to reduce risks associated with high anticoagulant dosage such as gastro-intestinal bleeding and improve patient quality of life. The models and approach employed here are in general applicable to modelling the cellular processes in biofluids, such as the transport of proteins cells, sampling of DNA from mucous, and so on. Finally, although this study focuses on the intrinsic coagulation pathway (dominant in MCS), which is different than in the vasculature, such analysis can be extended to incorporate both coagulation pathways, paving the way to assessing patient-specific risk levels from diseases such as atherosclerosis.

### **1.1.2 Project Scope and Organization of the Thesis**

The project will take a computational approach wherein simulation is used as an experimental surrogate for data collection on sublethal hemolysis and conditions in which thrombosis occurs (thrombogenesis). The scope of the work is limited to the non-physiological hemodynamic conditions inside of modern MCS systems under steady flow, and it is assumed that the vascular system and MCS pump are completely uncoupled. Furthermore, to maintain computational feasibility, the work only considers thrombus initiation (thrombogenesis) inside of the MCS device and does not examine extensive thrombus development or thrombus once they leave the MCS. Though embolization of platelets from surfaces is examined, thrombus breakage is not and predictions of thrombus growth over a timeframe longer than 30 minutes is shown to be unreliable. The study examines sublethal hemolytic modelling and the relationship between the fluid and strain experienced by the RBC membrane and is not concerned with lethal hemolysis or membrane rupture. Long-term sublethal damage effects to the RBC membrane such as loss of deformability and the ensuing changes to the RBCs dynamic and physiological properties are also not examined.

## **1.2 Hypotheses and Objectives**

The analysis and experimental design is organized around the following hypotheses that are made with respect to addressing the gaps noted in the above motivation. The gaps addressed attempt to answer basic questions with regards to the effect of red blood cell concentrations on hemolysis, and the connection between hemolysis and thrombosis.

- I. Hematocrit has a strong positive correlation to membrane stress and sublethal hemolysis.
- II. Hemolysis has a significant effect on thrombus formation in mechanical circulatory support, even at sublethal levels, and can trigger thrombosis.

The first hypothesis seeks to address and quantify the commonly made assertion red blood cell interactions and collisions have no significant effect on hemolysis and can be neglected in blood damage modelling. The second objective seeks to answer the question of whether subclinical levels of hemolysis influence thrombogenesis, and whether it should be considered in future modelling efforts and as a clinical risk factor. Consequently, the following objectives are set to guide the scope of the work.

- I. Investigate the relationship between shear rate and RBC volume fraction on areal strain and transmembrane hemoglobin diffusion rate.
- II. Determine the degree to which hemolysis affects thrombogenesis and which of the known interaction mechanisms most significantly affects thrombogenesis.



## Chapter 2: Literature Review

---

### 2.1 Design Considerations for Mechanical Circulatory Support Devices

The design of any blood-wetted biomedical devices is centered on achieving a given task while minimizing adverse health consequences to the patient. This requires a thorough understanding of the possible complications, which are specific to the device, their pathogenesis, the tools available for their prediction, and strategies for their management. In the context of MCS, these objectives are in general to minimize the size of the device, minimize blood damage, and produce required pressure and flow rate (20-100 mm Hg of pressure and 3-5 LPM of flow). A non-exhaustive list of complications associated with MCS (in order of severity) includes lethal and sublethal hemolysis, pump thrombosis, MCS-induced right ventricular failure, stroke (thromboembolic and hemorrhagic), gastro-intestinal bleeding and MCS-induced von-Willebrand Factor (vWF) deficiency, infections, thromboembolism, and valve fusion.

This section gives a brief historical overview of the design of mechanical circulatory support and then discusses epidemiology and pathogenesis of these complications. Blood damage is a central theme that cuts across these complications, and so is covered in greater detail in the subsequent sections, but the pathogenesis of all but the last two is discussed to give context to the work. The current state of MCS design is then examined and future perspectives are discussed.

#### 2.1.1 Historical Overview of MCS

The first mechanical circulator support (MCS) systems were extracorporeal pulsatile-flow (PF) positive displacement pumps<sup>19</sup>. Initially, MCS was used to prolong life until a suitable donor heart was available, known as a bridge to transplantation therapy (BTT). 1-year survival rates on early MCS were low (69%<sup>20</sup>), due primarily to poor mechanical reliability and unphysiological flow conditions that led to the formation of occlusive thrombus or hemolysis<sup>5</sup>.

Early intracorporeal pulsatile blood pumps such as the Novacor, HeartMate (HM) IP1000/VE/XVE, Ab50000 pumps, suffered from mechanical reliability issues, with average 1-year and 2-year survival rates of 65-71%, and 24-33%, respectively<sup>21-24</sup>. Driven to improve mechanical simplicity and reduce size, second-generation pumps such as the Jarvik 2000, HearAssist5, and the HeartMate 2 (HM2), were axial flow devices. Second-generation devices achieved significantly improved survival rates, primarily due to increased reliability, and lower

rates of stroke and thrombosis<sup>25–27</sup>. Axial flow LVADs operate at high rotational speeds (8000–15000 RPM<sup>112</sup>) to achieve the needed pressures, which in turn results in high hemodynamic shear stress. High non-physiological shear stresses caused blood damage and high rates of pump thrombosis, hemolysis, and vWF Disease. Following the need to reduce shear stresses, the third and most recent generation LVADs such as HeartMate 3 (HM3), DuraHeart, VentrAssist, and HVAD, used centrifugal pump configurations that operate at lower speeds (1000–6000 RPM)<sup>14</sup>. A signature feature of third-generation LVAD designs is to replace mechanical bearings in favour of magnetic or hydrodynamic levitation systems. HM3 and DuraHeart, which have fully magnetically levitated bearing systems have the biggest improvements in 1-year survival rates, at 86.2% and 77%, respectively<sup>28,29</sup>. The increased mortality rate (half of deaths) during the DuraHeart clinical trials can be attributed due to electrical reliability issues. Hydrodynamic bearing systems such as VentrAssist, or hybrids such as HVAD, exhibit higher rates of thrombosis and worse survival rates<sup>20</sup>. Incidence rates of pump thrombosis were nearly eliminated for HM3 (1-year <2%)<sup>30,31</sup>. Neal et al.<sup>32</sup> find evidence of microthrombi formation and significant sublethal despite the absence of pump thrombosis. Relatedly, average incidence rates of stroke and right ventricular failure are not significantly different between second and third-generation devices: 8% of patients experienced thromboembolic stroke after 1 year for both HM2 and HM3 and 27–28% of patients experience RVF after 1 year<sup>26,33,34</sup>. GI Bleeding and Infection rates are, however, improved for HM3 in comparison to HM2 (1-year incidence are 12% and 33% for HM3, vs 25% and 40% for HM2, respectively)<sup>33</sup>. The shift to centrifugal flow pumps and elimination of heat-generating elements has succeeded in dramatically reduced rates of lethal hemolysis and pump thrombosis in the HM3 and HVAD<sup>30,31</sup>. Due to these improvements and better clinical management procedures, medium-term survival rates of MCS have risen to rates that approach those of heart transplantation<sup>25</sup> (87% and 84%, 1- and 2-year, respectively).

MCS is consequently increasingly being used as an alternative to heart-transplantation (a destination therapy, DT); DT accounted for 70% of MCS implants in the US since 2019<sup>33</sup>.

### **2.1.2 Pathology of Complications Associated with Non-Physiological Flow**

The myriad MCS-associated complications can risk the lives of patients and severely reduce the quality of life. Gastro-intestinal (GI) bleeding and infections together account for over 50% of re-hospitalizations but are less severe, whereas the persistent risks of stroke, and right ventricular failure (RVF) are less common but are associated with substantially increased morbidity<sup>33</sup>. Consequently, five-year survival rates remain low due to the compounded risks

from secondary complications (in particular, thromboembolic, and hemorrhagic stroke), the incidence rates of which have not substantially improved<sup>20,33</sup>.

MCS-associated complications can be classified into those pathogenically linked to blood damage, and interactions with the body's various systems. The subsequent sections will briefly discuss the pathogenesis and diagnosis of these issues and the ever-present connection between blood damage and the negative health outcomes of long-term implantation. While MCS is used as a focus point for the analysis of medical devices, it is important to note that these phenomena are ubiquitous to any blood-wetted medical device that exposes blood to elevated levels of stress and or material foreign to the body for an extended time. These include artificial heart valves, stents, guidewires, cannula, extracorporeal oxygenation, and so on.

#### *Lethal and Sublethal Hemolysis*

Hemolysis is caused by the exposure of blood cells to elevate stress levels over time<sup>6</sup>. This can either rupture the RBC membrane (lethal hemolysis), spilling the RBC contents such as hemoglobin (Hb), ADP, ATP, etc., into plasma, or cause gradual (sublethal) damage that results in loss of RBC deformability, or the slower diffusive transfer of RBC contents through pores opened on the RBC membrane by stress application (mechanoporation). Other forms of sublethal hemolysis due to sustained load to the RBC membrane include degradation of membrane properties such as deformability leading to anemias, changes of blood viscosity similar to sickle cell disease and impaired oxygen transport in a kind of accelerated aging<sup>35–38</sup>. As noted, sublethal or subclinical hemolysis occurs at NIH ratios less than 0.1% and suffers from a lack of indicators such as bilirubin or lactate dehydrogenase (LDH) present during membrane rupture, making it difficult to detect. The application of stress leads to what can be viewed as the accumulation of strain on the red blood cell membrane over time, due to the viscoelastic and viscoplastic properties of the RBC membrane. High stress applied over a brief time can thus be as damaging as low stress applied over a longer time. Generally, when strain reaches a critical threshold, the RBC membrane ruptures, and the contents are released.

An elevated level of extracellular plasma-free hemoglobin (pfHb) has profound consequences for homeostasis. Low levels pfHb can cause spontaneous blood clot formation even at low concentrations (30 mg/dL, or about 8% of Hb concentration in an RBC)<sup>39</sup>, but is also highly toxic because Hb binds to nitric oxide (NO). NO is a natural vasodilation agent, and its removal leads to blood vessel contraction (vasoconstriction), hypertension, kidney (renal) damage, and enhances platelet activation due to increased shear stress levels. NO is also a potent thrombin

inhibitor, interfering with platelet aggregation by moderating vWF reactivity<sup>40</sup>, and from this perspective its absence leads to the increased risk of stroke, deep-vein thrombosis, atrial fibrillation and coronary atherothrombotic disease to name a few. PfHb also binds to the glycoprotein of von-Willebrand factor making it hyper-reactive, leading to hypercoagulability. Adenosine Diphosphate (ADP) contained in red blood cells is also a potent platelet activator, which can trigger blood clot formation.

Diagnostic indicators for hemolysis are elevated levels of pfHb, low haptoglobin, LDH, and bilirubin, which are produced during RBC membrane destruction<sup>41</sup>. Indirect indicators are symptoms of anemia in the absence of other bleeding, and diagnostic indices for thrombosis<sup>42</sup>. Diagnosis of hemolysis is strongly associated with increased morbidity and thrombosis<sup>43,44</sup>. Thrombus formation, by constricting the flow path, can also increase hemodynamic shear stresses leading to hemolysis<sup>45</sup>. Incidence of lethal hemolysis is, however, low in modern LVADs (<1%)<sup>42,46–50</sup> thanks to a decade of design optimization to reduce its incidence. Sublethal hemolysis can be difficult to detect due to a lack of indicators (bilirubin and LDH are generated during membrane destruction) and is consequently generally underreported<sup>51,52</sup>. Consequently, there are fewer studies relating sublethal hemolysis to clinical outcomes.

### Thrombosis

Blood clots form when the coagulation cascade is triggered. In the case of MCS, platelets are activated by shear stress, become adhesive and bind to surfaces where shear stress is low. If a sufficient level of platelet activation is reached so that activated platelets adhere to a surface, a thrombus can begin to grow. The thrombus impedes blood flow as it grows, increasing shear stress locally and reducing blood flow throughout the pump (pump thrombosis). Thrombus that are embolized (separated from the source surface) can block blood vessels (embolism), depriving organs and tissue of oxygen (ischemia) causing cell death; manifested as a stroke, local necrosis, organ damage, etc. Occlusive thrombus grown in in the LVAD (pump thrombosis) impair flow, which causes a sudden reduction of cardiac output and insufficient blood flow, causing stroke, organ failure, and death.<sup>25</sup> Thrombosis can be diagnosed through a variety of biochemical markers such as sharp spikes in levels of LDH (also a product of platelet activation), or subtherapeutic levels of international normalized ratio (INR) (<0.7), which is an indirect measurement of thrombin levels<sup>53</sup>. Pump thrombosis is also indicated by hemolysis, and by mechanical indicators of blockage such as a sharp rise in pump electrical power with a corresponding decrease in blood pressure.<sup>54</sup> To mitigate the risk of thrombosis, MCS is accompanied by the administration of antithrombotic drugs such as anticoagulation and

antiplatelet therapy. Antithrombotic therapies, interfering with clotting, increase the risk of hemorrhage, bleeding, GI issues, and can cause myriad other issues such as heparin induced thrombosis<sup>55</sup>. Until 2018, pump thrombosis was the leading cause of death in MCS patients<sup>33</sup> due to the limited efficacy of non-surgical interventions such as thrombolytic drug therapy. Failing immediate thrombolytic drug therapy, LVAD explant and replacement or heart transplant remain the only effective interventions<sup>56–59</sup>.

#### Stroke and neurological events

Stroke is caused by a loss of blood flow to the brain, which leads to oxygen deprivation (ischemia) and cell death. This can occur by a variety of mechanisms, but generally when a blood vessel is blocked by a thrombus (thromboembolic), or when a blood vessel ruptures (hemorrhagic). Thromboembolic stroke, and hemorrhagic stroke account affect nearly one third of LVAD implants<sup>60,61</sup>. Hemorrhagic stroke is influence by fibrillation (stiffening), high blood pressure, NO deprivation, aneurysm, calcification among other factors, but generally occurs when excessive pressure causes a weak spot in a blood vessel to burst. The causes of thromboembolic stroke, occurs in between 5%<sup>31</sup>-24%<sup>62</sup> of LVAD implants, are difficult to ascertain as the pathogenesis of thromboembolism is multifactorial. A blood clot can develop locally, or it can be developed upstream and then carried into a location where it is lodged. Despite substantial reduction in rates of both hemolysis and pump thrombosis in third generation MCS, incidence rates of thromboembolic stroke remain stubbornly high at nearly 10% for HM3<sup>34</sup>. Neal et al.<sup>32</sup> suggested that there is a link between microthrombi formed in MCS, which are embolized and carried into the blood stream. In general, however, the pathogenesis of MCS-related thromboembolism is largely unknown.

#### GI Bleeding and von-Willebrand Factor Disease

GI bleeding occurs in approximately 23% of LVAD patients with a 9.3% recurrence rate<sup>63</sup>. It occurs far more frequently in continuous flow LVADs (28% overall, but slightly less frequently in centrifugal pumps<sup>33</sup>) rather than pulsatile LVADs (6%)<sup>64–67</sup>. The bleeding itself is caused by lesions in the stomach and the duodenum<sup>63</sup>, though there is some debate regarding the root cause. Healy et al.<sup>68</sup> implicate the long-term usage of anti-coagulation and anti-platelet therapies, but it is difficult to establish causality because anticoagulation therapies are universally used in MCS whereas GI bleeding is not universal. Letsou et al.<sup>69</sup> suggest that the lack of pulsatility causes valve dysfunction that leads to endothelial dysfunction. Pulsatility helps blood enter the microvasculature, its absence leads to poor blood flow in small blood vessels leading to regional hypoxia, vascular dilation and angiodysplasia. Several studies<sup>70–72</sup>

suggest that GI bleeding is linked to acquired von-Willebrand Factor Disease (vWFD). vWFD is caused by degradation of von-Willebrand Factor (vWF), a long, spiral protein present in plasma that is essential to platelet adhesion and angiogenesis (formation of new blood vessels); impaired function in turn causes bleeding. The high mechanical shear stresses in LVADs have been shown to lead to cleavage of high molecular weight molecules, decreasing vWF concentrations, and causing vWFD<sup>73–76</sup>. Stress also activates thrombogenesis and leads to increased platelet adhesion<sup>77–80</sup>. These combined effects lead to increased incidence of formation of weaker clots than normal.<sup>67,81</sup> Due to higher rates of clot formation, and weaker clot strength, GI bleeding and vWFD are associated with a 7.4x increase in the likelihood of another thromboembolic event.<sup>82</sup> It is noted here, however, that due to the comorbidity of many of these effects, it is often difficult to disentangle vWFD from the other MCS-associated complications. Gastrointestinal bleeding is diagnosed by checking for plasma coagulation by injecting a sclerosing agent to detect the lesions and is generally treatable by enteroscopy<sup>63</sup>.

#### Right Ventricular Failure

Right ventricular failure (RVF) after LVAD implantation is the single greatest risk factor for early mortality in modern LVADs<sup>83</sup>. RVF occurs overwhelmingly in the first month, then between 29-33% of device implants experience RVF after the first year<sup>33</sup>. RVF can be caused by many factors, though in general, is the result of progressive overstraining of the heart muscle leading to gradual loss of RV contractility<sup>84</sup>. Implantation of an LVAD increases cardiac output and venous return to the RV from the left ventricle (LV)<sup>85</sup>, which dilates the RV and decreases RV output to the LV, and in turn LV output. A significant portion of RV output comes from the LV, and thus RV contraction is impaired further in a feedback effect, increasing load to the RV<sup>86</sup>. The increased load on the RV can overwhelm patients with weakened right ventricles. RVF is generally indicated by increases in the ratio of pulmonary capillary wedge pressure relative to central venous pressure<sup>87–90</sup>, as well as a variety of biochemical indicators<sup>88,91</sup>, though there is a general lack of accepted diagnostic criteria<sup>92</sup>. Treatment options for RVF are effectively limited to Bi-ventricular support, for which survival rates are significantly lower than left ventricular support (60% vs 84% after 2 years)<sup>93</sup>. Clinical management options involve the administration of inotropes to increase RV contractility, or modification of LVAD speed to mitigate load on the RV. Several studies have attempted to develop indices to predict RVF using pressure, ECG signals, inter-ventricular septum geometry<sup>90,94,95</sup>, as well as ECG imaging of RV geometry<sup>96–99</sup>, with limited success. The biggest risk factor is the prior presence of an arrhythmia, which can double the chance of RVF<sup>100</sup>. There is a strong need to improve

the predictive capability of RVF risk and to better understand the hemodynamic interaction between LVAD and an individual's LV and RV dynamics. For a more detailed discussion, the reader is referred to Konstam et al.<sup>84</sup>

### Infections

Infections are the most common complication of MCS, occurring in between 33-43% of MCS implants<sup>33</sup>, and are the main cause of rehospitalization<sup>101–103</sup>. Three major types of infections are associated with LVADs, driveline infections, pocket infections, and bloodstream infections<sup>104,105</sup>. Driveline and pocket infections are most common but are treatable with standard antimicrobial techniques<sup>106</sup> and are not themselves associated with high mortality, though up to 43% of patients with driveline infections developed bloodstream infections<sup>107</sup>. Bloodstream infections are relatively rare, and though also treatable are associated with increased risk of both hemorrhagic and ischemic stroke<sup>108–110</sup>. The risk of infection is pernicious, however, and cumulatively after four years is the largest contributor to MCS mortality<sup>111</sup>. For a comprehensive review of infections, the reader is referred to O'Horo et al.<sup>105</sup>.

### **2.1.3 Future Perspectives on Non-Physiological Flow Associated Pathologies**

Recent developments in LVADs have focused on addressing secondary complications. For example: using advanced control schemes to incorporate pulsatility to reduce GI bleeding, vWFD, as well as attaining better RV compatibility<sup>112</sup>. Other works aim to replace percutaneous drivelines using transcutaneous wireless power transmission<sup>113,114</sup>, with several promising in-vitro and in-vivo studies completed<sup>115</sup> or in-progress<sup>116</sup>.

Important fundamental challenges remain, however, such as the fluid-structure coupling between LVAD and the vascular system and ventricles, as well as developing more accurate models of blood damage that can predict things such as thromboembolism. Hemodynamic modelling is a crucial tool for virtually testing medical devices exposed to blood flow and can reduce both the cost of device development and the risk to patients undergoing experimental therapy. Improved prediction not only helps eliminate MCS complications but can be useful for clinical management to assess the increase in patient-specific risks from stroke<sup>117</sup>, aneurysm rupture<sup>118</sup> and atherosclerosis<sup>119</sup>, assessing dangers from comorbid conditions, for aiding clinical decision making<sup>120,121</sup>, and developing novel drug delivery systems<sup>122</sup>, and lab-on-a-chip devices.

Furthermore, while hemolysis can cause thrombosis and vice versa, it is unclear which precedes which, what level of hemolysis causes thrombosis, and under what conditions. Furthermore,

though microthrombi growth on VADs is theorized to cause thromboembolism, it is unknown whether microthrombi can grow in the VAD (they are difficult to detect or as the event is fast and inherently transient), under what conditions this occurs, how long they can survive in the bloodstream, and whether varying blade speed in the VAD can exacerbate thrombus growth and embolization.

## 2.2 Fluid Dynamics of Blood Flow

Homeostasis is the system of physiological processes that maintain blood flow and pressure through the vascular system and thus ensure a steady oxygen and nutrient supply to vital organs and tissue throughout the body. Blood is a complex multiscale dynamic system, macro-scale modelling of blood flow requires addressing several challenges unique to blood: complex non-Newtonian rheology, the relative motion of the constituent phases of blood, and the turbulent behaviour of blood. The vasculature adapts to hemostatic disturbances, and in general blood flow involves biochemical and cellular feedback mechanisms. The muscular response of the vasculature and formation of hemostatic plugs, for example, is regulated by the mechano-sensitive endothelial cell layer lining the vascular system<sup>123</sup>.

Blood is a dense suspension that is composed of red and white blood cells (RBCs, and WBCs), and platelets. RBCs comprise 35-55% of blood volume (the volume fraction is called 'hematocrit'), another ~1% is WBCs and <1% platelets. RBCs are approximately 6-9 $\mu\text{m}$  in diameter and biconcave ellipsoid in shape, WBCs are 10-15 $\mu\text{m}$  diameter spheres, whereas platelets are ~2 $\mu\text{m}$  elliptical discoids. There is approximately  $5 \cdot 10^6$  RBCs and  $3 \cdot 10^6$  platelets per millimetre of blood<sup>124</sup>. Plasma, the carrier fluid, is a Newtonian mixture of 92% water, and a variety of proteins, metabolites, and ions that are necessary for various physiological processes<sup>125</sup>. Cytoplasm, the fluid inside of RBCs, and plasma have similar density, though the viscosity of Cytoplasm, which is mostly hemoglobin, is 4-5 times that of plasma<sup>126</sup>. RBCs, which have a dominant impact on the mechanical properties of blood<sup>127,128</sup>, behave like fluid-filled sacs (vesicles), whose lipid bi-layer membrane has hyperelastic and viscoelastic and -plastic properties allowing it to experience immense deformations in shape. The RBC membrane has a spectrin cytoskeleton organized as a triangular mesh with hexagonal symmetry that reinforces the membrane and makes it highly resistant to area extension<sup>129</sup>. These complex material properties make the dynamics of the RBC very difficult to model and predict, and effectively give blood its unique properties. The effect of other major constituents of blood such as WBCs and platelets on the bulk fluid properties can be neglected because of their relatively minor volume fraction.



### 2.2.1 Dynamics of Blood Cells and Blood Constituents in Flow

Direct cell simulations that resolve fluid and structural dynamics of plasma and RBCs are increasingly used as a surrogate for experimentation to study mechanisms of cellular dynamics, though such simulations are immensely computationally expensive. Red blood cells have been observed to experience a variety of dynamic states, depending on the shear rate experienced, illustrated in Figure 1. At shear rates below  $1 \text{ s}^{-1}$ , the intercellular osmosis and attractive ionic forces between cells and plasma proteins such as fibrinogen cause the formation of stacked RBC aggregates called rouleaux. Below shear rates of approximately  $100 \text{ s}^{-1}$ ,<sup>130–132</sup> the bending and mechanical stiffness of the RBC membrane resists deformation applied by the viscous and normal stresses in the fluid, and the red blood cells tumble like solids. Between these shear rates, the rouleaux break up and blood cells gradually begin to tumble. Above these shear rates the cell membrane rotates about the contents of the cell like the tread of a tank (called ‘tank-treading’). At this point the red blood cell takes an approximately ellipsoidal profile as it is stretched by the shear and becomes approximately aligned with the principal axis of the stress tensor. Generally, the transition to tank-treading motion depends on the ratio of viscosity between the inner and outer fluid (between 0.125-0.25) and peak extension of the stretched RBC. Increasing viscosity ratio leads to rigid-body like behaviour.<sup>133</sup> These studies neglect membrane bending stiffness and membrane viscoelasticity, which is required to reproduce experimentally observed<sup>134</sup> viscosity ratios at which tumbling transitions to tank-treading. Immersed Boundary methods are often used for multi-cell studies<sup>135–139</sup>. Some notable insights from these studies are that lubrication forces generally prevent cell-cell collisions<sup>138</sup>, and that RBC deformability contributes to the shear-thinning behaviour<sup>140</sup>. An important finding is that the RBC deformation and tank-treading behaviour induced by high shear near walls results in a wall-normal component of lift force on the RBC, resulting in an RBC-depleted layer near walls<sup>137</sup>. This is part of the Fåhræus-Lindqvist effect, which is discussed in more detail later.

Multiphase CFD modelling can improve hemodynamic predictions of shear stress by accounting for RBC concentration effects on rheology and turbulence as well as elucidating platelet and chemical aggregation mechanics relevant to thrombosis and other blood-flow ailments. A major challenge in multiphase hemodynamic modelling is the general lack of closure relationships for interphase interactions. In the Lagrangian scheme, lift and drag models for RBC’s are extremely limited. Interphase forces are modelled using rigid<sup>141,142</sup> or deformable<sup>143</sup> particle analogies, or by droplet or bubble analogy<sup>144</sup>. RBC lift and drag forces are very sensitive to changes in RBC shape<sup>145,146</sup>, which is deformed substantially not only by

local flow conditions but also by the motion of nearby cells. The effect of deformation on lift is, however, generally better accounted for when using correlations measured from bubbly flows, which can qualitatively reproduce the Fåhræus–Lindqvist effect<sup>147</sup>. RBC-RBC interactions are yet another difficulty: lubrication forces and high deformability preclude the application of hard-sphere collision models.<sup>148</sup> All RBC lift and drag models assume that inter-particle spacing is much larger than particle diameter, and to date, no constitutive model accounts for the effects of nearby RBCs and deformability<sup>149</sup>. Virtual mass and buoyancy forces, however, can be neglected because RBC and plasma densities are similar. Explicitly tracking RBCs is prohibitively computationally expensive, due to the enormous RBC density. The largest known full-cell simulation study (5e6 RBCs)<sup>150</sup> uses a Fully Eulerian approach for membrane mechanics<sup>151,152</sup>, where the deformation tensor of solid phases is transported and conserved in the Eulerian reference frame, the merits of which are discussed later.

The diffusion and transport of dispersed phases such as platelets are driven by RBC motion. The diffusion mechanism is generally shear driven, several orders of magnitude higher than Brownian diffusion, and is strongly affected by collisions with red blood cells<sup>127,153–155</sup>. Effectively, as shear rate increases the frequency of collisions between platelets and RBCs increases, as does the velocity induced on platelets trapped between RBCs and the likelihood that they can pass between layers of RBCs. Consequently, platelet diffusion rate increases in proportion to shear rate<sup>138</sup>; this is also discussed later.

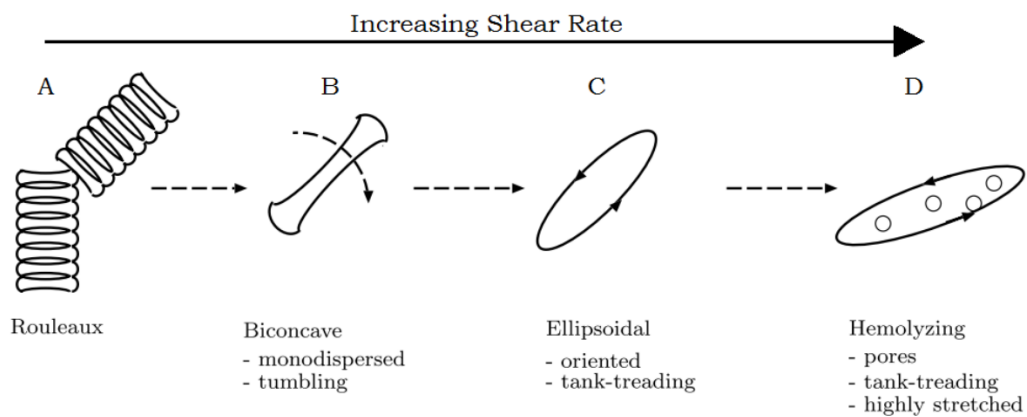


**Figure 1: Schematic depiction of the various RBC dynamic states at the different shear rates.**  
*Adapted from Arora et al<sup>7</sup>*

### 2.2.2 Continuum Modelling of Whole Blood and Blood Flow

#### Viscosity

Blood is a shear-thinning fluid, meaning that at low shear rates viscosity increases exponentially with decreasing shear rate, illustrated in Figure 2. The viscosity of blood is profoundly important to homeostasis. Abnormalities in blood viscosity are associated with disorders such as leukemia, sickle cell disease and polycythemia<sup>156</sup> and significant risk of adverse cardiovascular events<sup>157</sup>. At lower shear rates the red blood cell membrane is stiff relative to forces imposed by the fluid. The inter-cellular forces caused by concentration gradients (osmotic forces) and electrostatic forces between proteins in plasma and the RBC membrane have sufficient time to influence intercellular mechanics.<sup>158</sup> These forces bind RBCs into stacked aggregates called ‘rouleaux’, and it is the process of overcoming these forces, and their diminished magnitude as the relative velocity between RBCs increases, that results in the order of magnitude increase in viscosity at lower shear rates<sup>159</sup>. Consequently, the viscosity of blood also depends on RBC deformability and diameter, hematocrit<sup>160,161</sup>, and protein concentrations in plasma. Hemoglobin properties in RBCs have a direct effect on red blood cell viscosity<sup>127</sup>, abnormalities such as polymerization between hemoglobin molecules cause sickled cell anemia<sup>162</sup> resulting in reduced RBC deformability, and tendency to aggregate.

Blood rheology can generally be understood by conceptualizing it as a suspension of particles, mixture viscosity varies as a function of shear rate and constituent volume fractions: this reflects mechanisms of inertia and interparticle interactions on the fluid stress tensor<sup>163,164</sup>.

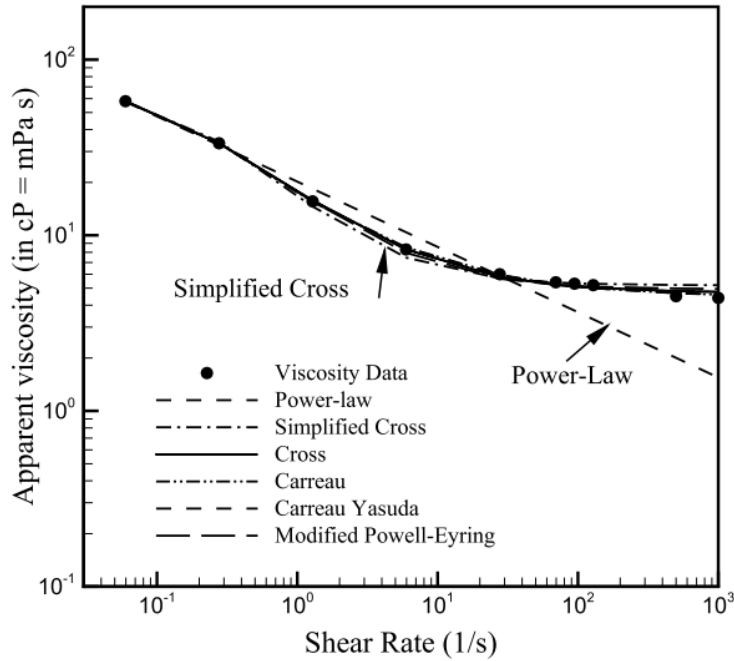


**Figure 2: Apparent blood viscosity is shown as a function of shear rate, along with several well known non-Newtonian constitutive viscosity models. Adapted from Robertson<sup>162</sup>.**

As shear rate increases, RBC clusters and rouleaux break up, and finally, red blood cells cease tumbling but disperse and align with the flow. After some threshold shear rate consequently, blood begins to behave like a Newtonian fluid.<sup>165</sup> As might be expected, the shear rate threshold is a function of hematocrit, and any parameter affecting intercellular forces,<sup>166</sup> but is generally between  $50^{165}$  and  $300^{167} \text{ s}^{-1}$ . Consequently, in cases such as flow in large arteries where the shear rate is expected to be high, blood rheology is often approximated as Newtonian. This is a good assumption in steady flows and is shown to produce similar wall shear stress values to non-Newtonian rheology models<sup>168</sup>. Blood is in general pulsatile, however, and shear rates vary between 0 and  $1000(\text{s}^{-1})$  during the cardiac cycle<sup>169</sup>. In complex and highly unsteady flows such as stenosed blood vessels, the Newtonian (and non-viscoelastic) assumption has been shown to fail to reproduce important phenomena such as flow separation and underpredict shear stress in unsteady flows<sup>168,170</sup>.

Many rheology models for blood have been derived from numerous existing rheological datasets, which are reviewed exhaustively by Yilmaz and Gundogdu<sup>171</sup> and more recently by Beris<sup>172</sup>. Popular data-driven models with sole dependence on shear rate (that predict shear stress well at intermediate shear rates in steady flows<sup>173</sup>) are the generalized power law<sup>174</sup>, Carrau,<sup>169</sup> Casson<sup>166</sup>, Cross, and Powell-Eyring models. The power law is the most simple to

implement but as can be seen in Figure 2, does not produce a great fit of rheological data and doesn't capture phenomena such as the yield stress in blood.

The Casson model has the most flexibility to incorporate various physiological parameters such as fibrinogen concentration and hematocrit, though is difficult of being complex to implement numerically. For this reason, popular Computational Fluid Dynamics (CFD) solvers such as ANSYS Fluent make this model available in laminar but not turbulent solution schemes. The Casson<sup>175</sup> and Walburn-Schneck<sup>173</sup> models incorporate hematocrit and perform well at low shear rates<sup>176</sup>. The Generalized Carreau-Yasuda generalized model is given as:

$$\mu = \mu_{\infty} + (\mu_0 + \mu_{\infty})(1 + (\lambda\dot{\gamma})^p)^{\frac{n-1}{p}} \quad 2-1$$

Parameters for this model can be found abundantly in the literature<sup>171</sup>, though accepted values are, 1.902 [s], 0.22, 1.25, 0.056 [cP] and 0.00345 [cP] for  $\lambda$ ,  $n$ ,  $p$ ,  $\mu_{\infty}$  and  $\mu_0$ , respectively. The Carreau model has an identical form, but  $p = 2$ , and 25, 0.25, 0.025 and 0.0035 for  $\lambda$ ,  $n$ ,  $\mu_{\infty}$  and  $\mu_0$ , respectively. Apostolidis and Beris<sup>177</sup> develop a temperature, hematocrit, and fibrinogen concentration-dependent modified Casson model, given below. The parametric Casson model gives stress fluid stress,  $\tau$ , as

$$\sqrt{\tau} = \sqrt{\tau_y} + \sqrt{\mu\dot{\gamma}} \quad 2-2$$

$$\tau_y = \begin{cases} 0.3126c_f^2 - 0.468c_f + 0.176, & Hct > Hct_c \\ 0, & Hct \leq Hct_c \end{cases} \quad 2-3$$

$$Hct_c = \begin{cases} 0.3126c_f^2 - 0.468c_f + 0.176, & c_f < 0.75 \\ 0, & c_f \geq 0.75 \end{cases} \quad 2-4$$

$$\frac{\mu}{\mu_p} = (1 + 2.07Hct + 3.72Hct^2) \cdot \exp\left(-7.03\left(1 - \frac{T_0}{T}\right)\right) \quad 2-5$$

Where  $\mu$ ,  $\mu_p$  are blood and plasma viscosities,  $\tau_y$  is a yield stress,  $\dot{\gamma}$  is the shear rate, and  $c_f$  is normalized fibrinogen concentration.

Models have also been developed to account for thixotropy or viscoelasticity, though no model accounts for all complexities. The Carreau model is most commonly used to model blood viscosity in simulations of low shear rate blood flow where hematocrit is not highly variable. In high-shear rate flows in excess of  $10^3 \text{ s}^{-1}$  it has been shown<sup>173</sup> that there is no significant difference between the wall shear stress distribution obtained by using Newtonian viscosity

models and non-Newtonian viscosity modelling. It is consequently common in high blood-flow cases where shear rate exceeds  $10^3 \text{ s}^{-1}$  to use a Newtonian viscosity of approximately 3.5 cP to model blood rheology. Presently, it is noted that this assumption is somewhat erroneous in complex flows, hematocrit can vary significantly spatially as a function of shear rate, modifying rheology. Furthermore, when modelling hemolysis, the particle residence time is nearly as important as the magnitude of shear. In a typical device, the volume of blood exposed to high shear is much lower than that exposed to low shear, meaning that increased viscosity in low-shear regions with relatively stagnant flow such as vortices produces a significant effect on hemolysis. Finally, although peak shear rates are high in large arteries and MCS, important mechanics such as blood clot formation generally occur in regions of stagnant flow and low shear rate.

#### Viscoelasticity and Thixotropy

The thixotropy behaviour of blood, which is the time-dependant viscosity of blood, is generally manifested at shear rates  $<1(\text{s}^{-1})$  and is resultant of the osmotic forces<sup>178</sup>. In this study, we consider supra-physiological conditions and thus thixotropy of blood is generally outside of its scope. The viscoelastic behaviour of blood arises from the RBC membrane's ability to store and dissipate elastic energy. In general, viscoelasticity is often neglected when modelling blood. Here it is acknowledged that blood viscoelasticity is important, but because this study focuses on dynamics within the steady-state portion of flow the effect of viscoelasticity is left for future work and is not covered in depth.

The most popular viscoelastic models for blood are Oldroyd-B models, developed, for example by Yeleswarapu,<sup>179</sup> due to their simplicity and ability to predict stress well in simple shear flows. Good<sup>180</sup> notes that these models tend to overpredict the polymeric stress component in extensional flows, and so add a Giesekus and Leonov term to incorporate a drag force into the stress formulation. Simulating pulsatile blood flow in an aorta, they find that Newtonian viscosity models grossly overpredict stress compared to their viscoelastic formulation. Pinto et al.<sup>181</sup> present the most comprehensive viscoelastic treatment, wherein Eulerian transport equations are used to model fluid deformation by conservation of the left Cauchy deformation tensor which is used to compute the solid stress component. Likewise, they find that Newtonian viscosity treatments generally overpredict wall shear stress in pulsatile physiological-range flows, as does the Generalized Oldroyd-B model.

### CFD Modelling of Blood Flow in MCS

Computational fluid dynamics (CFD) is a popular tool for hemodynamic analysis. Velocity and pressure fields of the fluid are solved by discretizing and linearizing mass, momentum, and energy conservation equations<sup>182</sup> which idealize the fluid as a single or combination of homogeneous continua. In the classical finite-volume approach, the Eulerian reference frame is used for analysis. A fluid-filled volume is broken up into geometric primitives so that the conservation laws in these primitives when discretized form a sparse system of linear algebraic subproblems. An extensive body of work is devoted to solving such systems as well as the modelling complexities of CFD in general<sup>183–186</sup>; CFD methods are discussed exhaustively in the methods. In the context of MCS, which almost always includes non-physiological flow conditions, computational fluid dynamics simulations typically use Newtonian viscosity models, neglecting temperature changes, and assuming uniform phase behaviour.

### Turbulence in Blood Flow

Most (96%<sup>187</sup>) hemodynamic CFD studies do not model turbulence because Reynolds numbers of physiological flows are typically in the laminar regime by hydrodynamic stability criteria<sup>182</sup> and the shear-thinning effect is known to increase stability<sup>188</sup>, while studies that do model turbulence generally use standard two-equation models<sup>187</sup>. Laminar hemodynamic modelling is controversial, as the turbulent contribution to shear stress in non-physiological flows such as in the HM2 is generally between 60-100 Pa, enough to cause sublethal hemolysis<sup>189,190</sup>. Furthermore, hydrodynamic turbulence stability criteria are not applicable because vascular flows are highly unsteady, and indeed recent stability calculations find that unsteady vascular flows are globally unstable<sup>191</sup>. Furthermore, turbulence has been measured in-vivo in the Carotid arteries of healthy patients<sup>192,193</sup>, and is known to behave very differently from typical single-phase hydrodynamics. The decay rate of the turbulence kinetic energy cascade measured in the carotid artery is also substantially greater than in similar hydrodynamic flows. As the conventional-two equation modelling predicts that the Kolmogorov length scale in non-physiological flows is an order of magnitude higher than the average RBC diameter, due to the increased dissipation arising from relative motion between red blood cells Antiga and Steinman suggest that the RBC diameter should be the limiting scale<sup>194</sup>. Unfortunately, little work exists on the subject, and methodological guidance and validation on the hemodynamic application of common two-equation models is badly needed. In the presence of high-frequency flow oscillations, and non-physiological flow conditions, these effects generally become more important<sup>194–196</sup>.

### 2.3 Mechanical Properties of the Red Blood Cells Membrane

The red blood cell's main function is to transport oxygen and carbon dioxide, which is accomplished by the highly oxidative hemoglobin protein contained in abundance in the Cytoplasm found in RBCs. The cytoplasm also includes ADP, ATP, and other constituents. Red blood cells are anucleate and eject their nucleus and most of their organelles, such as their mitochondria, within 24 hours of entering the bloodstream. Remarkably, the red blood cell can survive for approximately 120 days without any of the organelles which normally are responsible for regeneration, cell life, and reproduction. This feat is accomplished by the remarkably resilient red blood cell membrane, which is composed of a lipid bilayer that is reinforced by a spectrin fibre mesh (see Figure 3). Spectrin fibres are connected primarily by actin, and myriad other proteins that bind it to the lipid bilayer. The spectrin fibres are what give the red blood cell its remarkable toughness and ability to resist biaxial (area) stress. There are a wide variety of molecules that make up the red blood cell membrane, for reference, the reader is referred to Lux<sup>197</sup>.

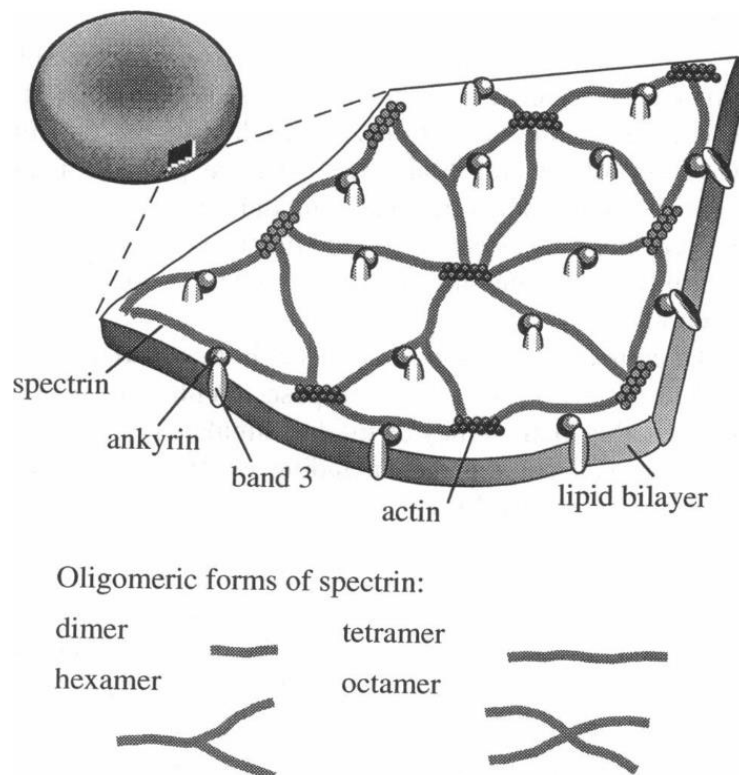


**Figure 3: Schematic illustration of the red blood cell membrane and arrangement of proteins that comprise the cytoskeleton. Adapted from Hansen et al<sup>198</sup>.**



### 2.3.1 Resting Shape of the Red Blood Cell

The red blood cell has an ellipsoid biconcave shape at rest, a bit like a donut. Evans and Fung<sup>129</sup> and Fischer<sup>199</sup> measured the bi-concave undeformed resting shape of red blood cells extracted from a 30-year-old male using the form given below.

$$D(r) = \sqrt{1 - \left(\frac{r}{R_0}\right)^2} \left( C_0 + C_2 \left(\frac{r}{R_0}\right)^2 + C_4 \left(\frac{r}{R_0}\right)^4 \right) \quad 2-6$$

Where  $D(r)$  is the thickness in the direction outside of the circular plane,  $R_0$  is the average cell radius in the circular plane, and  $C_0$ ,  $C_2$ , and  $C_4$  are coefficients obtained from measurements which depend on the tonicity (degree of concaveness) of the red blood cell, which ranges from 131 to 300 mOsm. For a nominal tonicity of 131 mOsm, the values of  $R_0$ ,  $C_0$ ,  $C_2$ , and  $C_4$ , are 3.80  $\mu\text{m}$ , 2.10  $\mu\text{m}$ , .58  $\mu\text{m}$ , and -5.59  $\mu\text{m}$ , respectively.

Nominal RBC diameter and thickness are approximately 7.8 and 1.58  $\mu\text{m}$ , respectively, and membrane area is approximately 135  $\mu\text{m}^2$ . Parameters of the red blood cell shape seem to be normally distributed in shape, with standard deviations generally increasing for increasing tonicity (Osmolarity or fluid content), for tonicity of 300 mOsm, diameter, minimum thickness, maximum thickness, and surface area, and volume can vary by up  $\pm 0.62 \mu\text{m}$ , 0.35  $\mu\text{m}$ , 0.27 $\mu\text{m}$ , and 15  $\mu\text{m}^2$ , respectively.

There are a variety of approaches to modelling the red blood cell membrane. The seminal work by Skalak et al.<sup>200</sup> models the hyperelasticity of the RBC membrane as a two-dimensional hyperelastic material with strain energy given by Equation 2-7 from experimental measurements of membrane elasticity. Such a formulation captures the unique area-inextensibility of the hyperelastic membrane.

$$W = \frac{B}{4} \left( \frac{1}{2} I_1^2 + I_1 - I_2 \right) + \frac{C}{8} I_2^2 \quad 2-7$$

Here, B and C are constants that give the membrane stiffness properties, and  $I_1$  and  $I_2$  are the first and second invariants of the Green deformation tensor, respectively.  $I_1$  corresponds directly to the principle stretch, and  $I_2$  corresponds to the area stretch. Consequently, B is the linear elasticity modulus, and C is a kind of area extension modulus. The Piola-Kirchoff stress tensor,  $\sigma_{ij}$ , is obtained by differentiating strain energy by extensions in the coordinate system of choice.

$$\sigma_{ij} = \frac{\partial W}{\partial e_{ij}} \quad 2-8$$

Owing to its simplicity, Skalak's strain energy model is the de-facto gold standard and is used extensively<sup>151,201–203</sup>. Equation 2-7 is however often recast<sup>203</sup> in terms of an area expansion coefficient,  $\alpha = \frac{c}{2B}$ , and a membrane Stiffness coefficient,  $E_s$ .

$$W = \frac{E_s}{4} \left( I_1 \left( \frac{1}{2} I_1 + 1 \right) + I_2 (\alpha I_2 - 1) \right) \quad 2-9$$

Pozrikidis notes, that the area dilation coefficient of Skalak's original model, in which  $\alpha > 1e3 - 1e6$ , is excessively large and can result in numerical instability in simulation models. Freund et al.<sup>204,205</sup> found that  $16.2 \leq \alpha \leq 200$ , yielded adequately stiff membranes. Consequently, values for  $E_s$  range from  $4.2 \cdot 10^{-3} \frac{dyn}{cm}$ , and  $\alpha$  can have values ranging from 16~1000. Updated measurements of the RBC deformability and viscoelasticity by Dao et al.<sup>206</sup> Mills<sup>207</sup> have validated the strain-energy based model of Skalak. The ambiguity in the area extension coefficient and desire to model viscoelastic behaviour and rupture, however, has motivated more complex models of the RBC membrane based on filament networks to mimic the spectrin mesh. Inspired by earlier work by Hansen et al.<sup>198,208</sup>, Dao and Lim<sup>209,210</sup> sum the elastic energy of a regular isotropic mesh of spectrin filaments to create a unique continuum model, though this has not been implemented due to its complexity. Dao et al.<sup>206</sup> note however that there is a high degree of dependency of membrane behaviour on the mesh topology. The spectrin network is often idealized as a triangular mesh organized in a hexagonal array around hubs, and many of these triangular elements are uniformly sized. In reality, the spectrin network of the red blood cell is not so uniform and is composed of spectrin fibres connected in a wide variety of shapes and sizes.<sup>211</sup> Furthermore the ability of the network topology to dynamically readjust itself at both moderate and high levels of strain is a key feature of its highly resilient and viscoplastic behaviour<sup>212,213</sup>. This heterogeneous structure behaves quite differently from a triangular mesh network, which tends to add significant stiffness to linear deformation<sup>209</sup>. Furthermore, the spectrin tetramer fibres range from 20-100 nm in length, meaning that there are millions of spectrin tetramers on a single membrane, though often the membrane is approximated using a coarse triangular mesh. Consequently, such network-based approaches have a hard time consistently fitting bulk parameters due to the high degree of dependence of the stiffness on network topology, and usually the network parameters need to be fit to reproduce experiments with each simulation incarnation. Dao et al also note that RBC

mechanics and deformation are vastly different when incorporating internal and surrounding fluid. Although adequately resolved coarse-grained spectrin networks arguably better represent the physical mechanisms binding the membrane, continuum models are far more flexible, are not sensitive to topology, can incorporate material properties such as viscoelasticity without tuning, and are computationally more efficient. Early strain-energy based approaches therefore remain popular when simulating RBC dynamics<sup>152</sup>, and indeed Dimitrakopoulos<sup>214</sup> found that the shear-modulus hardening mechanism of the original Skalak formulation accounts for the hardening behaviour of the red blood cell under high shear. Recent work by Feng et al<sup>215</sup> attempts to bridge coarse-grained and continuum-based constitutive modelling of the RBC membrane using updated measurements of the protein network tomography. Following Discher et al.<sup>216</sup> and Boey et al,<sup>217</sup> they represent the energy of the spectrin network in terms of Cauchy-green deformations and, using natural distributions of the spectrin filament lengths obtained from Electron tomography, they obtain a strain-energy function per unit area depending on the distribution of spectrin-fibre lengths and topology angles. Aside from these few examples, however, there is a strong need for more continuum-based models for the red blood cell membrane.

### **2.3.2 Deformation of the Red Blood Cell Membrane**

The deformation and measurement of individual red blood cells is challenging owing to the small size of the red blood cell, the fact that its physics changes when immersed in fluid, and its viscoelastic properties. A variety of techniques have been developed to measure the mechanical response of micro-scale structures including nanoindentation, micropipette aspiration, optical tweezers, electrodeformation, electroporation, and micro-Couette shear flows, which are reviewed by Piontek et al.<sup>218</sup>. The micropipette aspiration and optical tweezer techniques remain the most reliable approaches to measure mechanical response of the red blood cell membrane. Micropipette aspiration<sup>199</sup> involves sucking the red blood cell into a micropipette whose aperture is smaller than the red blood cell diameter. The red blood cell deforms and the exposed portion which is in tension takes a spherical shape. The stress on the red blood cell membrane can be calculated from suction pressure. More recently, the usage of an optical trap (known as optical tweezers, illustrated in Figure 4)<sup>206,207</sup> provides the best available force-displacement measurements of the red blood cell. High refractive index silica

beads are bound to the red blood cell membrane. A 1.5W laser beam is used to trap one silica bead and can be used to exert a force of up to 600 pN<sup>219</sup>.

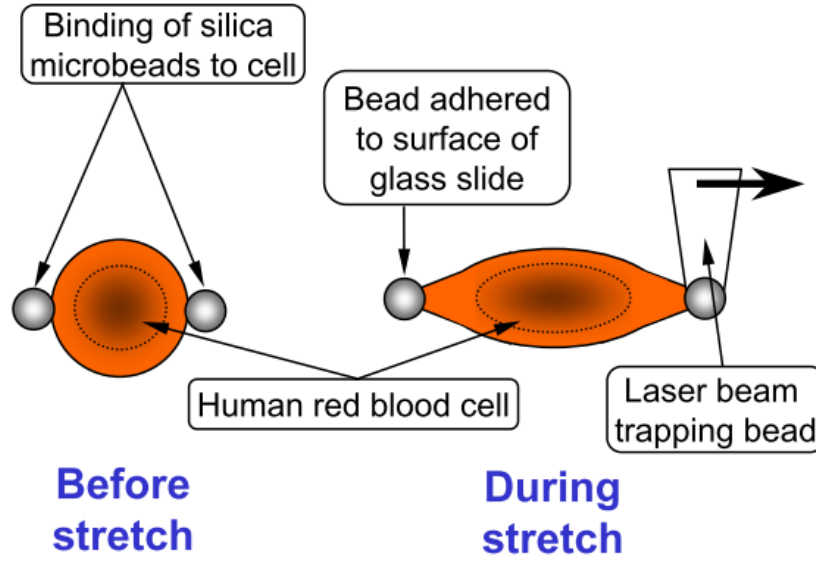


**Figure 4:** Schematic illustration of the process of stretching a red blood cell using the optical tweezer approach. Adapted from Dao et al<sup>206</sup>.

Dao et al. performed FEA of the red blood cell membrane using a neo-Hookean continuum strain energy and Yeoh model, the elastic strain energy function of which is given in Equation 2-10.

$$W = \mu_0 \left( (I_v - 3) + \mu_f (I_v - 3)^3 \right) \quad 2-10$$

They found that by using an area-incompressible elastic model (in which areal stiffness modulus was chosen to be sufficiently high) they could accurately reproduce the shape and force stiffness characteristics of the RBC membrane. Like Skalak<sup>200</sup>, who found that the initial shear modulus was between  $\mu_0 = 6 - 10.0 \frac{\mu N}{m}$ , they find a linear shear modulus of  $\mu_0 = 11.1 - 17.7 \frac{\mu N}{m}$  using a neo-Hookean model was necessary to fit the experimental deformation behaviour of the red blood cell. A follow-up study<sup>207</sup> found that the Yeoh hyperplastic model provided better representation of the elastic behaviour of the red blood cell membrane at higher strains (shown in Figure 5), and corrected the shear moduli to  $\mu_0 = 5.3 - 11.3 \frac{\mu N}{m}$ , and  $\mu_f = 13.9 - 29.6 \frac{\mu N}{m}$ .

Mills et al.<sup>207</sup> also characterized the viscoelastic behaviour of the red blood cell membrane by fitting elastic relaxation data after the releasing optical tweezer force, finding characteristic

relaxation time to be  $19 \pm 6$  ms, in line with previous estimates from Chien<sup>220</sup> and Hochmuth et al.<sup>221</sup> characterizing relaxation time between 10 – 30 ms. Although useful for obtaining the shear modulus of the red blood cell membrane, a notable omission of these works is the area of inextensible behaviour of the red blood cell membrane. In general, the Neo-Hookean and Yeoh models do not restrict area extensibility, which in higher strain regimes provides an asymptotic limit to the uni-axial strain. Furthermore, the loading of the red blood cell in this context is somewhat unphysical and loading by hydrodynamic forces does not concentrate the load at the ends of the membrane.

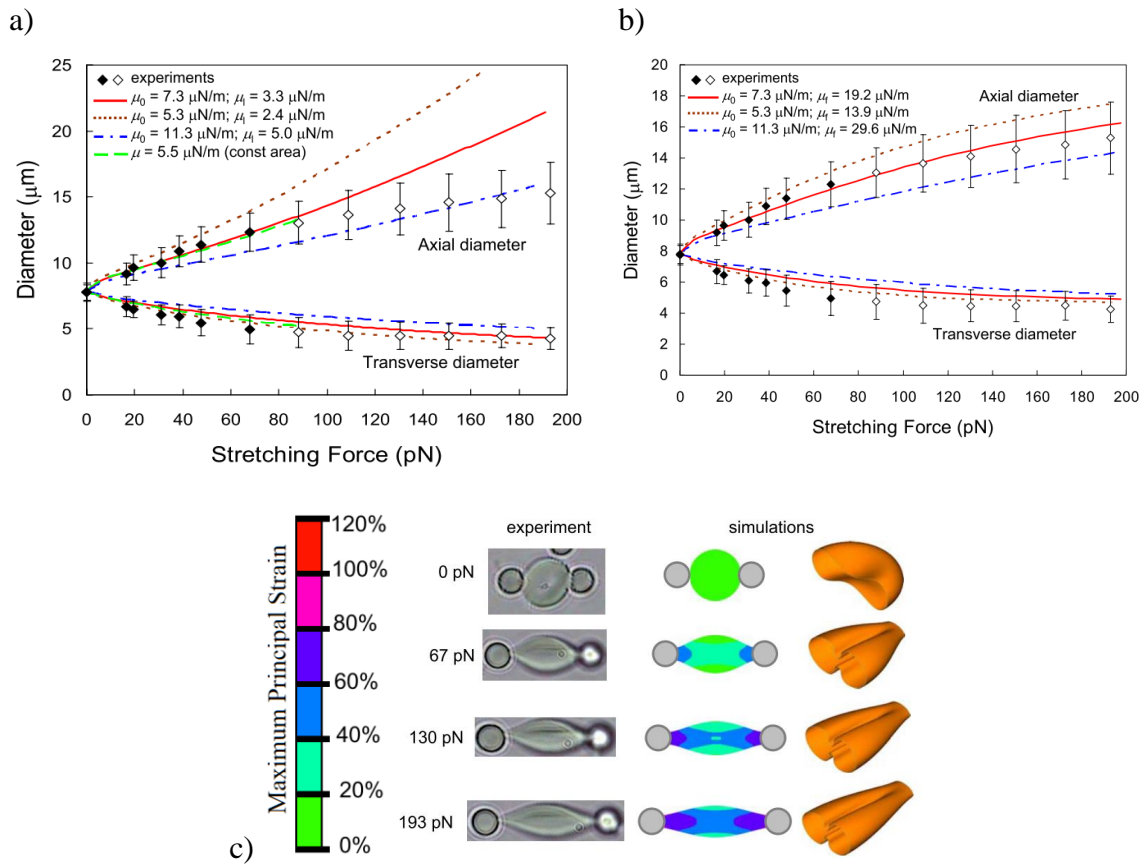


**Figure 5: Comparisons of deformation computed from FEA simulations using a) Neo-Hookean model and b) Yeoh model with optical tweezers experiments. Adapted from Mills et al.<sup>207</sup>**

### 2.3.3 Viscoelastic Modelling of the Red Blood Cell Membrane

The viscoelastic characteristics of the RBC membrane were first observed in a Pioneering study by Rand et al.<sup>222</sup>, which studied the time required to partially draw in red blood cells into a micropipette at constant pressure. They found that cells would either hemolyze or be fully drawn in after a fixed amount of time had passed. Rand proposed to model RBC bulk viscoelasticity similarly to polysulfide rubber using Kelvin-Voigt elements. They idealize the

entire cell and surrounding fluid as a system of springs and dashpots. Using their model, stress,  $S$ , is calculated as a function of load,  $F$ , and time, per Equation 2-11.

$$S = \left[ \frac{1}{Y_2} + \frac{1}{Y_2} \left( 1 - \exp \left( -\frac{Y_1}{\eta_1} t \right) \right) + \frac{1}{\eta_2 t} \right] \quad 2-11$$

Evans and Hochmuth<sup>223</sup> developed the Kelvin-Voigt element theory proposed by Rand into a finite-element material model to simulate the viscoelastic stress distribution on the RBC. They showed that the mechanical power loss from viscous drag on the membrane by the intra and extracellular fluid is much smaller than the mechanical power produced by membrane elastic forces when the recovery time is greater than a few milliseconds. Furthermore, they found that for stress application times less than approximately 5-10 minutes, the RBC membrane behaved as a viscoelastic solid, whereas after this time, the membrane passes through a fluidization process to liquid-like flow. An et al.<sup>213</sup> later found that this fluidization process was due to the cytoskeletal spectrin elements being dynamically broken and reconnected under long-term loading.

Hochmuth et al.<sup>224</sup> also carried out extension-recovery experiments by micropipette aspiration, imaging the recovery with a high-speed camera. They used their material Kelvin-Voigt model and first-order finite-strain mechanics to describe the viscoelastic deformation of the RBC. They model the RBC as a flat disk, and viscous forces from cytoplasm and carrier fluids are neglected. In their model, membrane tension,  $T$ , is simply the sum of principle stretch and the product of strain rate with viscosity:

$$T_s = T_s^l + T_s^v = \frac{\mu}{2} (\lambda^2 - \lambda^{-2}) + \frac{2\eta}{\lambda} \frac{\partial \lambda}{\partial t} \quad 2-12$$

The characteristic response of the principal stretch was then:

$$\lambda(t) = \left( \frac{\Lambda + e^{-\frac{1}{t_c}}}{\Lambda - e^{-\frac{1}{t_c}}} \right)^{\frac{1}{2}} \quad 2-13$$

Where,  $\Lambda = \frac{\lambda_m^2 + 1}{\lambda_m^2 - 1}$  is the extension ratio squared, and  $\eta = \mu t_c$  which can be reformulated to give the characteristic recovery time,  $t_c \equiv \frac{\eta}{\mu}$ .

Characteristic recovery time is the standard means of evaluating RBC membrane viscoelasticity. Hochmuth et al.<sup>224</sup> found over an average of 46 cells that characteristic recovery time,  $t_c$ , was between 0.1 and 0.13 s. This was similar to the characteristic recovery time of 0.2s from similar extension recovery experiments conducted earlier by Chien et al.<sup>220</sup>. Given that shear modulus was approximately 6  $\mu\text{N/m}$ , the resulting surface viscosity of the membrane was between  $0.6 \cdot 10^{-6}$  and  $0.8 \cdot 10^{-6}$  [ $\text{Pa} \cdot \text{s} \cdot \text{m}$ ]. Divided by the nominal overall RBC thickness is approximately .23 – 0.31 [ $\text{Pa} \cdot \text{s}$ ]. This was later revised to  $0.6 \cdot 10^{-6}$  to  $2.7 \cdot 10^{-6}$  [ $\text{Pa} \cdot \text{s} \cdot \text{m}$ ], or 0.23 – 1.04 [ $\text{Pa} \cdot \text{s}$ ].<sup>221</sup> Mills et al.<sup>207</sup> produced updated measurements of viscoelasticity using the optical tweezer force application technique. They obtain on average  $0.19 \pm 0.06$  s for  $t_c$ , over 8 extension release experiments; the corresponding corresponds to a surface and bulk viscosities are between  $0.3 \cdot 10^{-6}$  and  $2.8 \cdot 10^{-6}$  [ $\text{Pa} \cdot \text{s} \cdot \text{m}$ ], and 0.12 to 1.08 [ $\text{Pa} \cdot \text{s}$ ], respectively.

These early studies provide a basic framework through which RBC membrane viscoelasticity is studied. More recently, Gomez et al.<sup>225</sup> applied the optical tweezer method to determine the membrane viscosity as a function of external applied load. Using the same procedure as Mills et al.<sup>207</sup>, a sinusoidal tensing force was applied to the red blood cell at frequencies ranging between 1 and 35 Hz. A generalized Maxwell-Weichert membrane rheology model (comprised of a spring and an infinite number of Maxwell blocks in parallel) was fit to the experimental data. As might be expected, the complex shear modulus was found to increase with load application frequency indicating a significant contribution of viscoelasticity for impulse loading. By assuming linear elasticity of the membrane, the relationship between complex stiffness modulus and frequency was used to compute the steady-state viscosity,  $\eta_0$ , which was found to be  $9.9 \pm 0.6$  Pa s. This study is flawed, however, because of the uni-axial strain response assumption which is valid only up until approximately 5% uni-axial strain.

## 2.4 Modelling and Prediction of Hemolysis

The accumulation of damage on the red blood cell membrane occurs when it is exposed to supraphysiological flow conditions. This section will give an overview of the properties of red blood cell membranes, methods of modelling lethal hemolysis, and the process of sublethal diffusion through the RBC membrane. Hemolysis modelling generally uses the hemodynamic flow field computed from CFD to predict shear applied to blood and the corresponding level of plasma-free hemoglobin released during RBC damage.

### 2.4.1 Measurement of Hemolysis and Index of Hemolysis

Hemolysis is measured using the index of hemolysis, ( $IH$ ), which is the change in the concentration of extracellular hemoglobin above the physiological value ( $[\Delta Hb]$ ), shown below. Note that square brackets denote volumetric concentrations.

$$IH = \frac{\Delta[Hb]}{[Hb]} \cdot 100\% \quad 2-14$$

Extracellular hemoglobin is related to  $IH$  by using the following relationship.

$$[fHb] = \frac{1 - Hct}{[Hb] \cdot IH} \quad 2-15$$

$[Hb]$  is the total hemoglobin contained in the blood sample, and  $\Delta$  refers to the observed increase after a hemolytic event. As Hematocrit varies greatly both between patients and within the vasculature, the index of hemolysis is normalized, denoted  $NIH$ , as shown in 2-16 to account for the relative change in total hemoglobin present in blood.

$$NIH = IH(1 - Hct)[Hb_{blood}] \quad 2-16$$

### 2.4.2 Mechanics and Criteria of Red Blood Cell Lysis

As has been noted, the mechanics and criteria for RBC lysis are complicated by the complexity of RBC behaviour. Membrane rupture is in general a function of applied stress and load application time. Several studies report that there is in general a threshold stress below which lethal hemolysis does not occur, between 150-250 Pa<sup>4,226</sup>. Sharp and Mohammad<sup>227</sup> formulate the threshold stress as a function of stress and exposure time.

$$(\tau_t - \tau_0)t^{0.5} = const \quad 2-17$$

Where  $\tau_t$ ,  $\tau_0$ , and  $t$  is the threshold stress, the stress under which no hemolysis occurs, and exposure time, respectively.

The dynamics of the red blood cell rupture are in general dominated by cytoskeletal instability<sup>228</sup>. There are three stages to red blood cell rupture<sup>229</sup>: the deformation of the RBC, the formation of nanopores, and when an areal strain criterion and the RBC membrane is destabilized and irreversibly damaged. At this point, the strain causes the Spectrin cytoskeleton to disconnect from the actin filaments connecting it to the membrane. As the bi-lipid membrane loses this support, it ruptures<sup>212</sup>. As noted, the viscoelastic and viscoplastic properties of the membrane make it difficult to give precise rupture criteria. Early studies of the rupture of red



blood cells such as those by Leverette et al.<sup>4</sup> using micropipette aspiration over periods of dozens of seconds to minutes found that rupture of the red blood cell membrane occurred between approximately 2-6.4%<sup>230</sup>, whereas others found that at high loading rate and low exposure time rupture occurred at and 42%<sup>222</sup> of the global area strain. In this case, global area strain is measured by the computing area expansion from a spheroid RBC sucked partially into a micropipette. Evans et al.<sup>231</sup> find that the maximum area change was approximately 3.6-4.4%, though cells subjected to area strain as low as 2% experienced lysis after 20-30s. Molecular Dynamics simulations conducted by Li et al.<sup>212</sup> explicitly model the bonding force between the spectrin tetramers and actin-binding sites by applying attractive Lennard-jones potentials between the bonding sites using the appropriate experimentally measured chemical association constants values for spectrin and actin. They compute that given the chemical bonds between spectrin and actin, each spectrin tetramer can withstand approximately 24.9pN before breaking, which corresponds to approximately a linear tetramer length extension of 10.9%. If a perfectly biaxial extension is applied to an equilateral triangular spectrin mesh topology with no uniaxial tension, this corresponds to an ultimate area strain of approximately 23.0%. Notably, this means that the ultimate strain limit should be a function of both linear and area strain. Using a molecular dynamic model of the cytoskeleton, they reproduce the experimentally measured hyperplastic, viscoelastic, and viscoplastic properties of the RBC membrane. They found complete fluidization behaviour of the red blood cell membrane occurs between uni-axial strains of approximately 30-50%, suggesting this as yet another ultimate strain limit. They furthermore find that the largest flaw in the RBC Cytoskeleton cannot be beyond a critical size, lest the lipid membrane may flow out from the cytoskeleton via vesiculation instability.

More recent experimental studies<sup>232</sup> corroborate this, finding that at high load rates on the order of 10-50  $\mu$ s caused by a cavitation bubble, red blood cells could withstand global areal strains up to 30-50%, and global uni-axial strains between 100-200%. Xu et al.<sup>228</sup> studied membrane rupture similarly to Li. DPD simulations of the RBC cytoskeleton and membrane enabled the rupture event to be simulated while the red blood cell was immersed in fluid. While validating the structural response to point and axial loading to the optical tweezer experiments of Mills et al.<sup>207</sup>, they note that destruction due to shearing begins at membrane tension of 89.29-93.75 Pa and observe very different shapes and stress distributions depending on whether the membrane is experiencing pure axial (point-to-point) or shear-based tank treading load, with tank-treading RBCs tending to rupture earlier.

### 2.4.3 Predicting Lethal Hemolysis

#### The Giersiepen-Wurzinger Equation

Empirical hemolysis modelling uses data typically relating shear stress and exposure time to some index of hemolysis. Hemolysis data has been collected from a host of experimental configurations, reviewed by Yu et al.<sup>233</sup> Giersiepen et al.<sup>6</sup> set the gold-standard approach to predicant hemolysis (known as the Giersiepen-Wurzinger (GW) equation) by fitting experimental extracellular Hb data collected from a bi-leaflet heart-valve to a power-law surface as a function of shear stress and time (shown below and in Figure 6).

$$IH = C\bar{\tau}^{\alpha}t^{\beta} \quad 2-18$$

Where  $\bar{\tau}$ , is the shear stress metric,  $t$ , is the exposure time, and  $C, \alpha$ , and  $\beta$ , are coefficients obtained from the fitting process. Giersiepen estimated shear stress computed using PIV measurement and hot-wire anemometry in turbulent regions to compute turbulent components of shear. The hemodynamics in a valve are complex and unsteady, however, and knowledge of the shear-stress distribution was incomplete in high shear areas such as small gaps due to inadequate resolution and view inaccessibility. Furthermore, coming from a complex mechanism, much of the hemolytic activity in Giersiepen's data could be attributed to secondary hemolysis. This led to substantial errors in the initial fit when predicting hemolysis. The need to control or know precisely the stress applied to the fluid sets the basic limitations to the sources of data. The most accurate data comes from Couette-type rheometer devices which provide an accurate measurement of the applied shear stress,<sup>234,235</sup> which can be controlled precisely and separately from exposure time. Such studies suffer from the opposite problem, however. In such controlled experimental conditions, there is insufficient complexity to account for how complex flows affect RBC hemodynamics. The viscoelastic and inertial properties of blood mean that effective stress experienced, the rate of strain accumulation, and the lysis criteria are all time- and load application-dependent. Indeed, even in the case that hemolysis data is obtained from a complex flow such as a heart valve, the power law relationship neglects important transient effects as no time derivative of stress is included. These effects are discussed in more detail in a subsequent section.

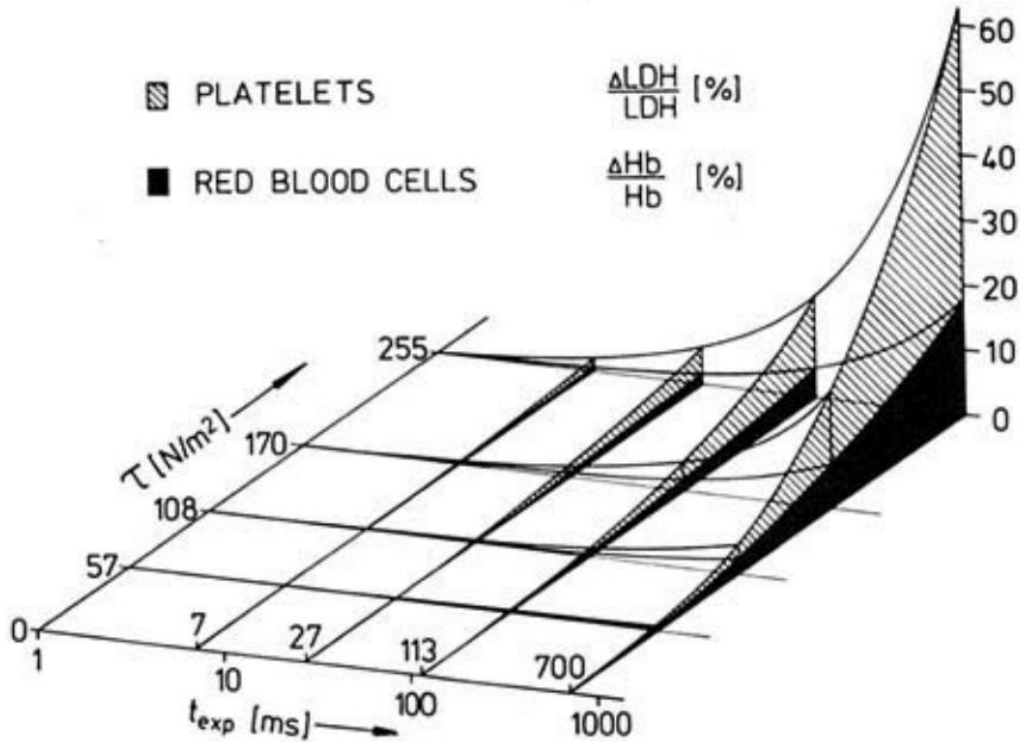


*Figure 6: Surface of Index of Hemolysis as a function of exposure time and shear stress experienced. Adapted from Giersiepen et al.<sup>6</sup>*

Several sets of data have been collected producing several competing coefficient sets. A review of the empirical approaches discussed here is written Yu et al.<sup>236</sup>, whereas Faghhi and Sharp<sup>234</sup>, provide a thorough and recent review of the data relating to controlled hemolysis experiments with human blood that have been fit to power law models. In this study, the coefficient set for human blood given by Ding et al.<sup>237</sup> is used and shown in Table 1.

*Table 1: Power law coefficient sets for hemolysis index (%)*

Study	C	$\alpha$	$\beta$	$\bar{\tau}$ [Pa]	$t$ [s]
<b>Giersiepen<sup>6</sup></b> <b>(Human)</b>	$3.620 \cdot 10^{-5}$	0.7850	2.416	$\tau < 255$	$t < 0.7$
<b>Ding<sup>237</sup></b> <b>(Human)</b>	$3.620 \cdot 10^{-6}$	0.2777	2.063	$25 < \tau < 320$	$0.04 < t < 1.5$
<b>Heuser &amp; Optiz<sup>238</sup></b> <b>(Porcine)</b>	$1.8 \cdot 10^{-4}$	0.7650	1.991	$\tau < 700$	$0.003 < t < 0.6$

Several extensions have been proposed to the classical power-law model, Yeleswarapu et al.<sup>229</sup> introduce the mechanical dose concept – an integral of the stress applied over the transit time

– to account for loading history over a path line. Grigioni et al.<sup>239</sup> extended shear stress and exposure time ranges compared with previous models. Following Rand<sup>222</sup>, Arwatz and Smitz<sup>240</sup>, create a viscoelastic model of hemolysis using two Kelvin-Voigt elements in series with a purely viscous element. They find that most hemolysis occurs in the first 100 ms of exposure, but as much as 25% of hemolysis occurs after 50 s due to viscoelastic rupture at low stress. Unlike previous studies, they find that after longer exposure times, hemolysis does occur at levels as low as 50 Pa after 5 minutes, indicating that there is no minimum threshold for hemolysis given long enough time of load application.

Despite the growing popularity and proliferation of alternative constitutive techniques, power-law-based modelling is still the go-to method for hemolysis prediction due to its simplicity and thorough experimental validation. In cases where 3D flow-field data is available from CFD or experimental measurement, the mechanical dose concept is employed and a differential form of the GW equation<sup>229</sup> is integrated so that IH can be computed over RBC path lines<sup>241–243</sup>. Alternatively, hemoglobin can be treated as a scalar and solved using an advective-diffusion-reaction (ADR) equation in which hemoglobin is released at some stress-dependant rate in each compute cell and solved with the mass and momentum equations. These two approaches are known as the Lagrangian and Eulerian approaches to predicting hemolysis.

#### Computation of Shear Stress in Complex Flows

The application of the GW equation to complex flows is complicated by several considerations. This is because blood flow is 3D, time-varying and turbulent, and generally as a blood cell traverses a path, the direction and rate of application of the stress can vary in both space and time. Stress in general is a symmetric tensor with 6 degrees of freedom and can be difficult to capture using a single scalar. Selecting a scalar indicator that adequately represents the effect of the stress tensor is important. Faghieh and Sharp<sup>244</sup> use the von-mises stress, which represents the total or most damaging aspect of the stress tensor on the fluid flow. In a shear flow, the von-mises stress is equal to  $\sqrt{3} \tau_s$ . They note that there is substantial inconsistency in how stress is computed in hemolysis studies and find that correcting the scalar stress component used can result in a change of power law coefficients by up to a factor of 2. In this work, the von-mises stress is considered a sufficient description of instantaneous stress. Furthermore, several authors<sup>196,245,246</sup> find that in any suitably complex 3D flow with significant streamline curvature, a single scalar representation of stress is insufficient to capture how the red blood cell is deformed. Particularly, cases with high loading rates are dramatically

underpredicted by power law models, as are cases where load application is complex (anisotropic, biaxial, or some combination of axial and biaxial).

Faghih and Sharp<sup>196</sup> critically examine the scalar stress hypothesis by calculating the stress response of a red blood cell to various loading conditions. In general, there is not a direct correspondence between scalar stress in the fluid and stress on the membrane. Membrane stress can vary by up to three orders of magnitude depending on the manner of application of the stress. Pure extensional tension, as is applied by an optical tweezers experiment, produces a steady membrane tension that is approximately an order of magnitude more damaging than pure shear. In a shear flow, however, tank treading produces a cyclic stress on the membrane, and because of this, the overall stress is reduced as the constant membrane motion tends to even out stress concentrations<sup>228</sup> a single scalar stress computed from the shear rate will be severely insufficient for characterizing the stress on the red blood cell membrane in most the conditions induced by blood-wetted devices.

#### Constitutive Approaches to Modelling Lethal Hemolysis

The complexity of red blood cell deformation and lysis, and the need to incorporate complex loading conditions frustrate efforts to develop purely empirical correlations between loading conditions and hemolysis, as much information is lost due to the difficulty in measuring the flow field instantaneously. By necessity, an empirical approach neglects substantial physics relating to how loads are applied and the instantaneous characteristics of how load is applied. This has led to a very characteristic underprediction of hemolysis in the subclinical ranges, and overprediction in complex loading cases. To improve the generalizability of hemolysis modelling techniques, significant efforts have been made to develop constitutive approaches to hemolysis. Such models can be developed incrementally to take into account the complexities such as the relationship between the fluid stress and membrane tension, inertia, viscoelasticity, turbulence, RBC collisions, and transmembrane diffusion of hemoglobin. These modelling approaches can be broadly categorized as stress-based, strain-based, and multiscale models that directly simulate the deformation of the red blood cell membrane.

In an early classical work, Keller and Skalak<sup>133</sup> developed an analytical model for an ellipsoid vesicle deformed in a plane shear flow by assuming a fluid velocity distribution. In their model, the surface of the body has a tank-treading motion that is predefined by the shear rate. Tran-Son-Tay et al.<sup>247</sup> used this model with experimental measurements of the membrane axis lengths in a plane shear flow to infer the membrane tension and cytoplasmic overpressure for

the first time of a tank-treading RBC. They measured peak membrane tension of 445 Dyne/cm at an equivalent shear rate of approximately  $8500 \text{ s}^{-1}$ . Richardson<sup>248</sup> also presents an analytical solution for the deformation of an ellipsoid in pure shear flow with Rand's<sup>249</sup> viscoelastic membrane model. Chen et al<sup>250</sup> incorporate both a viscoelastic critical threshold stress and area strain to develop a constitutive hemolysis model. An equilibrium relation is used to relate the fluid stresses to biaxial cell membrane tension, which is then related to areal strain at equilibrium. They experimentally calibrate their stress model with measurements of RBC extension extracted from images of RBCs in a micro-confined planar Hagen–Poiseuille flow<sup>251</sup> experiencing shear rates between  $20 \cdot 10^3$  and  $40 \cdot 10^3 \text{ s}^{-1}$ . Using equilibrium relationships, however, the model assumes direct correspondence between fluid stress and cell strain and therefore does not account for the accumulation of strain or time-dependant membrane response, except indirectly through viscoelastic modelling. Chen et al.<sup>250</sup> note that because of this, the model is not appropriate for short exposure times of less than 1 ms. Furthermore, using a purely ellipsoidal geometry and a single scalar stress is known to under-predict the true maximum membrane tension experienced by the RBC in a complex flow<sup>245</sup>. As has been noted<sup>196</sup> the relationships presented by Kellar and Skalak<sup>133</sup> are not generally validated by experimental measurements.

An alternative constitutive approach is the so-called deformation tensor-based approach developed by Arora et al.<sup>7,252,253</sup>. Inspired by Barthas-Biesel and Rallison<sup>254</sup> who develop constitutive relations that describe the deformation of a droplet in a Couette shear flow, Maffettone and Minale<sup>255</sup> express the deformation of a circular droplet into an ellipsoid using a symmetric morphology tensor. The eigenvalues of the morphology tensor give the lengths of the major and minor axes of the ellipsoid. Maffettone and Minale then derive a transport equation to compute the evolution of this morphology tensor as it traverses a complex flow field. Their model takes into account the competing effects of tension which tend to return the ellipsoid to a spherical shape, and the fluid forces which deform it into an ellipsoid. In their seminal paper, Arora et al.<sup>7</sup> modify these transport equations to model the deformation of red blood cells modelled as spherical droplets with 40% excess area. The final form includes the effect of vorticity to model the effect of tank treading. Arora et al. use the morphology tensor to compute the deformation parameter,  $D$ , and an effective scalar stress necessary to achieve that deformation under equilibrium planar Couette flow, which is then used to compute hemolysis index using the GW power law. Applied to CFD, hemolysis predictions were substantially improved for complex flows such as those within a ventricular assist device<sup>252,253</sup>.

*Direct Cellular Simulation and Multiscale Approaches for Lethal Hemolysis*

The increasing availability of computational power has led to more sophisticated approaches constitutive approaches, to the extent that several studies have attempted what is known as multiscale approaches<sup>10,12,151,196,245,246,250,256</sup>. Such studies generally follow the approach of extracting hydrodynamic loading conditions from several path lines or trajectories for RBCs computed using CFD and apply the extracted loading conditions to a finite-element or spectrin network representation of the red blood cell membrane, typically in a 1-way fluid-structure coupling process. Nakamura et al.<sup>245</sup> use this approach on a spectrin network model of the RBC membrane to study RBC dynamics in a steady and cyclically reversing planar shear flow. They find that RBC deformation and the assumed direct correspondence between membrane stress and fluid shear stress is valid in steady flow, but severely inconsistent even under relatively simple flows such as an unsteady plane Couette flow, or physiological flow in a stenosis. They conclude that neglecting viscoelasticity leads to substantial differences in correspondence between fluid stress and membrane tension. Ezzeldin et al.<sup>246</sup> use this approach to critically examine Arora's droplet model, replacing the droplet representation of the RBC using the spectrin spring-network cytoskeletal representation. Generally, they find that the response of the red blood cell lags the application of stress by the fluid by a significant margin. They find that blood damage using Arora's model is overpredicted by an order of magnitude in cases of high load application rate to an inadequate treatment of the viscoelastic nature of the red blood cell, further emphasizing its importance. They also find that constraining the deformed RBC shape to an ellipsoid shape leads to substantial under-prediction of stress as the red blood cell is prevented from developing significant local stress concentrations.

**2.4.4 Effect of Turbulence on Hemolysis**

As the rate of hemolysis and the effective stress experienced by the red blood cell membrane is dependent on the complexity of load application and the load application rate, it is logical to conclude that turbulent fluctuations will have a strong effect on hemolysis. Although this question has been examined by several authors, it is yet unknown how turbulence affects hemolysis because the interaction with small-scale turbulent eddies and red blood cells is quite complex and has not been simulated adequately in a 2-way FSI at high shear.

Jones<sup>257</sup> notes that generally, Kolmogorov scale eddies are an order of magnitude larger than the size of the red blood cell, approximately 46  $\mu\text{m}$  in the blood flow downstream from the bi-leaflet heart valve<sup>258</sup>. They argue that because of this, the Reynolds stress does not represent a physical force on the red blood cells. As red blood cells only experience local velocity

fluctuations and membrane tension correlates with turbulent viscous stress alone rather than Reynolds stress. They similarly note that Reynolds number is essentially laminar at the cellular scale. Using the Experimental data of turbulent flow through a prosthetic heart valve they estimate that the shear stress experienced by the cell was an order of magnitude lower than the measured Reynolds stress (56 vs 520 dyne/cm<sup>2</sup>). Antiga and Steinman<sup>194</sup> consider the fact that the average spacing between RBCs must be less than the dimensions of the RBCs themselves in a concentrated suspension, and note that because of this, turbulence scales that cause relative motion between RBCS will be amplified. They argue that the RBCs must be the eventual recipient of the turbulent kinetic energy. The increased viscosity between red blood cells and the highly viscous red blood cell membranes themselves will break up the smallest eddies. In their words “RBCs may be thought of as irreducible “quanta” of momentum, which must, in turn, ultimately dissipate their kinetic energy mainly through viscous interactions mediated by the thin plasma layers between them and the elasticity of the cell membrane”. Further, they argue that the fact that RBCs are tank treading and aligned in the flow implies that the Kolmogorov scale needs to be on the same order as the RBC, as the tank treading motion of the RBC can be thought of as a kind of turbulent eddy. In general, because of the close packing of RBC, the cell-cell collisions and interactions play a key role in hemolysis in turbulent flows. Their arguments are consistent with later observations finding non-Kolmogorov turbulence in blood flow using laser Doppler velocimetry<sup>192,259</sup>, and by DNS by Ge et al.<sup>260</sup> In their analysis, Antiga and Steinman estimate red blood cells experience a viscous stress of 160 dyne/cm<sup>2</sup> that is on the same order as the Reynolds stress.

Later Quinlan<sup>261</sup>, shows using 1-way 2D FSI simulations of single red blood cells in turbulent eddies, that Reynolds stress and Kolmogorov scale are insufficient to quantify the effect of turbulence in blood. The unsaid implication is that the Boussinesq hypothesis is not a valid means of calculating shear stress in blood and on red blood cells, and that turbulence is in general not isotropic in blood. Indeed, they note that unlike traditional turbulence the shear stress contribution is almost flat between turbulent eddies with length scales between 17 mm and 0.170 mm. They indicate that it is unclear if the Kolmogorov theory is a reliable predictor of blood damage, and in particular may not be valid in rapid pulsatile flows and multiphase flows. They also note that the two-phase flow dynamics are considerably important as large variations of hematocrit can occur along turbulent spatial scales due to inertial sieving caused by shear-dependant lift in RBCs.



Faghih and Sharp<sup>196</sup> examine various RBC membrane tensions when an RBC interacts with a turbulent eddy using 1-way FSI, finding that the greatest fluctuating stress occurs in the most energy eddies and peaks when the red blood cell passes between eddies. Re-examining the data from Liu et al, the viscous stress experienced by the most energetic eddies is approximately  $57.8 \times 10^{-2}$  dyne/cm. That this value is surprisingly close to the prediction of Jones<sup>257</sup> should not necessarily be surprising, as both studies make similar assumptions such as neglecting the effect of red blood cell collisions, and that the characteristics of turbulence are not affected by the red blood cells themselves. Due to the complex nature of the 2-Way FSI, there is yet to be a consensus as to how turbulence causes blood damage. Early notions that the most damage is done by turbulent viscous stress rather than Reynolds stress persist, however. Hund et al.<sup>262</sup> show that the application of the Reynolds stresses to predict hemolysis using power law formulations systematically overpredicts blood damage, whereas using dissipation results in less systematic error. More recently, Wu et al.<sup>263</sup> fit the data of Boehnig to a new model where hemolysis is proportional only to energy dissipation rate, showing improved predictions at higher Reynolds Numbers and turbulent cases than simple application of a classical power-law model based on Reynolds stress fit from the same data.

#### **2.4.5 Effect of RBC Collisions and Hematocrit on Hemolysis**

Generally, little work has been done on the effect of hematocrit and RBC-RBC collisions on hemolysis, but in general the evidence is mixed. Early work by Fok and Chubothé<sup>264</sup> found that mechanical hemolysis depends on hematocrit though to a lesser extent, finding an increase of 2-3% as the hematocrit increases in similar proportion. Another early study by Leverett et al.<sup>4</sup> examined the effect of RBC collisions experimentally and found that varying hematocrit had little to no effect on hemolysis at constant shear stress in a Couette rheometer. This early study is often used as a justification for neglecting red blood cell interactions even in dense suspensions and at shear rates far outside of the single shear rate where the Leverett study was conducted. Antiga and Steinman<sup>194</sup> who argue that intercellular shear forces in dense RBC suspensions are key mechanisms for RBC damage note that these experiments are done under laminar and low-shear conditions in which the magnitude of RBC interactions is minimal. It is therefore unsurprising that the RBC-RBC induced stress is minimal. Miziguchi et al.<sup>265</sup> find that hematocrit had a strong and statistically significant effect on in-vitro hemolysis test results in MCS, finding a correlation coefficient of approximately 0.976. Hughes et al.<sup>266</sup> also found that in vitro administration of blood with higher hematocrit values in mechanical circulatory support led to up to a 30-fold increase in measured hemolysis, compared to transfusion with

lower hematocrit blood. What is generally understood from these studies is that hematocrit has a significant effect in complex flow conditions such as LVADs, but generally does not affect hemolysis in controlled conditions such as Couette rheometers. This is consistent with the argument by Antiga and Steinman<sup>194</sup>, that RBC collisions are driving mechanisms for turbulent damage to hemolysis – shear stress increases more rapidly relative to velocity at smaller scales, particularly those with average spacing between RBCs in a dense suspension. More recently, Omori et al. simulate the collision of two red blood cells under mild shear rate and find that there is a distinct increase of membrane tension during the collision process<sup>267</sup>.

#### 2.4.6 Predicting Sublethal Hemolysis

Sublethal hemolysis occurs due to the partial destruction of red blood cells at low levels of stress, or due to the transmembrane release of hemoglobin through nanopores formed due to mechanoporation – the formation of pores in a bio-membrane due to strain. Sublethal hemolysis generally occurs without any obvious symptoms or indicators (LDH and bilirubin are generated by membrane rupture) and is defined simply as a low level of hemolytic index,  $NIH < 0.1$ . As it often goes undetected, it is difficult to diagnose and therefore difficult to link to any pathology. For this reason, until recently it has been a blind spot in the hemolysis literature. Low hemolysis levels are typically poorly predicted by power law methods because load complexity becomes increasingly important at low hemolytic levels. This section will survey the relevant aspects of sublethal hemoglobin release and discuss recent advances in its modelling.

##### Mechanoporation of the Red Blood Cell Membrane

Mechanoporation is the process wherein the red blood cell membrane develops nanopores when stretched by mechanical loading. Tolpekina et al.<sup>268</sup> use the 2D analysis similar to classical cavitation theory approach to develop constitutive models for the formation of a single pore on a membrane. The free energy of a bi-lipid membrane is given by the sum of the elastic energy from the area tension and line tension at the edge of the pore.

$$FE = \frac{K_A}{2A_0} (L_{||}^2 - \pi R^2 - A_0)^2 + 2\pi K_c R \quad 2-19$$

where  $K_A$  and  $K_c$  are the surface tensions and the line tension at the pore edge,  $A_0$  and  $R$  is the initial membrane area and radius of the pore, and  $L_{||}^2$  is the expanded length of the 2D square of the membrane. Minimization of this energy provides a constitutive relationship between pore radius and area strain. At some critical radius and area strain, the energy of the intact membrane and the punctured membrane are equal, after which the punctured membrane has a

lower energy. The authors were able to fit this constitutive model into coarse-grained molecular dynamics (CGMD) simulations. Coarse-grained simulations, unlike atomic molecular dynamics (MD), do not resolve all atoms and the forces between them, and only two particles are used to represent each of the phospholipids -a hydrophobic head and a hydrophilic tail. The critical strain and radius for pore formation occur at the points at which the elastic energy of the intact membrane is equal to the energy of the punctured membrane indicating that further tension of the membrane requires the opening of a pore. Tolpekina et al.<sup>268</sup> note that critical radius, and critical strain obtained from the solution of Equation 2-19 above are dimensional quantities related to the initial area as shown below.

$$\epsilon_{A,C} = 3 \left( \frac{k_c}{2K_A} \right)^{\frac{2}{3}} \left( \frac{A_0}{\pi} \right)^{-\frac{1}{3}} \quad 2-20$$

$$R_C = \left( \frac{K_C}{K_A} \frac{A_0}{2\pi} \right)^{\frac{1}{3}} \quad 2-21$$

In their simulations, they found that the critical strain for pore formation was 14.8% (far greater than the rupture area). Notably, this is a dimensional relationship. As the initial area in their analysis was approximately 272 nm<sup>2</sup>, whereas a typical RBC has a surface area of 135-152 μm<sup>2</sup>, critical strain and pore radii must be scaled by the critical radius. Effectively, because  $k_c$  and  $K_A$ , the line tension and the area dilation modulus, are material properties and do not change,

$$\frac{\epsilon_{A,C}|_{MD}}{\epsilon_{A,C}|_{real}} = \left( \frac{A_0|_{MD}}{A_0|_{real}} \right)^{-\frac{1}{3}} \quad 2-22$$

The radius of pores formed must likewise be scaled. Following this procedure gives an area strain of pore initiation of approximately 0.2%. This procedure has been used by several studies<sup>83,269,270</sup> to scale CGMD simulation data to larger membranes but is notably omitted in the multiscale sublethal hemolysis simulations of Sohrabi et al.<sup>10</sup>.

How pores themselves are initiated is ambiguous; Evans et al.<sup>271</sup> propose that Brownian motion creates infinitesimally small variations of lipid density. Tolpekina et al.<sup>272</sup> suggest that mechanical stretching creates gaps that are just large enough for a water molecule to permeate into the membrane and create a small defect. Koshiyama et al.<sup>269,270</sup> found that the likelihood of this occurring is proportional to the density of water particles outside of the membrane and can occur spontaneously after a certain water particle density is reached. Once pores are formed

defects in both thickness and lipid orientation persist after resealing, making pore re-opening significantly easier than pore initiation.<sup>273</sup> Pores that are formed below the cavitation energy barrier can be dynamically resealed<sup>271,272</sup>. Atomistic simulations performed by Zhang et al.<sup>273</sup> calculate that a 90-angstrom pore can be closed in between 9-50 ns. Once pores are formed, however, permanent deformations persist on the membrane making it easier to reopen pores<sup>272,273</sup>.

As was noted by numerous authors, the rate of load application strongly affects both the rupture tension and the rate of pore formation.<sup>212,231,232</sup> Koshiyama<sup>270</sup> found using unsteady CGMD simulations that as load application rate increased the likelihood of forming multiple pores was increased. Only in their steady simulations and in uniaxial stretching cases were single pores formed. This issue was more thoroughly studied recently by Razizadeh et al.<sup>83</sup> using unsteady CGMD simulations of a spectrin fibre-reinforced bilipid membrane, the results of which are summarized in Figure 7. They find that while the frequency of pores drastically increases with load application rate, the average size of these pores decreases though the growth rate of total pore area is constant with respect to loading rate. As load application rate increases, the critical strain of pore initiation increases drastically (in line with previous work as well as experimental evidence). In the case of cyclic loading situations such as during tank treading, the average pore radius decreases, as pores do not have sufficient time to close fully before being reopened. This, however, has been shown to occur on the order of nanoseconds, far more quickly than the load application rate.

Finally, it was found that the RBC-like cytoskeleton had a strong effect on pore formation on a bilipid membrane. Average pore size is reduced due to the mechanical constraint the tetramer fibre poses on the membrane, though at length though at 80 nm (the nominal length of the RBC spectrin fibre) the effect was minimal. At 40nm fibre length, pore density and pore radius are significantly higher and smaller, respectively. Overall, the growth rate of total pore area with strain is reduced and delayed as the tetramer length decreases.

Little experimental information has been published about the size distributions of the pores at different strains during mechanoporation. This is because of the metastable nature of the pores and the speed at which these processes occur. Indeed, the closest experimental studies of pore formation and distribution come from electroporation studies where cells are frozen during the application of a steady electric field. Electroporation and mechanoporation are qualitatively similar<sup>274</sup>, although it is unknown how well the actual pore distributions can be compared

electroporation applies a uniaxial load whereas mechanoporation is based on biaxial strain, meaning the mechanisms are indeed different.

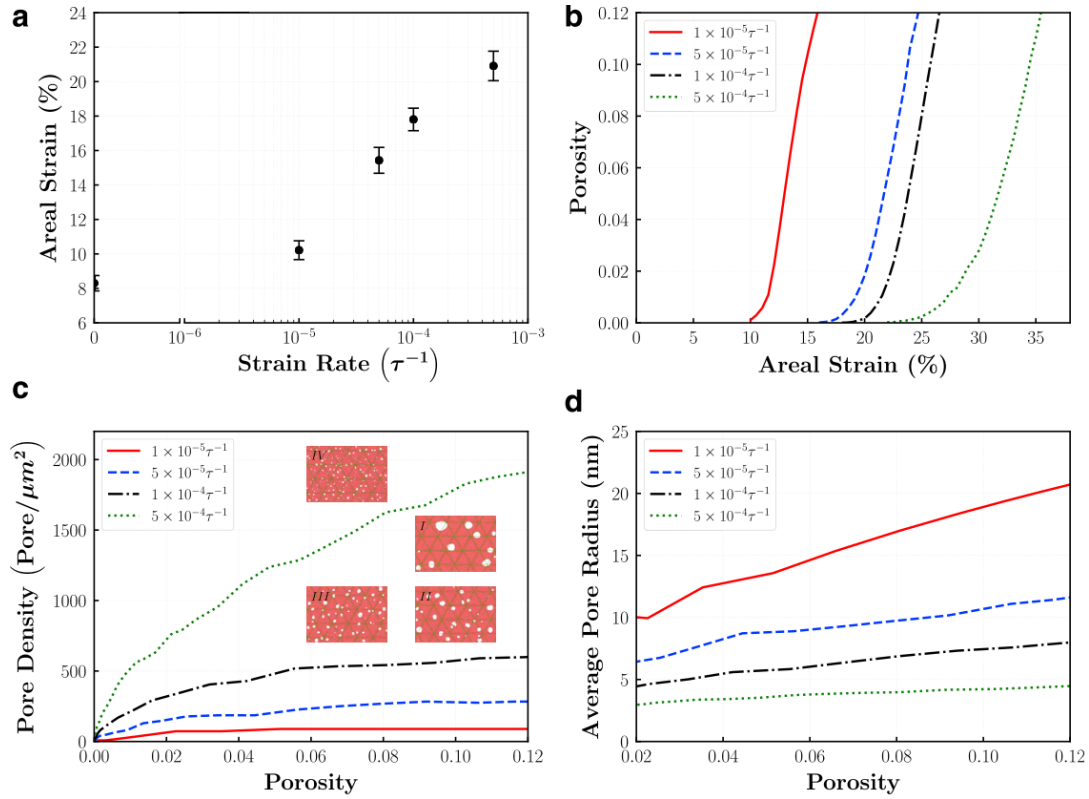


**Figure 7: Molecular dynamics simulations of a lipid bilayer membrane reinforced by a 80nm spectrin triangular mesh, showing the variation of a) critical area strain for poration initiation b) poration area ratio, c) pore density, d) and average pore radius at four different shear rates. Adapted from Razizadeh et al.<sup>83</sup>**

### Transmembrane Diffusion of Hemoglobin

Hemoglobin transport is governed by convective and diffusive transport, given in differential form in the Eulerian frame below<sup>185</sup>.

$$\frac{\partial([Hb])}{\partial t} + \nabla \cdot (u \cdot [Hb] - D \cdot \nabla([Hb])) = 0 \quad 2-23$$

Where  $[Hb]$  is hemoglobin volumetric concentration,  $u$  is fluid velocity, and  $D$  is the effective mass diffusivity.  $D$  can be either an isotropic diffusivity or a matrix in the case of anisotropic diffusion. Through the cell membrane, it can be assumed that convective mechanisms are minimal (though in fact, this is not the case), and so transport is governed entirely by diffusion, but is often neglected.

The self-diffusion coefficient of hemoglobin in water varies as a function of concentration and can be varied by a wide variety of techniques such as tracer diffusion and membrane diffusion

methods. Self diffusion coefficient is maximum at zero concentration at a value of approximately  $10.2 \times 10^{-7} \text{ cm}^2/\text{s}$ ; and decreases logarithmically with increasing protein concentration<sup>275</sup>. Longeville and Stingaciu<sup>276</sup> provide recent and accurate measurements via neutron spin-echo spectroscopy as well as modelling of hemoglobin diffusion. Hemoglobin has an almost spherical structure and high molecular weight and thus is well-modelled by Brownian diffusion mechanisms. Inside the RBC, Hb concentration is approximately 330 g/L, self-diffusivity is approximately  $0.45\text{-}0.93 \times 10^{-7} \text{ cm}^2/\text{s}$ . Analytical descriptions of the dependence of self diffusivity with concentration are well characterized by models proposed by Bouwer et al.<sup>277</sup> (shown in 2-24) and Ross and Minton<sup>276</sup>, shown in Figure 8.

$$D(|Hb|) = D_s(0) \left( 1 - \frac{|Hb|}{C_1} 10^{-\frac{|Hb|}{C_2}} \right) \quad 2-24$$

The fitting by Longeville and Stingaciu gives values of  $D_s(0) = 10.2 \pm 0.6 \cdot 10^{-7} \frac{\text{cm}^2}{\text{s}}$ , and  $C_1 = 404 \pm 43 \frac{\text{g}}{\text{L}}$  and  $C_2 = 2684 \pm 3188 \frac{\text{g}}{\text{L}}$ .

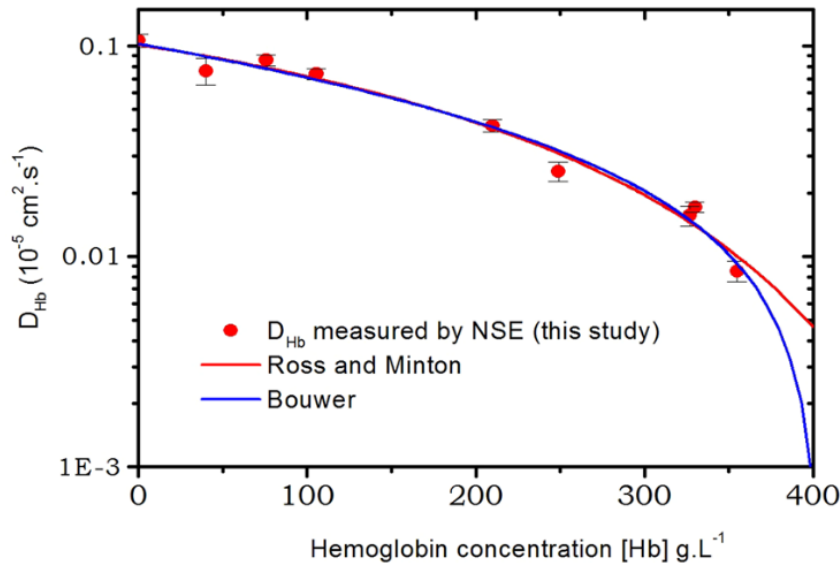


**Figure 8: Self-diffusivity of hemoglobin at varying physiological concentrations. Adapted from Longeville<sup>276</sup>**

In general, the self-diffusion of hemoglobin through a nanopore is hindered by repulsion by the hydrophobic lipid molecules of the RBC membrane, and increased hydrodynamic drag. Davidson and Deen<sup>278</sup> lay out a procedure for estimating the rate of reduced diffusion as a ratio of the solute to pore radius, this is covered in the methods section in more detail.

### Predicting Sublethal Hemolysis

In general, modelling the partial rupture of red blood cells in any kind of macroscopic scheme is exceedingly difficult because of the complexity of red blood cell membrane mechanics. Furthermore, as there is no clear correspondence between shear stress and the strain experienced by the membrane, parameters such as strain-dependent pore formation are also difficult to predict. Measuring pore formation, stress or strain on RBCs is made very difficult by their microscopic size, and thus little data exists to validate cellular strain distributions. Indeed, no model yet exists that predicts the distribution of strain on the RBC membrane at a given shear rate.

Only a handful of constitutive approaches have been developed for sublethal hemolysis. A pioneering study by Vitale et al.<sup>8</sup> adapts the strain-based approach of Arora<sup>7</sup> to compute nominal pore size using the constitutive relations for pore size developed by Tolpekina et al.<sup>268</sup> and Koshiyama and Wada<sup>270</sup>. This model includes several strong assumptions, however. For example, the number of pores is obtained by assuming that all excess area induced by stretching is equal to pore area, and a Boltzmann-type probability distribution is assumed for pore size and number. Mass diffusion is restricted to pore sizes  $> 30$  nm, which is approximately the largest dimension of the hemoglobin molecule. Furthermore, without giving a specific reason, they choose much lower coefficients for the strain accumulation terms,  $f_2 = f_3 = 4.3 \cdot 10^{-4}$ , as opposed to  $1.25 \cdot 10^{-3}$  used by Arora. The mass diffusion coefficients for hemoglobin are fit from the steady Couette rheometer experiments of Heuser and Optiz<sup>238</sup>, which gives this approach a semi-empirical flavour. McKean<sup>9</sup> attempted to reduce some of this empiricism by incorporating the constitutive hydraulic impedance relations of Davidson and Deen<sup>278</sup> to compute hemoglobin diffusion rate through a nanopore and incorporating the experimentally measured nanopore size distribution data obtained from electroporation. Like Vitale et al.<sup>8</sup> McKean also used an area strain threshold to model lethal hemolysis and assumed that all area increase resulted in pore area.

### Direct Cellular Simulation and Multiscale Approaches for Sublethal Hemolysis

Sohrabi et al.<sup>10</sup> adopt a cellular simulation approach to predict sublethal hemolysis, simulating a single RBC as it experiences the shear loading conditions extracted from path lines from CFD of hemodynamics in a centrifugal ventricular assist device. Path lines are computed from CFD simulations executed using a classical incompressible finite-volume Navier-Stokes approach with Newtonian viscosity. The loading conditions extracted from the path lines are applied to cellular scale simulations that use spring element spectrin-network mesh representations of the

RBC membrane. The fluid simulation is coupled to the membrane using an immersed boundary method with a Lattice Boltzmann (LBM) solver to solve the fluid flow surrounding the RBC membrane. Similarly to Vitale et al.<sup>8</sup> and McKean<sup>9</sup>, the relationship between pore radius and strain is computed using the method of Tolpekina<sup>272</sup>, and the hemoglobin diffusion rate is computed following Davidson and Deen<sup>278</sup>. Unlike the other studies, however, no distribution is assumed for the number of pores, but rather it is assumed that one pore forms per triangular surface patch. Furthermore, they do not apply the thermodynamic scaling procedure suggested by Tolpekina to scale the nanoscale molecular dynamics simulation data up to the microscale required by the triangular patches upon which their pores form, leading to rather high critical area strains. Interestingly, there does not appear to be critical area strain or other RBC rupture criteria. The area strains reported by their model are shown in Figure 9.

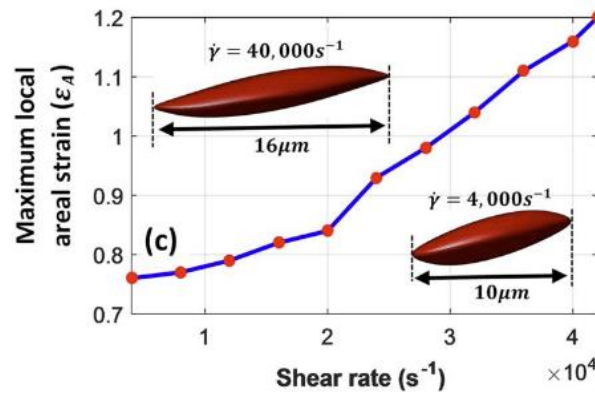


*Figure 9: Maximum area strain at different shear rates. Adapted from Sohrabi and Liu.<sup>10</sup>*

The computational methodology developed by Sohrabi and Liu is continued by Nikfar<sup>12</sup>, who improved upon the methodology by adding an overpressure force to the cell membrane immersed boundary model that ensures volume incompressibility. Applied it to compute hemolysis in a continuous flow VAD they overpredict experimentally measured hemolysis by a factor of between 2 to 3. In general, there are few multiscale hemolysis models. No sublethal hemolysis model considers the effect of RBC collisions, no model considers the advective contribution to transmembrane hemoglobin transfer, which is driven by overpressure during strain. Finally, the formation of nanopores is still a process that is poorly understood, and in general there is no experimental data to validate the mechanoporation hypothesis.

#### 2.4.7 Lagrangian and Eulerian Implementation of Hemolysis Models in CFD

CFD simulation is a powerful tool that can be used to compute the velocity, pressure, and stress field on any blood-wetted device. This information can be used to compute blood damage using



any of the approaches discussed previously, using either a Lagrangian or Eulerian approach. Lagrangian approaches are less computationally intensive but less accurate, whereas the contrary is true for Eulerian approaches. In a Lagrangian approach, tracer particles that represent blood cells are released at the inlet and tracked as they pass through the flow domain of interest and accumulate damage, forming path lines (or streamlines in a steady flow). It is noted that a vast multitude of Lagrangian and Eulerian schemes are available, including viscoelastic schemes, these are evaluated thoroughly and extended Yu et al.<sup>279</sup> For this study, the mechanical dose concept is preferred, wherein the classical (GW) power laws reformulated into a form that accounts for loading history. The GW equation is rewritten and differentiated as:

$$dD = C^{\frac{1}{\beta}} \tau^{\frac{\alpha}{\beta}} dt_{res} \quad 2-25$$

$$D = IH^{\frac{1}{\beta}} \quad 2-26$$

In the Lagrangian frame, the particle residence time,  $t_{res}$ , or the exposure time, is simply the time the particle has elapsed to get to a particular point on a path line. Hemolysis index can be computed from the integral of hemolysis index over a path line.

$$IH = C \left( \int_{t_0}^{t_1} \tau^{\frac{\alpha}{\beta}} dt \right)^{\beta} \quad 2-27$$

The integral can be computed using any suitable numerical integration method. This simple step can generally be executed after the simulation using any standard CFD post-processing software. A typical procedure is to choose a seed location such as the inlet and terminate path lines at the outlet or after a fixed amount of residence time has passed. The hemolysis index is averaged over a suitable number of path lines such that the result becomes insensitive to the number of path lines, and so that sufficient path lines are chosen to adequately represent the entire flow domain<sup>9</sup>. In practice this can be difficult, as regions such as stagnation zones and vortex cores are under-represented. Consequently, the result is highly sensitive to the seeding location, the number of path lines, and the technique used to average the hemolysis result. Furthermore, as the spatial density of path lines is variable, it is possible to over-emphasize highly sheared regions and so it is often necessary to adjust for the path line density.

In an Eulerian approach<sup>280–282</sup>, hemolysis is accounted for by summing the material derivative of a passive scalar representing extracellular hemoglobin concentration within all stationary

computational cells throughout the domain of interest. This is more complex and requires the co-solution of advection-diffusion-reaction (ADR) transport equations in which hemoglobin release (or mechanical dose) is added as a source term. This is complicated because of the non-linear dependence of the power law on residence time (which is not equal to simulation time). To accomplish this, a scalar transport equation can be written for  $D$ ,

$$D = IH^{\frac{1}{\beta}} \quad 2-28$$

which is then solved and integrated in addition to the flow field.<sup>280,281,283,284</sup>

$$\frac{\partial D}{\partial t} + (v \cdot \nabla)D = \delta C^{\frac{1}{\beta}} \tau^{\frac{\alpha}{\beta}} (1 - D) \quad 2-29$$

$$S_D = IH^{\frac{1}{\beta}} = C^{\frac{1}{\beta}} \tau^{\frac{\alpha}{\beta}} \quad 2-30$$

$$\delta = 1 \text{ if } \tau \geq \tau_c, 0 \text{ otherwise} \quad 2-31$$

The left side of Equation 2-28 is the material derivative of the mechanical dose equation, and the right side represents the release of hemoglobin in the cell. The term  $(1 - D)$  is introduced to ensure that the hemoglobin release rate decreases with time in steady shear (i.e., red blood cells are destroyed locally, and do not continue to release hemoglobin), and  $\delta$  is a step function that turns on the hemolysis model when stress is sufficiently high. The constants  $C$ ,  $\alpha$ , and  $\beta$ , are the constants of the GW power law, fit from experiments. Alternatively, a somewhat more complex version is proposed by Yu et al.<sup>233</sup> for the mechanical dose,  $D_b$ , in this case a proxy of the exposure time.

$$\frac{\partial D_b}{\partial t} + (v \cdot \nabla)D_b = \tau^{\frac{\alpha}{\beta}} \quad 2-32$$

$$\frac{\partial H_L}{\partial t} + (v \cdot \nabla)H_L = c\beta D_b^{\beta-1} \tau^{\frac{\alpha}{\beta}} \quad 2-33$$

Similarly, to above,  $c$ ,  $\beta$ , and  $\alpha$  are the fitting constants of the GW equation. The total hemolysis index after a particular flow is obtained by computing the difference in the mass-flow average of  $IH$  between the inlet and the outlet. Generally, Eulerian approaches are more suitable for application in a CFD solver and have furthermore been seen to be generally better predictors of hemolysis<sup>233,285</sup>

The additional computational cost of this procedure is deceptively small because the cost of solving scalar equations is small compared to the cost of solving the flow field, and thus no significant increase in computational time is required to adopt the Eulerian approach.

## 2.5 Modelling and Prediction of Thrombosis

Thrombosis is the process of hemostatic plug formation in the vasculature. Blood coagulation is initiated when the coagulation cascade<sup>286,287</sup>, a complex chemical signalling network, is triggered either when plasma passes through the endothelium<sup>288</sup>, or when platelets are self-activated by shear stress<sup>289</sup> or contact with a foreign surface<sup>288,290</sup>. The coagulation cascade produces the thrombin enzyme, which catalyzes the conversion of fibrin gel from fibrinogen polymer present in plasma<sup>291</sup>. Platelets initially adhere to one another to form a weak porous matrix that shields the clot from local thrombin concentrations<sup>155,292,293</sup>, allowing fibrin gel to form and solidify the platelet matrix, binding it to the endothelium. High platelet concentrations near the endothelium thus are essential to the clotting process.<sup>292,294</sup>

Full thrombosis modelling is multiscale and requires the capture of molecular scale protein-mediated adhesion processes between platelets, platelet motion, and the chemical kinetics of the coagulation cascade (affected by concentration gradients<sup>295,296</sup>). Furthermore, convection in porous media and the interaction with the fluid stresses can break up or free clots from surfaces. In general, in recent years there has been a great expansion of simulation techniques for thrombosis at the microscale level and for simple flows, and consolidation is badly needed. The following sections will survey the literature on thrombosis simulation. The thrombosis process will be described broadly, and then certain aspects of thrombosis will be delved into in detail, such as platelet adhesion, and anticoagulation. Finally, an overview will be given of thrombosis simulation efforts and the myriad approaches that have been attempted.

### 2.5.1 Overview of Thrombosis

Although coagulation is profoundly complicated, it is described in this section in sufficient detail to understand how reduced-order modelling might be approached. For detailed reviews on the coagulation signalling cascade, the fluid mechanics of blood clot formation, and the mechanics of platelet activation and adhesion, the reader is referred to Diamond<sup>287</sup>, Belyaev et al<sup>286</sup>, and Fogelson and Neeves<sup>293</sup>, respectively. A blood clot generally has two main elements; a porous mesh of platelets adhered to one another that forms the basic structure of the hemostatic plug, and fibrin polymer gel that solidifies and seals the wound. The essence of thrombosis is the action of platelets, and their activation and adhesion to vessel walls, foreign substances, and each other.

The process of thrombosis itself is controlled by the coagulation cascade - a network of proteins and enzymes that trigger one another, visualized in Figure 10, that work together to regulate

whether blood clots are formed, how rapidly, and to what size. In general, the coagulation process is activated either when blood plasma passes through the sub-endothelium, or by exposure of blood to extreme flow conditions or foreign objects. Once the cascade is triggered it produces the thrombin enzyme which activates platelets in blood. Platelets can also be activated by numerous other biochemical agonists such as adenosine diphosphate (ADP) when exposed to shear stress over time, or by adhering to a foreign surface or another platelet. Once activated, platelets release thrombin and agonists that activate nearby platelets and trigger the coagulation cascade. Becoming adhesive, platelets bind together to form a porous matrix that forms the base of the blood clot. Thrombin, the main product of the cascade catalyzes the production of fibrin polymer from fibrinogen in plasma, which solidifies the clot. High blood flow rates can wash away important enzymes such as thrombin, as well as other signalling proteins, thereby arresting further platelet activation and thrombosis. The porous platelet matrix helps this by slowing down blood flow within it, allowing clotting in high-flow conditions. Before solidification by fibrin, the porous platelet structure can be broken down by high stress applied by the flow. For thrombogenesis to occur, local concentrations of platelets, thrombin, platelet activation rates and concentrations of enzymes that modulate these reactions must reach a critical level, which is heavily influenced by flow conditions. Once this occurs the production of thrombin and platelet activation becomes self-sustaining, and the thrombus grows steadily in time until reaching a critical size, determined by the balance of platelet adhesion and embolization rates, the rate of fibrinogen conversion, and mechanical properties of the clot.

The coagulation cascade can broadly be separated into two coagulation pathways, the extrinsic pathway, and the intrinsic (or contact) pathway. The extrinsic pathway is activated when Tissue Factor (TF) present in the sub-endothelium interacts with Factor VII present in blood plasma that passes through an injured blood vessel. Factor VII becomes activated, which then leads to the activation of factor X. Factor X is a key point in the coagulation process, because it activates platelets, which themselves activate and produce Factor X, and leads to the conversion of prothrombin (Factor II) into the thrombin enzyme (Factor IIa). The Thrombin enzyme, which is the endpoint of the coagulation cascade, catalyzes the conversion of fibrinogen polymers abundant in blood plasma to form a cross-linked fibrin polymer gel that adheres strongly to platelets (via abundant  $\alpha_{IIb}\beta_3$  glycoprotein receptors). This has the effect of stabilizing and sealing the clot, preventing embolization of platelets or the erosion of the clot by shear stress<sup>293</sup>. The extrinsic coagulation pathway is regulated in several ways, through increasing levels of

Tissue Factor Protein Inhibitor (TFPI) that inhibit TF binding, the action of protein C (PC) present in the endothelium. Other effects of the endothelium are the synthesis of Nitrous Oxide and Prostacyclin produced by endothelial cells, which are vasodilators and thrombosis inhibitors.<sup>297,298</sup> One of the most important regulating mechanisms is the deactivation of thrombin by antithrombin,<sup>287</sup> which is naturally present in plasma. At physiological antithrombin levels, antithrombin will arrest the coagulation process, providing a kind of minimum threshold for thrombogenesis to occur.

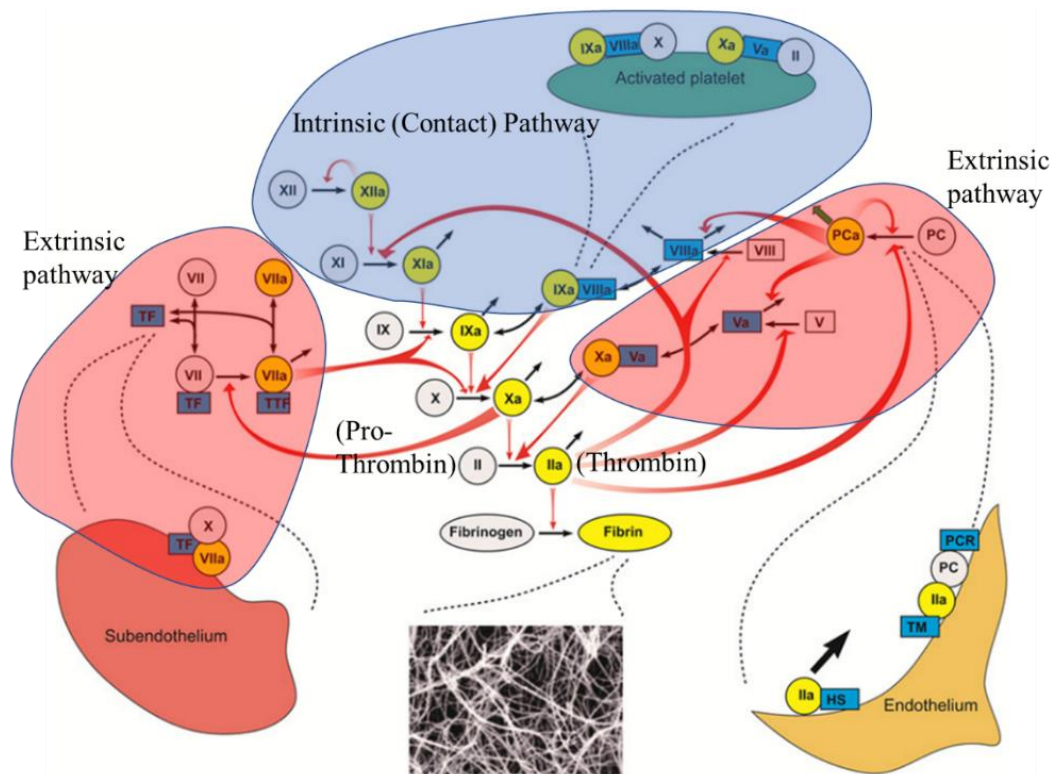


**Figure 10: Schematic illustration of the coagulation cascade illustrating the extrinsic and intrinsic pathways, and feedback mechanisms due to interaction with platelets, endothelium and subendothelium. Adapted from Belyaev et al.<sup>286</sup>**

The intrinsic coagulation pathway, also known as the contact pathway, begins when Factor XII is activated by contact with negatively charged surfaces<sup>299,300</sup>, leading to the activation of Factor X, which activates platelets and subsequently converts prothrombin into thrombin. A review of the intrinsic coagulation pathway and effect of Factor XII is given by Gailani and Renné<sup>301</sup>. Thrombin itself activates the intrinsic pathway in a feedback cycle but also activates other factors such as Factor VIII, which deactivates Factor X on the platelet surface<sup>286</sup>. Included in the intrinsic coagulation pathway is also activation by the exposure to shear. In general, the most comprehensive chemical kinetic model of the coagulation cascade available is that of Hockin et al.<sup>302</sup> In the present study, as extrinsic coagulation is not modelled, the action of the

coagulation cascade can be truncated to thrombin conversion, the interaction with platelet activation, and production of fibrin.

### 2.5.2 Platelet Anatomy and Function in Thrombosis

Platelets (or thrombocytes) are key elements in the process of thrombosis, and in general, are vital to maintaining homeostasis. With up to 100,000 glycoprotein receptor sites, they have critical roles in triggering and regulating the thrombogenic reaction during, and sometimes in anticipation of injury. In addition to their role in homeostasis, they are an essential component of the body's immune response to inflammation and infection (coating and killing malarial parasites for example), and facilitating tumor angiogenesis, and cancer metastasis, among numerous other key functions.<sup>298</sup> They have therefore been the subject of tens of thousands of studies. Platelets are anucleate cells produced by megakaryocytes (bone-marrow cells) without DNA of their own, but rather a truncated set of mRNAs. Circulating for approximately 10 days, they contain the necessary cellular machinery to produce proteins and enzymes, such as thrombin, and adenosine diphosphate. The surface of the activated platelet catalyzes the activation of Factors V, VIII, IX, X, XI as well as the production of thromboxane TxA<sub>2</sub>, a paracrine signalling agent that activates nearby platelets and potent vasoconstrictor (that signals the vasculature to restrict blood flow to the site of the clot). Consequently, the local concentration of platelets helps determine whether blood clots form and the rate at which they proceed.

In their inactive state, platelets are shaped like semi-elliptical disks (approximately 0.5  $\mu\text{m}$  and 2-3  $\mu\text{m}$  in thickness and diameter), with a stiff spectrin skeleton as well as an actin-based cytoskeleton that makes the cell far more rigid than other blood cells. The shape and stiffness of platelets facilitate the platelet margination (Fåhræus-Lindqvist) effect in blood flow resulting in their near-wall aggregation. It permits them to slip between red blood cells more easily and to tumble rather than tank-tread so that velocities induced by red blood cells help them towards the blood vessel walls<sup>154,303,304</sup>. The increased concentration near-wall platelet concentration is essential to achieve the necessary levels of thrombin, ADP, TxA<sub>2</sub>, as well as locally increasing adhesion rates<sup>124</sup>.

The inherent complexity formed by the confluence of convective effects, chemical kinetics, cellular mechanics and signalling is essential to the ubiquitous role of platelets, as it ensures that a blood clot forms in certain situations, but not in others. Indeed, the local concentration of platelets determines which factor in the coagulation cascade dominates thrombin generation,

determining the effectiveness of certain types of anticoagulation<sup>155,305</sup>. For example, low-shear mechanisms are dominant in the pathogenesis of deep-vein thrombosis and stagnant flows, where clots tend to be softer have a higher concentration of entrained blood cells and do not rely heavily on the highly adhesive porous platelet mesh.<sup>306</sup> In areas that experience high shear stress on the other hand, blood clots tend to grow layer by layer, have relatively less entrainment of red blood cells (so-called ‘white’ blood clots), and be mechanically stronger but more prone to catastrophic embolization. This complexity also results in numerous negative pathologies that can be life-threatening, comorbid, multifaceted, and very difficult to predict.

### Platelet Activation

Platelet activation refers to the transition of platelets from a resting passive state to a highly adhesives state, and the various important processes occurring during and after the process of activation. This section discusses these changes, the key factors governing the phenomena, and approaches to predicting the transition that are useful for continuum modelling of thrombosis.

During activation the platelet experiences drastic morphological changes, illustrated in Figure 11, losing its symmetric disc shape to develop a semi-spherical globular shape (decreasing in diameter by 30-40%) with short and long actin fibre bundle tendrils (pseudopodia / filopodia) emanating from the rim<sup>307</sup>. The increase in short filopodia actin-filaments has an essential role that helps adhesivity of the platelet, whereas the long filopodia seem to help fill the gaps between adhered platelets<sup>308</sup>, and help increase hydrodynamic resistance. Morphological changes are facilitated by responses in the structural proteins of the platelet<sup>307</sup>, namely the skeleton of the platelet experiences severe changes which facilitate the change in stiffness allowing its globular form. These morphological changes are accompanied by the secretion of microparticles, called alpha granules, that contain Thrombin, ADP, Serotonin, epinephrine, and von Willebrand Factor which activate nearby platelets making them available for bonding<sup>308</sup>. The cellular machinery inside of the platelet also begins to produce TxA2, which is diffused steadily through the cell membrane and helps encourage thrombosis, functioning synergistically with thrombin and other agonists to activate platelets.

Activation itself is accomplished by the vast number of glycoprotein receptor sites on the platelet cell membrane that are sensitive to certain signalling agonists; Thromboxane A2 (TxA2), Adenosine Diphosphate (ADP)<sup>306</sup>, and most potently, Thrombin. Activation of platelets by Thrombin is dependent on Factor XI, making, which makes it a therapeutic target to interrupt self-activation feedback.<sup>309</sup> Receptor sites exist for a variety of other hormones such

as epinephrine and estrogen (which helps account for the disparity in HF risk by gender)<sup>310</sup>, though with much-reduced sensitivity. Because the platelet membrane has such a large variety of receptors there, are a wide variety of agonists that can trigger an activation-like response in platelets, cause indirect activation or act synergistically with other agonists<sup>307</sup>. It has been found that decreased extracellular sodium concentration results in decreased sensitivity to ADP and TxA2<sup>311</sup>, and that Serotonin (for which there is a receptor on the platelet as well) increases platelet sensitivity to ADP and Thrombin<sup>312</sup>.

In addition, glycoprotein receptors exist for the binding of collagen, von-Willebrand Factor (vWF), and fibrin(ogen), depending on the medium being adhered to, so that a binding process also triggers platelet activation. Shear-stress activation of platelets can begin to occur at stresses as low 5 -25<sup>313,314,315</sup> Pa. Though it might be tempting to link cytoskeletal changes and cell lysis to activation, the shear-stress activation of platelets is not a result of cell lysis, but rather depends on the presence of shear sensitive proteins in plasma such as vWF, collagen and fibrinogen<sup>316</sup>. Interestingly, there are differences in the resulting platelet structure when activated by shear or by agonists. Shear-activated platelets cause the formation of tethers (long cylindrical extensions of the membrane) that enhance adhesion substantially.<sup>317</sup>

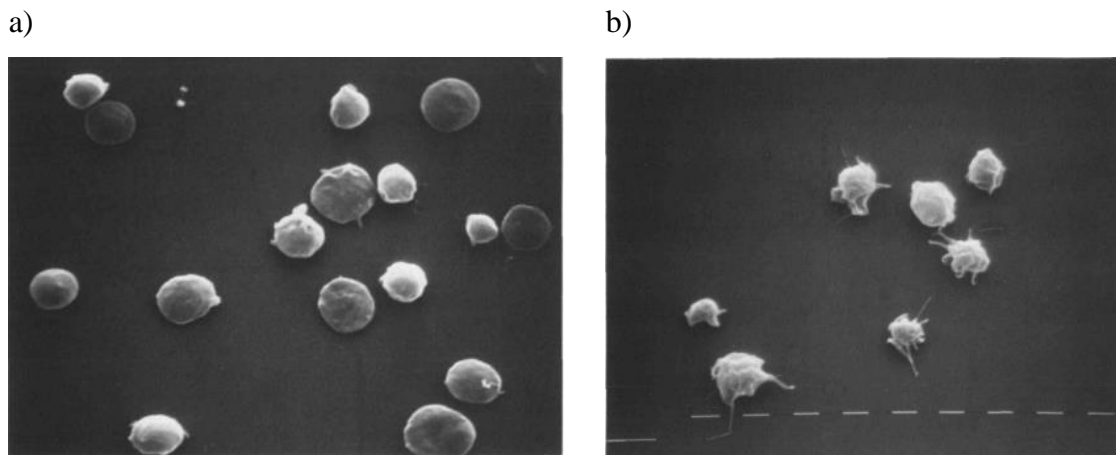


**Figure 11: SEM images of (a) resting discoidal platelets and (b) platelets activated by ADP.**  
*Adapted from Zucher and Nachmias<sup>307</sup>*

When considering the modelling of platelet activation, generally it is neatly divided by activation via concentrations of agonists, and activation via exposure to shear stress.

It is well documented that multiple chemical agonists interact together synergistically.<sup>307,318</sup> For example, Nylander et al.<sup>319</sup> show that only 1/5<sup>th</sup> of the combined thrombin and ADP concentration is required to achieve the same effect as either agonist individually. Quantitative



information on the synergy between the action of multiple agonists together is not readily available, however. Consequently, few models exist that model platelet activation by agonists. One such attempt has been made by Sorensen et al.,<sup>320</sup> using a simple threshold model that assumes a linear combination between various agonists, and that platelet activation rate,  $k_{pa}$ , increases linearly after a certain threshold is reached, shown in Equation 2-34.

$$k_{apa} = \begin{cases} 0, \Omega < 1.0 \\ \frac{\Omega}{t_{act}}, \Omega \geq 1.0 \end{cases} \quad 2-34$$

$\Omega$  is an activation threshold function, defined by the sum of the proportion of concentration of agonists,  $a_j$ , to their threshold,  $a_{j,threshold}$ .

$$\Omega = \sum_{j=1}^{n_a} w_j \frac{[a_j]}{[a_{j,threshold}]} \quad 2-35$$

Where  $w_j$  are weights associated with the receptivity to a particular agonist, and  $t_{act}$  is a timescale for actuation. A value of 1 s is suggested as a worst-case based on the data Frojmovic et al.<sup>321</sup> indicating that at 1s, 63.3% of all platelets are activated. Aside from assuming a very simplistic linear synergy between various agonists, a simple on-off threshold is also assumed, whereas realistically, activation is typically sigmoidal and each agonist has a unique minimum threshold. A more complex approach was attempted by Chatterjee<sup>322</sup> who trains a neural network to produce an activation function that quantifies the cross-talk between six platelet agonists (convulxin, ADP, thrombin, TxA2, Collagen, Prostaglandin PGE<sub>2</sub>, and extracellular calcium), from a single donor. There are generally very few attempts to model agonist platelet activation, leaving many thrombosis models to neglect this aspect entirely. Indeed, aside from the approach by Sorensen et al.,<sup>320</sup> a thorough search reveals that little to no work has been done to develop a model for agonist activation usable in simulation studies.

Generally, platelet activation does not occur below a shear stress of approximately 1-3 Pa, but given sufficient shear stress platelets can be activated even for very short exposure times.<sup>323</sup> An early study by Hellums et al.<sup>324</sup> combines shear-activation data from several authors and shows that the logarithm of threshold stress (measured by onset of serotonin release) for platelet activation fits nearly linearly with exposure time until the onset of serotonin release. Goodman et al.<sup>325</sup> fit this data to a power law function:

$$t_{onset} = 4.0 \cdot 10^{-6} \tau^{-2.3} \quad 2-36$$

Where  $\tau$  is the exposure shear stress (not von-misses stress). Hellums<sup>326</sup> later notes that the onset of platelet activation shifts considerably depending on the dose of coagulants added such as epinephrine and ADP. Measuring the true activation rate by shear stress is complicated, however, as activated platelets contain feedback mechanisms to continue the activation process. Jetsy and Bluestein find that acetylating prothrombin can inhibit the feedback mechanism of thrombin while maintaining normal thrombin conversion rates, as acetylation prevents thrombin from binding to its glycoprotein platelet receptor<sup>327,328</sup>. Furthermore, in general the same arguments against empirical approaches to hemolysis modelling apply to platelet activation by shear. For example, loading history is important, as exposure to high shear stresses for short durations sensitizes platelets for activation at lower-than-expected shear stresses later<sup>329</sup>, though generally, exposure time has a less significant effect than shear stress<sup>243</sup>. To capture this effect, Soares et al.<sup>330</sup> employ the mechanical dose concept from hemolysis to model the platelet activation state (PAS):

$$\frac{d(PAS(t))}{dt} \bigg|_{\tau} = C^{\frac{1}{\beta}} \beta PAS(t)^{\frac{\beta-1}{\beta}} \tau^{\frac{\alpha}{\beta}} \quad 2-37$$

$$\frac{d(PAS(t))}{dt} \bigg|_{\dot{\tau}} = C_r^{\frac{1}{\delta}} \delta PAS^{\frac{\delta-1}{\delta}} |\dot{\tau}|^{\frac{\alpha}{\delta}} \quad 2-38$$

The two equations correspond to the static shear contribution to platelet activation, and dynamic flow condition contribution to platelet activation. When  $PAS(0) = 0$  and the shear stress is constant, the general solution is:

$$PAS(t) = C \tau_0 t^{\beta} \left( 1 + \frac{C_1}{C^{\frac{1}{\beta}} \tau^{\frac{\alpha}{\beta}} t} \right)^{\beta} \quad 2-39$$

Soares et al.<sup>330</sup> fit this model using data extracted from both static (constant shear stress) platelet activation experiments, stepped variation of shear stress over time, triangular shear stress wave-forms, and negative control of constant low shear stress over long duration (14 minutes). Platelet Activation State itself is measured by the chemically modified prothrombinase method.<sup>327,328</sup> Activation feedback mechanisms of platelets were inhibited by acetylation of prothrombin. PAS itself is a function ranging from 0 to 1, corresponding to local ratio of activated platelets (measured by total thrombin granule release from all platelets). Sheriff et al.<sup>329</sup> evaluate the platelet activation state as a cumulative power law model,

$$PAS_{CPL}(\tau(t), t) = C_1 \int_{t_0}^{t_f} \beta \tau(t)^\alpha t^{\beta-1} dt + C_2 \int_{t_0}^{t_f} \alpha \tau(t)^{\alpha-1} t^\beta |\dot{\tau}| dt \quad 2-40$$

Where  $t$  is the Lagrangian exposure time in a fluid path line. The inclusion of the shear stress time derivative is often neglected in power law formulations because the causality principle<sup>243</sup> is somewhat controversial and requires a continuous stress field. The models differ on two points, firstly, the model by Soares et al has a plateau at  $PAS = 1$  by inclusion of  $PAS$  into the power law fit turning it into a differential equation. Secondly, the removal of the variable of time from the formulation by Soares et al. renders it easier to implement into an Eulerian transport and solution scheme in CFD. From their respective data, Soares and Sheriff arrive at different coefficient sets of ( $S_r = 1.5701 \cdot 10^{-7}, C = 1.4854 \cdot 10^{-7}, \alpha = 1.4854, \text{ and } \beta = 1.4401, C_r = 1.3889 \cdot 10^{-7}, \gamma = 0.572, \delta = 0.5125$ ), and ( $C = 3.31 \cdot 10^{-6}, \alpha = 3.075, \text{ and } \beta = 0.77$ ), respectively. Interestingly, neither model predicts the threshold behaviour of Hellums et al.<sup>77</sup> (observed through setting  $\dot{\tau} = 0$ ), though the fitting of Sheriff et al. seems to corroborate the increased importance of shear stress (i.e. that  $\alpha > \beta$ ). This can be for a wide variety of reasons, such as the fact that Hellums' does not measure platelet activation. Though both models incorporate dynamic shear loading data (up to 6 Hz), both only fit data for loads up to 7 Pa (which is extremely low). Furthermore, neither incorporates data for short-time exposure of high shear stress. In MCS exposure time is typically on the order of 0.001-0.1s, and stresses can range up to several hundred Pa. This is problematic because it appears that platelets are particularly sensitive to the application of stress at high frequencies. This was shown by Consolo et al.<sup>331</sup> who decompose the frequency content (obtained using CFD) of stress experienced by platelets downstream from a tri-leaflet synthetic polymeric heart valve into low, medium and high-frequency wave forms (up to ~100 Hz) using Fourier decomposition. They experimentally subject bovine PRP to the waveforms using a programmable shearing device, finding that the high-frequency waveforms account for much of the platelet activation, despite their lower amplitudes. Evidently, even more than for hemolysis, it is unclear to what extent high-frequency oscillations affect platelet activation. This means that unfortunately, the threshold approach by Goodman<sup>325</sup> remains more appropriate for predicting the activation of platelets by shear in non-physiological flows, and that much work remains to quantify platelet activation.

#### Diffusion of Platelets in Wall-Bounded Blood Flow and Platelet Margination

The margination of platelets to non-slip walls in blood flow, known as the Farrhaus-Lindquist effect, is essential to homeostasis as it facilitates a nearly 4-fold increase in platelet

concentration near injury sites.<sup>305</sup> The effect generally increases with increased shear and hematocrit.<sup>332</sup> This has several effects, it reduces the likelihood of non-mural thrombogenesis (where an injury is most likely to occur), it modulates the effect of flow so that platelet concentration is increased when flow is increased, thereby facilitating thrombosis at higher shear rates, and it decreases the likelihood of thrombus formation in smaller blood vessels where shear rates vastly reduced. Until recently, the mechanisms of platelet margination were not well understood, and the diffusion rate of platelets was assumed to be governed by Brownian diffusion mechanisms. Cell-scale simulations by Zhao et al.<sup>136</sup> demonstrated two things: red blood cells, which tend to migrate away from the wall due to their deformability and the lift force induced by tank-treading,<sup>333</sup> induce velocities onto platelets as they rotate. Consequently, the lateral migration rate of platelets is dependent on the tank-treading membrane velocity of the RBC, and thus diffusion rate is dependent on shear rate. Simulations by Vahidkhan, Diamond, and Bagchi<sup>138</sup> show that in whole blood due to decreased concentration of red blood cells near the wall (caused due to hydrodynamic lift and deformability), and decreasing shear rate, there is a reduced likelihood of collisions between RBCs and platelets. This causes a general concentration gradient of platelets away from locations of increased collision likelihood with RBCs. This is known as the volume exclusion effect of red blood cells and is the reason why platelet margination also increases with increasing red blood cell concentration in whole blood.

Thus, the diffusion rate of platelets is shear-driven and generally several orders of magnitude higher than Brownian diffusion, and as noted, the diffusion rate of platelets is critically important to capturing thrombosis. Several attempts have been made to model the process using a shear- and hematocrit-dependant diffusion coefficient. Early modelling efforts such as Zydney and Colton<sup>334</sup> model migration by analogy to dilute deformable suspensions so that diffusion rate is governed by relative particle size,  $a$  [ $\mu m$ ], and shear rate,  $\gamma$  [ $s$ ], capturing the volume exclusion effect:

$$D_{plt} = C a^2 \gamma \phi_{plt} (\phi_{RBC})^n \quad 2-41$$

where  $C = 0.15 \pm 0.03$ ,  $n = 0.8 \pm 0.3$ , are fitting constants, and  $\phi_{RBC}$  is the red blood cell volume fraction, or hematocrit. Zavodsky et al<sup>304</sup> find that this overpredicts diffusivity severely away from the walls in a cylindrical channel flow. Instead, they propose an extended shear-induced diffusivity:

$$D_{eff} = C' \frac{\sigma(\gamma)}{\sigma(0)} \gamma \phi_{RBC} \quad 2-42$$

$$\sigma(\gamma) = \pi \left( r_{plt}(\gamma) + r_{rbc}(\gamma) \right)^2 \quad 2-43$$

$$r_{RBC}(\gamma) = 3.92[\mu m] \left( \frac{1}{1.6} e^{-0.0013\gamma} + 0.375 \right); r_{RBC} = 1.2 \mu m \quad 2-44$$

They fit the cellular scale simulations of whole blood flow in a cylindrical channel, obtaining a value of  $C' = 1.0184 \cdot 10^{-6} \left[ \frac{cm^2}{s} \right]$ .

Hund and Antaki<sup>335</sup> follow the ideas of Phillips<sup>336</sup> to model the anisotropic convective flux induced by the tank-treading RBC.

$$D_{eff} = [D_{plt} + D_{RBC}]I + \begin{vmatrix} 0 & 0 \\ 0 & 1 \end{vmatrix} D_{mig} \quad 2-45$$

Where effective diffusivity,  $D_{eff}$ , is given in terms of the sum of the isotropic Brownian platelet diffusivity,  $D_{plt,B}$ , the shear-dependant RBC diffusivity,  $D_{RBC} = 0.01\gamma$ , and the migration diffusivity  $D_{mig} = 1.75\gamma$ . Wu et al<sup>337</sup> follow similar notions and represent diffusive flux as:

$$J_{plt} = D_{plt} \nabla[\phi_{plt}] + D_{plt} q(\phi_{plt}) \nabla[\phi_{plt}] + D_{plt} C \nabla(q(\phi_{plt})) \quad 2-46$$

$$D_{plt} = D_{plt,B} + \xi \phi_{plt} \gamma \quad 2-47$$

$$q(\phi_{plt}) = 0.26\phi + 10.6\phi^2 + 537\phi^3 \quad 2-48$$

Where  $D_{plt,B} = 1.58 \cdot 10^{-7} \left[ \frac{cm^2}{s} \right]$  is the Brownian diffusion constant of platelets,  $\xi = 6.0 \cdot 10^{-8} \left[ \frac{cm^2}{s} \right]$  is an empirical constant,<sup>325</sup> and  $q(\phi_{plt})$  is a polynomial function obtained by making simulations that reproduce experimental platelet concentration in a cylindrical channel.

### Platelet Adhesion and Embolization

Platelet adhesion is mediated by three main proteins abundant in plasma, fibrinogen, collagen, and von Willebrand Factor (vWF), illustrated in Figure 12. Fibrinogen generally functions to activate and adhere to platelets in low-shear environments with stress less than 1 Pa. High shear stress activation and adhesion, greater than 3-30 Pa<sup>317</sup> is exclusively mediated by von-Willebrand factor, whereas collagen mediates adhesion in the intermediate range between 1.2 to 10 Pa. Conversely, following the model that adhesion is governed by chemical kinetics,

adhesion strength generally has an inverse relationship with shear stress and shear rate owing to the decreased time available to bond the platelet, do to their increased near-wall speed. Fibrinogen, collagen, and vWF each have different chemical kinetic behaviours with their respective platelet receptors; vWF generally has a high association constant (and both ‘slip’ and ‘catch’ bond behaviours), whereas fibrinogen has a longer association time but forms a stronger bond. Platelet adhesion at high shear stress is generally a two-step process due to the high relative velocity between platelets that are in motion. At a distance on the order of the platelet thickness,  $\sim 1 \mu\text{m}$ , vWF binds to the Glycoprotein (GP)Ib receptor on the platelet, in a rapid but unstable bond that helps slow down the relative platelet velocity.<sup>338</sup> This allows the slower but stronger fibrinogen-GPIIb/IIIa bond to form. This is termed here as ‘platelet stabilization’ as once the fibrinogen bond has formed it is significantly more difficult to embolize the platelet. As this occurs and platelets are bound together by fibrinogen, they form this canonical porous platelet structure that allows for ever-increasing platelet adhesion and strength to occur. On a surface at high shear, vWF and fibrinogen function together; whereas at lower shear the role of vWF is replaced by collagen. Chen et al<sup>305</sup> show that in general, the adhesion probability and rate increases with both hematocrit, and shear rate, but find that the effects of this are directly explainable by increased platelet concentration near the wall due to the Farrhaus-Lindquist effect. The adhesion of platelets to a non-reactive surface such as stainless steel occurs generally at a slower rate than the adhesion of platelets to a surface coated by a layer of platelets ECM, or collagen (by approximately a factor of 3<sup>320,339</sup>). If it is assumed that platelet adhesion rate can be well approximated using first-order reaction kinetics as is suggested<sup>15,320,340</sup>, then adhesion or deposition rate,  $k_{dep}$ , is:

$$k_{dep} = k_{ad}\phi_{plt} \quad 2-49$$

This is a kinetic constant of platelet adhesion that varies depending on the material’s affinity to bind to collagen, fibrin, and vWF, several values found in the literature are summarized in Table 2. Bark and Ku<sup>341</sup> find that at shear rates greater than 7000 [ $\text{s}^{-1}$ ], near-wall platelet aggregation due to diffusion explains the relationship of adhesion rate and shear rate. Thus at high shear reaction kinetics govern thrombus growth rate and that deposition has a sigmoidal character<sup>342</sup>. The adhesion characteristics of materials in general are not in general well understood. There is a scarcity of data understanding how adhesion behaves. For example the process of protein immobilization is poorly understood, as is the precise quality of a surface that determines adhesion rates. Indeed, Moradi et al.<sup>355</sup> find that platelet adhesion (PRP) is

dependant on material wettability, finding that surface roughness either exacerbates or reduces platelet adhesion rate depending on whether the material is hydrophilic or hydrophobic.

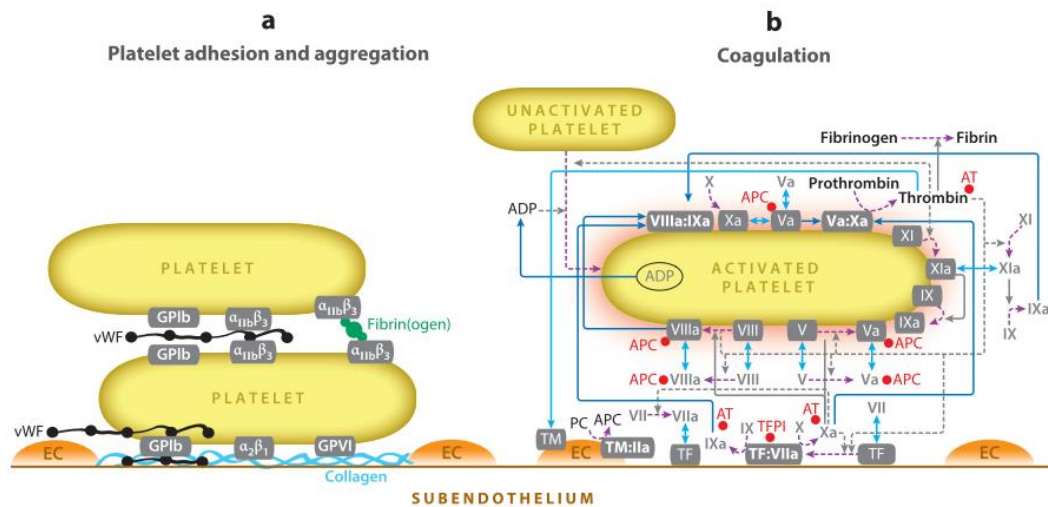


**Figure 12: Schematic illustration of bonding via vWF, collagen, and fibrinogen, and the corresponding mechanisms of platelet activation. Adapted from Fogelson and Neeves<sup>293</sup>**

The breakage of the adhesive bonds between a blood clot and its attached surfaces (embolization) is tremendously complex. The bonds formed between Glycoprotein receptors and the mediating proteins such as vWF have nonlinear responses to force in general. Evans et al.<sup>343,344</sup> use kinetic theory to model the bond dissociation rate as a function of force, where an increasing dissociation with respect to force represents what is called a “slip” bond, and the contrary a “catch bond” (vWF has both behaviours). By integrating the dissociation rate over all bonds between a cluster of platelets it is possible to construct a constitutive model of thrombus embolization. An obvious advantage of cellular simulations such as that by Fogelson<sup>292,345,346</sup>, is access to constitutive approaches for platelet aggregation, and the ability to simulate embolization. In a continuum model, a constitutive model of platelet adhesion is complicated by the myriad factors that can contribute to its strength, such as platelet spacing and orientation, red blood cell content, and the particular combination of bond types. Fogelson<sup>347</sup> attempts to reconcile this by defining a quantity called the link density between platelets in a linked spring system and then specifying an isotropic distribution of links which in concert with a platelet density defines the adhesive strength. Link density increases with time when activated platelets are in proximity to one another and decline when force is applied in accordance with the dissociation of bonds. While some thrombosis simulation methods such as Samra<sup>3481</sup>, and then Taylor<sup>349</sup> use this approach in a continuum model to define

embolization, it amounts to defining a (somewhat arbitrarily chosen) constant rate of platelet embolization,  $B$ , representing constant link destruction rate, following a critical shear stress.

Basmadjian<sup>350,351</sup> surveys early experimental work on platelet embolization, finding that in general individual platelets are embolized from a surface by shear stresses that begin to occur between 2.5 to 75 Pa for small thrombi. They note that when thrombus size increases, embolization strength increases as well, exceeding 100 Pa. In a subsequent work<sup>352</sup> they combine embolization stresses from several studies to produce an approximate embolization probability map for single platelet cells, the lower and upper limits of embolization at 2.5 and 55 Pa (Taylor et al.<sup>342</sup> find embolization begins at 0.9 Pa) for thrombi with height lower than 1 cm. Goodman et al.<sup>325</sup> perform experiments where clots are permitted to form downstream of a series of sharp expansions and contractions in a polyethylene (PE) cylindrical channel and then are washed away by various degrees of shear stress. Whole clot embolization is monitored manually through video microscopy, and the percentage of single remaining platelets after shear application is monitored through scanning electron microscopy. They fit the percentage of platelets washed away by shear stress showing a simple exponential relationship of the likelihood of single platelet embolization from the surface with shear stress.

*Table 2: Platelet deposition and binding coefficients for various surfaces*

Material	$k_{a,s} \left[ \frac{\mu m}{s} \right]$	Experiment type	Study
<b>Polyurethane-Urea (PUU)</b>	$0.0793 \frac{\mu m}{s} *$	Immersed Circular spinning disk	Navitsky et al. <sup>353</sup> (Derived)
<b>MPC</b>	$\sim 1 \frac{\mu m}{s}$	N/A	Wu et al. <sup>339</sup>
<b>Acrylic BFS</b>	$\sim 0.9074 \left[ \frac{\mu m}{s} \right] **$	1cm cylindrical backward-facing step	Taylor et al
<b>Glass</b>	$(\sim 15-30 \frac{\mu m}{s})$	Stenotic cylinder	Flannery (2007) <sup>354</sup>
<b>Polyethylene (PE)</b>	$1-2.5 \frac{\mu m}{s}$	Sharp Contractions and expansions in a Cylindrical Channel	Goodman et al. (2005) <sup>325</sup>
<b>Ti6Al4V</b>	$10 \frac{\mu m}{s} *$	Rectangular microchannel with 75 $\mu m$ groove	Wu et al. <sup>339</sup>

\* Estimated by fitting present simulation approach to experimental data presented in the cited study



\*\* converted value from normalized units

Fitting platelet embolization times, they also estimate a kinetic constant of platelet adhesion of  $1 < k_{ps} < 2.5 \frac{\mu m}{s}$  for PE tubing (other values for different materials are given in Table 2). Goodman also suggests 120s for the characteristic embolization time, noting that this was obtained from one data point. They suggest that as adhesion rate and embolization constants can be scaled to produce the same platelet distribution, the real embolization time should be much lower. More than other aspects of thrombosis, there is a profound scarcity of data regarding the embolization of platelets from different materials, for example, it is not known if embolization should be treated as material dependant.

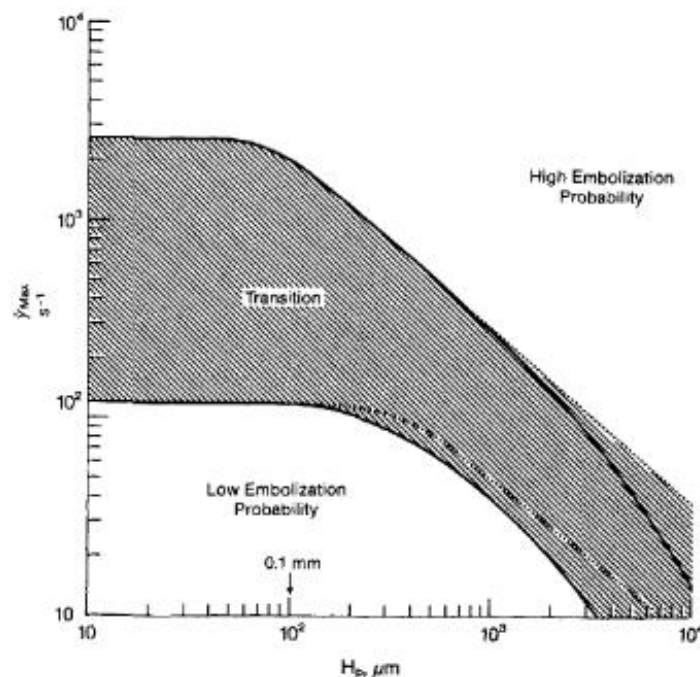


**Figure 13: Embolization probability maps of Basmadjian. Shows the probability of embolization based on the shear rate and lesion height. Adapted from Basmadjian<sup>352</sup>**

### 2.5.3 Anticoagulation

Due to the complexity of the coagulation process, there exists a wide variety of treatments available to clinicians to reduce thrombosis. Such therapies can be divided broadly into drugs that target the coagulation cascade and antiplatelet therapies. Warfarin(s), which was discovered by chance in the 1920s, is a class of drugs that are vitamin K antagonists. They function by initially blocking proteins C and S, leading to indirect inhibition of factors II, VII, IX, and X in the extrinsic coagulation process.<sup>355</sup> Heparins (which has several forms such as Unfractionated Heparin or UFH, Low Molecular Weight heparin, etc.), generally function by

catalyzing the inactivation of thrombin by antithrombin III, thereby reducing platelet activation, the formation of fibrin gel from fibrinogen, and preventing blood clot stabilization and formation of large clots. Furthermore, Heparin binds to the A1 domain of vWF, which inhibits the binding of vWF to platelet GP-*Iba* receptor, and prevents shear activation of platelets and their adhesion to surfaces<sup>356,357</sup>; though low LMW heparin exhibited reduced binding to vWF-A1 by three orders of magnitude<sup>356</sup>.

This makes heparins particularly appropriate for anticoagulation via the intrinsic coagulation pathway in high-shear situations by effectively increasing the threshold of platelet activation required for coagulation. UFH has been known to trigger heparin-induced thrombocytopenia (HIT), which occurs due to an immune response to UFH intake wherein the immune system produces antibodies that activate platelets to counter UHF, triggering excessive coagulation. Other anticoagulants target Factor Xa, which converts prothrombin to thrombin<sup>358</sup> (also at risk of HIT), but do not directly suppress thrombin levels like Heparins or Direct Thrombin Inhibitors (DTIs). DTIs directly deactivate thrombin, and stop the thrombin platelet activation feedback loop yielding a powerful anticoagulation effect.

Antiplatelet therapies are extremely robust and widely used from daily doses to individuals at risk of thromboembolism to modest degrees of atherosclerosis, to preventing clotting during surgery. These generally function by disabling the highly specialized receptors on platelets. The most common antiplatelet therapy, ASA and/or Aspirin, functions by inhibiting the synthesis of Thromboxane A<sub>2</sub>, thereby functioning to reduce platelet activation (TxA<sub>2</sub> works synergistically with ADP and Thrombin to enhance activation), and also by reducing blood viscosity. Others (Abciximab, Eptifibatide, and tirofiban) target the function of vWF by inhibiting binding to the GP1b receptor complex,<sup>359</sup> whereas still others target the ADP receptor on platelets. Major risks aside from HIT of anti-thrombotic therapies are that all encourage excessive bleeding, and increase the risk of hemorrhaging, as well as the development of resistance (particularly in the case of Aspirin)

As all anticoagulants target endpoints of the coagulation cascade or the platelet activation mechanisms, their function can be easily incorporated into a coagulation cascade model or in the case of Heparin, by their effect on thrombin production rate. The effect of heparin is described by Griffith<sup>360–362</sup> using chemical kinetics to model the catalyzing effect of heparin on the deactivation of Thrombin by Antithrombin III:

$$-\frac{d[T]}{dt} = k' \cdot [AT \cdot H \cdot T] \quad 2-50$$

Where  $[AT \cdot H \cdot T]$  is the ternary molecule formed by heparin that accomplishes catalyzation, and  $T$ ,  $AT$ , and  $H$  correspond to Thrombin, antithrombin, and heparin concentrations, respectively. Assuming random (kinetic) binding of heparin to thrombin and antithrombin, and a degree of site independence, this reduces to<sup>361</sup>:

$$-\frac{d[T]}{dt} = k' \cdot \frac{[H][AT][T]}{\alpha K_{AT}K_T + \alpha K_{AT} + \alpha K_T[AT] + [AT][T]} \quad 2-51$$

Where  $\alpha$  is an efficiency factor for binding multiple proteins to heparin, ( $\alpha = 1.0$ ),  $K_T$  and  $K_{AT}$  are heparin/thrombin and heparin/antithrombin dissociation constants, respectively.

#### 2.5.4 Links Between Hemolysis and Thrombosis

Although it is well established that there is a link between hemolysis and thrombosis, there is a general scarcity of studies examining this effect, in particular concerning modelling. The interaction is in general two-way, as hemolysis tends to activate and trigger thrombosis. The growth of a thrombus constricts flow in a blood vessel, increasing shear stress and leading to hemolysis. This connection is why LDH spikes (produced during RBC membrane destruction) are used as an indicator of pump thrombosis in MCS. Hemolysis can trigger platelet activation because ADP is contained in RBCs in large quantities, and is a potent platelet activator. Furthermore, Hb in plasma binds to NO (released by endothelial cells) which inhibits thrombin function, though this is complicated by the fact that ADP release also triggers NO production in endothelial cells<sup>363</sup>. Extracellular hemoglobin itself is very thrombogenic, and recent studies report that Hb concentrations  $\geq 50 \frac{mg}{dL}$  predicted mortality in ECMO<sup>364,365</sup>. Hemoglobin can bind to the A2 domain of vWF<sup>365,366</sup>, which regulates the adhesive mechanics of the A1 domain, both of which bind to platelet glycoprotein receptors. Hb binding to both domains tends to increase reactivity by increasing surface area. At low shear rates, the A2 site can bind to platelet GP  $\alpha$ Ib $\beta$ 3 receptors, but at high shear rates ( $500-800 \text{ s}^{-1}$ ) only the association rate between vWF-A1 to GP1b $\alpha$  is sufficiently high to form a stable bond<sup>367</sup>. By binding to the A2 site on vWF, pfHb also blocks the usual cleavage of vWF Multimers by the ADAMTS13 enzyme which also uses the A2 site for this function.<sup>366</sup> At higher shear stress, the exposed A1 domain of vWF can itself also bind to pfHb, in effect making vWF hyper-reactive and increasing binding affinity to platelet receptors, fibrin, and collagen. This means that shear activation of platelets is augmented and that the adhesion rate, the bond strength of platelets, and the rate of

clot stabilization are also increased. This furthermore inhibits the anticoagulatory effect of heparin on platelet adhesion by preventing heparin from interfering with vWF function. Da et al.<sup>289</sup> find a dose-dependant and linear correlation between hemoglobin concentration and platelet adhesion rate to extra fibrinogen, collagen and vWF-coated surfaces at 6 Pa shear stress by up to a factor of 5, 10, and 2, respectively. They found that platelet adhesion to fibrinogen and collagen varied in direct proportion to the quantity of vWF present in the blood. Moreover, the introduction of anti-glycoprotein *Iba* antibodies (blocking vWF binding to platelets) or the absence of vWF effectively eliminated the increased platelet binding and clot strength. In general, this functions because of the increased affinity and surface area provided by the Hb molecule, acting as a mediator to help it bind to platelet receptors. Unsurprisingly, elevated pfHb levels are correlated to increased thrombotic risks such as myocardial infarct and multi-organ failure during<sup>368</sup> and microthrombi formation and thrombosis during ECMO<sup>369</sup>. Unfortunately, while the increase in adhesion rate is quantified relative to concentration of pfHb, a thorough literature search has not revealed any study that estimates the increase in platelet adhesion strength, the pfHb modified binding rate to external materials or alterations to embolization mechanics with hyper-adhesive vWF. Furthermore, the assays conducted by Da et al.<sup>289</sup> perform these at the relatively low shear stress of 6 Pa, and no study has been found that examines this effect under varying shear stress or at higher shear stresses as might be found in MCS. Furthermore, because pfHb can bind to multiple sites, including to platelets themselves (which also triggers platelet hyper-reactivity<sup>370</sup>) There is in general a strong need for experimental data regarding this effect, as sublethal hemolysis is nearly ubiquitous in thrombosis.

In general, though several studies examine the mechanisms by which hemolysis affects thrombosis, it is difficult to disentangle the relative dominance of the various mechanics. Furthermore, although hemolysis triggers thrombosis, it is well established that platelet activation occurs at a far lower shear stress than hemolysis, and thus it is difficult to gauge precisely what level of hemolysis will trigger thrombosis, whether thrombosis will occur first before hemolysis and then trigger it, or if there is a strongly coupled feedback mechanism.

### 2.5.5 Simulation of Thrombosis

In the past two decades the expanded knowledge of the myriad processes in thrombosis, and access to ever-increasing computational resources have made the simulation of thrombosis feasible at a macroscopic scale. The multiscale nature of thrombosis presents a unique challenge and requires a high degree of constitutive modelling at the cellular and molecular

scale to bridge the gap to macroscopic simulations. Cellular-scale simulation alleviates the need for some of this modelling by explicitly simulating the mechanics of complex processes such as thrombus rupture. On the other hand, the scope of such simulations is inherently limited to small domains of single injuries, or processes that are not particularly useful for the engineering of medical devices. This section will review some of these efforts and provide a picture of the current state of the art, but the reader is referred to Manning et al.<sup>371</sup> for a recent review of thrombosis simulation.

#### Cellular-Scale Simulations

Cellular scale simulations of whole blood are possible for small-scale domains such as near capillaries and near small wounds, using immersed boundary methods and lattice boltzman<sup>135</sup>, boundary integral methods<sup>136,139</sup>, or the Fully Eulerian method<sup>152,372</sup> for simulation the fluid-structure interaction.

A series of cellular scale studies by Fogelson et al.<sup>135,155,292,293,340,345,346,373,374</sup> attempt to simulate the full or partial coagulation cascade along with the activation, and most prominently binding mechanics of platelets, including correct diffusion and reaction of enzymes such as thrombin, tissue factor, collagen, and fibrin polymerization in the most comprehensive microscale simulations seen to date. They find that platelet concentration and platelet count are critical to maintaining the coagulation process and which coagulation pathway is most prevalent<sup>155</sup>. Leiderman and Fogelson<sup>340</sup> use cellular scale models to study the mechanisms of hemophilia and find that the confluence of the advective and diffusive transport effects of high flow tend to arrest the transport process, whereas platelet count and activation rate by shear stress counteract this to create the unique threshold starting thrombosis. Fogelson and Neeves<sup>293</sup> give a comprehensive review of cellular-scale thrombosis simulations and perform an in-depth analysis and model the adhesion mechanics of vWF by allowing bonds to form spontaneously between adjacent platelets. Others such as Belyaev et al.<sup>286</sup> focus on the coagulation reaction kinetics and fibrin polymerization at the injury site. Vahidkhah et al.<sup>138,139,335</sup>, and Zhao et al.<sup>136</sup> do not focus on the chemical process itself, but rather on the platelet margination effect via the interaction between RBCs, platelets and shear.

#### Macroscopic Continuum Simulation Approaches to Thrombosis

Continuum approaches to thrombosis do not explicitly resolve the individual mechanics of cells as particles, but rather consider them as populations and model mechanics that alter their concentrations. Consequently, it is necessary to model each of the mechanics discussed in the previous sections with the greatest possible accuracy to predict thrombosis. It is useful to

separate macroscale models by whether they target the extrinsic or intrinsic (contact) pathways. The intrinsic coagulation process is more difficult to model because it must consider the interactions with the endothelium and body and involves several pathways toward platelet activation and regulatory mechanisms. Fogelson<sup>347</sup> created the first comprehensive continuum model of platelet aggregation. Although their constitutive approach to clot embolization is unique, it neglects platelet activation except by contact with already activated platelets. At the time of writing, few studies attempt to simulate the extrinsic coagulation and thrombosis in the vasculature, with some notable exceptions. Kuharsky and Fogelson<sup>345,375</sup> model the extrinsic coagulation process and find that vastly simplified models of the coagulation cascade are sufficient to describe the mechanisms of blood clotting. Neither of these modelling approaches has been validated experimentally to any significant degree, however. Wang et al.,<sup>376</sup> include ADR equations for all factors in the extrinsic coagulation pathway but do not model the endothelial cell response. They are however able to reproduce experimentally measured thrombin levels at the injury site. Only Xu et al.<sup>377</sup> consider the endothelial cell response in their multiscale simulation studies of the extrinsic coagulation process.

Sorensen et al.<sup>320,378,379</sup>, develop the first continuum model to describe blood clotting in blood-exposed medical devices using 10 advection-diffusion-reaction (ADR) equations to model the production of prothrombin, antithrombin, thrombin, ADP, thromboxane, and platelets in the activated and adhered states. They neglect the extrinsic pathway but include the contact pathway by supposing that platelet adhesion to a surface results in activation (though activation of FXII is neglected). Adhesion is treated using first-order reaction kinetics, but embolization is neglected entirely. This model is significant because for the first time, it includes the (linear) synergistic action of ADP, thromboxane and Thrombin to reach a threshold to activate platelets and trigger a feedback loop. Goodman et al.<sup>325</sup> extend Sorensen's model by adding empirical relationships for platelet embolization, and platelet adhesion rates derived from experiments. Through a fitting process they are to qualitatively reproduce the thrombus formation sites on a cylindrical polyethylene tube with several contractions simulating stenosis. Bark<sup>380</sup> and Samra<sup>348</sup> attempt to simulate thrombosis using macroscale particles that represent platelet clusters and the agonist-threshold platelet activation of model of Sorensen et al.<sup>320</sup> Bark and Ku<sup>341</sup> predict thrombus growth simply by performing a time and surface integral of activated platelet concentration at blood exposed surfaces (yielding a proxy for platelet growth without embolization or convection), which appears to predict thrombus formation in a stenotic channel. Wu et al.<sup>15,339,381</sup> extend the model of Sorensen<sup>320</sup> and Goodman<sup>325</sup> to allow thrombus

growth to restrict channel flow using a modified Brinkman porous media restriction. Using this approach, they can reproduce the thrombus formation inside of a microchannel, and qualitatively predict the platelet formation inside of a mechanical circulatory support.

More recently, Du et al.<sup>373,374</sup>, followed a similar ADR equation approach as Sorensen<sup>320</sup>, but only included activation by ADP. They follow Fogelson's<sup>347</sup> early constitutive approach for describing platelet binding strength by including the inter-platelet link density as a spatially varying parameter of platelets (this requires the solution of two additional ADR equations). Furthermore, they use experimentally measured values of blood clot porosity and flow impedance values<sup>374</sup>. Unlike Wu et al.<sup>263</sup> however, Du et al.<sup>374</sup> use a truly (Eulerian) two-phase model where the blood and clot phases have their own mass and momentum conservation equations. Rojano et al.<sup>18</sup> follow Wu's approach but include ADR equations for fibrin polymerization and thus platelet stabilization (which was neglected by Wu). They can accurately reproduce the experimental thrombus formation experiments of Taylor et al.<sup>342</sup> for bovine blood, though the deviation from Yang<sup>382</sup> is larger for both human and bovine blood.

Taylor et al.<sup>349</sup> use Sorensen's platelet activation model but differ in the representation of the thrombus, defining a new quantity termed aggregation intensity. Similarly to Sorensen<sup>320</sup>, the aggregation intensity is a kind of volume fraction that represents the thrombus as a porous media obstacle in the flow; Like Wu et al.<sup>339</sup> the flow restriction is modelled using a modified Brinkman term. Unlike Wu however, embolization of platelets occurs at a constant rate after a critical minimum (0.9 Pa) shear stress is reached, following Fogelson's<sup>347</sup> platelet link model. Their model compares favorably against 3D fMRI images of a thrombus growing downstream from a backward-facing step in a cylindrical microchannel<sup>342</sup> using bovine blood. The same dataset used for validation, however, was used to determine platelet deposition rates and embolization stress. Yang<sup>383,384</sup> uses Taylor's model to predict device thrombosis over a backward-facing step in a cylindrical microchannel but remove agonist platelet activation due to thrombin and thromboxane (Sorensen's threshold model was found to underpredict activation by ADP). They compare their model and reproduce 3D FMRI data<sup>382</sup> (of human blood). Tobin and Manning<sup>385</sup> follow Taylor et al.<sup>349</sup> and Yang et al.<sup>384</sup>, but include a constitutive cohesive stress intensity term, again following Fogelson's link intensity approach<sup>347</sup>. They model link formation, however, as a function of mean fibrin length and separation distance between platelets, and breakage as proportional to mean fiber length. Like previous authors in the same group, they simulate flow in a backward-facing step up to a transitional Reynolds number of 3500. Belyaev<sup>386</sup> also look at thrombus formation due to

platelet aggregation effects at the near wall, but entirely neglect the coagulation cascade, platelet activation and adhesion chemistry. Muralidharan and Payne<sup>387</sup> apply this approach to construct a reduced-order model to simulate thrombus formation in a vascular tree.

Such work presents an opportunity to improve the understanding of thrombogenesis in blood devices. To date, no study has quantified the effect of hemolysis on thrombosis, however, which is a significant gap in the prediction of thrombogenesis given the interrelation of these mechanisms. Developing constitutive relationships for the interaction between hemolysis and thrombosis at a macroscopic scale is difficult because of the complexity of modelling hemolysis itself, the myriad ways in which hemolysis can interact with thrombosis, and the reported sensitivity of thrombosis to hemolysis. As the effect is strongly dependent on the magnitude of hemolysis, and begins in the sublethal hemolytic range, it is also important to model sublethal hemolytic activity.

#### Multiscale Simulations

Thrombosis in general spans multiple length and time scales. Clot aggregation is a process that spans days, whereas fluid, biological response, and platelet activation phenomena have time-scales on the order of seconds, and clot adhesion and embolization are microscale processes. Multiscale modelling involves the modelling and simulation of several sub-models that describe mechanics at varying length and time scales and are integrated into one another using some kind of averaging scheme. It is by far the most complex form of simulation available and consequently, few examples exist, but helps alleviate the need to accurately model and validate complex physical phenomena such as embolization. All thrombosis simulation has a multiscale aspect, however, because the computational expense of resolving day-long processes with microsecond time-steps is immense. Wu et al.<sup>15,339,381</sup> for example deal with this by scaling their adhesion rates by a factor of 30, whereas Sorensen<sup>320</sup> and Goodman<sup>325</sup> only simulate surface chemistry.

There has been a recent proliferation of multiscale studies, owing to increased computational capacity, advances in alternative particle-based simulation techniques for fluid simulation, and advances in coupling the relevant spatial and time scales. Yazdani et al.<sup>388</sup> describe a comprehensive mesoscale to microscale scheme that captures thrombus growth in the microvasculature. In their scheme, dissipative particle dynamics (DPD) is used to solve the fluid pressure and velocity fields of the plasma carrier fluid, the advection-diffusion-reaction of chemical species in plasma, whereas coarse-grained molecular dynamics (CGMD) are used



to simulate the platelet membrane transition from discoid to activated, and explicitly model the receptor-ligand interactions with the surfaces. In their simulations, averaging is used to bridge the coarse and fine spatial scales, and domain decomposition to solve fine spatial mechanics at necessary areas such as on the platelet surface where nano-scale interactions occur. They use a concurrent multi-timestepping procedure, where the stochastic Trotter product (similar in principle to Reynolds averaging) was used with Velocity-Verlet integration to bridge the interaction between short and long timescale interactions. These approaches yield appreciable time savings, for example the multiscale approach led to a reduction of computation time from 2.6 years to 3.5 days. They note, however, that more work needs to be done to bridge the very fast initial thrombus-surface adhesion mechanics, which occur on the order of seconds, to the slow thrombus growth and remoulding that occurs over hours or days.

Zheng et al.<sup>389</sup> perform quasi-multiscale simulations where thrombus growth and remodelling processes are simulated at different timescales. An early study by Xu et al.<sup>377</sup> conducts one of the only computational approaches to incorporate the cellular response in their early multiscale work. Along with the continuum model of fluid flow Flamm and ADR models of thrombo-agonists, they model the fibrin entrapment of (red) blood cells in the clot, platelet adhesion, and embolization. Flamm et al.<sup>390,391</sup> construct one of the more comprehensive multiscale models. They use the lattice-Boltzmann technique to simulate the fluid flow and pressure field in a thrombus, finite element analysis to solve the ADR equations governing agonist biochemistry and include a sub-simulation of platelet adhesion and embolization on the clot surface. One of the more interesting aspects of this work is that they use Chatterjee's<sup>322</sup> neural network model to capture a specific patient's platelet activation response to concentrations of a variety of agonists, emphasizing the unique patient-specific response to thrombo-agonist levels and their interactions. Most recently, Shankar et al.<sup>392</sup> conducted multiscale simulations of clot formation in a microfluidic device, resolving cell scale mechanics with constitutive models for platelet adhesion and chemical bond breakage due to shear, while simultaneously executing a lattice-Boltzmann simulation of the fluid interaction with the thrombus. Although these simulations have sub-simulations for key mechanics, the computational domain remains idealized to planar or cylindrical geometries, and domain sizes only on the millimetre scale. In fact only, Wu et al.<sup>15</sup>, Murallidharan and Payne<sup>387</sup>, and Wang et al.<sup>376</sup> attempt to model thrombosis in any kind of complex flow situation such as an LVAD or in the aorta.

## **2.6 Summary and Overview**

In this section, the reader is given an overview of the key points covered in the section. For more details, the reader is referred to the corresponding sections.

### **2.6.1 Design Considerations for Mechanical Circulatory Support Devices**

Medical Circulatory Support (MCS) devices have become an essential tool to the management of late-stage heart failure and related conditions by aiming to assist or even replace the heart's function. This ensures a continual and adequate blood flow, mimicking the heart's natural ability to oxygenate and nourish every part of the body. With the devices being an integral part of the circulatory system, minimal size, energy efficiency and long-term reliability are non-negotiable design criteria. These characteristics promote the patient's safety and the device's efficacy over extended periods. MCS devices are not without risks, however. Stroke, infections, and right ventricular failure loom large among these. Tackling the severity of these issues, strokes and right ventricular failures demand immediate attention, given the grave, life-threatening repercussions they pose. Blood damage is intricately linked with the pathophysiological concerns surrounding the use of MCS devices. Even with cutting-edge design enhancements geared towards mitigating hemolysis, the issue remains tenacious. Among the palette of complications presented by these devices, the twin challenges of stroke and right ventricular failure stand out due to their potential to cause immediate, life-threatening repercussions. These should, thus, be at the forefront of design modifications.

In particular, the connection between hemolysis and thrombosis warrants attention. The rupture of red blood cells, or hemolysis, has multifaceted repercussions to patient health. Hemolysis, even at low levels lead to kidney failure and increases the risk of thrombosis and thromboembolic complications like myocardial infarctions, deep-vein thrombosis or stroke. Sublethal hemolysis is in general enigmatic, as the typical hemolytic markers such as rises in LDH and Bilirubin are only triggered by membrane destruction, and there is information linking sublethal hemolysis to patient outcomes. In general, despite three generations of MCS and significantly reduced rates of lethal hemolysis, the rate of thromboembolism and stroke remains unchanged and suggests a deeper issue.

### **2.6.2 Blood Flow Modelling**

To comprehend the mechanics of blood flow, it is necessary to consider composition of blood itself, which derives its non-Newtonian, thixotropic and viscoelastic properties from its major constituents from the highly deformable nonlinear structural properties of RBCs. Modelling

efforts focused on hemolysis and thrombosis must consider the relative phasic motions of these cells, the lift effect that causes RBCs to drift away from shear, and the volume exclusion effect that compels platelets to aggregate in areas of high shear. Several models have been developed to understand platelet diffusion rates, yet the drift and diffusion of red blood cells are poorly understood. A further complication arises when addressing blood rheology, which is profoundly complex. While for low shear rates, its non-Newtonian and thixotropic characteristics can be neglected, viscoelasticity is generally crucial to reproduce high shear regions. Studies, such as those by Pinto et al.<sup>181</sup>, demonstrate how viscoelastic modelling can profoundly influence wall shear stress calculations. Many current Computational Fluid Dynamics (CFD) studies, especially when evaluating complex flow devices like MCS, oversimplify conditions by assuming bloodflow to be Newtonian and Laminar. Indeed important effects like thrombosis and sublethal hemolysis occur at low shear stresses, and consequently, there is a consistent tendency to underpredict sublethal hemolysis and such events at low shear.

### **2.6.3 Blood Damage Prediction**

Hemolysis, the process of red blood cell rupture, presents complexities in prediction, especially within regions characterized by low shear and intricate flow regimes. One key challenge arises from transient stress applications and pronounced streamline curvature. Red blood cells, given their highly deformable nature, experience heightened loading under these conditions due to inertial loading. Empirical power law methods often fall short in representing these peculiarities, especially when the data derived from Couette rheometers is considered.

A phenomenon that further complicates the understanding of hemolysis is the reduced damage that red blood cells undergo due to Reynolds stress, the reasons for which are yet to be entirely understood. The collisions of red blood cells within both laminar and turbulent flows stands central to the discourse on blood damage. However, its importance is often downplayed or overlooked entirely. Key questions remain unanswered pertaining to how turbulent fluctuations damage red blood cell membranes, and how collisions affect membrane stress. Recent revelations also indicate that blood displays turbulent behaviour even in the physiological flows within major arteries<sup>393</sup>. This finding further accentuates the need for comprehensive studies. In this realm, while Leveret's classical work<sup>4</sup> on the influence of hematocrit on hemolysis stands out, few others have ventured into this niche, leaving a substantial gap in our understanding.

Thrombosis, the process wherein blood clots form, is multifaceted in its origin and manifestation. Predictive modelling for thrombosis, though nascent, has made discernible strides, especially concerning simulations within medical devices. Two prominent avenues dominate thrombosis simulations: the cellular-level constitutive approaches and the continuum approaches rooted in the Navier Stokes solution. The latter integrates advective-diffusion-reaction equations to simulate key players including cells, proteins, and paracrine signaling.

At its core, thrombosis is a multiscale problem, mandating a multiscale approach for its comprehensive understanding. Continuum thrombosis models, with their empirical foundations, have successfully replicated in-vitro thrombus growth patterns. However, the activation of platelets, a key component in thrombosis, demands intricate modelling. While shear stress activation of platelets is decently represented, a gap exists in understanding platelet activation under high-frequency loading and in higher shear regimes as seen in non-physiological flows, typical of medical circulatory support devices and heart valves. Moreover, the activation dynamics, influenced by thrombo-regulators such as thrombin, ADP, and thromboxane, require refinement, especially concerning endothelial cell interactions and the biological variability manifested in patients.

High-frequency loading has a notable impact on platelet activation, making them considerably more sensitive to turbulent stresses. The mechanics of platelet adhesion and embolization are modelled predominantly using first-order reaction kinetics. Nuances such as the Fåhræus-Lindqvist effect, which accounts for the effect of shear rate on platelet adhesion, and the heterogeneous structural properties of blood clots, are areas still rife for exploration.

Hemolysis and thrombosis are intricately linked. Hemolysis can amplify thrombotic risks through several pathways: the release of ADP and ATP from ruptured red blood cells activates platelets; Hemoglobin's binding with von Willebrand factor's A1 and A2 domains prompts platelet hyperadhesion, reinforcing bonds with walls and other platelets; this hyperadhesive von Willebrand factor is also immune to heparin inhibition; and lastly, Hemoglobin scavenges Nitric Oxide, a powerful vasodilator and thrombosis regulator, from endothelial cells, which can further exacerbate the thrombotic process.

## **2.7 Key Challenges and Future Perspectives**

The study of blood flow and its related pathologies presents a labyrinth of intricacies. A paramount challenge in this domain is the effective modelling of shear stress in blood. This is particularly relevant in areas proximate to vessel walls, in low shear regions, and requires a

finesse that amalgamates improved constitutive models with viscoelastic modelling. The turbulence phenomenon in blood flow is also a significant area of concern. Presently, there is an absence of any turbulence model specific to blood flow. However, emerging evidence underscores the vitality of turbulence in blood flow modelling, especially in accurately predicting low-shear regions.

The mechanics of cellular collisions in blood, in laminar and within turbulent flow regimes, is another pivotal subject to hemolysis. There exists an ambiguity about how turbulence and shear forces conspire to inflict damage on red blood cells. While the phenomenon of hemolysis is well-acknowledged, a more profound understanding of sublethal hemolysis's pathophysiology is warranted. Furthermore, the interrelation between hemolysis and thrombosis, especially within the framework of anticoagulation, remains a subject that merits examination.

Central to blood flow modelling is the accurate prediction of shear stress, especially in low shear and transient domains where non-Newtonian modelling and viscoelasticity are crucial and remains a blind spot in the literature. Moreover, there is a great need for reliable blood-flow specific turbulence models to reliably predict fluid-dynamic phenomena like stagnation zones that are central to blood damage. Another gap is the quantification of stress on red blood cells, as it is unclear how fluid stress transfers to the red blood cell membrane.

The heavy reliance on empirical methods in both hemolysis and thrombosis modelling is in general a pernicious issue. Emergent demands in this field include the development of constitutive models for red blood cell damage, which can reflect the multifaceted nature of flow and, importantly, the mechanics of cellular collisions. Another area demanding attention is understanding the mechanics behind platelet adhesion to diverse materials, given its marked dependence on surface wettability and sample-specific attributes. The processes governing protein immobilization, platelet-surface interactions, platelet embolization, and thrombus detachment, though fundamental, remain inadequately understood. These are not only pivotal for designing thrombo-resistive materials and enhancing modelling techniques but also for understanding pathologies like thromboembolism, deep-vein thrombosis, cardiovascular diseases, and infarctions. Finally, the inclusion of red blood cells in (red) thrombus formation remains untouched and necessitates further research. As the scientific community delves deeper into understanding the complexities of blood flow and homeostatic pathologies, multiscale modelling will emerge as an invaluable tool. It offers a promise to shed light on constitutive modelling intricacies of hemolysis and pivotal thrombosis aspects such as platelet

adhesion and embolization. By diving deep into the microscale, multiscale modelling can illuminate the processes governing platelet adhesion and embolization, elucidating the binding mechanics to surfaces with varying roughness and wettability attributes.

Finally, hemodynamic DNS (Direct Numerical Simulation) and LES (Large Eddy Simulation) studies can provide an avenue to explore the genesis of turbulence in blood. Nonetheless, this endeavour is complicated due to the presence of red blood cells and the resultant breakdown of the single-phase blood approximation at microscopic scales. Several emergent technologies also hold potential. For example, physics-informed Neural Networks, powered by multiscale simulation data. Such networks can be a revolutionary tool for constitutive modelling, possessing the adaptability required to encompass the vast biological variability observed from one patient to another.

## **Chapter 3: Methodology**

---

Two computational studies are executed to examine the effect of RBC-RBC interactions on sublethal hemolysis, and to examine and quantify the effect of hemolysis on thrombosis.

The first study aims to answer the simple question of whether RBC-RBC interactions have a strong effect on transmembrane hemoglobin diffusion. It is first necessary to address the impact of cellular interactions and volume fraction on the distribution of transient strain, stress, experienced by the red blood cell membrane, and consequently transmembrane diffusion of hemoglobin, at various shear rates and conditions. In addition, the effect of viscoelasticity on these phenomena, and the overall effect of strain experienced by the red blood cell due to impulse loading conditions lasting on the order of 0.01s. Cell-scale simulations will be executed to collect data on sublethal hemolysis and RBC membrane dynamics in uniform and varying shear rates and RBC concentration. A multiphase computational fluid dynamics approach is used with a fully Eulerian structural model to capture the deformation mechanics of the membrane and compute the distribution of stress and strain on the membrane.

The second computational study will examine thrombus formation in an open-hub LVAD focusing on the effect that hemolysis has on thrombosis, in static and dynamic flow conditions. Incompressible computational fluid dynamic simulations are executed to compute the hemodynamics of blood flow in an open-hub left-ventricular assist device. Thrombosis is simulated using the continuum approach pioneered by Sorensen et al.<sup>320,378</sup> and a modelling approach is developed to examine the interaction of thrombosis with hemolysis.

All computational studies are executed on local machines. ANSYS Fluent<sup>TM</sup> was chosen as the solver of choice due to thorough documentation, flexibility and customizability, stability, as well as superior meshing and multiphase modelling capabilities.

### 3.1 Overview of the Finite-Volume Method

The following section provides a general overview of the finite volume method employed for both computational studies and discusses it in the context of the particular implementation and settings employed in ANSYS Fluent<sup>TM</sup>. First, an overview is given of the governing equations, and then the discretization, computation of gradients, and solution scheme are discussed in sufficient detail to understand the present work.

#### 3.1.1 Overview of Computational Fluid Dynamics Simulation and Solution

The Navier-Stokes equations describe the motion of fluid in a domain in the Eulerian reference frame. The governing equations for fluid flow are the continuity equation, which describes the conservation of mass, momentum, and energy in a stationary domain. In this work, compressibility effects are neglected due to the low speeds involved in biological flows, and the energy equation is not solved. The domain is broken up into geometric sub-volumes during a process called meshing, and the equations are discretized on the meshed domain. The continuity equation is given in conservative form as:

$$\frac{\partial \rho}{\partial t} + \nabla \cdot (\rho \vec{v}) = 0 \quad 3-1$$

where  $\rho$  is the density of the fluid,  $t$  is time,  $\vec{v}$  is the velocity vector. The vector dot product of the gradient with another vector (known as the divergence),  $\nabla \cdot$ , gives the sum of the fluxes of a quantity entering and exiting a volume. In general, in this work, the arrow above the velocity,  $\vec{v}$ , is used to denote vectors, the bullet operator,  $\cdot$ , denotes multiplication or the inner product, and bolded symbols denote tensors of rank 2 or more. The momentum equation is given by:

$$\frac{\partial(\rho v)}{\partial t} + \nabla \cdot (\rho v v) = \nabla \cdot (\boldsymbol{\sigma}) + \vec{f} \quad 3-2$$

Where  $f$ , is body force per unit volume, the divergence of the stress tensor  $\boldsymbol{\sigma}$ , gives the total forces acting on the boundaries of the volume. The fluid stress tensor,  $\boldsymbol{\sigma}$ , is given by:

$$\boldsymbol{\sigma} = \mu(\nabla v + (\nabla v)^T) - p\mathbf{I} \quad 3-3$$

The gradients are discretized and approximated from the values of local and neighbouring cells by assuming a linear or polynomial relationship between cells.

### 3.1.2 Numerical Discretization and Solution

In ANSYS Fluent, the convective and diffusive terms in the momentum equation are discretized separately. The convective terms are generally discretized using the upwind scheme, which considers the direction of flow to avoid numerical oscillations. The diffusive terms are discretized using the Green-Gauss node-, cell-, or least-squares-based method for approximating gradients.

In this work, the second-order accurate upwind (SOU) scheme is generally used, which uses a Taylor expansion of the cell-centred solution. The value of a solution variable,  $\psi$ , at the face is given in terms of the gradient and the displacement vector from the upstream cell centroid to the face centroid,  $\vec{r}$ .

$$\psi_{f,SOU} = \psi_c + \nabla\psi_{upstream} \cdot \vec{r} \quad 3-4$$

$\nabla\psi_{upstream}$  is the approximation of the gradient in the upstream cell. In general, the gradients are approximated from the values at the centroids of surrounding cells, using the Green-Gauss theorem, discussed subsequently. As the gradient is computed in the upstream cells, the discretization when summed over all faces of the cell is second-order accurate. The gradient is limited to prevent the introduction of new maxima and minima, making the SOU scheme highly stable. The result is a mass and momentum conservation equation for each cell, which is a function of the value of  $\psi$  in all neighbouring cells. The resulting system of equations is linearized and forms a large sparse matrix that can be solved using sparse matrix inversion techniques.

The ability of large sparse matrices to be solved efficiently by splitting the workload over numerous processing cores (the scalability) is of paramount importance in CFD. Delving deeply into the numerical solution is beyond the scope of this work, but generally, scalability is influenced by the number of neighbours and other variables that  $\psi_c$  is a function of. When the mass and momentum equations, which are coupled, are solved simultaneously to obtain the velocity and pressure, the solution is fully coupled, but the high connectivity leads to poor scalability. To improve scalability, the mass and momentum equations are solved separately (i.e. a segregated solver) using a coupling algorithm to correct pressure and velocity iteratively. This is done by transforming the mass conservation equation into a pressure equation and eliminating pressure from the momentum equation. The subsequent sections describe in more detail the numerical mechanics involved in solution linearization, gradient computation, and multi-grid approaches.



In general, the momentum and pressure equations are discretized using the unique schemes described below. ADR and scalar transport equations, which are in both studies are discretized in space using the third-order MUSCL scheme in the first study, and the second-order upwind scheme. In the third-order MUSCL scheme, a central difference spatial discretization is blended with an upwind scheme, that is the gradient is computed at both the center and upwind cells to estimate the local cell values, whereas in the second-order upwind scheme, the gradient is computed from the upwind cell and used to approximate the value in the local cell to obtain the second-order discretization. The fraction equation was discretized using the compressive scheme, which helped improve stability. Fluent employs flux limiters in the second-order upwind scheme to reduce momentum undershoots based on the upwind gradient, but not in the MUSCL scheme. Temporal discretization is achieved via the bounded second-order implicit backward Euler scheme.

#### Gradient Computation

The Green-Gauss theorem is used to compute the gradient of a variable at a finite-volume cell in computational fluid dynamics simulations. The theorem states that the gradient of a variable at a cell can be computed by taking the surface integral of the variable across the boundaries of the cell. Mathematically, the Green-Gauss theorem can be expressed as:

$$\nabla\psi = \frac{1}{V_c} \sum_{f \in \partial V_c} A_f \psi_f \quad 3-5$$

Where  $V_c$  is the volume of the element,  $A_f$  and  $\psi_f$  are the area of face  $f$  and the value of  $\psi$  on the boundary of the volume element,  $\partial V_c$ . The sum is taken over all faces  $f$  that belong to the cell. The area vector  $A_f$  is defined as the area of the face times the unit vector normal to the face. The value of the variable  $\psi$  at the center of the face  $f$  is computed by interpolating values of  $\psi_c$  of the two cells of which  $f$  is the interface.

In this work, two approaches are used, the least squares approach and the node-based gradient computation approach.

The least-squares approach involves computing the gradient by minimizing the sum of the squares of the difference between the calculated value and the actual value at the neighbouring nodes. To compute the gradient using the least-squares approach in ANSYS Fluent, the cell is first surrounded by a set of neighbouring nodes. A linear least-squares fit is then performed on the nodal values of the variable at the neighbouring nodes to obtain the gradient at the center of the cell. The least-squares fit is performed by minimizing the sum of the squares of the

difference between the calculated value and the actual value at the neighbouring nodes. The least-squares gradient computation approach in ANSYS Fluent provides an accurate and stable method for computing the gradient particularly when the grid is irregular and unstructured, or when the variable being computed is not smooth.

The node-based approach involves computing the gradient of the variable at a node by averaging the values of the variable at neighbouring nodes to obtain the face value.

$$\overline{\psi_f} = \frac{1}{N_f} \sum_n^{N_f} \overline{\psi_n} \quad 3-6$$

The nodal values,  $\overline{\psi_n}$  are obtained by performing a least-squares fit of the values of  $\psi_c$  at the surrounding cell centers to a linear surface, preserving second-order spatial accuracy around each node. As the stencil of cell values sampled is larger than other methods, and because values are averaged at neighbouring nodes and involve multiple least-squares fits, the process is highly computationally expensive. The node-based approach, however, provides the most accurate approximation of the gradient compared to other methods, particularly for uniform meshes and discontinuous functions.

#### Pressure Velocity Coupling

Adequate pressure velocity coupling is necessary to help avoid numerical instability associated with the highly coupled and nonlinear nature of the Navier-stokes equations. ANSYS Fluent provides many different algorithms to achieve pressure-velocity coupling, two are discussed here: the PISO (Pressure-Implicit with Splitting of Operators) method and the SIMPLE (Semi-Implicit Method for Pressure-Linked Equations) algorithm. The PISO method is an iterative algorithm that splits the pressure correction into two steps, while the SIMPLE algorithm is a semi-implicit method that couples the pressure and velocity fields. The choice of algorithm depends on the specific requirements of the simulation, and both methods have been extensively validated and widely used in computational fluid dynamics simulations.

The PISO method is an iterative method that splits the pressure correction into two steps: the first step involves predicting the velocity field using the guessed pressure, while the second step involves computing the pressure correction by solving a Poisson equation based on the velocity correction. The algorithm is iterated until the convergence criterion is met.

The SIMPLE algorithm, on the other hand, is a semi-implicit method that couples the pressure and velocity fields by introducing a correction to the pressure field based on the velocity field.

The algorithm involves several steps, the velocity field is predicted using the current pressure field. Then a correction is computed for the pressure field based on the predicted velocity, and the corrected pressure field is used to update the velocity field. If continuity is satisfied, the iteration is considered converged. Overall, both the PISO and SIMPLE algorithms have been shown to couple the pressure velocity solution, though the PISO algorithm is preferred in multiphase flows and offers greater scalability when the convective courant number is on the order 1.

#### Pressure Discretization

Discretization of the pressure equation is complicated because the segregation of the mass and momentum equations leads to artificial checkerboard-type numerical errors when the pressure and velocity are both stored at the cell center. To alleviate this, the PRESTO! algorithm is used in this work, where pressure is staggered (stored on cell faces), interpolated onto cell centers, and corrected. The velocity field is predicted using a first-order upwind scheme based on the guessed pressure field. The pressure correction is computed by solving the Poisson equation for the pressure correction term. The pressure and velocity fields are corrected using the pressure correction term, and the algorithm is iterated until the pressure and continuity are converged. The use of a pressure-correction method helps mass-momentum coupling and improves the rate of convergence.

#### Linearization

Linearization is generally a complex procedure and is only discussed at a high level. ANSYS Fluent linearizes the Navier-Stokes equations by using the Newton Iterative linearization technique. The Jacobian matrix, which contains the partial derivatives of the governing equations for the solution variables, is used to estimate the current state of certain solution variables from the value at a previous iteration. For example, the value of  $\psi v$  at the current iteration,  $k$ , can be expressed relative to the value at the previous iteration,  $k - 1$ .

$$\psi^k v^k = \frac{\partial \psi}{\partial v} (v^k - v^{k-1}) + \frac{\partial v}{\partial \psi} (\psi^k - \psi^{k-1}) + \psi^{k-1} v^{k-1} \quad 3-7$$

In this way, a linear system can be formed by solving for the values at iteration  $k$  only. The Jacobian matrix is thus used to linearize the nonlinear terms in the governing equations, making it possible to solve the equations iteratively, until convergence is achieved. The linearization process in ANSYS Fluent provides accurate solutions for nonlinear partial differential equations.

### Algebraic Multigrid

The Algebraic multigrid (AMG) solver in ANSYS Fluent uses a hierarchy of coarser grids to accelerate the convergence of the solution. AMG improves convergence by providing a good initial estimate of the next solution step at low computational cost, while filtering numerical error on the order of the coarsest grid spacing. In Algebraic multigrid, the coarser grids are obtained by grouping together adjacent cells and representing them as a single cell in the coarser grid. The AMG solver in ANSYS Fluent uses a V-cycle multigrid method, in which the grid is successively coarsened, and then refined. The linear system of equations is solved at each level of the hierarchy. The use of a hierarchy of coarser grids and the V-cycle multigrid method accelerates convergence of the solution and reduces computational time. A smoothing method further improves the accuracy and stability of the AMG solver.

### Computational Platform

Simulations are conducted on two 64-vCPU server nodes. Each node has two Intel Xeon E5-2697v3 CPUs and 64 GBs of memory. 48 of the 64 threads were used to maximize the performance of the Ansys Fluent Solver. In total, 128 vCPU academic licenses were available in Ansys fluent to execute the simulations between 2021 and 2022.

## **3.2 Microscale Modelling of the Interaction of Red Blood Cells**

Unsteady incompressible finite-volume computational fluid dynamics simulations are executed using Ansys Fluent<sup>TM</sup>. We select the fully Eulerian structural methodology for membrane modelling developed by Pozrikidis<sup>203,394</sup>, and extended by Takagi et al. Sugiyama, and several others<sup>152,372,395–397</sup>. The methodology uses the volume-of-fluid (VOF) multiphase numerical scheme to model plasma and hemoglobin as coupled interpenetrating phases, wherein a common (mixture) velocity and density field is solved to reduce computing cost, but mass conservation equations are solved for each phase separately. This methodology is selected because it provides several key benefits in addition to the reduction in computational cost for complex fluid-structure interaction problems requiring frequent remeshing. The chief reason is that it permits flexibility in modelling the RBC membrane using the hyperelastic strain-energy approach and that the fully Eulerian method is particularly applicable to modelling very large deformations, as well as properties such as viscoelasticity and viscoplasticity. Furthermore, unlike Lattice-Boltzmann-based methods, the multiphase approach ensures volumetric incompressibility of the RBC cytoplasm, as well as the ability to simulate different viscosities, and incorporate a constitutive viscoelastic model of the membrane, as well as the ability to solve an advection-reaction-diffusion equation easily to examine the aggregation of

extracellular hemoglobin. Finally, the stability and well-validated aspect of finite-volume CFD solvers was desired to minimize the complexities of numerical simulation, as was the extensive documentation and flexibility inherent from using a feature-rich yet versatile commercial CFD solver such as ANSYS Fluent™. The subsequent sections describe in detail the implementation of the fully Eulerian fluid-structure interaction approach, as well as the deviations developed and adopted in this work to improve stability and performance in high shear.

### 3.2.1 Computational Scheme

This section describes in detail the equations approach and numerical implementation of the fully Eulerian approach to fluid-structure modelling which is used to simulate the dynamics of multiple red blood cells at high shear. The method is built on top of the Volume of Fluid (VOF) multiphase method. A structural model for the red blood cell membrane is defined at the interface between the cytoplasm and plasma phases, which is implemented in ANSYS Fluent.

#### Governing Equations

The mass conservation equations for the VOF multiphase scheme in differential form are:

$$\frac{1}{\rho_q} \left( \frac{\partial}{\partial t} (\phi_q \rho_q) + \nabla \cdot (\phi_q \rho_q \vec{v} - D_q \nabla \phi_q) \right) = 0, \quad \sum \phi_q = 1; \forall q \in \{p, c\} \quad 3-8$$

Here,  $\phi_q$ ,  $\rho_q$ , and  $D_i$  denote the phasic volume fraction, density and isotropic mass diffusion of the  $q^{\text{th}}$  phase, whereas  $\rho$ , and  $\vec{v}$ , denote the mixture density and velocity vector, which are defined as the sum of phasic values weighted by volume fraction. Subscripts  $h$ , and  $p$  denote hemoglobin and plasma phases. The momentum conservation equation is solved for the mixture velocity and density field common to both phases:

$$\frac{\partial}{\partial t} (\rho \vec{v}) + \frac{\partial}{\partial x_i} (v_i \rho \vec{v}) = \nabla \cdot \boldsymbol{\sigma} + b(\phi_c, \nabla \phi_c) \vec{f} \quad \forall i \in \{1, 2, 3\} \quad 3-9$$

where  $\boldsymbol{\sigma}$  is the fluid stress tensor, which for both phases is modelled as laminar and Newtonian, and  $\vec{f}$  is an immersed-boundary force vector that transfers momentum between the structural model and the fluid.  $b(\phi_c, \nabla \phi_c)$  is an indicator term to locate the interface between plasma and hemoglobin phases, given in the subsequent section.

An immersed boundary approach is used transfer momentum between the structural model and the fluid by applying a force as a source term to the momentum conservation equation, coupled implicitly to the structural equations. An elastic membrane is defined at the interface between the plasma and hemoglobin phases. The deformation of the membrane, relative to the deformed

frame, is represented by the left Cauchy-Green deformation tensor,  $\mathbf{G}_s$ , conserved in the Eulerian reference frame:

$$\frac{D}{Dt}(\mathbf{G}_s) = \mathbf{L} \cdot \mathbf{G}_s + \mathbf{G}_s \cdot \mathbf{L}^T, \quad 3-10$$

where  $\mathbf{L}_{ij} = \partial_j v_i$  is the velocity gradient tensor,  $\mathbf{G}_s \equiv \mathbf{P}_s \cdot \mathbf{G}_{i,j} \cdot \mathbf{P}_s$  is the surface-projected left Cauchy deformation tensor, and  $\frac{D}{Dt} = \left( \frac{\partial}{\partial t} + v_i \frac{\partial}{\partial x_i} \right)$  is the material derivative.  $\mathbf{P}_s = \mathbf{I} - \vec{n}\vec{n}^T$  is the surface projection tensor, computed from the surface normal vector,  $\vec{n} = \frac{\nabla \phi_h}{|\nabla \phi_h|}$ , computed at the plasma-hemoglobin interface. The bullet operator,  $\cdot$ , denotes the inner product. In addition, the (spherical) reference bending curvature is tracked and used to compute the bending moment.

$$\frac{D}{Dt}(\kappa_r) = 0 \quad 3-11$$

In total, 10 transport equations are solved in tandem with the Navier-Stokes equations. The force applied to the momentum equation,  $\vec{f}$ , is computed from the in-plane tension,  $\boldsymbol{\tau}_s$ , and stress,  $\mathbf{q}_s$ , using the surface-projected divergence.

$$\vec{f} = (\mathbf{P}_s \cdot \nabla) \cdot (\boldsymbol{\tau}_s + \mathbf{q}_s); \quad 3-12$$

In-plane Piola-Kirchoff stress,  $\boldsymbol{\tau}_s$ , stress can be obtained by differentiating the energy, and projecting it onto a surface. The final relation for stress is:<sup>150,152,203</sup>

$$\boldsymbol{\tau}_s = \frac{2}{\sqrt{(II_s + 1)}} \left( \frac{\partial W_s}{\partial I_s} \mathbf{G}_s + (II_s + 1) \frac{\partial W_s}{\partial II_s} \mathbf{P}_s \right) \quad 3-13$$

$I_s$  and  $II_s$  are the first and second invariants of the deformation tensor,  $\mathbf{G}_s$ .  $W_s$  is material strain energy given as a function of  $I_s$  and  $II_s$ . The spectrin-based RBC membrane model of Skalak et al,<sup>200</sup> for example Skalak's model which was given in Section 2.3. is:

$$W_s = \frac{E_s}{4} ((I_s + 1)^2 + \alpha II_s^2 - 2 II_s - 1) \quad 3-14$$

Where  $E_s$ , and  $\alpha$ , are surface modulus of elasticity and the resistance to area dilation, respectively, as given by Skalak. Note that  $I_s$  and  $II_s$  are surface invariants, and along with  $W_s$  are generally defined by the principle stretches,  $\lambda_i$ . It is, however, much more convenient to compute them from  $\mathbf{G}_s$ .

$$I_s = \lambda_1^2 + \lambda_2^2 - 2 = \text{tr}(\mathbf{G}_s) - 2 \quad 3-15$$

$$II_s = \lambda_1^2 \lambda_2^2 - 1 = (tr(G_s^2) - tr(G_s)^2) - 1 \quad 3-16$$

The bending stress is computed from bending moment,  $\vec{m}$ , following Pozrikidis et al,<sup>394</sup> is computed by subtracting surface curvature,  $\kappa$ , from the reference (initial) spherical curvature,  $\kappa_r$ .

$$\begin{aligned} \mathbf{q} &= ((\mathbf{P}_s \cdot \nabla) \cdot \vec{m}) \cdot \mathbf{P}_s \vec{n} \\ \vec{m} &= E_b(\kappa - \kappa_R \mathbf{P}_s) \\ \mathbf{k} &= \partial_i n_j \\ \kappa_r(t=0) &= \nabla \cdot \mathbf{n}|_{t=0} \end{aligned} \quad 3-17$$

This model neglects the mass and inertia of the RBC membrane. Furthermore, the bending moment computation assumes locally spherical reference curvature such that the undeformed equilibrium shape of the RBC is only slightly bi-concave<sup>394</sup>.

#### Fluid Material and Multiphase Modelling Parameters

Two fluids are considered in our simulations, plasma and cytoplasm, which are treated as incompressible Newtonian fluids with densities of 1.050 and 1.118 [kg m<sup>-3</sup>], respectively, and viscosities of 1.003 and 5.015 [cP], respectively. In the non-viscoelastic cases, material properties in computational cells containing both fluids are computed simply as an average weighted by each fluid's respective volume fraction.

In the viscoelastic case, membrane viscosity is implemented quite simply by specifying a user-defined viscosity function that varies with the boundary indicator function, such that viscosity is:

$$\mu = \begin{cases} (1 - b(\phi_c, \nabla \phi_c))\mu_c + \mu_m b(\phi_c, \nabla \phi_c) & \text{if } \phi_c \geq 0.5 \\ (1 - b(\phi_c, \nabla \phi_c))\mu_p + \mu_m b(\phi_c, \nabla \phi_c) & \text{if } \phi_c \leq 0.5 \end{cases} \quad 3-18$$

Where the membrane viscosity,  $\mu_m = 0.12$  [Pa s]. A viscosity for the membrane was chosen on the lower range because at higher shear rates very small time-steps are required to perform these simulations, and large differences in viscosity can cause significant challenges to numerical stability.

#### Computational Domain and Boundary Conditions

Two flows are simulated due to the controlled conditions and the availability of validation data which is generally scarce in such small scales. RBC flow through a cylindrical microchannel (Haagen-Poiseuille) flow is simulated to recover the characteristic and very high strain parachuting behaviour of RBCs and to compare with experimental visualizations, and planar

Couette flow is chosen for the ability to accurately and easily control the shear rate independently from hematocrit as the constant shear rate precludes the red blood cell concentration gradients. Boundary conditions for the simple Couette flow cases are illustrated in Figure 14 below. Planar Couette flow simulations are executed in a cube domain. No-slip walls are set at the upper and lower walls with velocities in opposing directions. Translation periodicity is set on the streamwise and cross-stream directions. Each side of the domain is 20  $\mu\text{m}$  in length with 40 cube-hexahedral elements spanning it.

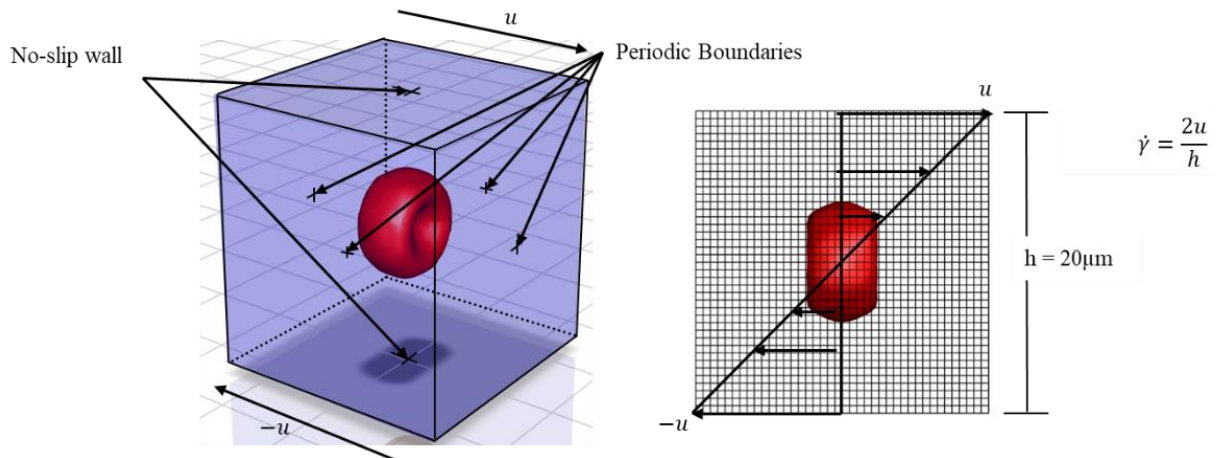


**Figure 14: Schematic illustration of computational domain used for RBC collision simulations**

Simulations are also executed of RBC flow in a cylindrical microchannel. Periodicity is not used in this case as it was impossible to specify a pressure gradient which was necessary to recover the parabolic Haagen-Poiseuille velocity profile. Uniform velocity was set at the inlet, zero relative pressure was set at the outlet, and no-slip walls were set on the circular cylindrical outer wall. The diameter of the cylindrical microchannel is set to 10  $\mu\text{m}$  to reproduce experimental images of Tomaiuolo et al,<sup>398</sup> and the length is set to that which was sufficient for the red blood cell to reach equilibrium and cease changing. A hexahedral grid is generated using Ansys mechanical with an isotropic spacing of 0.5  $\mu\text{m}$ . The computational domain and boundary conditions for this case are also visualized in Figure 16.

In general, the maximum wall velocity is approximately 0.45 m/s. The total Reynolds number based on the channel width is between 1 and 5. This means that it is not quite stokes flow, but is certainly laminar, and as such no turbulence modelling is necessary. Blood vessel diameter can range from as little as a few micrometers, up to several centimeters in diameter, and thus we have a very wide range of inertial regimes in the vasculature. In the present case however, we simply wish to examine the effect of RBC collisions under fairly controlled circumstances, and speculate that the addition of turbulence, cross stream velocities, inertial effects, and non-



uniformity in the spanwise direction would either have no effect or serve to exacerbate the collision frequency and stress exerted on the red blood cells.

Both cases use an adaptive meshing approach implemented in Fluent, which is used to achieve the required grid spacing at the mesh interface to reduce the computational cost. Consequently, isotropic elements are favoured for this purpose as it makes it easier to predict the required remeshing frequency, and because the complex dynamics of the RBC make it impossible to choose an anisotropic grid refinement profile. The Polyhedral Unstructured Mesh Adaption (PUMA) algorithm is used because it does not create hanging nodes, which cause gradient discontinuities (one-sided differencing is used) in elements containing them. Nevertheless, three extra refinement layers are specified so that the boundary is sufficiently distant from refinement boundaries to prevent any such influence on the gradient calculation.

#### Numerical Solution Scheme and Timestep

The numerical requirements of this problem are unique for several reasons. As is typical in multiphase CFD, numerical diffusion must be minimized along the multiphase membrane. Secondly, as computation of stress from the left Cauchy deformation tensor entails numerous projections onto the surface and a gradient operation (i.e. curvature, or quadruple gradient in case bending is included), the computation of the gradient must be effectively third-order accurate to facilitate smoothness across the RBC boundary. This was one reason why bending was not included in this analysis. The volume fraction discretization uses the second-order implicit compressive scheme with a sharp interface formulation and implicit cutoff of  $1e-8$ . Gradient calculation uses the node-based approach, which creates the largest stencil around the computational cell and approximates the gradient using third-order numerics. Pressure-velocity coupling is accomplished using the highly scalable PISO scheme, and momentum discretization uses the second-order upwind scheme which maximizes stability. User-defined scalar equations are discretized with the 3<sup>rd</sup> Order MUSCL scheme to reduce numerical diffusion of deformation.

Grid convergence analysis is approached by gradually increasing the refinement depth of the adaptively refined grid. Each level of depth corresponds to a factor of 2 decreases in spacing, and in total 3 levels are attempted. It was found that 2 levels were sufficient to reproduce the strain and red blood cell dynamics observed by Mills et al.,<sup>207</sup> and are twice as refined as the grid used by Takagi et al.<sup>152</sup> who used the fully Eulerian method to model single-cell RBC mechanics.

Time-step convergence is likewise approached similarly, it was found that a convective courant number of  $0.1 > U_{\max} \frac{\delta t}{\delta x_{\min}} \geq 0.5$  was required due to the general VOF multiphase requirement that the RBC interface does not traverse more than one cell per timestep.

The time-step was varied with shear rate for each case,  $\Delta t \dot{\gamma} = 5.625 \cdot 10^{-3}$  in general to keep the maximum courant number at 0.4. As time-step was varied, simulations were generally executed for approximately 10,000 - 20,000 timesteps, as it was found that after a time of  $t \dot{\gamma} > 200$ , the degree of numerical diffusion experienced by the fully Eulerian method was excessive ( more than 2% of the mean cellular value). Some simulations terminated early due to other numerical problems, particularly when modelling viscoelasticity or more than 8 RBCs.

### 3.2.2 Implementation of Deformation Transport Equations in ANSYS Fluent

The method is implemented in ANSYS Fluent™ using the user-defined scalar (UDS),  $\phi$ , equation framework, which permits simultaneous solution of up to 51 scalar advection-diffusion-reaction equations along with the flow, in the following form<sup>399</sup>.

$$\left( \frac{\partial}{\partial t}(\phi_i) + \nabla \cdot (\vec{v}\phi_i - D_i \nabla \phi_i) \right) = S_i \quad 3-19$$

Where  $S_i$  is a source term for the local production or destruction of UDS<sub>i</sub> and  $D_i$  is the diffusivity.  $D_i = 0$  in this case, and thus Equation 3-20 is shown below.

$$\frac{\partial}{\partial t}(G_{s_{ij}}) + \nabla \cdot (\vec{v}G_{s_{ij}}) = \sum_k (L_{s_{ik}}G_{s_{kj}} + G_{s_{ik}}L_{s_{ki}}) \quad 3-20$$

$$\forall i = \{1..3\}, \forall j = \{1..3\}$$

Where  $L_s$  is the surface projected velocity gradient tensor. This deviation is made because it greatly simplifies the initialization of the membrane. Furthermore, it eliminates components of the strain tensor normal to the surface, which as the shear rate varies greatly in the cell-normal direction, causes an indefinite accumulation of strain artificially.

$$L_s = P \cdot L \cdot P \quad 3-21$$

The solution of the spatial field of  $G_{s_{ij}}$  is generally implicit (but not coupled with other deformation components), and the source term is both an implicit and explicit component. The explicit component,  $S^*$ , is computed from:

$$S_{ij}^* = S_{ij} - \left( G_{s_{ij}}' - G_{s_{ij}}^0 \right) \frac{\partial S_{ij}}{\partial G_{s_{ij}}} \quad 3-22$$

Implicit source terms for  $S_{i,j}$  are thus given as  $\frac{\partial S_{i,j}}{\partial G_{S_{i,j}}}$

$$\frac{\partial S_{ij}}{\partial G_{S_{ij}}} = L_{S_{ij}} + L_{S_{ji}} \quad 3-23$$

### Stress Computation and Momentum Coupling

The stress is computed from Equation 3-13, discussed previously. To better smooth the computation of stress on the membrane, however,  $\mathbf{G}_s$  is first projected onto the membrane surface, and  $\tau_s$  is multiplied by the boundary indicator function.

$$\mathbf{G}_s^* = \mathbf{P} \cdot \mathbf{G}_s \cdot \mathbf{P} \quad 3-24$$

$$\boldsymbol{\tau}_s^* = b(\phi_c, \nabla \phi_c) \boldsymbol{\tau}_s \quad 3-25$$

The specific form of  $b(\phi_c, \nabla \phi_c)$  is another deviation from Takagi et al.<sup>152,372,395–397</sup>, who simply set  $b(\phi_c, \nabla \phi_c) = \nabla \phi_c$ , which distributes the membrane tension over the cells that occupy the boundary. In general, when integrated it equals the reciprocal of membrane thickness, or  $\int b(\phi_c, \nabla \phi_c) d\phi_c \cong t_m^{-1}$ , converting 2D surface tension to stress.

$b(\phi_c, \nabla \phi_c)$  used in this work is designed to have two major characteristics: a maximum value at the interface center equal to the maximum of the volume fraction gradient at initialization, providing a consistent and smooth spatial distribution even if the boundary becomes diffuse. This was implemented because it was found that over long times significant interface diffusion resulted in inconsistent stress application along the RBC surface, and thus sufficient widening of the RBC membrane to cause unexpected shape deformations. The form chosen is given below:

$$\begin{aligned} \delta_n &= \frac{0.5 - \phi_c}{|\nabla \phi_c|} \\ \delta_n^* &= \frac{2}{\pi} \operatorname{atan} \left( -2 \frac{|\delta_n|}{t_m} \right) \\ g(\delta_n^*) &= \left( 0.5 - \frac{1}{2} \operatorname{erf} \left( 6\delta_n^* - \frac{3}{2} \right) \right) \\ b(\phi_c, \nabla \phi_c) &= 2|\nabla \phi|_{\max} |_{t=0} g(\delta_n^*) \end{aligned} \quad 3-26$$

The estimated signed distance to the membrane,  $\delta_n$ , is generally not linear, but provides a good estimate of distance to the membrane for small distances.  $\delta_n$  is linearized and scaled by membrane thickness, at values far above membrane thickness,  $t_m$ , maximum value of  $\delta_n^* = 1$ . The normalized erf function is used because  $\int_0^{>0.5} g(x) dx \cong 0.25$ .

In general, computing the implicit component of the solid stress is quite complicated, and so some assumptions are made following Takagi et al.<sup>152</sup> If we compute the substitute the implicit of the above into the momentum equation, and neglect bending moments, and advection in the above equation, it is also possible to gain an approximation for the source term to the momentum equation. The present approach differs however as in ANSYS Fluent™ the momentum equations are segregated.

$$\frac{\partial \boldsymbol{\tau}_s^n}{\partial \mathbf{G}_s^n} = \frac{2}{\sqrt{II_2 + 1}} \left( \frac{\partial W_s}{\partial I_s} + \frac{\partial W_s}{\partial II_s} \right) \quad 3-27$$

$$\Delta G_s^n \approx \Delta t (\mathbf{L}_s \cdot \mathbf{G}_s + \mathbf{G}_s \cdot \mathbf{L}_s^T) \quad 3-28$$

Then the implicit portion of the momentum source term becomes,

$$\frac{\partial \vec{f}_i}{\partial v_i^*} \Delta v_i = b(\phi_c, \nabla \phi_c) (\mathbf{P}_s \cdot \nabla) \cdot \left( \frac{\partial \boldsymbol{\tau}_s}{\partial \mathbf{G}_s} \right) : \frac{\partial \Delta \mathbf{G}_s}{\partial v_i^*} \Delta v_i \quad 3-29$$

Here, the colon denotes element-by-element multiplication, and the asterisk denotes differentiation by the solution at the  $k^{\text{th}}$  iteration (velocity gradients are discretized and estimated at the cell center).

Coupling between membrane deformation and fluid momentum is semi-implicit. In general, UDS equations are solved after the Navier Stokes equations, corrected up to 20 times each timestep. Implicit components of the transport of  $G_s$  are computed from the velocity gradient, whereas the implicit part of the momentum source term  $f$  is computed from variations of  $G_s$  caused by velocity gradients. The PISO scheme is used for pressure-velocity coupling.

As a final point, the surface normal vector,  $\vec{n}$ , can be very noisy as the gradient of volume fraction approaches zero, leading to poor grid resolution when the thickness of the boundary between hemoglobin and plasma phases is smaller or equal to the compute-grid spacing. Consequently, gradients are computed using the node-centered gradient scheme, which reduces this noise.

#### RBC Membrane Material Modelling and Properties

Continuum modelling of the red blood cell membrane is a topic that still requires much work. Continuing the precedent set by Skalak et al,<sup>200</sup> the present study uses the strain energy approach, and several material models are tested to find one that best fits known aspects of red blood cell deformation behaviour. In addition to Skalak's and the Yeoh model developed by

Mills et al. given in 2.3, we test the Neo-Hookean model, and develop a hybrid model between Skalak and Mills in this work, which is used for the majority of simulations. The Neo-Hookean model is derived by assuming a linear relationship between strain energy and the sum of the principle stretches.

$$W_s = \frac{\mu_0}{2}(\lambda_1^2 + \lambda_2^2 + \lambda_3^2 - 3) \quad 3-30$$

Which generally are equal to the first invariant of the Cauchy deformation tensor

$$I_v = \lambda_1^2 + \lambda_2^2 + \lambda_3^2 \quad 3-31$$

For simplicity, it is easier to work with the nonzero invariants, which are simply represented as  $I_0 = I_s + 2$  and  $II_0 = II_s + 1$ .

$$\lambda_3^2 = \frac{1}{\lambda_1^2 \lambda_2^2} = II_0^{-1} = (II + 1)^{-1} \quad 3-32$$

$$I_v = \lambda_1^2 + \lambda_2^2 + \frac{1}{\lambda_1^2 \lambda_2^2} = I_0 + II_0^{-1} = (I + 2) + (II + 1)^{-1} \quad 3-33$$

$$W_s = \frac{\mu_0}{2} \left( I_0 + \frac{1}{II_0} - 1 \right) \quad 3-34$$

It was found that all models presented in the literature were insufficient to produce appropriate membrane distributions and strains. The Yeoh model by Mills et al, which was fit to reproduce the lengths and widths of the RBC observed during stretching via optical tweezer experiments but does not enforce area (or volume) incompressibility, and as a result, area strains are not realistic at high shear rates on the order of >50%. Skalak's model on the other hand, does not provide sufficient resistance to uniaxial stretching to reproduce phenomena like parachuting at high shear, or the shapes observed by Mills et al. These results are presented in the next chapter, but to overcome this difficulty a hybrid model was developed between Skalak and Mills. Substitution of Equation 2-28, into Mills' Yeoh model recasts it into the surface formulation appropriate to application with the membrane method, shown below.

$$W_s = \frac{\mu_0}{2} \left( (I_0 + II_0^{-1} - 3) + C(I_0 + II_0^{-1} - 3)^3 \right) \quad 3-35$$

Where  $C = \frac{2\mu_f}{\mu_0}$ , and  $\mu_0$  is the surface modulus of elasticity presented in Mills et al.<sup>207</sup>. Equation 2-29 is modified to be area incompressible following Skalak's approach, where it is desired to add

a biaxial tension proportional to area strain and some area modulus,  $\alpha$ , into 3-13, then the slope added to  $\frac{\partial W_s}{\partial II}$  is:

$$\left. \frac{\partial W_s}{\partial II} \right|_{\alpha} = \frac{\mu_0 \alpha}{2} (II_0 - 1) \quad 3-36$$

Which, when integrated and added to Mills' Yeoh model, the strain energy becomes:

$$W_s = \mu_0 \left( (I_0 + II_0^{-1} - 3) + C_3 (I_0 + II_0^{-1} - 3)^3 + C_7 (I_0 + II_0^{-1} - 3)^7 + \left( \alpha_6 II_0^6 + \frac{\alpha_1}{2} \left( \frac{1}{2} II_0^2 - II_0 \right) \right) \right) \quad 3-37$$

The surface elasticity moduli, Mills suggest ranges between  $5.3 \leq \mu_0 \leq 11.3 \frac{\mu N}{m}$  and  $13.9 \leq \mu_f \leq 29.6 \frac{\mu N}{m}$ , and best fit values of  $\mu_0 = 7.3 \frac{\mu N}{m}$  and  $\mu_f = 19.2 \frac{\mu N}{m}$ . Pozrikidis suggests a value of between 16-1000 for the surface dilation coefficient. In the present study  $\alpha_1$  and  $\alpha_6$ , are chosen to try to achieve approximately 6.4% average area strain. In this study,  $\{\mu_0, C_3, C_7, \alpha_1, \alpha_6\} = \left\{ 4.6 \frac{\mu N}{m}, \frac{1}{30}, \frac{\sqrt{3}}{2}, 16.2, 11.2 \cdot 10^3 \right\}$  are chosen to reproduce the extensions observed by optical tweezer stretching during the Mills et al.<sup>207</sup> study in the validation analysis and the reduce area strain at rupture to be below 6.4%. The resulting area and uni- and bi-axial stiffnesses are represented by the material strain energy derivatives and are shown in Figure 15. strain are computed from the first and second surface invariants as:

$$\epsilon = \sqrt{I_s + 1} - 1 \quad 3-38$$

$$\epsilon_A = \sqrt{II_s + 1} - 1 \quad 3-39$$

$$I_s = \text{tr}(B_s) - 2 \quad 3-40$$

$$II_s = \frac{1}{2} (\text{tr}(B_s)^2 - \text{tr}(B_s^2)) - 1 \quad 3-41$$

### Initialization

Red blood cells are constructed by initializing the flow-field with hemoglobin inside of the RBC membrane in the undeformed bi-concave ellipsoid state<sup>129</sup>. The shape of the red blood cell is calculated using equation 2-6 on page 23.

$$D(r) = \sqrt{1 - \left( \frac{r}{R_0} \right)^2} \left( C_0 + C_2 \left( \frac{r}{R_0} \right)^2 + C_4 \left( \frac{r}{R_0} \right)^4 \right) \quad 2-6$$

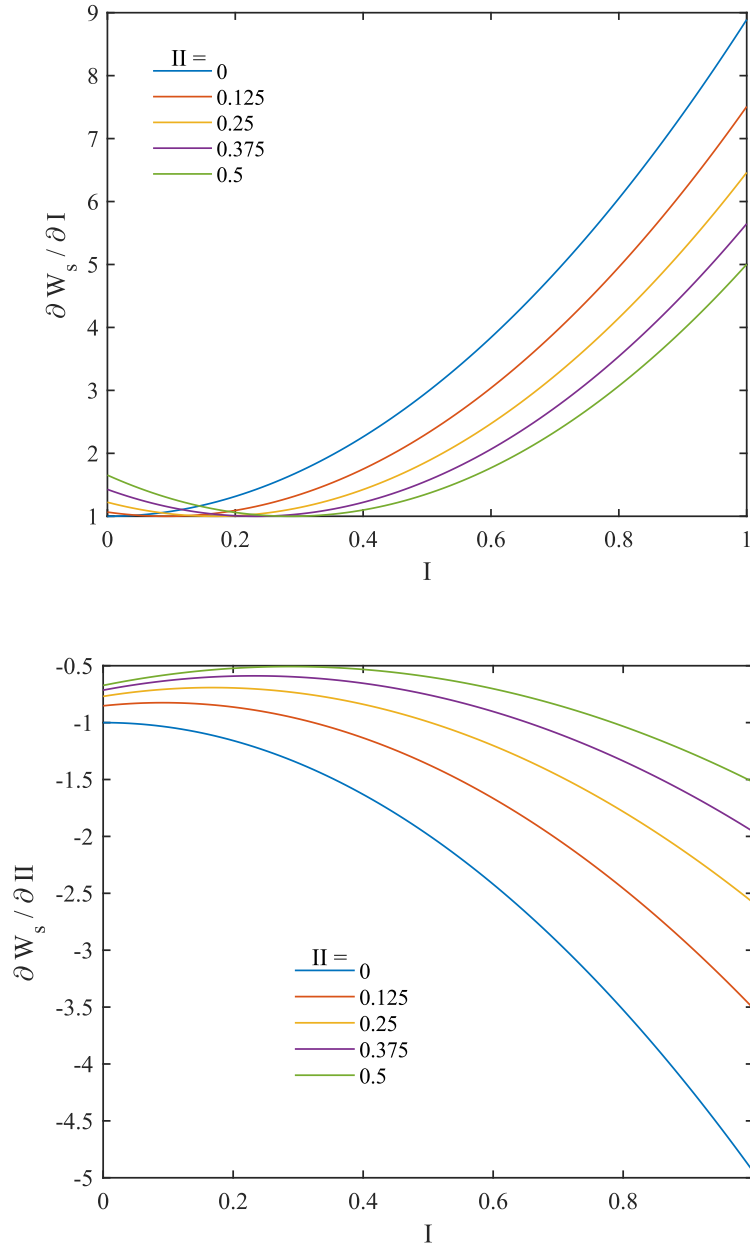


**Figure 15: Plot of derivatives of strain energy function for incompressible Yeoh material model developed in Eqn 3-37 against surface invariants  $I_s$  and at varying  $II_s$ , corresponding to varying uniaxial and biaxial strain, respectively.**

Signed minimum distance to the red blood cell membrane,  $\delta_m$ , is computed by a Newton Raphson method from the cell center. Volume fraction is computed as a function of  $\delta_m$ :

$$\phi_c\left(\frac{\delta_m}{t_m}\right) = \begin{cases} f_b\left(\frac{\delta_m}{t_m}\right) & -\frac{t_m}{2} \leq |\delta_m| \leq \frac{t_m}{2} \\ 0 & \delta_m > \frac{t_m}{2} \\ 1 & \delta_m < \frac{-t_m}{2} \end{cases} \quad 3-42$$

Where  $t_m$  is the membrane thickness, which is set to some sufficiently small value, typically 2-3 times the grid spacing. In the coarsest grid-spacing case this is  $0.125 \mu\text{m}$  which is kept constant throughout the study.  $f_b$  is a unit blending function, (a Hermite cubic spline in this work).

For multi-cell cases, volume fraction is not altered if it is already nonzero. ADP, and hemoglobin are treated as inert chemicals that can be diffused through the RBC membrane when pores are opened due to stress. pfHb is a separate quantity from Cytoplasm, and is treated as a passive scalar that does not contribute to the mass of either phase. This is done for the obvious reason that changing the mass of the cytoplasm phase would change the membrane thickness, which is problematic for the calculation of the membrane stress. It is therefore assumed that the total mass of hemoglobin diffused during the simulation is insufficient to cause a substantial change on RBC volume. Hemoglobin concentration inside of the cell is initialized as  $345 \text{ g/L}$ .

As  $G_s$  and  $L$  are projected at each iteration onto the RBC surface, the left Cauchy deformation tensor is initialized simply as  $G_s|_{t=0} = I$  for the entire domain. This eliminates the complexity of initializing with  $G_s|_{t=0} = P(\nabla\phi)$ , as was suggested by Takagi et al.<sup>152</sup>, which creates large discontinuities in  $G_s$  in regions where there are two membranes near one another.

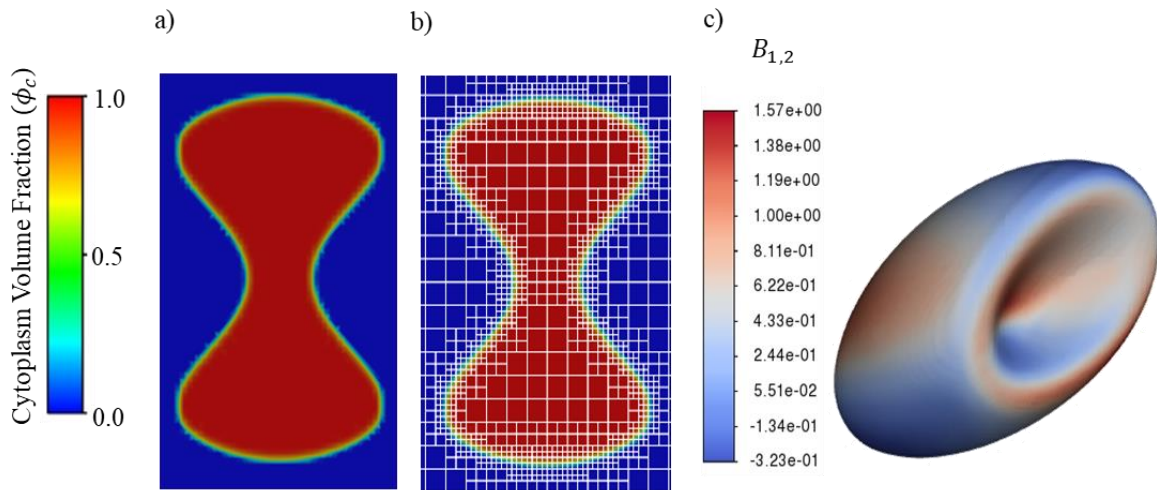


**Figure 16: Illustration of RBC initialization where red indicates cytoplasmic volume fraction,  $\phi_c = 1$ , and blue indicates  $\phi_c = 0$ , b) the adaptive grid used, and c) flood plots on the RBC surface of the  $xy$  component of the left Cauchy deformation tensor. RBC shape is initialized here with  $130 \text{ mOsm}$ .**



### Modelling Viscoelasticity

In the viscoelastic cases, viscoelasticity is modelled using a straightforward approach, which involves the application of the membrane viscosity of  $0.3 [\mu\text{Pa} \cdot \text{s} \cdot \text{m}]$  as computed by Mills.<sup>207</sup> The introduction of Newtonian viscosity in a simulation to the Navier-Stokes equations with the fully Eulerian structural model approach is functionally equivalent to a Kelvin-Voigt damper model. This model was utilized by Mills et al.<sup>207</sup> and it accurately represented the dynamic behaviour of a sudden release of tension from a stretched cell. Values computed by Gomez,<sup>225</sup> which are on the order of  $9 [\mu\text{Pa} \cdot \text{s} \cdot \text{m}]$ , are not employed due to the erroneous first-order assumption in their dynamic model. This assumption is suspected to result in excessive stiffness. A conveniently low value in the range of membrane viscosities is chosen because of the need to maximize stability. It was found that high viscosities necessitated very small grid sizes, which in turn necessitated very small timesteps, and thus the smallest computationally feasible viscosity was chosen that would provide meaningful data.

In the current study, the surface viscosity is divided by the membrane thickness,  $t_m$ , which is  $0.125 \mu\text{m}$ , and is then blended with the cytoplasmic and plasma viscosity using the boundary indicator function. Therefore, in the viscoelastic cases, the viscosity within the domain is represented by the equation below.

$$\mu = \begin{cases} b(\phi_c, \nabla\phi_c)\mu_m t_m^{-1} + (1 - b(\phi_c, \nabla\phi_c))\mu_c & \phi_c > 0.5 \\ b(\phi_c, \nabla\phi_c)\mu_m t_m^{-1} + (1 - b(\phi_c, \nabla\phi_c))\mu_p & \phi_c \leq 0.5 \end{cases} \quad 3-43$$

Where  $\mu_{m,s} = 0.3 [\mu\text{Pa} \cdot \text{s} \cdot \text{m}]$ ,  $\mu_c = 5.024 \cdot 10^{-3} [\text{Pa} \cdot \text{s}]$  and  $\mu_p = 1.024 \cdot 10^{-3} [\text{Pa} \cdot \text{s}]$  are the surface membrane viscosity, the cytoplasmic viscosity, and the plasma viscosity, respectively, and  $t_m$  is the membrane thickness described previously. This formulation is effectively a simple Kelvin-Voigt formulation, where the elastic force and a viscous force proportional to velocity are simply added together, and are generally equivalent to the formulations discussed, though the elastic force in this case is highly nonlinear.

### **3.2.3 Computation of Transmembrane Hemoglobin Diffusion**

Transmembrane hemoglobin diffusion is computed using the procedure outlined in 2.4.6, where hemoglobin concentration is conserved in the Eulerian frame using a scalar transport equation. Equation 2-23 is implemented using the UDS approach in ANSYS Fluent. The diffusivity coefficient,  $D$ , inside of the cell and in plasma is computed as the self-diffusion,  $D_0([Hb])$ , and on the membrane itself is the reduced membrane diffusivity which is a function of area strain and the local self diffusivity,  $D_m(D_0, \epsilon_A)$ .

$$D = b^*(\phi_c, \nabla \phi_c) D_{\text{eff}}(D_0, \epsilon_A) + (1 - b^*(\phi_c, \nabla \phi_c)) D_0([\text{Hb}]) \quad 3-44$$

In the equation above,  $b^*$  is the normalized boundary indicator given in Equation 3-26, (ie: just  $g(\delta_n^*)$ ),  $D_0$  is computed following Longeville et al.<sup>276</sup>, and  $D_m(D_0, \epsilon_A)$  is computed following Davidson and Deen<sup>278</sup> to compute the diminished diffusion rate with for a molecule through a nanopore. Pore size is computed following Tolpekina<sup>268</sup> and Koshiyama et al.<sup>270</sup>, with the notable deviation from Sohrabi et al.<sup>10</sup>, that the thermodynamic scaling procedure suggested by Tolpekina is used here. We compute the effective diffusion coefficient following Davidson and Deen<sup>278</sup>. The reduced rate of diffusion is estimated as a ratio of the solute to pore radius,  $\lambda = r_s/r_p$ . Generally effective diffusivity relative to the base self diffusivity coefficient for a spherical solute is given by the product of a partition coefficient,  $\Phi$  and the inverse enhanced drag,  $K^{-1}$ .

$$\frac{D_{\text{eff}}}{D_0} = \begin{cases} \Phi K^{-1} & \text{if } r_p > 5.5 \text{ nm} \\ 0 & \text{otherwise} \end{cases} \quad 3-45$$

Similarly to Arora et al.<sup>7</sup>, the cut-off for pore radius is included, but the smallest dimension of the Hb molecule (5.5 nm) is used rather than the largest dimension. The partition coefficient,  $\Phi$  represents the ratio of average solute concentration inside of the pore to that in the bulk solution. For spherical particles  $\Phi = (1 - \lambda)^2$ , and when  $\lambda \leq 0.4$ , the  $K^{-1}$  term can be simplified to give the Renkin equation.

$$\frac{D_{\text{eff}}}{D_0} = (1 - \lambda)^2 (1 - 2.1044\lambda + 2.089\lambda^3 - 0.948\lambda^5) \quad 3-46$$

More generally, the dependence of  $K^{-1}$  on  $\lambda$  is relatively weak, and can be approximated as:

$$K^{-1} = 1 - 2.848\lambda + 3.269\lambda^2 - 1.361\lambda^3 \quad 3-47$$

The partition coefficient is estimated by analytical formulation of Casassa<sup>400</sup> for a freely jointed chain with an infinite number of infinitesimally short segments.

$$\Phi = 4 \sum_{i=1}^{\infty} \left( \frac{1}{d_i^2} \right) \exp(-d_i^2 \lambda_g^2) \quad 3-48$$

Where  $d_i$  are the roots of the Bessel function of the first kind of order zero, and  $\lambda_g = \frac{r_g}{r_p}$  is the ratio of the particle radius of gyration to the pore radius.

$$\lambda_g = \frac{3\sqrt{3}\alpha + 5.77}{2} \lambda \quad 3-49$$

Where,  $1.3 \leq \frac{\lambda_g}{\lambda} \leq 1.8$  and  $10 \leq \alpha \leq 60$ .

Koshiyama and Wada<sup>270</sup> fit their molecular dynamics data to a normal distribution to find the probability of pore formation  $P_{pore}$ , at four membrane stretching speeds.

$$P_{pore} = \frac{1}{2} \left( 1 + \operatorname{erf} \left( \frac{(\epsilon_A - \bar{\epsilon}_A)}{\sqrt{2}\sigma} \right) \right) \quad 3-50$$

They perform at quasistatic stretching, and at speeds of 0.1, 0.3, and 1.0 m/s.  $[\bar{\epsilon}_A, \sigma]$  are, [1.07, 0.12], [1.23, 0.12], [1.33, 0.13], [1.57, 0.20], respectively. Note that as Koshiyama and Wada's patch size was a square of 8.62nm in length, the lowest velocity of 0.1 yields a stretch rate of approximately  $8.6 \times 10^8 \text{ s}^{-1}$ , indicating that using their quasi-steady data is appropriate for our desired shear rate regimes. This is reinforced by the fact that pores open and close in timescales on the nanoscale, several orders of magnitude smaller than the smallest timestep used in this work. Pore radius is given by Tolpekina et al. by minimizing the free energy of a lipid bilayer with a pore using the 2D cavitation approach. The stable pore radius is:

$$\frac{R_{min}}{\sqrt{A_0}} = 2 \sqrt{\left( \frac{\epsilon_A}{3\pi} \right)} \cos \left( \frac{\alpha}{3} \right) \quad 3-51$$

$$\cos(\alpha) = -\frac{k_c}{2K_A} \frac{1}{\pi \sqrt{A_0}} \left( \frac{\epsilon_A}{3\pi} \right)^{-\left(\frac{3}{2}\right)} \quad 3-52$$

Fitting minimum pore radius to their CGMD data, they find that  $k_c = 35 \frac{pJ}{m}$ , and compressibility modulus was  $K_A = 250 \frac{mJ}{m^2}$  calculated following den Otter and Briels and experiments<sup>268</sup>  $A_0$  in the study by Tolpekina was  $271.3 \text{ nm}^2$ .

The free energy model of Tolpekina for pore radius is modified by incorporating the probability of pore formation from Koshiyama, so that the expected radius,  $\bar{r}_p$ , is the product of  $R_{min}$  and the probability of pore formation.

$$\frac{\bar{r}_p}{\sqrt{A_0}} = 2 \sqrt{\left( \frac{\epsilon_A}{3\pi} \right)} \cos \left( \frac{\alpha}{3} \right) P_{pore}(\epsilon_A, \bar{\epsilon}_A^*, \bar{\sigma}_A^*) \quad 3-53$$

A consequence of the thermodynamic scaling procedure of Tolpekina, is that the larger the lipid membrane, the bigger the pore size, and the lower the radius. Razizadeh<sup>83,401</sup>, studied the effect of the spectrin cytoskeleton, and find that it acts as an upper limit to pore size by acting as a kind of anchor for deformation and the lipid membrane. It is therefore argued that pore size is limited by the nominal length of the spectrin fibre (approximately 80-100 nm), and not the total RBC area as was suggested by Tolpekina. We therefore choose the reference area for scaling pore size to be governed by the nominal length of the spectrin fibres on RBCs, approximately 100 nm.

$$A_1 = (100 \text{ nm})^2 \quad 3-54$$

This work deviates from previous works on calculation of pore density because it is reasoned that the assumption that all excess area is converted to pore area, which was assumed by McKean<sup>9</sup>, is not valid and that there is much evidence to contradict Sohrabi and Liu's<sup>10</sup> idea that one pore to forms per computational element is irrational. After all, their computational elements are unrelated to the physiological parameters of the RBC. In this work, the number of pores is calculated by assuming that in each  $(100 \text{ nm})^2$  patch, one pore can form, which is the case in quasistatic bilipid membrane simulations<sup>269,402</sup>. The scaling factor applied to scale pore radius and strain, as described by Tolpekina, is:

$$\left(\frac{A_1}{A_0} \frac{r_0}{r_1}\right)^{\frac{1}{3}} = \left(\frac{N_1}{N_0}\right) \quad 3-55$$

Where  $A$  is the total patch area,  $r$  is the average distance between particles,  $N$  is the number of particles in the CGMD simulation, and subscript 1 refers to the target patch size, and 0 is the source CGMD patch size. In the present simulation,  $r_0$  is taken as the same as that used by Razizadeh et al.<sup>83,401</sup>.

Multi-pore formation is observed in several CGMD simulations at fast deformation rates far higher than even the most extreme condition exerted on blood. Pore density,  $\rho_p$ , is:

$$\rho_p = P_{pore}(\epsilon_A, \bar{\epsilon}_A^*, \bar{\sigma}_A) \left( \frac{1e6 \text{ nm}^2}{1\mu\text{m}^2} \cdot \frac{1 \text{ pore}}{10000\text{nm}^2} \right) \quad 3-56$$

$$\rho_p = 156.25 P_{pore}(\epsilon_A, \bar{\epsilon}_A^*, \bar{\sigma}_A^*) \left[ \frac{\text{pores}}{\mu\text{m}^2} \right]$$

Consequently, porosity, which is the product of the expected radius by pore density is:

$$\mathcal{P} = \frac{4}{3} \frac{\epsilon_A}{\epsilon_A + 1} \cos^2 \left( \frac{\alpha}{3} \right) P_{pore}^3(\epsilon_A, \bar{\epsilon}_A^*, \bar{\sigma}_A^*) \quad 3-57$$

Where  $\bar{\epsilon}_A^*$  is the mean strain of pore initiation from Koshiyama et al.<sup>270</sup> scaled to Tolpekina et al.'s<sup>268</sup> grid sizes. Final radius, and porosity based on a grid of  $(L \text{ nm})^2$  square patches are given in Figure 17. Comparing the porosity and radial distributions between Tolpekina's free energy model and Razizadeh's recent much larger CGMD simulations. Remarkably, Comparing the above relationships to the much larger simulations Razizadeh et al.<sup>83,401</sup>, we obtain porosity and radial distributions that are similar to what was observed by Razizadeh et al., suggesting that the spectrin fibres are indeed the length scale that limits the size of the pore.

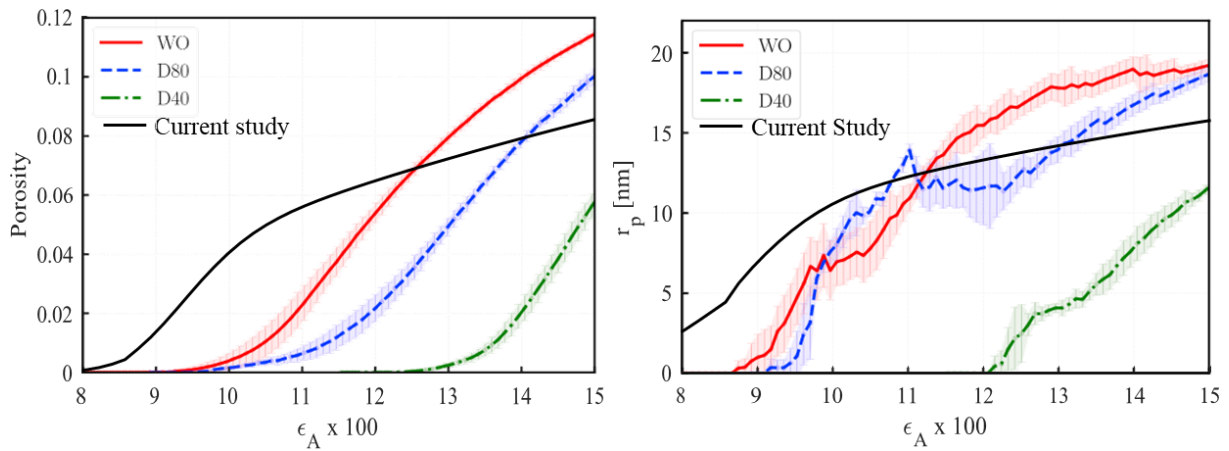


**Figure 17: Illustration of pore density and pore radius over the expected range of distributions (top), and comparison against Razizadeh et al.'s<sup>83,401</sup> CGMD simulation of mechanoporation of a 80nm (D80) and 40 nm (D40) spectrin cytoskeleton reinforced bi-lipid membrane patch (Patch Area = 0.1218  $\mu\text{m}^2$ )**

### 3.2.4 Objectives and Executed Test Cases

RBC volumetric concentration (hematocrit) is varied by adding more red blood cells to obtain a cytoplasmic volume fraction between 0.05 to 0.25. Shear rate is independently varied between  $1000 \text{ s}^{-1}$  to  $40000 \text{ s}^{-1}$ . The full range of simulations executed is shown in the table below. The computational cost of simulating a full sweep of hematocrit and shear rates, shear rate is only varied for colliding cases with two cells.

Finally, the effect of viscoelasticity on collisions is evaluated by setting the membrane surface viscosity to  $0.3 \cdot 10^{-6} [\text{Pa} \cdot \text{s} \cdot \text{m}]$ , which is the lowest value given in literature and is intentionally chosen for stability reasons. This approach to viscoelastic modelling is equivalent to a Kelvin-Voigt viscoelastic model, following classical approaches, albeit with a hyperelastic model.

In the multicell cases with more than two RBCs, a 2D arrangement of cells is employed as it was found that cells did not attain significant cross-stream velocity component due to the

uniform nature of the flow in the cross-stream direction thus allowing us to simplify the simulations. This is naturally not the case in a complex 3D flow such as in a boundary or free-shear layer and is noted as a limitation and discussed subsequently. The general consequence of this is that collision frequency per RBC will be lower in the present study as the number of possible interactions with other RBCs is increased in the fully 3D case.

As the arrangement of cells is 2D, hematocrit is computed as the ratio of cytoplasm volume to the total volume, with cross-stream stretch being equal to 1 RBC diameter, and in a truly 3D regime hematocrit value would be greater. 36% was the highest hematocrit that could be achieved without incurring issues due to excessive proximity of cells causing numerical instability of the Fully Eulerian membrane modelling technique at the grid spacing chosen. The shear rate is kept constant at  $20,000 \text{ s}^{-1}$ , as computational resources were not sufficient to execute a full range of shear rates at all hematocrit levels. The number of cells used per cell varies depending on the membrane area, between  $3 \cdot 10^5$  and  $1.0 \cdot 10^6$  elements are used to fully resolve each cell, for initial and fully stretched red blood cells, respectively. For the 12-cell case, the number of elements varied between 4 – 10 million cells, which at the low timestep of  $0.1 \text{ } \mu\text{s}$  at the highest shear rate, required between 2-4 weeks to run per case on the two 48 compute core nodes being used.

**Table 3: Summary of simulations executed to examine the effect of hematocrit on red blood cell stress and sublethal hemolysis**

Case	Parameters varied	Objectives
<b>RBC in a microchannel</b>	$U = 0.27 \text{ cm s}^{-1}$ $\dot{\gamma} = [0, 20,000] \text{ s}^{-1}$	Validation against Tomaiuolo et al. <sup>398</sup>
<b>Deformation of a red blood cell</b>	$\dot{\gamma} = [900, 40000] \text{ s}^{-1}$ $\mu_m = \{0\} [\text{Pa s}]$	Validation against Mills et al. <sup>207</sup>
<b>Effect of Shear Rate on Collisions</b>	$N_{cells} = \{2\}$ $\dot{\gamma} = [4820, 40000] \text{ s}^{-1}$	Examine the interaction of shear rate with simple collisions on transmembrane Hb diffusion
<b>Effect of Volume Fraction</b>	$N_{cells} = \{1, 2, 4, 8, 12\}$ $\dot{\gamma} = \{20,000\}$	Examine the interaction of hematocrit with collisions on transmembrane Hb diffusion
<b>Viscoelastic collisions</b>	$N_{cells} = \{2, 4\}$ $\dot{\gamma} = \{20,000\}$ $\frac{\mu_m}{t_m} = 0.3 \cdot 10^{-6} [\text{Pa} \cdot \text{s} \cdot \text{m}]$	Examine the effect of viscoelasticity on collisions

### 3.3 Continuum Modelling of Thrombosis and The Effect of Hemolysis

The second computational study will examine blood clot formation by simulating the formation of blood clots and the interaction between hemolysis and various subprocesses involved in thrombosis. The transient hemodynamic flow field in a mechanical circulatory support device is simulated using classical finite-volume computational fluid dynamics solutions of the incompressible Navier-Stokes equations, in which blood is modelled as a homogeneous Newtonian fluid. The mural thrombus modelling methodology pioneered by Sorensen<sup>320</sup> and Goodman<sup>325</sup> is extended, following the specific implementation of Wu et al<sup>15</sup>. This study builds on this methodology by simultaneously modelling hemolysis and incorporating the mutual interaction of thrombosis and hemolysis. The thrombosis modelling approach is used to examine hemodynamic mechanisms under which thrombus can form and examine the effect of hemolysis on thrombosis.

As the subject of interest is the mechanics of thrombus formation in non-physiological flow conditions in a VAD, the study is limited to the extrinsic portion of coagulation. Interactions with the sub-endothelium and endothelial cells are neglected to limit the scope. Furthermore, a simple particle kinetics argument is made that collisions of platelets in flow is far more infrequent than collisions with a surface and can be neglected. The analysis is thus limited to the formation of mural thrombus. The subsequent sections will develop and discuss the methodology to account for hemolysis in thrombosis in a continuum framework, and its implementation in Ansys Fluent, the solver of choice.

#### 3.3.1 Governing Equations of Fluid Flow

Blood is modelled as a homogeneous incompressible fluid using the incompressible Navier-stokes equations solved by ANSYS Fluent.

$$\nabla \cdot (\rho \vec{v}) = 0 \quad 3-58$$

$$\frac{\partial}{\partial t}(\rho \vec{v}) + \frac{\partial}{\partial x_i}(\vec{v} \rho \vec{v}) = \nabla \cdot \sigma + C_{imb} f(\phi_{p,d})(\vec{v} - \vec{v}_p) \quad 3-59$$

The mechanical stress tensor,  $\sigma$ , encompasses pressure, viscosity and turbulent forces. Subscript  $p$  in this study denotes platelets, such that  $\phi_p$  is the total volume fraction of platelets. The second term on the right-hand side represents a modified Brinkman term that applies resistance to flow in proportion to the fluid velocity relative to the thrombus velocity,  $\vec{v}_p$ , and deposited platelet volume fraction,  $\phi_{p,d}$ . The interaction force function,  $f(\phi_{p,d}) = \phi(1 + 6.5\phi)$ , used by Wu et al.<sup>339</sup> and Rojano et al.<sup>18</sup>, is modelled following Johnson et al.<sup>403</sup>

$f(\phi_{P_d})$  is the interaction force applied by a particle cluster to the fluid flow.<sup>404</sup>  $\phi_{P_d}$  is equal to platelet concentration divided by the maximum possible platelet concentration,  $[P_{ad}]_{max}$ .

The coefficient of the resistance,  $C_{imb}$ , is computed so that the interaction force is equal to the pressure gradient that reproduces a Blasius boundary layer on the thrombus surface. Its boundary layer displacement thickness,  $d^*$ , is set equal to the inverse of the volume fraction gradient. The resulting proportionality to the grid spacing is desirable because it results in improved stability in coarser grids. Furthermore, it reduces the degree to which the boundary layer profile changes with grid spacing, as generally a higher value of  $C_{imb}$  is required in smaller cells to simulate a no-slip surface.

$$d^* = (2 \cdot \nabla \phi_{P_d})^{-1} \quad 3-60$$

$$C_{imb} = \frac{\partial \tau}{\partial x} \frac{1}{U_\infty} = \frac{0.332}{2} \frac{\mu^2}{U \rho} (1.72 \cdot 2 \cdot \nabla \phi_{P_d})^{-3} \quad 3-61$$

This formulation is taken as a lower bound so that  $2 \cdot 10^6 \leq C_{imb} \leq \frac{(\rho U_\infty)^2}{\mu} [Pa \cdot m^{-1}]$ , which is generally 2 orders of magnitude lower than what is used by Wu et al.<sup>339</sup> and Rojano et al.<sup>18</sup>. Furthermore, the interaction force profile is modified to have an exponential profile. It was found that using Johnson's Brinkman profile formulation, resulted in peak von-mises stress far outside of the thrombus interface and consequently the effective embolization rate was severely underpredicted. This is appropriate because platelet filopodia, fulfilling their function, increases fluid resistance relative to a particle bed by filling interstitial spaces. As the thrombus is modelled to grow layer by layer, the interface tends to be on the scale of the grid cell spacing, and the volume fraction thus represents surface position in the grid cell.

$$f(\phi_{P_d}) = 7.5 \phi_{P_d} e^{\frac{\phi_{P_d}-1}{t_{33}}} \quad 3-62$$

$t_{33}$  is the volume fraction value at which 33% of peak intensity is reached, here  $t_{33} = 0.025$ . This formulation removes some of the modelling empiricism, sensitivity on the stiffness coefficient, and ensures that peak stress occurs at  $\phi_{P,d} \sim 0.5$ , better simulating a wall boundary. More importantly, it results in shear stress predictions in the immersed boundary that are less dependent grid spacing. In general, it is assumed that aggregated platelets behave as densely packed particles, and in practice it is found that little to no flow is present when  $\phi_{P,d} > 0.5$ . It was found that a true porous treatment, was not necessary consequently, and undesirable as it



reduced solver stability; the required timestep was very small, substantially increasing computation time. Therefore, fluid mass is not actually excluded from regions where a thrombus forms via multiplying density by porosity in Equation 3-58, but the effect of the Brinkman term is simply to arrest flow in that region and induce shear on the interface to mimic the flow constriction effects found in thrombus deposition. As the rate of thrombus growth is on the order of hours, whereas the relevant hemodynamic timescale is on the order of milliseconds, it is expected that the component of velocity normal to the thrombus surface induced by removing fluid mass from inside the thrombus region is not significant and thus a truly porous treatment that includes this effect is deemed unnecessary.

As with the membrane modelling, the transport equations are implemented in ANSYS Fluent using the User Defined Scalar Transport equation framework, and User Defined Source code is written in C to interface with ANSYS Fluent to define the custom source terms, diffusion, mass flux, gradient computation, and boundary conditions used in this model. The code is available upon request.

### **3.3.2 Equations Governing Thrombosis and Implementation in Ansys Fluent**

In the present work, the extrinsic coagulation process is not considered in detail because of the general absence of the sub-endothelium and endothelial cells inside of MCS. This assumption is made even though reendothelialization generally results in a layer of endothelial cells covering the surface of any long-term implanted medical device, and that the presence of endothelial cells is strongly antithrombogenic<sup>405</sup>. In general, this assumption is convenient as there are no well-validated models that can predict the regulation of thrombin concentration by the endothelium in-vivo<sup>286</sup>.

A robust modelling framework for intrinsic coagulation and thrombosis is pioneered by Sorensen<sup>320</sup>, the aspects of which are surveyed in Section 2.5. Sorensen's thrombosis simulation scheme is chosen as provides the most flexibility to integrate the effects of hemolysis due to the simple treatment of adhesion, and the ability to model anticoagulation. Furthermore, being one of the first thrombosis models, Sorensen's approach is better validated by authors such as Wu<sup>339</sup> and Rojano<sup>18</sup>. In this work, the implementation of Wu et al.<sup>339</sup> is generally used though several key deviations are made and discussed. The physics of thrombosis encompasses the following phenomena, discussed in Section 2.5.

1. Advection and diffusion of platelets and constituents of thrombosis
2. Localized flow impedance caused by clusters of adhered platelets

3. Activation of platelets
4. Adhesion and embolization of platelets
5. Conversion of Thrombin from Prothrombin and deactivation by Antithrombin

The essential elements of modelling thrombosis are therefore determining the concentrations of platelets in the inactive or active, and unadhered or adhered states; determining the concentrations of important agonists that govern platelet activation, Adenosine Diphosphate (ADP), Thromboxane A2 (TxA2), and Thrombin (T); and coagulation via the conversion of Thrombin, prothrombin (pT) and antithrombin (aT). The concentrations of each of these quantities at a particular point in space and time are modelled by solving advection-diffusion-reaction (ADR) equations of the form:

$$\left( \frac{\partial}{\partial t} ([C_i]) + \nabla \cdot ([C_i] \vec{v} - D_{C_i} \nabla [C_i]) \right) = S_{C_i}; \quad 3-63$$

$$\forall C_i \in \{P_{a\bar{d}}, P_{\bar{a}\bar{d}}, ADP, TxA_2, T, PT, AT\}$$

Where  $[C_i]$  is the concentration of a given species, denoted by square brackets. Platelets in the active and inactive phases are denoted with subscripts  $a$  and  $\bar{a}$ , respectively, whereas non-deposited (adhered) and deposited platelets that are adhered but can be embolized are denoted by subscripts  $\bar{d}$ , and  $d$ , respectively. Stabilized platelets that are assumed to be bound by fibrin and thus are fixed to a surface are denoted by subscript  $s$ . As deposited and stabilized platelets are not subject to convection and diffusion, their concentration is governed effectively by first-order nonlinear ODEs:

$$\frac{\partial}{\partial t} ([C_i]) = S_{C_i}; \quad \forall C_i \in \{P_{ad}, P_{\bar{a}d}, P_s\} \quad 3-64$$

Adhesion mechanics are directly affected by the local shear stress, and likewise platelet concentrations affect the local flow velocity via the modified Brinkman term in Equation 3-58. The source term,  $S_c$  captures the production, removal and/or state transition of these species by chemical reactions, activation, or adhesion<sup>15</sup>. Diffusion coefficients,  $D_C$ , are modelled as per the model of Wu et al<sup>337</sup> given in Eqns. (2-46 – 2-48) which sufficiently reproduces the nearly four-fold platelet concentration increase near sheared walls measured experimentally at high shear rates up to 20,000 s<sup>-1</sup>. Diffusion for small particles such as proteins and enzymes are assumed to follow kinetic theory, and thus can be computed using the stokes-Einstein relation:

$$D_{C_i} = \frac{k_B (310.15 \text{ K})}{6\pi\eta_{\text{plasma}} r_{C_i}} \quad \forall C_i \notin \{P_{a\bar{d}}, P_{\bar{a}\bar{d}}\} \quad 3-65$$

### 3.3.3 Platelet Activation and Adhesion

This section discusses the transition processes of platelets between the resting non-active states to the deposited and or activated states, the physical processes of which were reviewed in section 2.5.2. Broadly, platelets are activated by ADP, TxA2, Thrombin and shear stress. Activation and adhesion processes are modelled using first-order reaction rate kinetics. This assumes that proteins involved in adhesion are considered abundant in plasma and that their concentration does not change appreciably. Activation of coagulation factors that are implicitly included in processes such as thrombin conversion either occur much more quickly than the first-order reactions or are also first-order reactions themselves, are linear and can be lumped together. Using first-order reaction kinetics to model the instantaneous rate of transition for all source terms gives the following general form for each source term,  $S_{C_i}$ .

$$S_{C_i} = k_{C_j, C_i} C_j \quad 3-66$$

$k_{C_j, C_i}$  is a reaction rate giving production of species,  $C_j$  as a proportion of  $C_i$  and can be a function of any hemodynamic or other species. Wu et al,<sup>15,381</sup> gives a detailed accounting of the source terms used in the baseline model; source terms and the corresponding constants used in their calculation are summarized in Table 4 and Table 5. For example,  $S_{P_{a\bar{d}}}$  represents the net change of unadhered activated platelets without diffusion or convection in a cell and is simply the rate of platelet activation minus the rate of platelet adhesion to a surface, as shown below:

$$S_{P_{a\bar{d}}} = k_{P_{a\bar{d}}, P_{a\bar{d}}} [P_{a\bar{d}}] - k_{P_{ad}, P_{a\bar{d}}} [P_{ad}] \quad 3-67$$

The rate of platelet activation,  $k_{P_{a\bar{d}}, P_{a\bar{d}}}$  is the sum of agonist platelet activation,  $k_{apa}$ , and shear platelet activation,  $k_{spa}$ , whereas  $k_{P_{ad}, P_{a\bar{d}}} = k_{emb}$ , describes embolization. Activation of platelets occurs when they are exposed to critical levels of ADP, Thrombin, and TxA2, following Sorensen<sup>320</sup>, as well as by exposure to shear stress.

$$k_{P_{a\bar{d}}, P_{a\bar{d}}} = k_{apa} + k_{spa} \quad 2-38$$

$k_{apa}$  was given in Section 2.5.2 as:

$$k_{apa} = \begin{cases} 0, \Omega < 1.0 \\ \frac{\Omega}{t_{act}}, \Omega \geq 1.0 \end{cases}$$

$$\Omega = \sum_{j=1}^{n_a} w_j \frac{[a_j]}{[a_{j,threshold}]} \quad 2-35$$

$$\forall a_j \in \{T, ADP, TxA2\}$$

$t_{act}$  is a platelet activation time constant, such that if  $\Omega = 1$  and convection and diffusion are neglected, after  $3t_{act}$  [s], 95% of platelets are activated. As was noted, Taylor et al.<sup>349</sup> found that using the original thresholds proposed by Sorensen, this model underpredicts the effect of ADP concentration on platelet activation and does not adequately account for the synergistically thrombogenic effect of agonists. Therefore, the original formulation is modified to use the ADP-induced platelet activation concentration threshold measured by Frojmovic et al.<sup>321</sup>,  $[ADP]_{threshold} = 0.1\mu M$ , who furthermore note that activation rate saturates at an ADP concentration of  $100\mu M$ . Following Wu et al.<sup>339</sup> and Sorensen<sup>320</sup>, a value of  $t_{act} = 0.1$  s is used, which is the lower bound of generally accepted values.

The rate of platelet activation by shear stress given by Wu et al.<sup>339</sup> is derived from Goodman's<sup>325</sup> fitting of Hellums' data<sup>324,326</sup>, which fits exposure time until platelet activation onset (measured by serotonin release) as a function of shear stress. Goodman interpreted this as a time constant for platelet activation but the upper limit assumed that after platelet activation begins, 95% of platelet activation is completed after  $3t_{act}$ . This method, though flawed, is preferred to more recent methods presented by Soares et al.<sup>330</sup> because platelet residence times inside of MCS are in the order of 1-10 [ms]. This duration is two to three orders of magnitude shorter than the load application rates present in the data of Soares et al.<sup>330</sup> and Sheriff et al.<sup>329</sup> in their fitting, whereas Hellums' data covers this range entirely. This is done despite the flaws in Goodman's model, which also does not account for the platelet activation feedback by Thrombin. This is justified by noting that in high-shear environments, shear will by necessity be the dominant platelet activation mechanism.

$$k_{spa} = \min \left( 2.5 \cdot 10^{-7} \left[ \frac{1}{\left( \frac{dyn}{cm^2} \right)^{2.3} s} \right] \tau^{2.3}, \frac{1}{t_{act}} \right) \quad 3-68$$

Platelet activation releases ADP at a constate rate per activated platelet, in proportion to the amount released by 80% of alpha granules. Other agonists released such as serotonin are not modelled due to lack of available data on how they affect platelet activation. TxA2 is assumed to be synthesized at a constant rate by activated platelets. ADP is also released from hemolyzed

RBCs. Following Sorensen<sup>320</sup>, it is estimated that 80% of granules are released during activation.

$$S_{ADP} = \lambda_{ADP}(-S_{P_{\bar{a}\bar{d}}}) + S_{Hemo,ADP} \quad 3-69$$

$$S_{TxA2} = k_{TxA2,P_a}([P_{\bar{a}\bar{d}}] + [P_{ad}]) - k_{TxA2,TxA2}[TxA2] \quad 3-70$$

Where  $\lambda_{ADP}$  is the concentration of agonist released per platelet during platelet activation, and  $S_{ADP,Hemo}$  is the quantity of ADP released during hemolysis.

Fibrin production, and thus platelet stabilization is neglected in this work, as was done by Wu et al.<sup>263</sup>. It is assumed that fibrin production is a slower process that occurs after the formation of a porous platelet matrix as the fibrinogen bond does not form at high shear; the present work is focused on how hemolysis affects thrombus initiation in high-shear environments. This aspect is better examined by Rojano et al.<sup>18</sup>, who incorporate the kinetics of fibrin production by thrombin; the effect of hemolysis and red blood cells on fibrin polymerization is left for future work.

### 3.3.4 Platelet Adhesion and Embolization

Platelet adhesion to a surface or other stationary platelets is modelled using first-order reaction kinetics: the rates of platelet deposition,  $k_{P_{\bar{a}\bar{d}},P_{ad}}$  and  $k_{P_{\bar{a}\bar{d}},P_{ad}}$ , in general depend on hematocrit, shear rate and platelet concentration, but at high shear rates ( $> 7000 \text{ [s}^{-1}\text{]}$ ) concentration of platelets alone accounts for this variation and is constant at boundaries. It is assumed that inactive platelets that adhere to a surface or another platelet are activated instantaneously. The rates of platelet adhesion to surfaces and other platelets are material properties corresponding to biocompatibility and are fit from experiments or simulations which have been successfully validated<sup>15,325,342</sup> and are presented in Table 2.

$$k_{P_{i\bar{a}},P_{ad}} = k_{i_{dep,j}}^* = \frac{1}{\delta_j} k_{i_{dep,j}} \cdot k_{hemo} \quad \forall i \in \{a, \bar{a}\} \text{ and } \forall j \in \{P, W\} \quad 3-71$$

Where the \* superscript denotes adhesion modified by hemoglobin binding to vWF,  $\bar{a}$  and  $a$  denote resting platelet and activated platelets, respectively, and  $P_{lt}$  and  $W$  denotes deposition onto other platelets and wall boundaries, respectively. As  $k_{i_{dep,W}}$  is a 2D surface deposition rate, a length scale is required to convert it into a volumetric concentration fill rate. Wall boundaries are assumed to have a thickness equal to the platelet diameter,  $D_{plt}$ , so surface deposition rate is divided by  $D_{plt}$  to describe the rate that a surface is covered by one layer of platelets, and thus  $\delta_W = D_{plt}$ . Inside of computational cells, the magnitude of the platelet

volume fraction gradient,  $\frac{1}{\delta_{Plt}} = |\nabla \phi_{Pd}|$ , is used. This is because the volume fraction gradient is a proxy for the mesh spacing projected onto the normal vector of thrombus surface, and  $k_{i_{dep,j}}^*$  is a volumetric fill rate. If the thrombus surface grows steadily one platelet layer at a time, large elements should fill more slowly than smaller elements. Consequently, this deviation is made from Wu et al.<sup>339</sup> to the grid dependency of the thrombus growth rate.  $k_{hemo}$  is a scaling factor for the adhesion rate based on the local concentration of hemoglobin – hemoglobin acts as a catalyst for the reaction between vWF and the GP-1b $\alpha$  platelet receptor, discussed in the next section.

Deposited platelets can also be dislodged (embolized) by shear stress. Goodman<sup>325</sup> derive single-platelet embolization probability at varying shear rate from a Polyethylene (PE) flow cell, generally conform to the theoretical probability maps of Basmadjian<sup>352</sup>. The recent implementation of Fogelsons'<sup>347</sup> constitutive model for thrombus strength by Tobin and Manning<sup>385</sup>, has at the time of writing yet to be validated experimentally, leaving Goodman's probability approach as the only experimental data on platelet embolization for high shear and is thus commonly used.<sup>350,351</sup> The single-platelet embolization model of Goodman is given below. It should be noted here that a mistake made in equation (1) in the manuscript by Goodman et al.,<sup>325</sup> was corrected. In the version of their manuscript available online (as of March 2022), they make a mistake and place  $t_{emb}$  in the place of  $\tau_{emb}$ , it was only possible to reproduce Figure 18 from Goodman<sup>325</sup> by using equation 3-72 and assuming  $\tau_{emb} = 1$  [Dyne cm<sup>-2</sup>].

$$P_{emb}(\tau, \tau_{emb}) = \left( \left( 1 - \exp \left( -0.0095 \frac{\tau}{\tau_{emb}} \right) \right) \right) \quad 3-72$$

$$k_{emb,W}(\tau, \tau_{emb}) = \frac{P_{emb}(\tau, \tau_{emb,W})}{t_{emb}} [s^{-1}] \quad 3-73$$

$$k_{emb,P} = \begin{cases} \frac{P_{emb}(\tau, \tau_{emb,P})}{t_{emb}} [Plt \ s^{-1}] & \text{if } \phi_{Pd} > 0 \\ 0 & \text{otherwise} \end{cases} \quad 3-74$$

Where  $P_{emb}$ , the probability of embolization of a single platelet, is a function of the wall shear stress,  $\tau$  [Dyne/cm<sup>2</sup>], and is dimensionless.  $t_{emb}$  [s], and  $\tau_{emb}$  are the characteristic time and stress of embolization.

Values for  $t_{emb}$  and  $\tau_{emb}$  are not consistent in the literature, for example, Goodman<sup>325</sup> give  $t_{emb} = 120$  [s] and a value of  $\tau_{emb,W} = 1$   $\left[ \frac{dyne}{cm^2} \right]$  is implied. Wu et al.<sup>339</sup> give a value of

between  $\tau_{emb,P} = 15 - 30$  [dyne  $\text{cm}^{-2}$ ] for platelet-platelet embolization, and  $\tau_{emb,W} = 0.1$  [dyne  $\text{cm}^{-2}$ ]; Rojano et al.<sup>18</sup> give  $\tau_{emb,P} = 9$  [dyne/ $\text{cm}^2$ ] and  $\tau_{emb,W} = 0.275$  [dyne/ $\text{cm}^2$ ], respectively, whereas Navitsky et al.<sup>353</sup> and Taylor et al.<sup>349</sup> give  $\tau_{emb,W} = 0.375$  [dyne/ $\text{cm}^2$ ] and 9 [dyne/ $\text{cm}^2$ ], respectively. Rojano et al.<sup>18</sup>, like Wu<sup>339</sup>, set  $t_{emb} = 1$  [ $\text{s}^{-1}$ ]. There is in general a severe inconsistency of the published physical constants associated with platelet embolization in the literature.

In the present study, the maximum theoretical platelet concentration,  $[P_{ad}]_{max}$ , is computed by assuming that activated platelets are roughly spherical in shape, with a hydraulic diameter of  $D_{plt} = 2.1086 \mu\text{m}$ . To compute maximum spacing, following Wu, an ideal spherical packing in a cubic cell is assumed, which gives a volume ratio 0.7405. It is also assumed that there is a separation between platelets equal to the  $D_{plt}$  to account for filopodia. Thus,  $[P_{ad}]_{max} = 0.7405 \cdot 2.55 \cdot 10^{16}$  [ $\text{Plt m}^{-3}$ ].

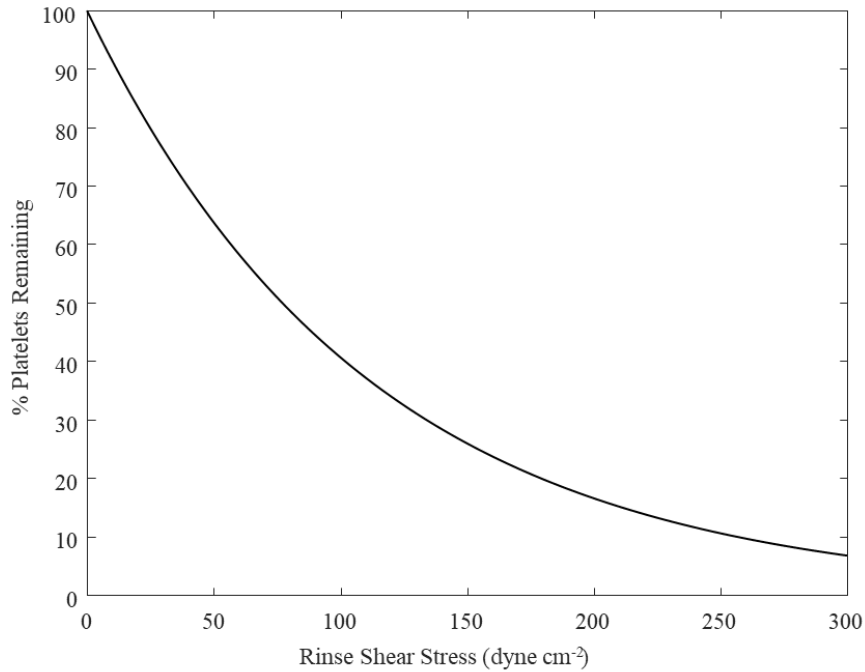


**Figure 18: Probability of embolization vs shear stress given by Goodman et al.<sup>325</sup>**

### 3.3.5 Deriving an Alternative Embolization Formulation

As there is substantial inconsistency in the data available on platelet embolization, two alternative models are proposed here. Given the viscoelastic nature of the vWF and fibrinogen bond, in general, embolization timescale should be inversely proportional to the shear rate:

$$t_{emb}^{-1} \approx \kappa_{emb} \dot{\gamma}_w^\kappa \quad 3-75$$

In the present study, the above model is referred to as the modified-Goodman model. In addition, following the empirical notions of cellular lysis, it is assumed that there is a power law relationship between embolization rate and shear stress as a kind of mechanical dose in parity to hemolysis modelling. In this “Power Law” form, embolization rate is:

$$k_{emb}(\tau, \tau_{emb}) = k_{emb} \left( \frac{\tau}{\tau_{emb}} \right)^\kappa \quad 3-76$$

In general, although it is well established that platelet adhesion rates are material-specific, all previous studies generally assumed that embolization rates are independent of material. The rationality for this assertion is that while platelet aggregation is related to chemical kinetics, receptor reactivity, and surface smoothness, embolization is related to the breaking of vWF, fibrinogen, or collagen bonds polymers by shear stress, which is not material or geometry dependant.

$k_{emb}$ ,  $\tau_{emb}$  and  $\kappa$  are fit from the experimental data of Navitsky et al.<sup>353</sup>, who give platelet concentrations at varying radial positions on a 10 mm disk immersed in a closed bath of PRP and spinning at a speed of 29.63 rad/s. Given that deposition occurs much more slowly than activation, that platelet concentration is measured after a relatively long time frame (120 minutes), and that the experimental setup is closed and no flow leaves the chamber, all platelets are assumed to be activated in the chamber and activated platelet concentration is assumed to be uniform, so that  $[P_{ad}] = 3.5 \cdot 10^{14} [\text{Plt m}^{-3}]$ . The spatial concentration gradient of activated platelets will also be low due to the relatively slow rotational velocity and consequently low velocity gradient in the radial direction. If the wall-normal gradient of activated platelet concentration is also neglected and only the surface platelet concentration is considered, the equation for  $P_{ad}$  can be simplified to the ordinary differential equation given below.

$$[P_{ad}] = (1 - \phi_{P,d}) \frac{k_{adep,W}}{D_{Plt}} [P_{ad}] - k_{emb} [P_{ad}] \quad 3-77$$

Shear stress is estimated using the equation by the analytical solution for fluid on a spinning disk derived by Grunenwald<sup>406</sup>, which reproduces CFD predicted  $\tau$  accurately.

$$\tau = \mu \dot{\gamma} = 0.8 \mu \sqrt{\frac{\omega^3}{\nu}} r \quad 3-78$$



Where  $\mu$  is the local dynamic fluid viscosity,  $\omega$  is the rotation rate,  $\nu$  is the kinematic viscosity, and  $r$  is the radius. The system is solved numerically to obtain the steady-state platelet concentration at the given radial position. A constrained minimum optimization problem is solved to find values of  $\tau_{emb}$  and  $k_{emb}$  for different values of  $\kappa$ . The results of this fitting are shown in the subsequent section, in Figure 51. This differs from the approach of Taylor et al.<sup>407</sup>, who rather than fit the embolization rate in the partial differential model, simply fit platelet concentration to a function of shear stress and use the output as an asymptotic value for the maximum possible surface concentration at a given time.

### 3.3.6 Anticoagulation and Thrombin Production

Thrombin is converted from prothrombin on the membranes of platelets from prothrombin, which is abundant in plasma, is consumed during thrombin production (at different rates on active and inactive platelets). The rate of thrombin conversion thus depends on platelet concentration. Thrombin catalyzes fibrin production which converts activated-adhered platelets into fibrin-stabilized platelets that are not easily embolized by shear stress. Thrombin conversion is modelled using the first-order reaction model of Sorensen<sup>320</sup>.

Thrombin, T, is synthesized by prothrombin, PT, and inhibited by antithrombin, AT, on the membranes of platelets at a rate depending on platelet concentrations, and the anticoagulation concentration. Anticoagulation is modelled following Griffith's<sup>362</sup> model of heparin-catalyzed deactivation of T by aT, so that reaction velocity,  $\Gamma$ , is given below:

$$\Gamma = \begin{cases} \frac{-k_{1T}[H][AT]}{\alpha K_{AT}K_T + \alpha K_{AT}[T] + \alpha K_T[AT] + [AT][T]} & [H] > 2022 \left[ \frac{nmol}{m^3} \right] \\ 7.083 \cdot 10^{-6} [AT] & [H] \leq 2022 \left[ \frac{nmol}{m^3} \right] \end{cases} \quad 3-79$$

In this model, the rate of thrombin generation is the sum of Thrombin deactivation by Antithrombin, and the production of thrombin from prothrombin on platelet surfaces at rates  $\psi_{at}$  and  $\psi_{\bar{at}}$  on activated and non-activated platelets, respectively.

$$S_T = -\Gamma[T] + [PT] \left( \psi_{at} ([P_{ad}] + [P_{\bar{ad}}]) + \psi_{rt} ([P_{\bar{ad}}] + [P_{ad}]) \right) \quad 3-80$$

Antithrombin, is consumed in proportion to the rate of thrombin deactivation:

$$S_{AT} = -\Gamma \varepsilon [T] \quad 3-81$$

Where  $\varepsilon$  is the conversion from U (NIH units, the standard for enzymatic activity) and mol. Likewise, prothrombin is consumed at the rate:

$$S_{PT} = -\varepsilon[PT] \left( \psi_{at} ([P_{ad}] + [P_{ad}]) + \psi_{rt} ([P_{ad}] + [P_{ad}]) \right) \quad 3-82$$

Thrombin converts fibrin, which converts activated and deposited (adhered) platelets to stabilized platelets,  $P_{ad} \rightarrow P_S$ , arresting flow and triggering coagulation. As noted, fibrin polymerization, which generally occurs in low-shear conditions (such as inside a thrombus) is neglected. It is assumed that fibrin polymerization is an equilibrium process, as platelet adhesion generally occurs before fibrin polymerization, and as clots once formed tend to grow, thrombogenesis is not affected by fibrin polymerization in a steady flow, which is the scope of this study. In unsteady flow, this must be re-evaluated.

### 3.3.7 Modelling the Effect of Hemolysis on Thrombosis

The effect of hemolysis on thrombosis, is modelled by incorporating two of the three major effects of hemolysis on thrombosis:

1. The effect of ADP released from hemolyzed RBCs
2. The effect of pfHb-induced hyper-adhesivity of von Willebrand factor

The binding of plasma free Hb (pfHb, fHb or eHb) to vWF-A1 is modelled using first-order reaction kinetics, adding two extra ADR equations of the form in Equation

3-63, to the model transition from vWF to its hyper-adhesive form, vWF<sub>ha</sub>.



The association and dissociation rates are estimated from the equilibrium dissociation constant,  $k_{d,vWF_{ha}} = 14.8 \mu M$  ( $14.8 \cdot 10^6$  [nmol m<sup>-3</sup>]), and the effective timescale of Hb binding to von-Willebrand Factor,  $t_{vWF_{ha}} = 175$  s (the time taken to reach 63.2% of maximum concentration) are calculated from Da et al.<sup>289</sup>. Notably, these experiments were performed using reflectometric interference spectroscopy of immobilized vWF-A1, which necessarily reacts more quickly than vWF in plasma. Da et al.<sup>289</sup> fit the Hill-Langmuir equation (n=1):

$$\frac{[vWF_{ha}]}{[vWF]} = \frac{[fHb]}{k_{d,vWF_{ha}} + [fHb]} \quad 3-84$$

In the current study first-order reaction kinetics are assumed. Thus, the dissociation rate constant,  $k_{D,vWF_{ha}}$  and the association rate constant,  $k_{A,vWF_{ha}}$ , are:

$$k_{A,vWF_{ha}} = (k_{d,vWF_{ha}} t_{vWF_{ha}})^{-1} \quad k_{D,vWF_{ha}} = t_{vWF}^{-1} \quad 3-85$$

$$S_{vWF_{ha}} = k_{A,vWF_{ha}} [fHb][vWF] - k_{D,vWF_{ha}} vWF_{ha} \quad 3-86$$

It is assumed that at higher shear rates, binding between Hb and vWF-A2 and A3 domain is suppressed due to the slower association rates being unable to form stable bonds, and thus neglect these reactions. Indeed, At shear rates above  $500-800 \text{ s}^{-1}$ , vWF and vWF<sub>ha</sub> bind to platelet GPIb $\alpha$  (mediated by ristocetin<sup>357</sup>) and trigger platelet activation<sup>77</sup>, allowing adhesivity of platelets to surfaces even at high shear rates due to the uniquely high vWF-GPIb $\alpha$  association rate<sup>367</sup>.

Furthermore, the adhesion process involves the immobilization of vWF onto the surface before the vWF-GPIb $\alpha$  bond, however, the protein immobilization process is not well understood and its surface chemistry is material and shear rate dependant. Without appropriate constitutive modelling, the kinetics of receptor-ligand binding are difficult to resolve in a continuum model, and concentration changes in vWF and vWF<sub>ha</sub> due to surface chemistry and binding to platelets are thus neglected and consequently, vWF concentrations will not be realistic. This modelling intends to quantify the relative effect of hemoglobin binding onto vWF by scaling the adhesion rate, and thus it is assumed that the kinetic binding rate of vWF<sub>ha</sub> onto platelets is simply 5.33 times more reactive than vWF, based on the data of Da et al.<sup>289</sup> This treatment is justified because platelets bind to either a surface-immobilized molecule of vWF or a molecule of vWF<sub>ha</sub> and not directly to surfaces; material dependency is encompassed by the mechanics of protein-surface chemistry, which is separate from vWF-GPIb $\alpha$  bonding. The platelet deposition rate is then simply the weighted average of [vWF] and [vWF<sub>ha</sub>]:

$$\frac{k_{i_{dep,j}}^*}{k_{i_{dep,j}}} = k_{hemo} = \frac{[vWF] + k_{vWF_{ha},P}[vWF_{ha}]}{[vWF] + [vWF_{ha}]} \quad 3-87$$

$$\forall i \in \{a, \bar{a}\} \text{ and } \forall j \in \{Plt, W\}$$

Where  $k_{vWF_{ha},P}$ , is the relative adhesion rate in the presence of vWF<sub>ha</sub> relative to regular vWF. It is assumed that at high shear, platelet adhesion is entirely dependent on vWF as the fast association rate binding to GP1b is necessary to slow the platelet to rates where it can bind fibrinogen, collagen or other exposed ECM proteins. Da et al. find that  $k_{vWF_{ha},P}$  is 5,9 and 2 for ECM, fibrinogen, and collagen-coated surfaces, respectively. In the present study, the average of these values is taken (5.33), assuming a homogenous mixture of adhesion-mediating proteins are immobilized on the surface.

Nominal concentration of vWF in plasma is commonly reported as 100 IU/dL, or (alternatively,  $10 \mu\text{g}/\mu\text{L}$  or  $\sim 37 \text{ mmol} \cdot \text{m}^{-3}$  assuming a molecular weight of 270 kDa)<sup>408</sup>, vWF is depleted by

conversion to  $vWF_{ha}$  and is replenished by release of vWF from  $\alpha$  granules during platelet activation at a rate of  $\lambda_{vWF} \left[ \frac{nmol}{Plt \cdot s} \right]$ .

$$S_{vWF} = -S_{vWF_{ha}} + \lambda_{vWF}(k_{apa} + k_{spa})[P_{ad}] \quad 3-88$$

$\lambda_{vWF} = 3.29 \cdot 10^{-8} \left[ \frac{nmol}{Plt} \right]$  is the average vWF released per platelet obtained by assuming that platelets contain 20% of all vWF<sup>367,408</sup>, and that 80% of all granules are released during activation, Fulling, Wu<sup>339</sup> and Goodman<sup>325</sup>.

The effect of NO on platelet activation and deposition is also not modelled, and thus neither is the scavenging effect of NO by pfHb. NO is produced in endothelial cells in the presence of ADP, however, which are absent in VADs, and it is thus reasonable to neglect this effect in this study. Furthermore, the effect of vWF cleavage under shear is neglected, as is the effect of Heparin on platelet adhesion. These last are important omissions because the sheltering of  $vWF_{ha}$  from cleavage compared to vWF has an important effect because of the ubiquity of Heparin as an anticoagulant in MCS and the prevalence of acquired vWF syndrome in MCS patients. Using the above framework, it is possible to include these effects if it were possible to estimate the rate of stress-dependant vWF cleavage, and Heparin-vWF binding rates, but this is left for future work.

Hemolysis is modelled using an Eulerian framework which is most compatible with the thrombosis model. The approach of Salazar and Antaki<sup>282</sup> is followed for the Eulerian implementation of the GW power law (Eqns. 2-29 to 2-31), using coefficients by Ding et al.<sup>237</sup> for human blood. Transmembrane hemoglobin modelling is not considered necessary as it is sufficient to examine the effect of sublethal hemolysis levels, and the question of whether transmembrane hemoglobin transfer is dominant in MCS is a separate research question. Furthermore, the inclusion of the extra equations makes an already large computational problem larger. This also somewhat simplifies modelling as it can be assumed that ADP is released from red blood cells at a rate proportional to the rate of hemolysis. The additional ADP released during hemolysis is simply calculated as:

$$S_{ADP,Hemo} = \frac{[ADP]_{RBC}}{[Hb]_{RBC}} [f\dot{Hb}]_{hemolysis} \quad 3-89$$

Where the subscript RBC denotes the nominal concentration inside of a red blood cell. The activating effect of ADP release on thrombosis is directly incorporated by adding  $S_{ADP,Hemo}$  to

the source term for ADP released from platelets. The hemoglobin release rate is given in proportion to the mechanical dose, obtained by solving Equation 2-29.

$$\frac{\partial \mathcal{D}}{\partial t} + (\mathbf{v} \cdot \nabla) \mathcal{D} = \xi C_{IH}^{\frac{1}{\beta}} \tau^{\frac{\alpha}{\beta}} (1 - \mathcal{D}) \quad 2-29$$

$$\mathcal{D} = IH^{\frac{1}{\beta}} \quad 2-30$$

$$\xi = 1 \text{ if } \tau \geq \tau_c, 0 \text{ otherwise} \quad 2-31$$

$$[fHb] = \mathcal{D}^{\beta} \frac{[Hb]_{RBC} Hct}{100\%}$$

$$S_{ADP,Hemo} = \frac{[ADP]_{RBC}}{[Hb]_{RBC}} [f\dot{Hb}]_{hemolysis} \quad 3-90$$

And [fHb] release rate by hemolysis is computed from the mechanical dose source term.

$$[f\dot{Hb}]_{hemolysis} = S_D^{\beta} \frac{[Hb_{RBC}] Hct}{100\%} \quad 3-91$$

$$[f\dot{Hb}]_{hemolysis} = \left( \delta C_{IH}^{\frac{1}{\beta}} \tau^{\frac{\alpha}{\beta}} (1 - \mathcal{D}) \right)^{\beta} \frac{[Hb_{RBC}] Hct}{100\%} \frac{10^9}{M_{Hb}} \left[ \frac{nmol}{s \cdot m^3} \right]$$

### 3.3.8 Model Assumptions

In general, the thrombosis model is given by Equations 3-58 to

3-63, the source terms and diffusivities for which are given in Table 4. The coefficients and constants used to compute each source term are given in Table 5. The model described operates under several major assumptions that must be considered when interpreting the results.

Firstly, regarding coagulation, the assumption of the absence of a sub-endothelium in Mechanical Circulatory Support (MCS) devices allows exclusion of the extrinsic portion of the coagulation cascade, the interaction with the endothelium, and its related factors from our model. Furthermore, first-order reaction kinetics are assumed to adequately describe adhesion and that fibrin polymerization occurs at a slower rate than platelet adhesion and is not part of initial thrombus formation.

In terms of platelet activation, the model presumes that adenosine diphosphate (ADP), thromboxane A2 (TxA2), and thrombin interact linearly with respect to activation rate.

Additionally, it was assumed that no interaction between agonists and shear stress exists concerning activation and that thrombin activation feedback could be neglected in shear-driven activation. While these assumptions allow the modelling process to remain manageable, they might not fully capture the complexity of platelet activation dynamics.

The model also substantially simplifies the processes of adhesion and embolization. It assumes that the adhesion rate at high shear rates is proportional to platelet concentration only and independent of shear rate. It does not account for how heparin affects the platelet adhesion rate as it does not bind to von Willebrand Factor (vWF). The adhesion mechanics between platelets, collagen, ECM, fibrinogen, and von-Willebrand factor are effectively lumped into one coefficient,  $k_{dep}$ , which is constant throughout the simulation. Furthermore, it asserts that embolization probability is a function of shear stress alone, the timescale of embolization is proportional only to the shear rate, and embolization as a process is independent of the adhered material.

Finally, with respect to the effects of hemolysis on thrombosis, the model presumes that nitric oxide (NO) is not produced by endothelial cells inside MCS, and the vWF-Factor VII functional complex is independent of the vWF-Hemoglobin (Hb) reaction. It also asserts that the vWF-Glycoprotein 1b (GP1b) bond is dominant in MCS, that  $vWF_{ha}$  increases adhesion rate proportionally for varying materials, and that the effect is independent of shear stress, and a host of other factors such as heparin concentration. This is an oversimplification but is used due to the lack of better data. Furthermore, the model neglects shear stress-induced vWF cleavage and interaction between vWF-mediated platelet adhesion and heparin. It also assumes that the vWF transition to  $vWF_{ha}$  does not interfere with other functions of vWF or the vWF-FVIII complex. These assumptions, made largely due to lack of data, might not capture the complete picture of the effects of hemolysis on thrombosis.

Assumptions are considered major by virtue of how sensitive the result (whether or not thrombosis occurs) is to the corresponding mathematical model. From this perspective, the most significant assumptions are assumptions made regarding adhesion and embolization mechanics. As in general, the model predicts whether a thrombus forms on a foreign surface based on the balance between adhesion and embolization rates, the relevant constants that govern these processes will have a large effect on the end result. Coefficients such as  $k_{emb}$  and  $k_{a_{dep,W}}$  underly profoundly complex biochemical processes that are in fact dependant on myriad factors such as vWF concentration and structure, shear rate, hematocrit, exposure time,

protein immobilization on surfaces, surface roughness, and the interaction of vWF with other adhesion influencing agents. Adhesion and embolization rates in this model are in general material specific and fit from experiment under controlled conditions because the mechanics of these processes are poorly understood. A better understanding of these mechanics with regard to the aforementioned factors would improve thrombosis modelling efforts, but in general there is a strong need for constitutive modelling of adhesion mechanisms to improve prediction accuracy. This is particularly important in continuum models, which are required to solve larger problems of practical importance to the design of biomedical devices. In general however, underlying all of these modelling efforts is a profound scarcity of data for validation.

### **3.3.9 Computational Domain and Simulation Setup**

Blood flow is simulated in an open-hub axial flow LVAD geometry being developed at McGill, for which hydrodynamic validation data is available. The geometry is developed by Bao<sup>410</sup>, and optimized to reduce hemolysis while maintaining hydrodynamic performance. This optimized geometry is used here and optimized further for the purpose of analyzing the effect of thrombosis.

#### **Validation and Verification**

To validate the computational model and to verify the equations are solved properly, a grid sensitivity analysis is performed. Grid sensitivity analysis is approached by reducing the near-wall spacing (by increasing the number of inflation elements), minimum volume spacing and maximum volume spacing are consecutively reduced until average and maximum shear stress at the walls varies by less than 2% and 10%, respectively. The mean overall mesh spacing is similarly reduced until the von-mises stress stops changing, being the most important hemodynamic variable relevant to hemolysis computation, platelet activation and embolization. The grid spacings tested and total number of elements and corresponding values of the parameters of interest are shown in in Figure 22.

In addition, the thrombus development is simulated downstream from a back-wards facing step in a small cylindrical channel, and compared to an in-vitro experimental data of a thrombus growing in such a geometry provided for human and bovine blood by Taylor et al.<sup>342</sup> and Yang et al.<sup>384</sup>, respectively. The schematic of the experimental setup is given below in Figure 19, which is used to reproduce the computational domain. The sizing for the computational domain used for the validation study is approached by setting the element size to be a fraction of the

resolution of the MRI (30 $\mu$ m), reducing it until the shear stress distribution on the surface does not change significantly. In addition, adaptive grid refinement is used at the thrombus interface until the thrombus shape does not change appreciably. It was found that only one level of refinement was needed. The channel, made from acrylic BFS, ( $k_{dep,w}$  specified in Table 2),



Modelling Hemolysis and Thrombosis in Blood-Wetted Medical Devices  
Chapter 3: Methodology

**Table 4: Overview of source terms used for equations in model**

$C_i$	$S_{c_i}$	Units	$D_{c_i}$	Description
$P_{\bar{a}\bar{d}}$	$-(k_{spa} + k_{apa} +  \nabla\phi_{Pad} k_{\bar{a}\bar{d}}^*)P_{\bar{a}\bar{d}}$	[Plt m <sup>-3</sup> ]	Equation 2-47	Inactive non-adhered platelets
$P_{a\bar{d}}$	$(k_{spa} + k_{apa})P_{\bar{a}\bar{d}} -  \nabla\phi_{Pad} k_{ad}k_{hemo}P_{a\bar{d}} + k_{emb,Plt}P_{ad}$	[Plt m <sup>-3</sup> ]	Equation 2-47	Active non-adhered platelets
$P_{ad}$	$(k_{spa} + k_{apa})P_{\bar{a}\bar{d}} +  \nabla\phi_{Pad} k_{hemo}(k_{ad}P_{a\bar{d}} + k_{\bar{a}\bar{d}}P_{\bar{a}\bar{d}}) - k_{emb,Plt}P_{ad}$	[Plt m <sup>-3</sup> ]	0	Active Adhered platelets
$AT$	$-\Gamma\varepsilon[T]$	[nmol m <sup>-3</sup> ]	$3.49 \cdot 10^{-11} [m^2s^{-1}]$	Antithrombin
$T$	$-\Gamma[T] + [PT](\psi_{at}([P_{a\bar{d}}] + [P_{ad}]) + \psi_{rt}([P_{\bar{a}\bar{d}}] + [P_{\bar{a}d}]))$	[IU m <sup>-3</sup> ]	$4.16 \cdot 10^{-11} [m^2s^{-1}]$	Thrombin (U refers to NIH units)
$PT$	$-\varepsilon[PT](\psi_{at}([P_{a\bar{d}}] + [P_{ad}]) + \psi_{rt}([P_{\bar{a}\bar{d}}] + [P_{\bar{a}d}]))$	[nmol m <sup>-3</sup> ]	$3.32 \cdot 10^{-11} [m^2s^{-1}]$	Prothrombin
$ADP$	$\lambda_{ADP}(k_{apa}([P_{\bar{a}\bar{d}}] + [P_{\bar{a}d}]) + k_{spa}([P_{\bar{a}\bar{d}}] + [P_{\bar{a}d}]) + k_{rpd}[P_{\bar{a}\bar{d}}]) + (S_D)^\beta \frac{Hct}{100\%} \frac{[ADP]_{RBC}}{M_{ADP}}$	[nmol m <sup>-3</sup> ]	$2.57 \cdot 10^{-10} [m^2s^{-1}]$	Adenosine Diphosphate
$TxA2$	$k_{Pa,TxA2}([P_{a\bar{d}}] + [P_{ad}]) - k_{TxA2,TxA2}[TxA2]$	[nmol m <sup>-3</sup> ]	$2.14 \cdot 10^{-10} [m^2s^{-1}]$	Thromboxane A2
$\mathcal{D}$	$\delta C^\beta \tau^\alpha (1 - \mathcal{D})$	[1]	0	Mechanical Dose, $IH = \mathcal{D}^\beta$
$vWF$	$-S_{vWf_{ha}} + \lambda_{vWF}(k_{apa} + k_{spa})[P_{\bar{a}\bar{d}}]$	[nmol m <sup>-3</sup> ]	$7.83 \cdot 10^{-11} [m^2s^{-1}]$	von Willebrand Factor
$vWF_{ha}$	$\frac{\mathcal{D}^\beta \frac{[Hb_{RBC}]}{100\%} Hct}{t_{vWF_{ha}} k_{d,vWF_{ha}}} [vWf] - \frac{vWF_{ha}}{t_{vWF_{ha}}}$	[nmol m <sup>-3</sup> ]	$7.83 \cdot 10^{-11} [m^2s^{-1}]$	Hyper-adhesive von Willebrand Factor

*Table 5: Constants and property values used in Thrombosis Model*

Variable	Value	Description
$[T]_{\text{threshold}}$	$3.33 \cdot 10^3 [NIH U m^{-3}]$	Thrombin activation Threshold
$[ADP]_{\text{threshold}}$	$1.0 \cdot 10^5 [nmol m^{-3}]$	ADP activation Threshold (0.1uM) <sup>321</sup>
$[TxA2]_{\text{threshold}}$	$1.0 \cdot 10^6 [nmol m^{-3}]$	TxA2 activation Threshold
$t_{act}$	0.1 s	Characteristic time of platelet activation by agonists
$k_{\bar{a}_{dep,P}}$	$3.0 \cdot 10^{-6} [m s^{-1}]$	Deposition rate of inactive platelets to other platelets <sup>339</sup>
$k_{a_{dep,P}}$	$3.0 \cdot 10^{-5} [m s^{-1}]$	Deposition rate of activated platelets to other platelets <sup>339</sup>
$k_{\bar{a}_{dep,w}}$	$0.1 k_{a_{dep,w}}$	Deposition (and activation) rate of inactive platelets to walls <sup>339</sup>
$k_{a_{dep,w}}$	See Table 2	Deposition rate of activated platelets to walls (material dependant)
$\kappa_{emb}$	$1.28 \cdot 10^{-5} [1]$	Embolization constant – Derived from fitting Navitsky <sup>353</sup>
$\tau_{emb,P}$	3.0 [Pa]	Characteristic embolization stress from other platelets <sup>339</sup>
$\tau_{emb,w}$	$0.1^{339} - 0.9^{349} [Pa]$	Characteristic embolization stress from wall boundaries
$\{k_{1T}, k_{AT}, k_T, \alpha\}$	$\{13.333, 0.1 \cdot 10^6, 3.5 \cdot 10^4, 1.0\}$	Rate constants used to compute thrombin deactivation rate $\Gamma$
$k_{T,P_a}$	$3.69 \cdot 10^{-15} \left[ \frac{U}{Plt \cdot nmol \cdot s} \right]$	Thrombin conversion rate from prothrombin on activated platelets
$k_{T,P_{\bar{a}}}$	$6.5 \cdot 10^{-16} \left[ \frac{U}{Plt \cdot nmol \cdot s} \right]$	Thrombin conversion rate from prothrombin on inactive platelets

Modelling Hemolysis and Thrombosis in Blood-Wetted Medical Devices  
Chapter 3: Methodology

$k_{TxA2,Pa}$	$2.4 \cdot 10^{-8} \left[ \frac{nmol}{Plt\ s} \right]$	Synthesis rate for TxA2 on activated platelet surface
$k_{TxA2,TxA2}$	$0.0161 [s^{-1}]$	Self inhibition rate for TxA2
$\varepsilon$	$9.11 \cdot 10^{-3} \left[ \frac{nmol}{IU} \right]$	Conversion factor from IU to nmol of Thrombin (i.e., specific reactivity)
$\lambda_i \forall i \in \{ADP, vWF\}$	$\{2.4 \cdot 10^{-8}, 3.29 \cdot 10^{-8}\} \left[ \frac{nmol}{Plt\ s} \right]$	Release rate for agonists during platelet activation <sup>325</sup>
$C_{imb}$	$\sim 2.0 \cdot 10^7\ Pa$	Force constant for immersed boundary momentum source term
$\{[Hb]_{RBC}, [ADP]_{RBC}\}$	$\{427\ kg\ m^{-3}, 34.18\ g\ m^{-3}\}$	Nominal concentration of ADP and Hemoglobin in RBCs
$M_{Hb}$	63.911 kDa	Molar Mass of Hemoglobin <sup>409</sup>
$M_{vWF}$	277	(nominal) Molar Mass of vWF (James & Rydz) <sup>406</sup>
$M_H$	16 kDa	Molar Mass of Heparin <sup>339</sup>
$M_{ADP}$	427.201 Da	Molar Mass of ADP
$[P_d]_{max}$	$3.458 \cdot 10^{-6} [Plt\ m^{-3}]$	Maximum spatial platelet concentration
$\{C, \alpha, \beta\}$	$\{3.458 \cdot 10^{-6}, 2.064, 0.2777\}$	Constants used to compute lethal hemolysis from Ding et al. <sup>237</sup>
$[H]$	$0.1 \cdot 10^6 [nmol\ m^{-3}]$	Heparin Concentration
$k_{ha}$	5.3	Relative increase in adhesion rate for hyper adhesive vWF, $vWF_{ha}$
$k_{d,vWF_{ha}}$	$14.8\ \mu M$	Equilibrium dissociation constant of $vWF \rightarrow vWF_{ha}$ [Da]
$t_{vWF_{ha}}$	175 s	Characteristic reaction time of hyper-adhesive vWF [Da]

is simulated and the length over time of the simulation method presented above is compared with the in-vitro data.

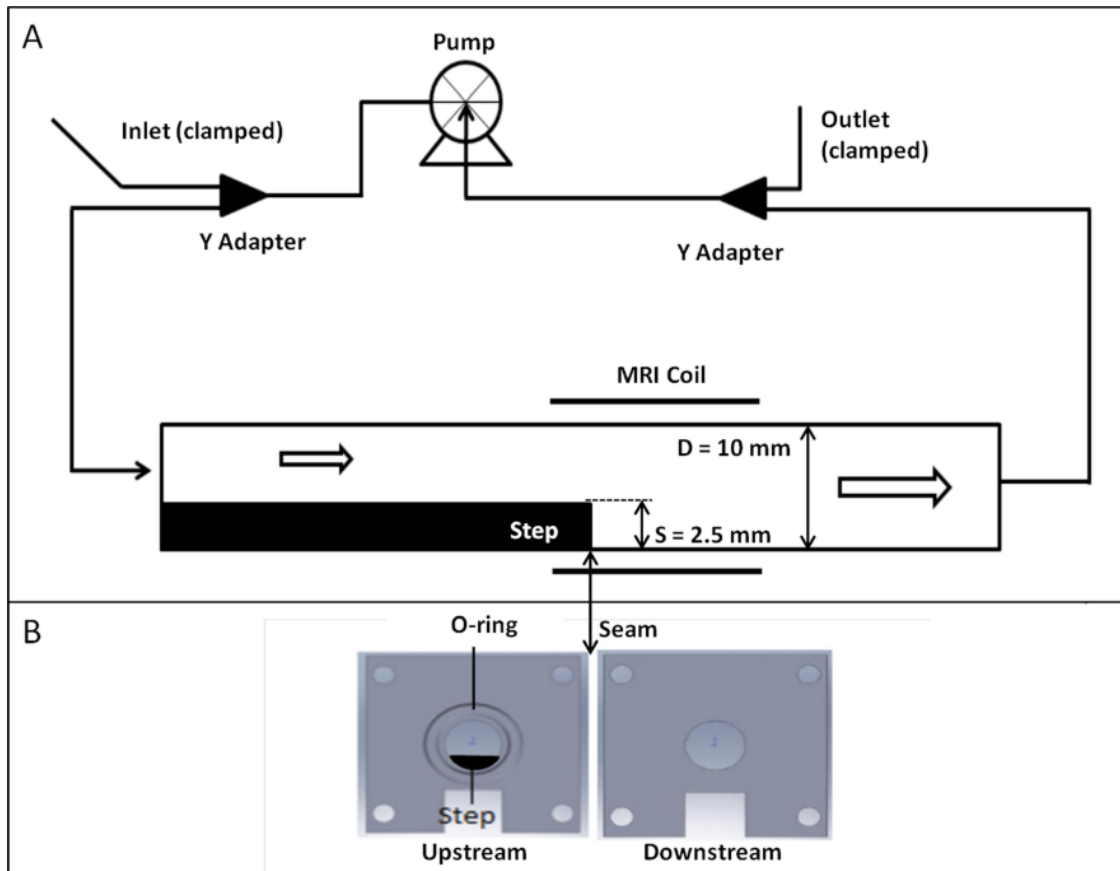


**Figure 19: Schematic illustration of the experimental setup of a thrombus growing downstream from a backward-facing step by Taylor et al.<sup>342</sup> and Yang et al.<sup>384</sup>.**

The adoption of the backward-facing step as a verification challenge was a choice made partly out of practicality, partly out of physiological significance, and partly as a hemodynamic modelling challenge. The main reason for choosing this data as a validation was because it used known materials for which adhesion rates could be obtained from a different experiment, and it was one of few datasets available that resulted in a controlled thrombus formation with very high-quality data available for validation. It serves as a very classical example of a flow, in which the fluid dynamics are well known and for which a wide variety of literature exists, albeit the complex rheology of blood makes much of this non-applicable. Furthermore, the geometry is clinically significant as it represents a stenosed artery resulting from plaque buildup. A downside of this geometry in particular being chosen as a validation case is however that the presence of a stagnation point ensures that nearly all thrombus models will predict thrombus formation, as a thrombus will always form if there is a sufficient quantity of activated platelets

at a stagnation point. A more challenging and relevant case to reproduce would have been a sloped geometry or a graduation of converging-diverging nozzles.

#### Computational Domain and Boundary Conditions

The computational domain of the validation case consisted of a backward-facing step cut out from a cylinder, shown in Figure 20 below. A mass flow inlet (0.0159 kg/s) and zero-relative pressure outlet are set at the locations indicated by blue arrows. All other boundaries are set as no-slip boundaries. Thrombosis-relevant boundary equations are set as per Table 6.

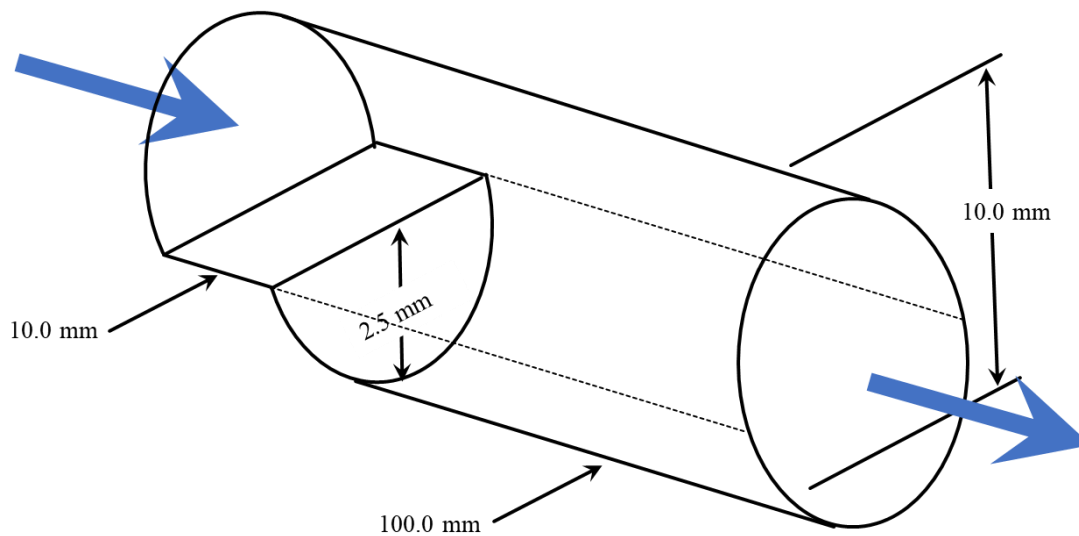


**Figure 20: Illustration of the computational domain of the validation case reproducing the test section of Taylor et al.<sup>342</sup> and Yang et al.<sup>384</sup>.**

The computational domain for the LVAD simulations, illustrated in Figure 21, consists of an open-hub inducer and rotor, a diffuser with an outer (primary) diffuser, and a secondary diffuser in the core region. This unique device is so named as it has an open-hub in the inducer and impeller regions, as well as two diffuser sections designed to deal with different parts of the flow. Uniform mass flow is specified at the inlet, ranging between [3-5 L/minute], and zero relative static pressure is specified uniformly at the outlet. No slip boundary conditions are specified at each of the grey surfaces, and a rotating reference frame is specified in the rotor region at a rotation between 2000-4000 RPM. The geometry, which was optimized previously to achieve the target pressure, allows us to vary rotor speed to produce the target pressure between 80-120 mm Hg (11-16 kPa).

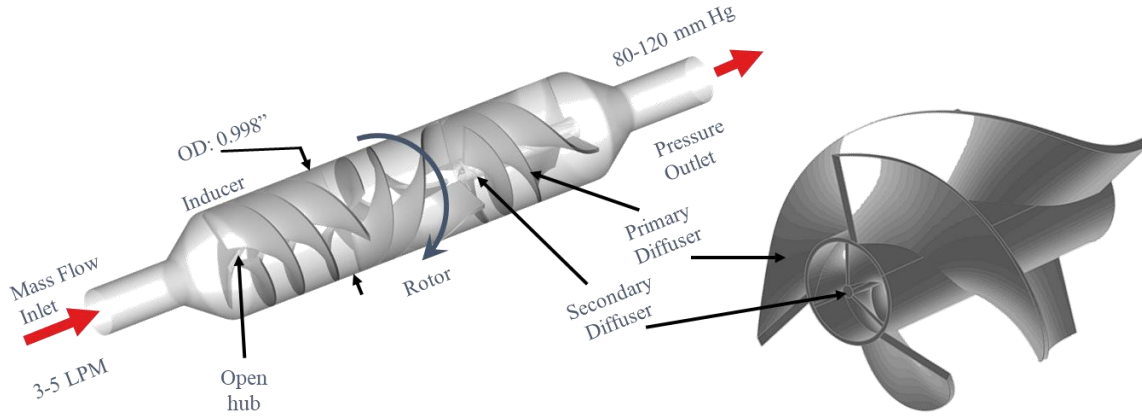


**Figure 21: Schematic Illustration of computational LVAD domain in which Thrombosis simulations are executed. The open-hub LVAD design is a novel LVAD developed at McGill.**

Validation simulations are performed to determine whether the model can reliably reproduce thrombosis in vitro. This is done by simulating thrombosis in a cylindrical 1 cm channel with a 2.5mm high notch cut forming backward-facing step, matching the test-section geometry of Taylor et al<sup>349</sup> measuring thrombus height, and length, and volume for bovine blood and Yang<sup>384</sup> for human blood. While it is tempting to attempt to reproduce the thrombus formation sites in explanted HM II Ventricular Assist Devices<sup>411</sup>, the need for precise physiological values for constituents in the thrombosis model such as platelet count precludes this analysis. Unfortunately, hemoglobin is not introduced into these experiments and flow conditions are insufficient to cause hemolysis.

The thrombosis model requires specific boundary conditions to be set at walls. In particular, face fluxes are specified at no-slip wall boundaries for  $P_{\bar{a}\bar{d}}$ ,  $P_{a\bar{d}}$ ,  $ADP$ ,  $TxA2$ ,  $PT$ ,  $T$ ,  $AT$ ,  $vWF$  to indicate their consumption at boundaries, whereas an ODE is solved at the boundary for  $P_{ad}$  so that the boundary is treated as a 2D element. The form of these boundaries is summarized in Table 6.

**Table 6: Boundary conditions used for thrombosis models.  $J$  indicates a flux boundary,  $C$  indicates a concentration boundary. Subscript  $W$  denotes values at the wall boundary.**

$C_i$	No-slip wall condition	Inlet $[C_i] / [C_i]_{t=0}$
$P_{\bar{a}\bar{d}}$	$J = -(k_{\bar{a}dep,W}^*)P_{\bar{a}\bar{d}}$	$3.0 \cdot 10^{14} [Plt\ m^{-3}]$
$P_{a\bar{d}}$	$J = -k_{a\bar{d},W}^*P_{a\bar{d}} + k_{emb,W}P_{ad,W}$	$3.0 \cdot 10^{12} [Plt\ m^{-3}]$
$P_{ad}$	$C = \int_0^t \left( (k_{a\bar{d},W}^*P_{a\bar{d}} + k_{\bar{a}dep,W}^*P_{\bar{a}\bar{d}}) - k_{emb,W}P_{ad,W} \right)$	0.0

<b>AT</b>	$J = -\Gamma\varepsilon[T]$	2.844 $\cdot 10^6 [nmol\ m^{-3}]$
<b>T</b>	$J = [PT](\psi_{at}([P_{a\bar{d}}] + [P_{ad}]) + \psi_{rt}([P_{\bar{a}d}] + [P_{ad}]))$	0.0
<b>PT</b>	$J = -\varepsilon[PT](\psi_{at}([P_{a\bar{d}}] + [P_{ad}]) + \psi_{rt}([P_{\bar{a}d}] + [P_{ad}]))$	$1.1 \cdot 10^6 [nmol\ m^{-3}]$
<b>ADP</b>	$J = \lambda_{ADP}(-J_{P_{\bar{a}d}}) + J_D^\beta \frac{Hct}{100\%} \frac{[ADP]_{RBC}}{M_{ADP}}$	0.0
<b>TxA2</b>	$J = s_{pj}([P_{a\bar{d}}] + [P_{ad}]) - k_1[TxA2]$	0.0
<b>D</b>	$J_D = \delta C^\beta \tau_w^\beta (1 - D)$	0.0
<b>vWF</b>	$J_{vWF} = \lambda_{ADP}(-J_{P_{\bar{a}d}})$	$3.7 \cdot 10^7 [nmol\ m^{-3}]$
<b>vWF<sub>ha</sub></b>	$J_{vWF_{ha}} = 0$	0.0

### Whole Blood Model

In the validation case, blood is approximated as a Newtonian fluid, which is not commonly done given the lower shear rate, but the choice is made because LVAD simulations also use a Newtonian approximation for blood,  $\mu_b = 0.0035 [Pa\ s]$ . Turbulence is not modelled in the validation case, as the Reynolds number (based on the tube diameter) is  $Re_D \sim 570$  and firmly within the laminar regime. Blood flow is considered incompressible, and density is set to the fixed value of  $1074\ kg\ m^{-3}$ .

In the LVAD case, as in the validation case, viscosity is Newtonian. Reynolds number in the LVAD varies between  $20 \cdot 10^3$  and  $40 \cdot 10^3$ . Turbulence in the LVAD case is modelled using the k-omega Shear Stress Transport formulation, with the Kato-Launder production limiter to reduce turbulence overproduction in stagnation zones. Although turbulence is modelled in this analysis to obtain the appropriate fluid physics and momentum transfer, following the discussions in sections 2.2.1 and 2.4.4 regarding the effect of turbulence on hemolysis and platelet activation, in the hemolytic formulation, the eddy viscosity is omitted when computing the von-mises stress, whereas it is included when computing platelet activation. This was done to reflect the relative insensitivity and sensitivity, of hemolysis and platelet activation, respectively, to the Reynolds stress.

### Numerical Solution Scheme

Thrombosis simulations use the SIMPLE scheme for pressure-velocity coupling due to the ability to attain good parallel scaling while maintaining a relatively high timestep. The bounded second-order implicit temporal discretization is used to advance the simulations in time, and relaxation factors for the pressure and momentum are set to 0.5, to increase convergence speed,

and all others are set to 1. The Second-order upwind scheme is used for momentum discretization, and for all user-defined scalar transport equations. The 4<sup>th</sup> order PRESTO! scheme is used to discretize the pressure (i.e.. mass) equation and eliminate grid-collocation induced checkerboard-shaped. A V-shaped algebraic multigrid scheme is used, which is standard for ANSYS Fluent. The second-order upwind scheme is used for turbulence kinetic energy, and for the specific dissipation rate.

#### Computational Grid

The fluid volume in the computational domain is broken down into small finite-volume cells using ANSYS Fluent Meshing software. A polyhedral element mesh is used for this case. Polyhedral cells have several advantages relevant to our case. Firstly, the increased number of faces of each cell means that the linearized solution matrix is wider, thereby increasing stability and reducing dependency on mesh quality to make the solution stable. Secondly, as gradients are computed using the node-based approach, the increased connectivity due to the high number of faces means that more elements are used in the computation scheme resulting in smoother gradient approximations. The overall result is that a higher quality solution can be achieved at reduced computational cost.

Grid spacing is generally limited by the size of the smallest scale that needs to be resolved. Property gradients in the case of thrombosis are highest at the walls and at the thrombus interface. At walls, the shear-dependant diffusion rate of platelets means that platelet concentrations vary on the order of the shear rate, and thus the first element near the wall should resolve the viscous sub layer (*ie*:  $y^+ \ll 10$ ).



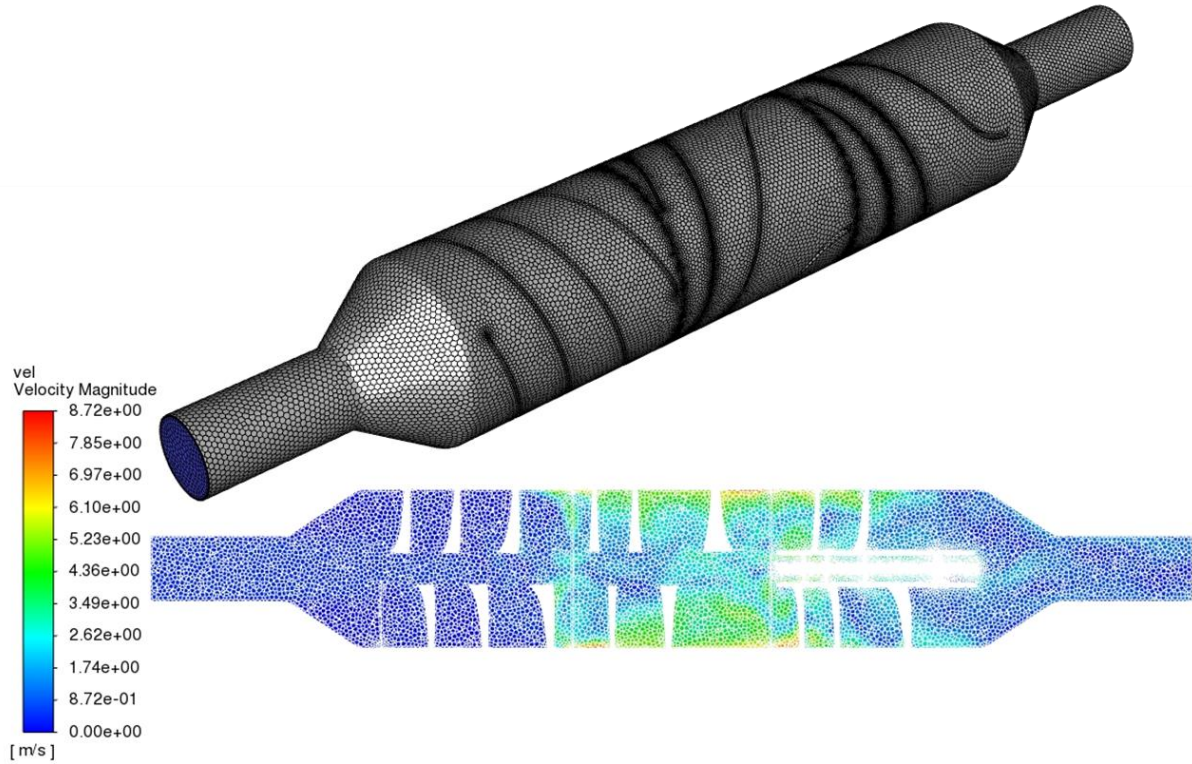


**Figure 22: Final computational grid selected to execute blood clot in the LVAD case (maximum and minimum grid spacing and inflation layer values are 0.75 mm, 0.05 mm, and 5, respectively).**

### Initialization

Pressure is initialized with zero average gauge pressure throughout the entire velocity field, whereas velocity is initialized with zero relative (to the local reference frame) tangential velocity, zero absolute radial velocity, and axial velocity equal to the volume flow rate divided by the inflow area. Initial conditions for each of the biochemical species in the thrombosis model are the same as concentrations specified at the inlet and are given in Table 6.

### Timestep and Pseudo Multiscale Treatment

The process of thrombosis is quite complicated as it includes physics that occurs over a wide range of spatial and time scales. In the continuum approach, nano and microscale interactions are modelled, which encompasses the wide range of physics and assumptions discussed above but greatly simplifies this. As thrombosis is however a fundamentally transient process there remains the issue that many processes occur still occur over different timesteps. The fluid mechanics generally scale with the convective courant number, which for our chosen mesh that adequately resolves the wall shear stress at the walls of the MCS from a hydrodynamic perspective, has a time scale on the order of 10-100  $\mu$ s, Thrombosis occurs much more slowly than this; the reaction rates of the platelet activation and kinetics of thrombin

conversion have timescales on the order of 10-100 ms to produce significant changes to concentration in time. The slow adhesion rate of platelets, embolization, and fibrin polymerization on the other hand have timescales on the order of minutes to hours, leading to a fundamental challenge as typically the simulation must run at the slowest timescale.

In the present work, this is addressed by adopting a pseudo-multiscale approach where different advection-diffusion-reaction (ADR) equations are solved with different time-steps. To achieve this, acceleration factors are used for the adhered platelet phases, as well as for the vWF and vWF<sub>ha</sub> equations, as both equations have very long convergence times. Fluxes at the boundary of each cell and source terms for these equations are multiplied by the scaling factor to simulate a higher timestep. This is possible because we have generally linear or weakly nonlinear interactions between the various ADR equations so that the fluctuating components of the fast equations have a small contribution to the slow equations. The most nonlinear term in the ADR equations is the interaction with fluid velocity. This is dealt with in two ways. In the case of adhered platelet equations,  $P_{ad}$ , there are no advective terms, and so it is only the source term is scaled. This is convenient as it eliminates the nonlinear coupling between the fastest and slowest equations, the evolution of the flow and platelet adhesion, and allows for a high scaling factor for the adhered platelet equations. From the perspective of the flow, the thrombus growth process occurs so quickly that any unsteady contribution to momentum from the growing thrombus surface, for example is minimal compared to inertia or viscosity. On the other hand, the hemolysis and vWF equations are also sped up, though with a smaller factor. This is possible because in general the flow is allowed to reach a steady state before turning on the hemolysis or thrombosis models. As velocities do not fluctuate appreciably from their mean values, the effect of the unsteady advection equation on hemolysis is minor. This is another reason why a steady flow is chosen, in the case of a pulsatile flow, this becomes far more complicated.

Non-adhered platelet equations and agonist equations are in general not scaled as they reach a quasi-steady state within the total simulation time (1-10 s). As a rule of thumb, the scaling factor for equations that have a large degree of interconnection and nonlinearity, such as those of von-Willebrand factor (vWF), hyper-adhesive vWF, and hemolysis index should be grouped together and be identical for stability purposes. Unless otherwise noted, the time-scaling factors for vWF conversion and hemolysis is 25, whereas the time-scaling factor for adhesion is 100. All other equations have time-scale factors of 1. Because of these points, it was elected not to implement more complicated multi-timescale bridging techniques, which is

left for future work. A time-scale factor sensitivity analysis was conducted and is shown in Appendix A.

It was found that adhesion could be scaled up to 500x the timestep of non-adhered platelets due to this fact without affecting the results or solution stability. In the case where advection cannot be neglected for adhered platelets (where platelet slipping and embolus detachment are considered), it becomes necessary to use operator splitting to separate the slow adhesion processes (on the order of minutes) and fast embolus detachment processes (on the order of seconds), this was also not done presently as it added substantial complexity. Furthermore, time-scale sensitivity analysis for activated platelets and agonists was conducted and found that platelets could run up to 10x the speed of the flow without affecting the results.

The selection of the flow timestep is also an important consideration in the simulation of thrombosis. In this model, the flow timestep was chosen based on the maximum Courant number, with a value of  $C = 35$  being selected. This value is within the acceptable stable region for implicit finite-volume schemes, and indeed a timestep sensitivity analysis revealed that the results do not change appreciably for  $C < 50$ . The Courant number is a dimensionless parameter that indicates the ratio of the numerical timestep to the characteristic time of the problem. The baseline timestep of flow equations for the validation simulations is 1 ms, and 0.5 ms for all LVAD simulations.

Overall, the effective timestep and time scaling factors play a crucial role in the accuracy and efficiency of the continuum model and simulation of thrombosis using the finite volume method. By carefully selecting the appropriate timescales and using acceleration factors for adhered platelet phases and platelet agonists, the model can accurately capture the spatiotemporal dynamics of thrombus growth and platelet recruitment under various flow conditions. The selection of an appropriate flow timestep based on the maximum Courant number also ensures that the numerical solution is stable and accurate.

### **3.3.10 Objectives and Executed Test Cases**

Due to these assumptions, the treatment of fHb-induced hyperadhesion is flawed and in need of refinement. It is however argued that the effect of hemoglobin on thrombosis is sufficiently captured to establish the relative importance of the Hb-vWF interaction and the relative importance of hyper-adhesive vWF in MCS. The purpose of this analysis is then to determine if a relative increase in vWF bonding rate on a scale that is physically realistic is a determining factor in whether thrombogenesis occurs in MCS.

*Table 7: Summary of thrombosis simulations executed*

Case	Parameters varied	Objective
<b>Thrombus Growth with Backward-facing Step</b>	N/A	Validation against in-vitro data
<b>Grid Convergence Analysis</b>	Maximum Cell Length, Minimum Cell Length, Number of Inflation layers	Verification
<b>Baseline Thrombus formation in MCS</b>	Rotor speed = { 1.5,3,4.5 } $10^3$ RPM Inflow rate { 4.5 } LPM	Thrombogenesis in MCS varying input flow rate and RPM
<b>effect of Hb-induced adhesion</b>	Hyperadhesion on Hemolysis-induced ADP release model off Rotor speed = { 1.5,3,4.5 } $10^3$ RPM	Model effect of Hb Release on thrombosis
<b>Effect of hemolytic ADP release</b>	Hyperadhesion off ADP release from hemolysis ON	Examine the effect of ADP release only
<b>Effect of combined hemolysis and thrombosis effect</b>	Hyperadhesion / ADP release ON Rotor speed = { 1,2,3,4 } $10^3$ RPM Inflow rate { 3-5 } LPM	Examine the effect of the combined effect
<b>Effect of Geometry Thrombosis on hemolysis</b>	Rotor speed = { 1,2,3,4 } $10^3$ RPM Simulation end time – 10 minutes thrombus time, 6 s, flow simulation	Examine parameter sensitivity to thrombosis

Due to these assumptions, the results of hemolysis modelling integration should be interpreted as qualitative until validation of the treatment can be done with experimental data. This was planned but constraints regarding obtaining lab space led to several delays in these experiments. To accomplish the objectives in this work the test cases shown in Table 7 below are executed, and the results are presented in the subsequent section.

## Chapter 4: Results

---

### 4.1 Simulation of Red Blood Cell Membrane Mechanics in Couette Flow

In this section, a series of Full Eulerian Fluid-Structure Interaction simulations are carried out on the mechanics of intercellular collisions between red blood cells at a range of shear rates and hematocrit values, as detailed in Section 3.1, using ANSYS Fluent 22R1. The primary objective is to verify and validate our computational approach. To achieve this, a grid convergence analysis is conducted by refining the mesh at the interface with the adaptive grid refinement features available in ANSYS Fluent. Additionally, two validation cases are performed: one that aims to reproduce the shape of the red blood cell observed experimentally in a cylindrical microchannel with a diameter on the order of the red blood cell, and another that replicates the optical tweezers red blood cell stretching experiments conducted by Mills et al.<sup>207</sup>. The results demonstrate a good overall agreement with the validation cases.

Following the verification and validation process, the deformation, and mechanics of a single cell in a Couette shear flow are investigated. In this section, linear and area strain averaged over the membrane are analyzed, as well as maximum and minimum area strain, varying with shear rates between  $900 \text{ s}^{-1}$  and  $45,000 \text{ s}^{-1}$ . Computing parameters of mechanoporation at each shear rate, the distributions of nanopore density and average radius are presented to illustrate these distributions. The hemoglobin diffusion coefficient is calculated, and average and maximum area strain is fit against the shear rate, providing the diffusion coefficient as a function of shear rate.

Finally, to satisfy the first objective, the impact of red blood cell collisions on membrane strain and sublethal hemolysis is examined. The effect of viscoelasticity during cellular collisions is also examined briefly. Lastly, the influence of hematocrit and red blood cell packing on the average area strain experienced by red blood cells at high shear rates is examined, as well as the corresponding differences in dynamics.

#### 4.1.1 Verification and Validation of the Computational Method

##### Grid Sensitivity

As in the present study, an adaptive grid refinement strategy is employed, and grid sensitivity is evaluated by using successively higher refinement levels until a satisfactory compromise has been reached between the error is relatively low compared to the increase in computational cost. Figure 23 shows the strain distribution of the two and three refinement level cases at peak stretch, where  $t\dot{\gamma} = 10$ . Note that the RBC membrane is depicted as an isosurface at a

cytoplasmic volume fraction of 0.5, and all subsequent RBC membrane images are constructed in this manner. The membrane-averaged area strain is compared in Figure 24.

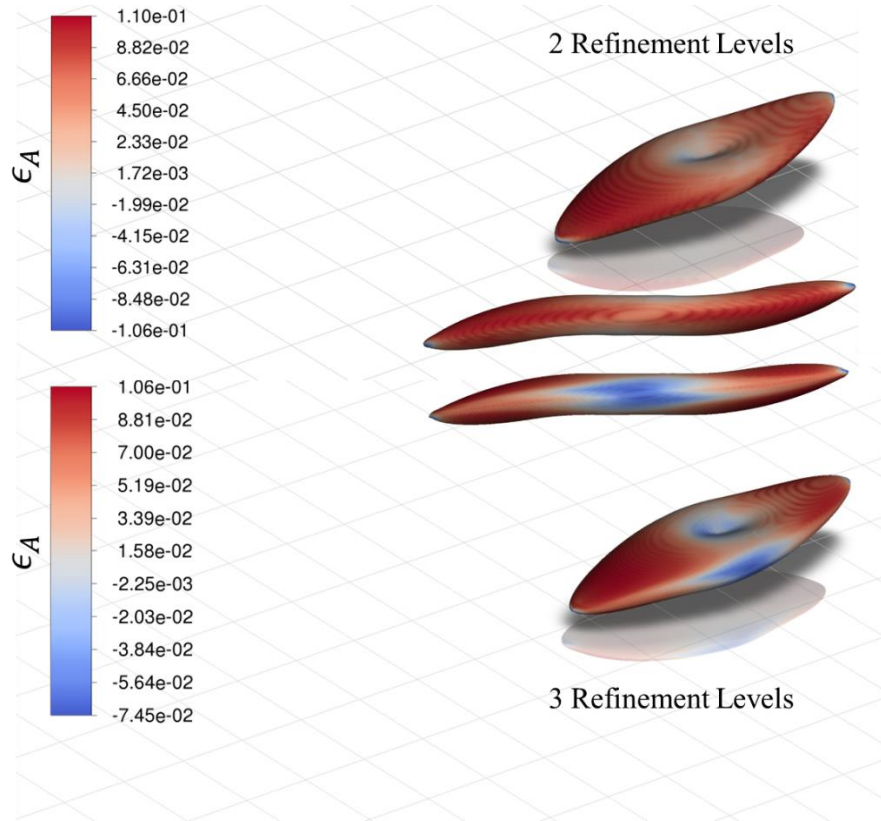


**Figure 23: Comparison of area strain distribution at peak stretch ( $t\dot{\gamma} = 10$ ) for the 2 and 3 refinement level cases, where mesh spacing corresponds to 125 nm and 62.5 nm.**

It is found that in the present study, this optimum point is found with two grid refinement levels. This resolution corresponds to half the resolution used by Takagi et al.<sup>152</sup>, in their simulations using the same model. One key difference here is that the strain rates examined are much higher, and thus result in much higher strain. It is noted that there are appreciable differences between the area strain measured, on the order of 1% average area strain, and in particular the minimum strain is significantly lower at extreme stretch cases, as is seen in Figure 23.

In the present study, this optimum point is found with two grid refinement levels. This resolution corresponds to half the resolution used by Takagi et al.<sup>152</sup>, in their simulations using the same model. One key difference here is that the strain rates examined are much higher, and thus result in much higher strain. From Figure 24 it is noted that there are appreciable differences between the area strain measured, on the order of 1% average area strain, and in particular the minimum strain is significantly lower at extreme stretch cases, as is seen in Figure 23. On the other hand, approximately 0.87 and 2.70 million elements are used in the two and

three-refinement level simulations, respectively, indicating approximately factor of 4 increase in computational cost. As the increase in elements with increased shear rate and number of RBCs is polynomial, and because for the sake of consistency, it is necessary to use the same number of elements for all cases, it is elected to use two refinement levels, as this achieves sufficiently low error in average strain while not being prohibitively computationally expensive.

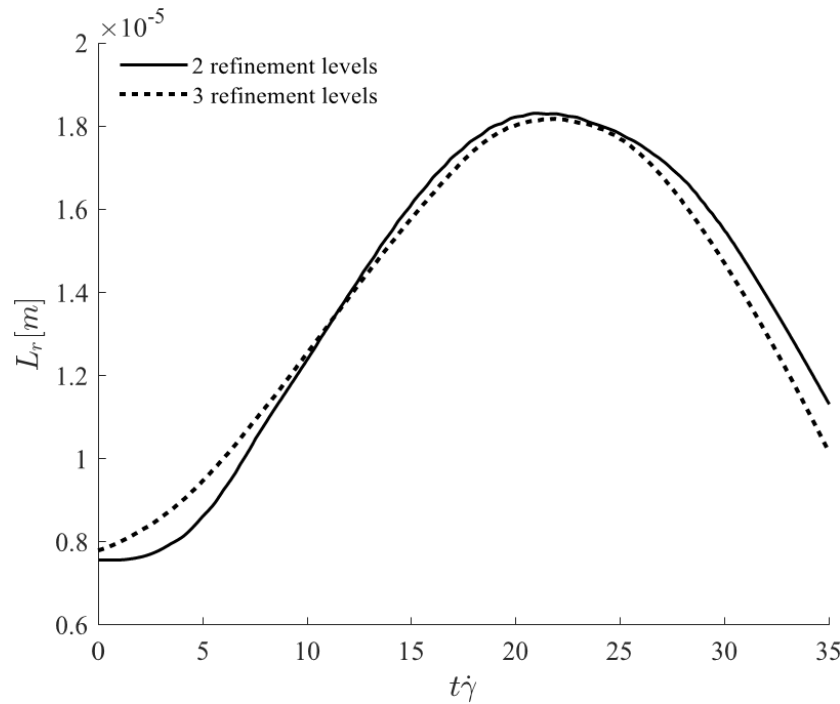


**Figure 24: Comparison of RBC length at shear rate of  $20,000 \text{ s}^{-1}$  using 2 adaptive grid refinement levels adaptive mesh and 3 refinement levels.**

#### Validation of Computational Method

To verify the computational approach employed in the study, it was sought to reproduce two canonical red blood cell experiments. The first validation task involved examining whether the fully Eulerian structural membrane model could accurately reproduce the parachuting shape of the RBC in a cylindrical microchannel that simulates the microvasculature. This task proved to be challenging due to the presence of a Hagen-Poiseuille flow in the microchannel, where the shear rate varies from  $0 \text{ s}^{-1}$  at the center to nearly  $20,000 \text{ s}^{-1}$  near the walls. Capturing the shape accurately required the mechanical model to effectively reproduce the red blood cell membrane elasticity across the entire range of shear rates. Initial attempts using the membrane material models of Skalak<sup>200</sup> and Mills et al.<sup>207</sup> revealed that the red blood cell membrane would stretch indefinitely at higher shear rates, as the model did not possess sufficient elasticity to accurately represent the membrane. The original 3rd-order hyperelastic Yeoh model

proposed by Mills et al. did not incorporate area elasticity. Thus, the area strains, which were not constrained could exceed 50-60%, far beyond any known measurement of RBC area strain. Thus, an additional task was to ensure that, at these high shear rates, the overall area strain did not surpass the 23% theoretical threshold computed from the actin-fibrin dissociation derived from Li et al.<sup>212</sup>. As shown in Figure 25, the steady-state shape of the red blood cell membrane under the experimental conditions described by Tomaiuolo et al.<sup>398</sup> was well captured by the fully Eulerian FSI model, which successfully reproduces the canonical parachuting shape. By extracting a spline at the leading edge of the shadow graph and subtracting it from the volume fraction isosurface, the RMS error was calculated to be approximately 4.61%, which was considered satisfactory.

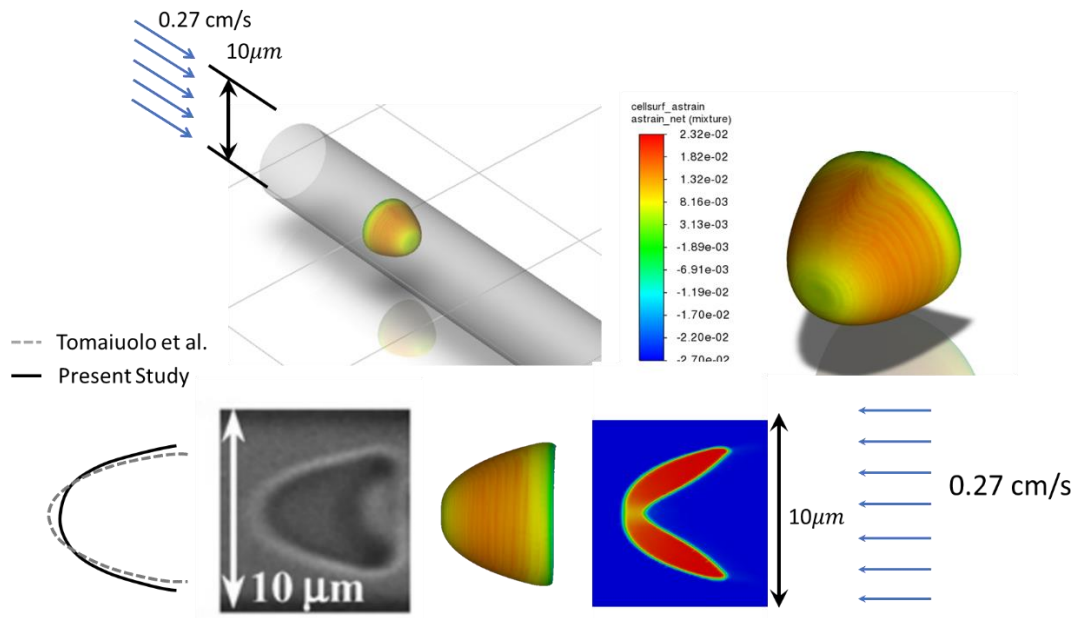


**Figure 25: Steady-state parachuting and comparison with Tomaiuolo et al.<sup>398</sup>.**

Furthermore, simulation results are compared with the optical tweezers experiments conducted by Mills et al.<sup>207</sup> in Figure 26. Simulations were executed, and the total stress was computed by integrating the shear stress over the red blood cell membrane. At peak extension (shown in Figure 26 at the bottom), which occurs after initializing the simulation with an RBC whose mean axis is  $45^\circ$  from the horizontal, the length and force were recorded and plotted. In Figure 26, it can be observed that the peak lengths of the red blood cells at the integrated shear stress align well with the optical tweezers experiments of Mills et al.



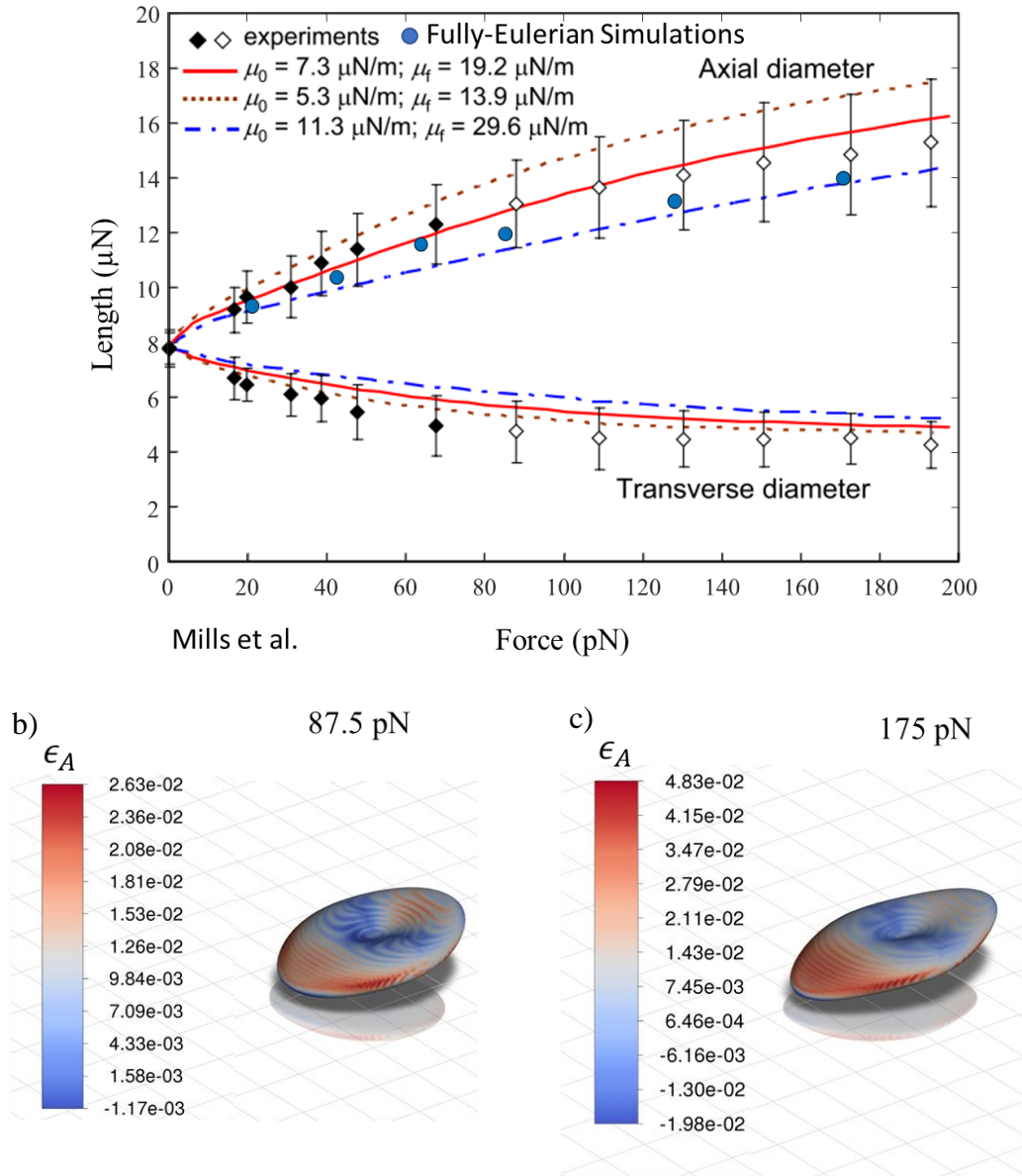


**Figure 26: Quantitative comparison a) of the length of an RBC stretched by shear in the present simulations at peak stretch (blue dots), with the optical tweezers experiments of Mills et al.<sup>207</sup> (black and white diamonds). The shape of the red blood cell at peak stretch shown for a total applied force of b) 87.5 pN and c) 175 pN.**

This result is not surprising, considering that in the present work, the Yeoh hyperelastic model developed by Mills was modified by adding higher-order terms in such a way that their contribution at low shear rates is minimal. The simulation results attain similar lengths at the various forces applied by Mills et al. during their experiments, and are within their experimental error bars, though the present model (shown in Equation 3-37) tends to be more stiff, due to the higher order terms that are functions of both  $I_s$  and  $II_s$ , and the choice of using the surface rather than volumetric invariants for these terms shown in Equation 3-37. Although not shown in Figure 28, the length of the red blood cell between shear rates of  $20,000 \text{ s}^{-1}$ –

$45,000 \text{ s}^{-1}$  reaches a threshold at approximately  $18\text{-}19 \text{ }\mu\text{m}$  due to the high-order terms added by the present material model. Furthermore, the red blood cell shape achieved at the  $175 \text{ pN}$  and  $87.5 \text{ pN}$  force levels is qualitatively similar to what was observed by Mills et al. in their experiments and FEA simulations. These comparisons provide further evidence of the validity and reliability of the computational approach used in the present work.

#### **4.1.2 Effect of Shear Rate on Strain and Sublethal Hemolysis for Dispersed Cellular Flows**

In this section, the results of single-cell Couette flow simulations wherein the shear rate is varied are presented, and the dynamics of the red blood cell in the shear flow are observed and described. The simulation runs for a sufficient period for the red blood cell shape to appear steady or for the length to reach a steady or statistically steady (i.e.... periodic) state. Time is normalized by the shear rate, so that if a blood cell is in the upper half of the domain, approximately 10 normalized time units are required for a red blood cell to pass through the length of the domain. Figure 27 and Figure 28 showcase iso-surfaces of cytoplasmic volume fraction of  $\phi_c = 0.5$ , representing the red blood cell membrane, and are coloured by contour plots of area strain computed from the second invariant of the left Cauchy deformation tensor,  $B_S$ , as shown in section 3.2.2.

The extents of the contour plot scale correspond to the global maximum and minimum area strain computed over all red blood cells at the instance in time shown in the figure; the maximum and minimum strains at the corresponding times are shown subsequently. Future figures illustrating the red blood cell membrane use this format.

Initially, the red blood cell is stretched as if being pulled in tension along the major axis of the shear stress tensor, extending to its full length. Gradually, as the red blood cell tips forward, the upstream end shifts into the opposite direction stream, and the extended red blood cell begins to contract in length, also shown in Figure 27. This contraction is the result of elastic recoil from the membrane and results in the skin of the red blood cell starting to wrinkle (or buckle in shear) due to the elastic response to the sudden contraction. Following this contraction, depending on the shear rate, the RBC either continues to tumble or goes into a steady tank-treading motion. Such wrinkling has been observed in simulation in complex tumbling-swinging regimes by Omori et al.<sup>130</sup>, for example.

At the lowest shear rates executed, between  $600\text{-}4820 \text{ s}^{-1}$ , the red blood cell experiences a transitional state between tumbling and tank-treading. The membrane deforms increasingly

with increasing shear rate, and at each turn, as the RBC is aligned with the shear axis, the membrane extension increases. Meanwhile, as the shear rate increases, the period of tumbling also increases. At approximately  $10,000 \text{ s}^{-1}$ , this extension is sufficient that the membrane cannot recover quickly enough during the tumbling period and the membrane is fully tank treading.

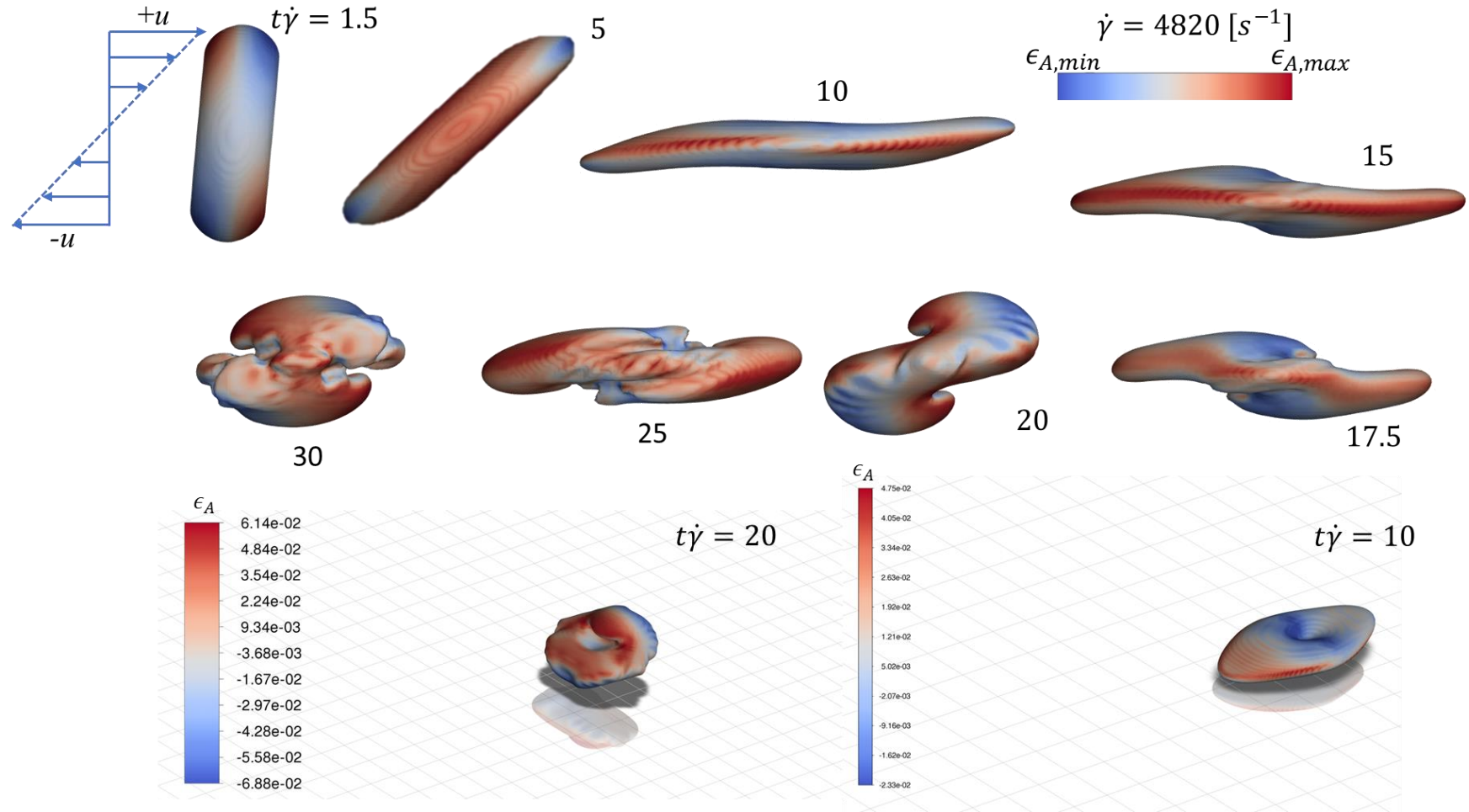


**Figure 27: Dynamics of complex tumbling at  $4800 \text{ s}^{-1}$ . The RBC vacillates between successive phases of tumbling and tank treading, being stretched out when aligned with the shear axis, and then contracted when perpendicular to it as the RBC rotates.**

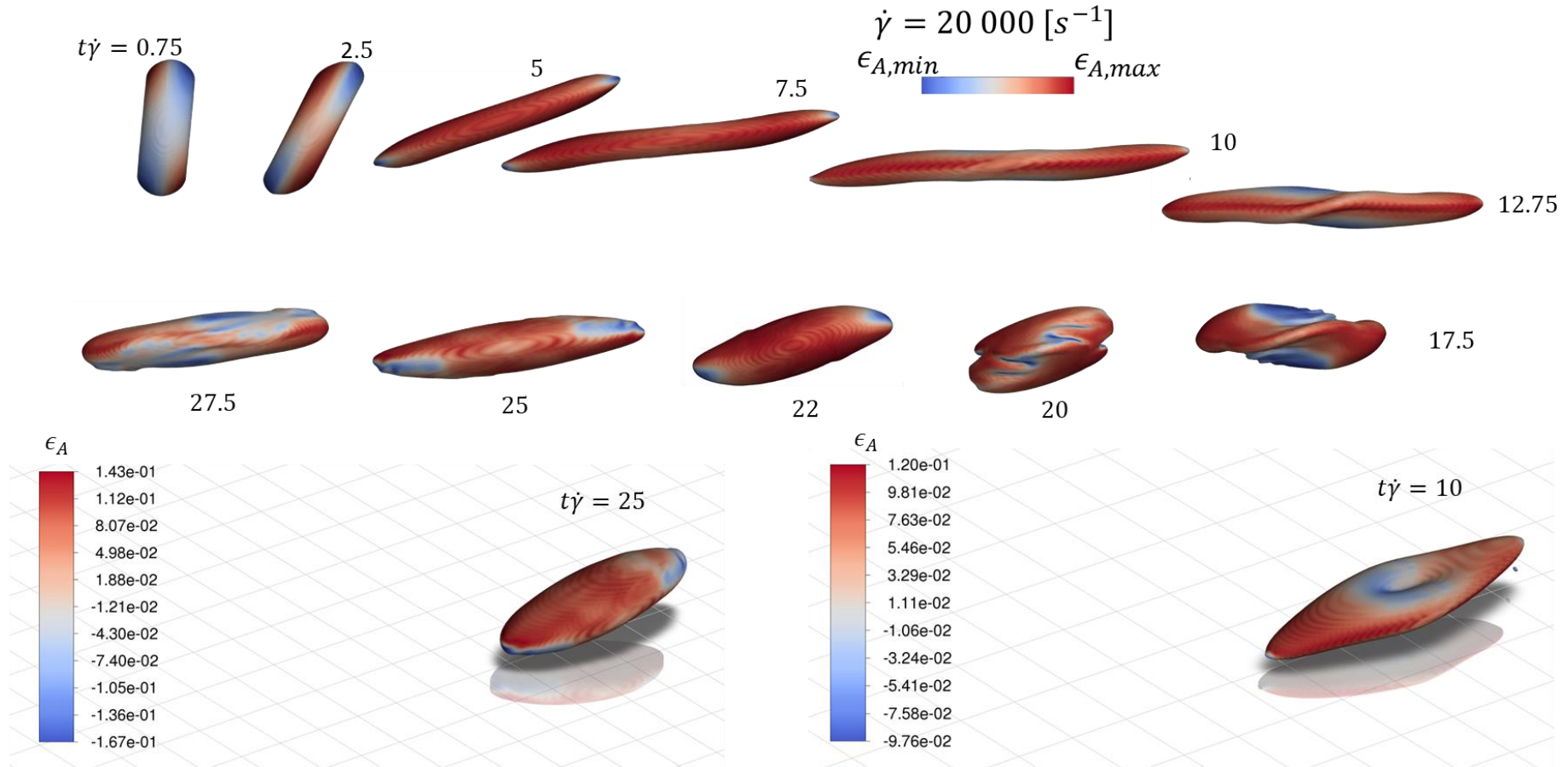


**Figure 28: Dynamics a RBC during tank treading at  $20\,000 \text{ s}^{-1}$ . RBC membranes are coloured by area strain,  $\epsilon_A$ , scaled by maximum and minimum values. Following peak extension, convection into the opposing stream causes membrane contraction and wrinkling, or shear buckling. Wrinkling events are associated with contraction and high local peaks of contractile stress.**

The tank-treading RBC at  $20,000 \text{ s}^{-1}$  is visualized in Figure 28. Although the membrane is in a steady tank-treading motion, the RBC length varies periodically between phases of recovery and extension, resulting in transient wrinkling during contraction. The shape parameter,  $D$ , which gives a normalized aspect ratio in terms of deformed Length,  $L$ , and RBC height,  $H$ , describes the ratio of the major and minor axis of an ellipsoid and is used by Arora et al. to infer the average area strain of the ellipsoidal droplet<sup>7</sup>:

$$D = \frac{L - H}{L + H} \quad 4-1$$

and presented in Figure 29 for lower shear rates and Figure 30 for higher shear rates. A distinction is made between lower and higher shear rates because the dynamics of the red blood cells change significantly after  $4,820 \text{ s}^{-1}$ . Due to the complexity of the RBC dynamics, particularly during the initial stretch stage, there is a good correspondence between the shape parameter and average strain. However, this correspondence is not observed for maximum strain. During contraction phases, the membrane often experiences wrinkling, due to the lack of bending moments in the model employed.

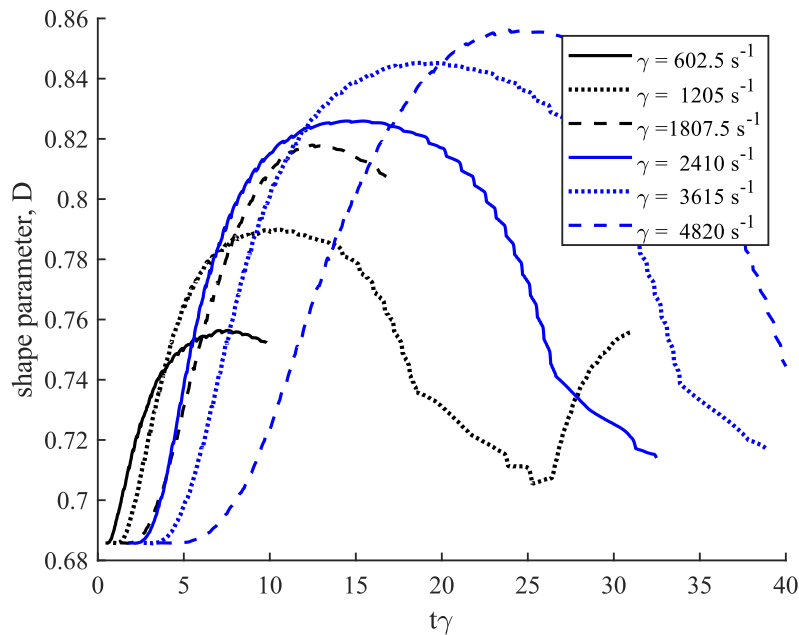


**Figure 29: Evolution of Shape parameter over time for a single red blood cell in a Couette shear flow in the tumbling and pseudo-tumbling dynamic regime.**

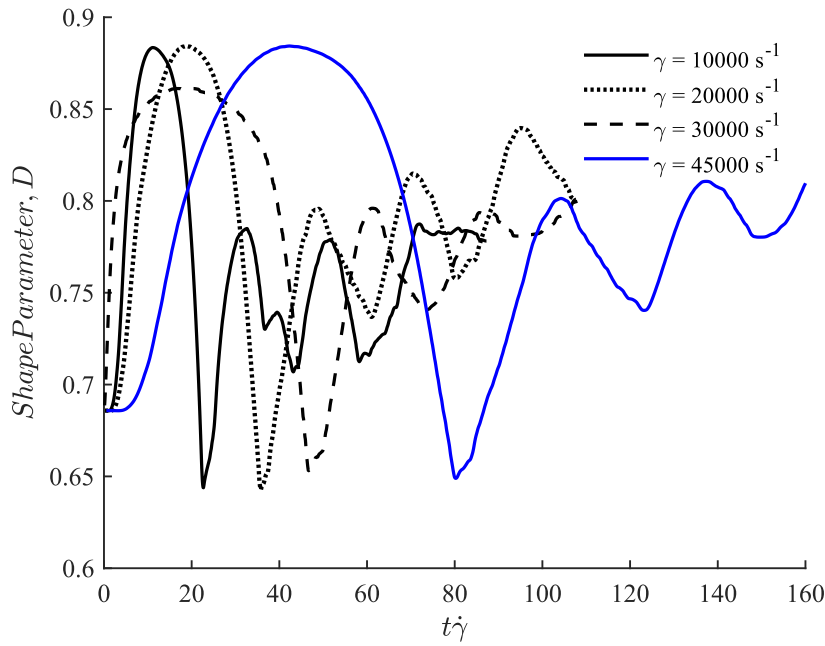


**Figure 30: Evolution of shape parameter over time for a single red blood cell in a Couette shear flow in the tank-treading dynamic regime.**

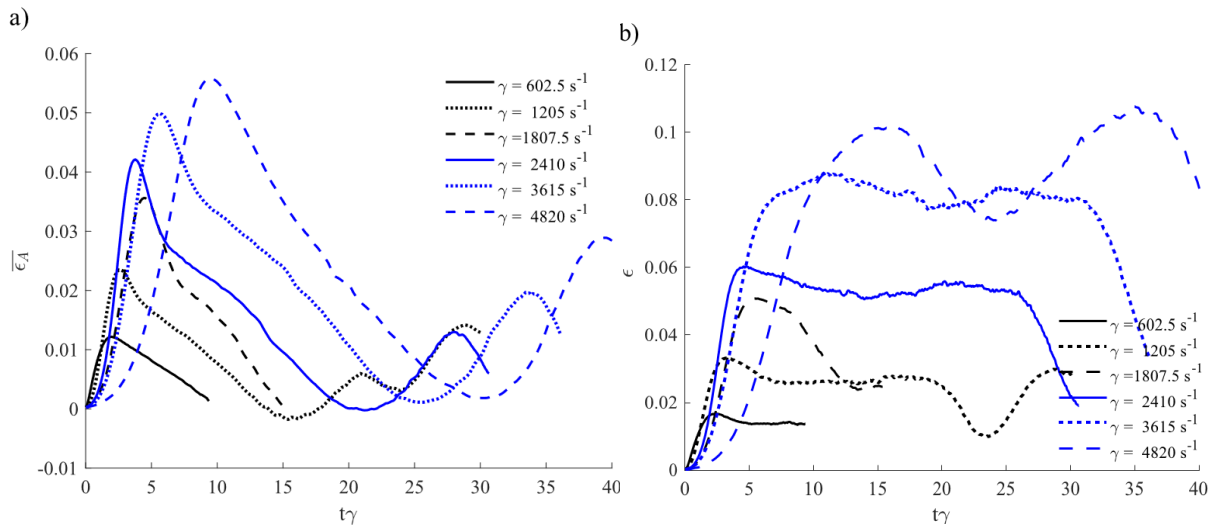
The result is rather unpredictable strain patterns due to the local concentrations present in such a complex structural process. As a result, it can be observed in Figure 32 that although the average strain extension and area strain decrease with the contraction phase, the maximum area strain remains quite high due to the wrinkling effect of the red blood cell membrane during contraction events. This has interesting and severe consequences for lethal and sublethal hemolysis, as the contraction phase can generally be triggered by collisions or flow deceleration, as is common in turbulent flows, pulsatile flows, or situations of flow separation.

It should be noted, however, that as bending moments in viscoelasticity are not included in the formulation used in this work, the actual degree of wrinkling may be significantly reduced in the real RBC membrane. Furthermore, as viscoelasticity is not modelled, the contraction process would likely be much slower, in which case it is unknown if wrinkling is an issue. These aspects are beyond the scope of the current work and are left for future investigation. As will be demonstrated later, the collision events induce wrinkling in both regular and viscoelastic cases due to the high shear imposed on the membrane when cells collide.

Figure 31 shows the variation of membrane-average area strain and uni-axial strain over time at lower shear rates. At lower shear rates, the membrane alternates between contraction and extension phases as the RBCs tumble. For clarity, one extension contraction phase is shown in



the figure for each shear rate. Strain initially increases linearly but begins to plateau near the 6% area strain limit imposed by the stiffening membrane.



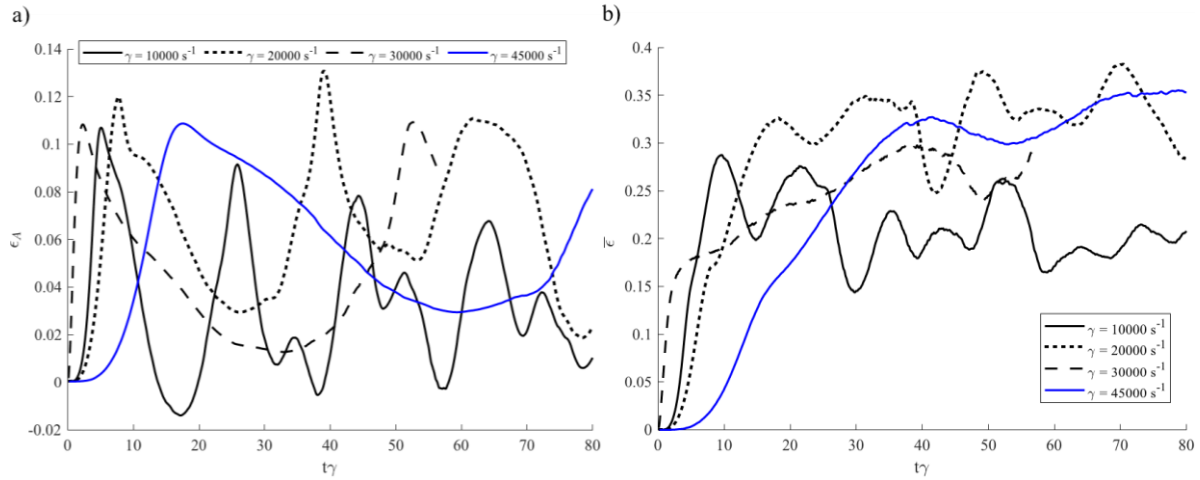
**Figure 31: Time variation of membrane-averaged a) area and b) uni-axial strain at shear rates in the tumbling and pseudo-tumbling regime in a Couette shear flow.**

Figure 32 presents the (linear and area) strain averaged over the membrane (membrane-averaged) at each point in time at higher shear rates; several key observations can be made. Firstly, it should be noted that the period of the strain oscillations seems to extend with increasing shear rate. This is because time is normalized by shear rate, as in general it was expected that the frequency of the collision dynamics scales with the shear rate. The period of oscillation is constant in the single-cell cases irrespective of the shear rate. These oscillations result from the natural tendency of the elastic-viscous-inertial system of the fluid-membrane to vibrate, which is generally independent of the force magnitude or load application rate. As viscoelasticity is not modelled in the single-cell cases, the settling time and or period of oscillation would likely be much longer in actual cells. The relaxation time of the viscoelastic simulation (on the order of 0.1-0.2 s) would result in excessively long simulation times, as the timestep for the  $45,000 \text{ s}^{-1}$  case was  $0.1 \mu\text{s}$ , a viscoelastic case would require approximately 32 days of simulation time on 48 cores. These long simulation times were one reason why viscoelasticity was not modelled in the single-cell cases as an extensive analysis is prohibitively time-consuming.

Interestingly, as the shear rate increases, the maximum area strain does not exceed the 23% maximum area strain threshold proposed by Xu et al, even at  $45,000 \text{ s}^{-1}$ , based on the idea that at this area strain the actin-spectrin connection begins to dissociate. This was somewhat unintended, as the high-order material model coefficients were set to try to ensure that average



area strain was approximately 6.4% at rupture, which begins at 42,000-45,000  $s^{-1}$ , which required  $C_7$  stiffness coefficients in Equation 3-37 that limited maximum area strain at approximately this level. The minimum area strain mirrors the maximum area strain, though overall it is lower.



**Figure 32: Time variation of membrane-averaged a) area and b) uni-axial strain at shear rates in the tank-treading regime in a Couette shear flow.**

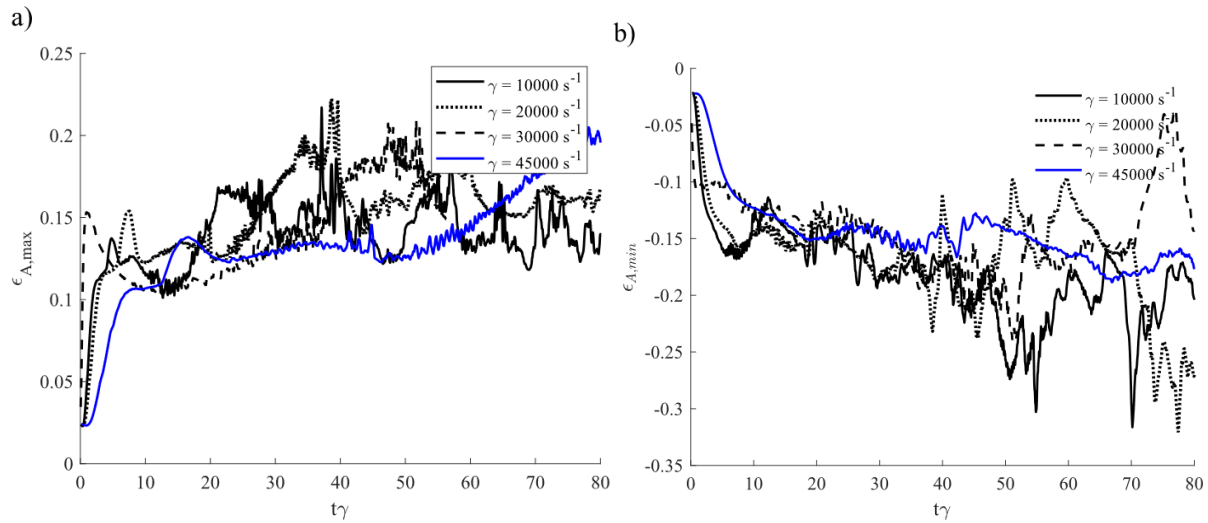


**Figure 33: Time variation of a) membrane-maximum and b) membrane-minimum area strain at shear rates in the tank-treading regime in a Couette shear flow.**

Figure 34 presents time-averaged area strain, maximum area strain, and uni-axial strain as a function of shear rate. The averaging process is done over a period between the first and last full period (measured as peaks) of membrane-averaged area strain. It should be noted that in the 45,000  $s^{-1}$  case, only one peak was captured, and a good average was not obtained. It was found generally that each parameter had a threshold behaviour, due to the stiffening effect of the high-order terms present in the material model, and thus this is expected. The elastic

behaviour was captured well by an exponential function, which was chosen so that it is possible to approximate the system as a linear elastic mass damper system and extract parameters from the fit. Coefficients were chosen to minimize the square of the error using a Newton-Raphson solution process. Exponents are chosen to maximize the fit, selecting 1, 0.5, and 1.5 for area strain, maximum area strain, and average uni-axial strain, respectively.

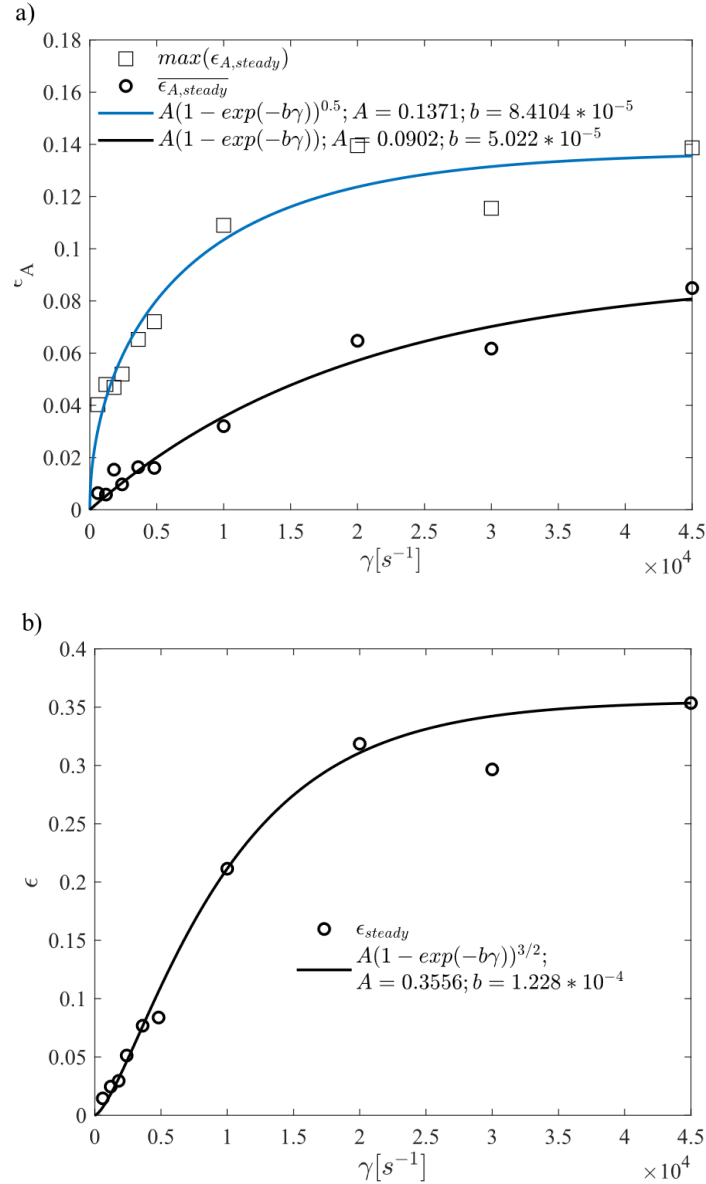


**Figure 34: (a) Membrane-averaged and membrane-maximum area strain and (b) membrane-averaged strain time averaged at dynamic steady state.**

The maximum steady value of average area strain is between 6-8%, though the fit amplitude coefficient implies an ultimate threshold of 9%, whereas the maximum time-averaged peak membrane strain is approximately 14%. Similarly, uni-axial strain has a steady-state time-

averaged value of approximately 35%. Average area strain and maximum area strain generally reach peak values between 10,000 and 20,000  $s^{-1}$ .

Pore diameter and pore density distributions are shown in Figure 35 and Figure 36. Figure 35 and Figure 36 show the pore diameter and density distribution at peak stretch and during steady tank treading, at the shear rate of 20,000  $s^{-1}$ . Using the probability of pore formation from Koshiyama and Wada<sup>270</sup>, imposing a critical strain for pore formation, and a minimum radius for diffusion, results in a kind of threshold for sublethal hemolysis. Effectively, transmembrane hemoglobin diffusion begins to occur after 6% local area strain, which means that at shear rates below 5,000  $s^{-1}$  the load applied on the cell is insufficient to cause significant transmembrane hemoglobin diffusion in the single-cell case. Consequently, nanopore formation occurs primarily on stretched extremities of the RBC membrane. Furthermore, at moderate shear rates, even if nanopore formation does occur, the diffusion coefficient is limited because only a relatively small blood cell area is porous.

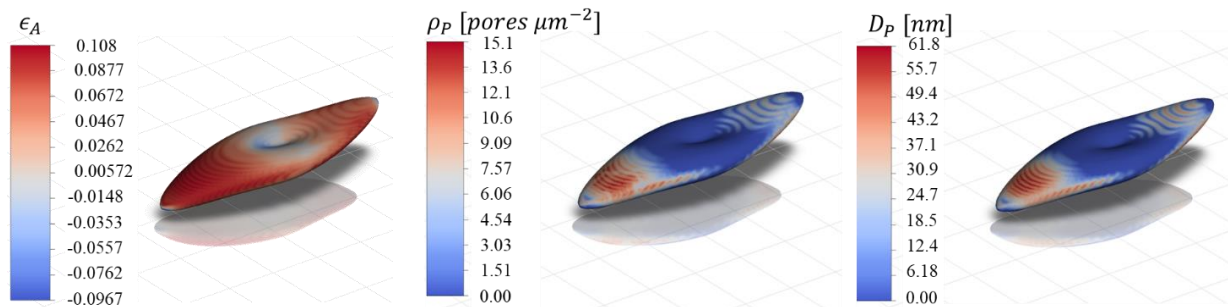


**Figure 35: Distribution of area strain, pore density, and pore diameter at peak stretch at  $\dot{\gamma} = 20$  at high shear rate,  $\dot{\gamma} = 20\,000\,s^{-1}$ . Peak length of the stretched RBC is 18.3  $\mu m$ .**

There is a significant difference in pore distributions at the fully extended peak and during tank treading, visualized below in Figure 38. Somewhat surprisingly, during tank treading, the

maximum area strain and thus the degree of nanopore formation and the average diameter appear to be significantly higher.

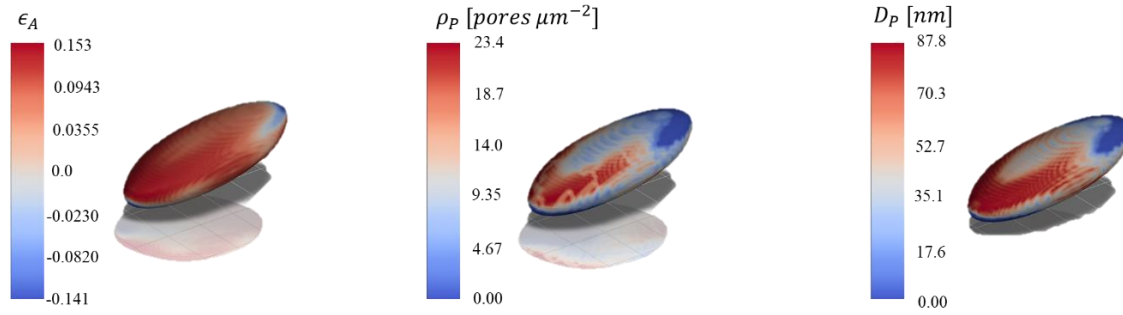


**Figure 36: Distribution of area strain, pore density, and pore diameter during tank-treading at  $t\dot{\gamma} = 50$  at high shear rate of  $\dot{\gamma} = 20 \cdot 10^3 \text{ s}^{-1}$ . Length of the stretched RBC at peak stretch is  $14.3 \mu\text{m}$ .**

It is important to note that although the velocity gradient tensor is generally projected onto the membrane surface to prevent out-of-plane strain accumulation, it is still possible that out-of-plane strain accumulation might be occurring, causing higher than expected peak strains as time increases. However, as the averaged area strain appears to be oscillatory and the peaks decline steadily, indicating that this is not an issue. The resulting effective transmembrane hemoglobin diffusion coefficient, computed as illustrated in section 0, is averaged over the entire red blood cell membrane and is shown for all shear rates in Figure 37 as it varies in time, and against area strain in Figure 38. In general, due to the thresholding behaviour of the model, it is observed that the effective diffusion coefficient below  $5000 \text{ s}^{-1}$  is very low, and  $\frac{D_{eff}}{D_0} < 10^{-3}$ , which can be seen in Figure 38. This implies that below shear rates of  $5000 \text{ s}^{-1}$ , sublethal

hemolysis does not occur, at least with respect to single cell deformation mechanics in Couette-like flow.

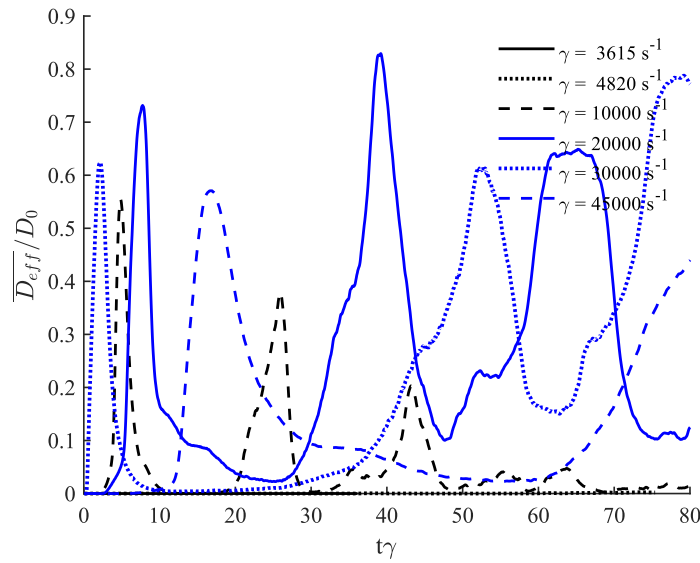


**Figure 37: Time-variation of membrane-averaged transmembrane effective diffusion coefficient normalized by self diffusion coefficient for a single RBC in a couette shear flow.**

The thresholding behaviour of the pore and radius distributions results in a complex relationship between area-averaged effective diffusion and area-averaged area strain. As a result, although at high membrane-averaged area strain, the correlation between area strain and diffusion coefficient tightens at intermittent values, there is a wide envelope of possible average diffusion coefficients. A mean value can be obtained for membrane-averaged effective diffusion coefficient as a function of area strain by fitting an erf (error function) function to the data. Exponential, rational, and Hill-Langmuir functions were also attempted, but it is found that the erf function provided by the best fit overall by a wide margin, which is shown in Figure 39. In general, this analysis offers insights into the relationship between area strain and diffusion coefficient, which can be valuable for gaining a more realistic understanding of the actual pore distributions on red blood cells when modelling sublethal hemolysis, and for building reduced order models of the phenomenon.

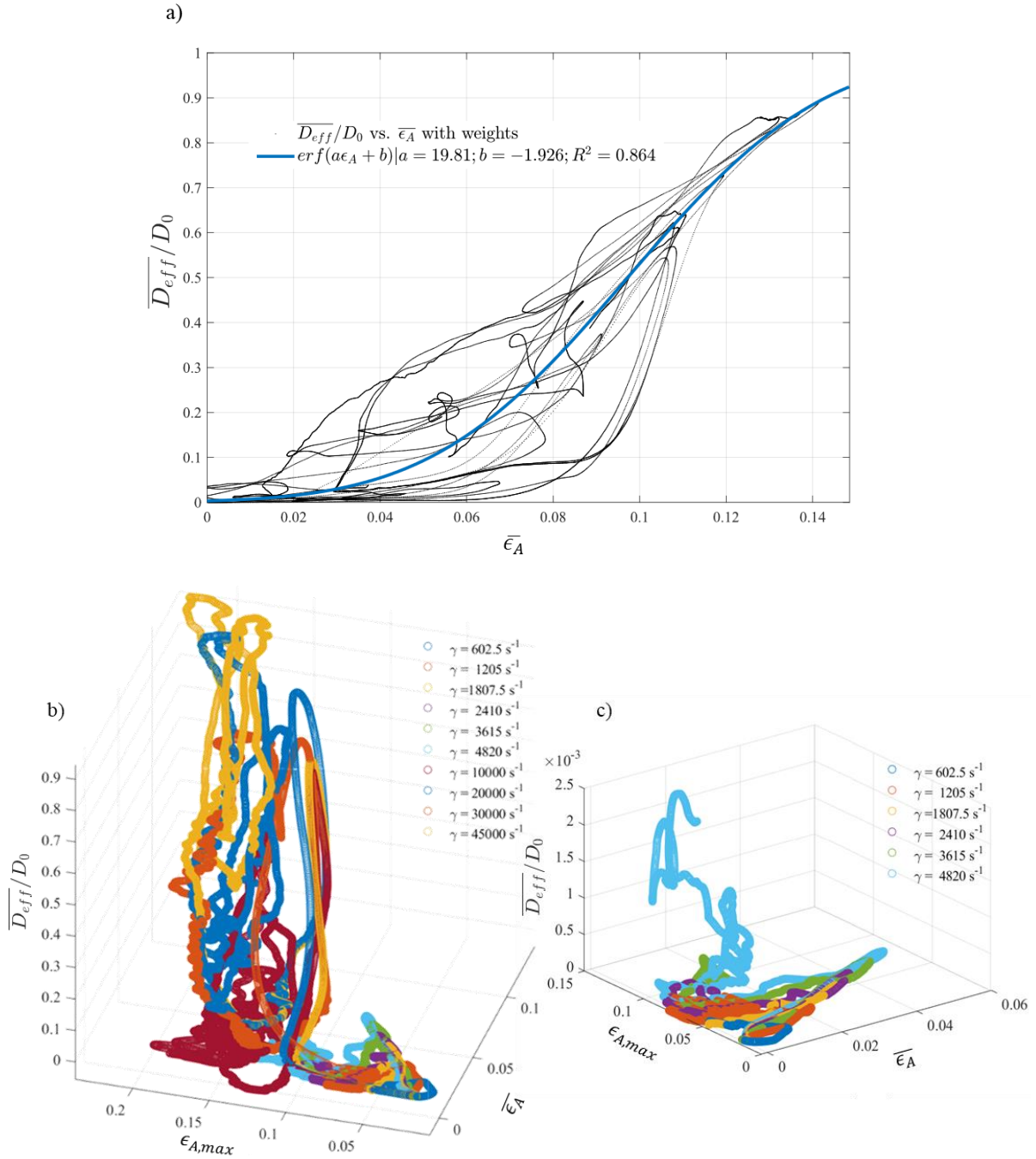


**Figure 38:** a) Effective transmembrane hemoglobin diffusion coefficient vs mean area strain for high shear cases fit to an error function, and effective transmembrane hemoglobin diffusion coefficient vs membrane-averaged area strain and maximum area strain for b) all cases and c) low shear rate cases. Transmembrane diffusion at lower shear cases is clearly shown to be  $\ll 0.1$ , as significant diffusion only occurs if  $\epsilon_{A,max} > 0.1$ .

The poor correlation between effective diffusion coefficient and mean area strain on the red blood cell membrane however is problematic for such modelling. It was discovered that effective diffusion coefficient was far better correlated to a 2D surface that included maximum area strain as a parameter, which is logical as this in essence considers the strain variance in

the correlation. Fitting the data to several surface formulations, such as exponential, sigmoid, Hill-Langmuir, and erf (error function) surfaces, yields correlation coefficients between 0.821 and 0.943 with the Hill-Langmuir and erf surface corresponding to worst and best fits, respectively. The erf surface fit is shown in

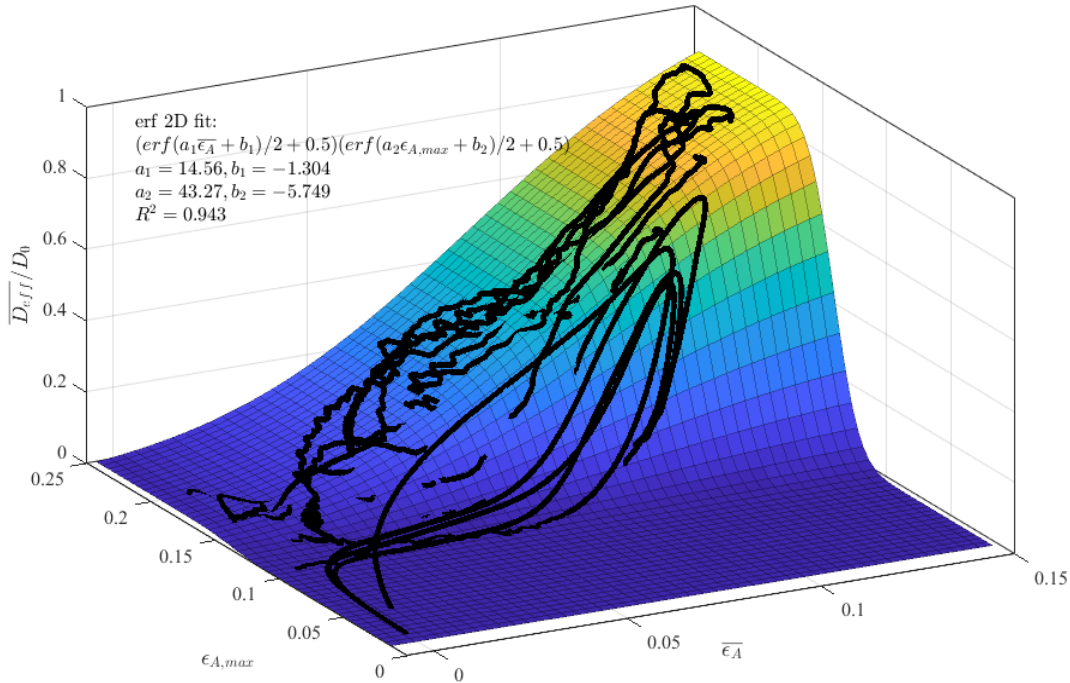
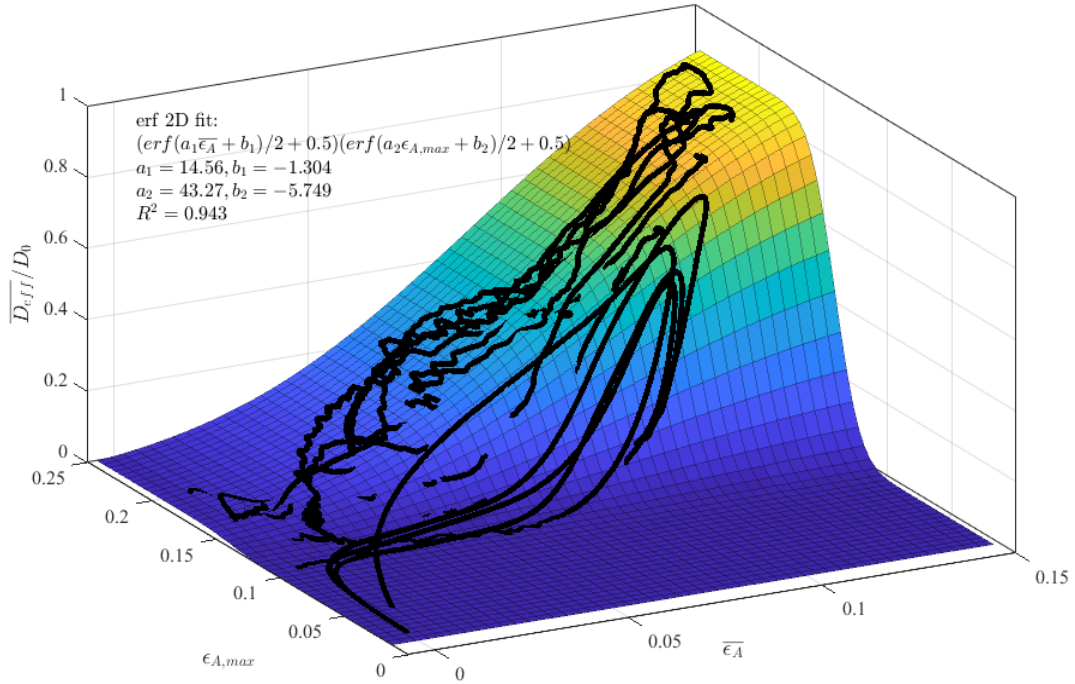


Figure 39. The fact that an erf function provides the best fit is not necessarily surprising, as both pore density and radius are functions of the pore formation probability obtained from the CGMD simulations of Koshiyama and Wada<sup>270</sup>, which are likewise modelled using an erf function. An interesting implication of the finding that diffusion has a distinctive erf fit is that mechanoporation parameters, such as pore density and pore radius, are normally distributed. This insight can be useful for understanding the behaviour of red blood cells under various flow conditions and their potential consequences on overall blood flow dynamics.





**Figure 39:** Fitting of high shear transmembrane hemoglobin diffusion cases to erf surface of membrane-averaged and membrane-maximum area strain.

#### 4.1.3 Effect of Shear Rate on Red Blood Cell Collisions on Sublethal Hemolysis

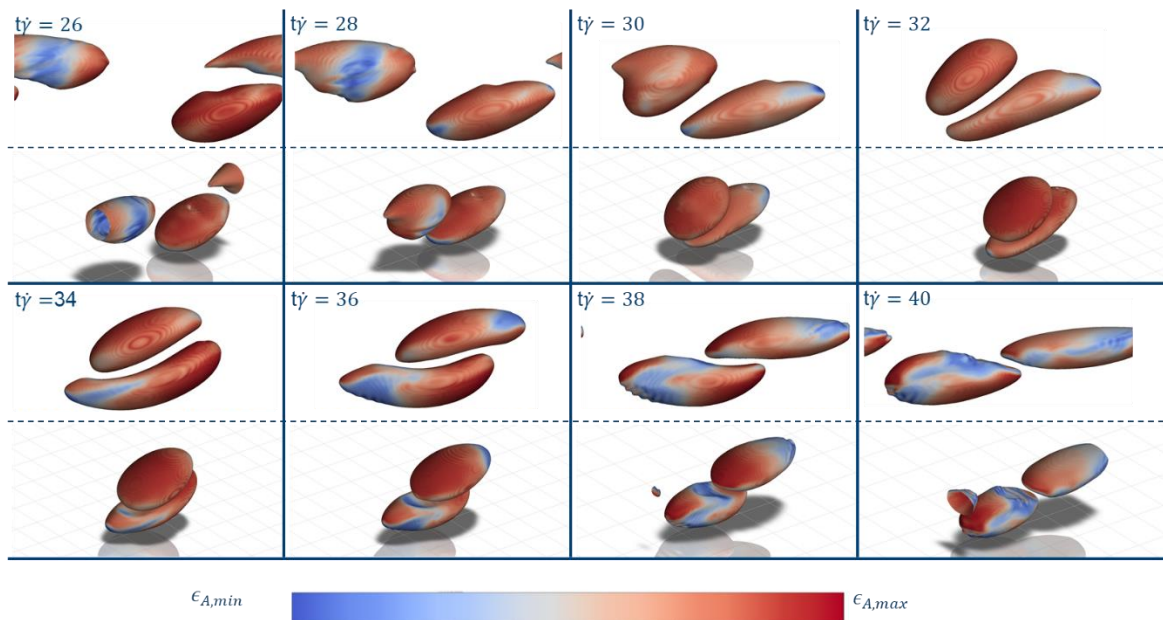
This section examines the impact of simple red blood cell collisions between two cells in a simple shear flow at varying shear rates on strain and sublethal hemolysis. Cells are initialized with the same y-coordinate one RBC diameter upstream and downstream from the domain centroid. Each cell is initialized, with a small y-component of velocity, equal to 10% of the maximum streamwise component of velocity, which perturbs each cell into opposite stream to facilitate the collision. The dynamics of these collisions are analyzed, and the consequences of these dynamics are manifested in the time-traces of strain experienced by the red blood cells. Results are compared with the single cell results to examine the effect of collisions on RBC membrane linear and area strain, shape parameter, and the sublethal diffusion of hemoglobin.

Figure 40 shows the dynamics of a collision between two red blood cells. In general, hydrodynamic lubrication forces build as the red blood cells approach each other, and as the red blood cell membrane is highly deformable, these forces tend to prevent explicit contact between the cells. The distance between them, which is proportional to the internal RBC pressure, is generally constant. Two types of collisions are observed and discussed throughout the remainder of the section: glancing collisions and head-on collisions, the dynamics of which depend on the mean red blood cell spacing. Area strain is observed to reach a local maximum and minimum near the site of the collision, observed for example by the deep blue in the



depressed region indented unto the lower cell by the upper cell at  $t\dot{\gamma} = 38$ . The shape, dynamics and local minimum of membrane stress at the region of contact agrees qualitatively with similar observations made by Omori et al.<sup>267</sup> for a simple collision between two RBCs.

In general, significant strains are applied to the red blood cells during any collision event, the instantaneous membrane-averaged mean strain fluctuates by 10-20% of the time averaged strain, as visible in Figure 41. Additionally, unlike in the single-cell case, Comparing Figure 40 and Figure 28, the length and general shape of the red blood cells are significantly shorter and more ellipsoidal at the same shear rates. This is a visual assessment, as it was not possible to calculate shape parameter for multi-cell cases due to the inability to track the individual membranes and measure their length in an automated and reliable way.



**Figure 40:** Visualization of collision between two red blood cells in a Couette shear flow at  $20\,000\text{ s}^{-1}$ . Red blood cells are in general prevented from tumbling by the collisions, and significant strain is observed in the areas where the collision is occurring. Lubrication forces keep the red blood cells from actually coming into contact, and generally result in a constant minimum spacing.

Figure 41 shows the correspondence between the time traces of membrane-averaged area strain and sublethal hemoglobin diffusion coefficient between one cell and two cells at varying shear rates. The first and most obvious point is that peak area strain in nearly all cases is, on average, higher, and peaks in area strain occur far more frequently and can be correlated with individual collision events. Furthermore, unlike in the single-cell cases, the period between the peaks remains constant as shear rate increases indicating it is well normalized by the shear rate, because collision frequency, which in the two-cell case scales directly with shear rate, drives the dynamics. As there are more peaks, furthermore, the dynamics become steady much more

quickly, and the time averages become more accurate because a dynamic steady state is reached much more quickly within the simulation period.

Interestingly, the maximum and minimum strains have similar peak values between the single and two-cell cases. Evidently, collisions increase the degree of shear experienced by the red blood cells, and consequently substantially increase peaks of the membrane-averaged area strain. However, it is difficult at this point to predict exactly how these collisions affect the average membrane strain, as numerous factors influence these mechanics. This includes hematocrit, the proximity of other cells that tend to force the red blood cells together, and the viscoelastic effect on collisions (which is discussed in the next section). In general, a simplified constitutive model is needed to predict stress on the red blood cell based on the mean expected spacing and the expected spacing. The general collision frequency is, however, directly proportional to red blood cell spacing and the shear rate. Further work must be done to model this phenomenon, which will lead to improved constitutive models. This is, however, beyond the scope of the current work.

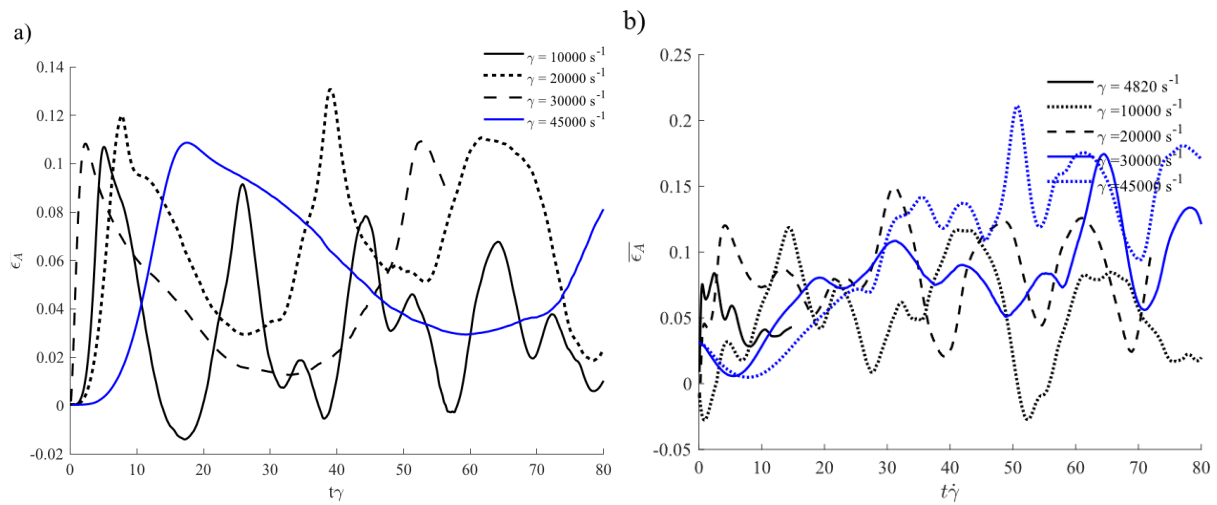


**Figure 41: Comparison of time and shear rate variation of membrane-averaged area strain between (a) a single cell case b) two cells in a Couette shear flow.**

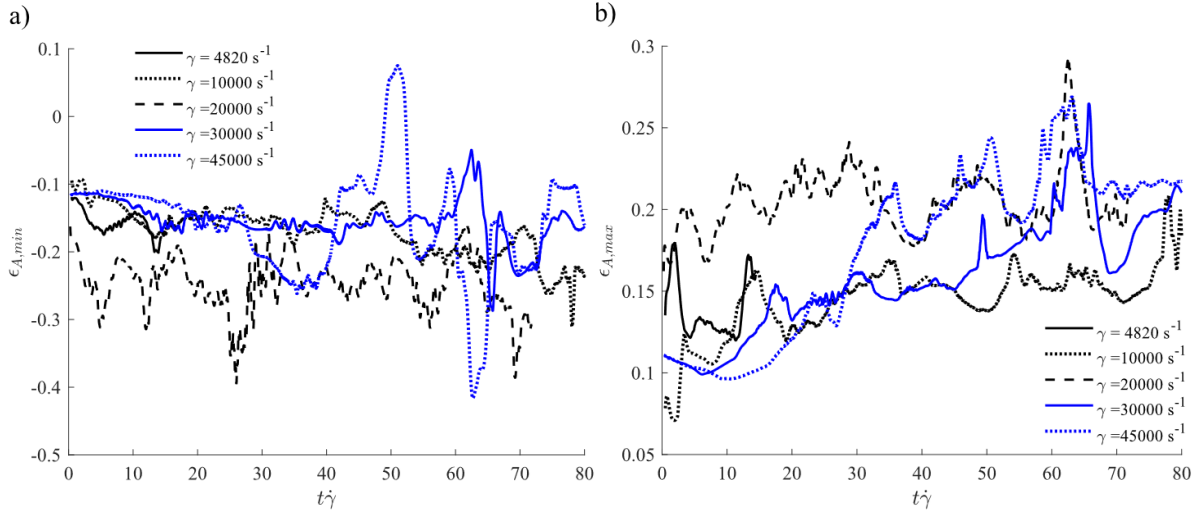


**Figure 42: Time and shear rate variation of a) membrane-minimum and b) membrane-maximum area strain of two cells in a Couette shear flow.**

Figure 43 displays the time traces of membrane-averaged effective transmembrane diffusion coefficient. As expected, higher mean area strains in the two-cell case lead to significantly higher diffusion coefficients. However, the increase in effective diffusion is disproportionate to the increase in area strain, due to the thresholding behaviour of the mechanoporation model. From the figure, increased hemoglobin diffusion coefficient is evident after 4820  $s^{-1}$ . This highlights the complex relationship between area strain and effective diffusion, emphasizing the importance of capturing both collisions and the distribution of area strain accurately to capture sublethal hemolysis.

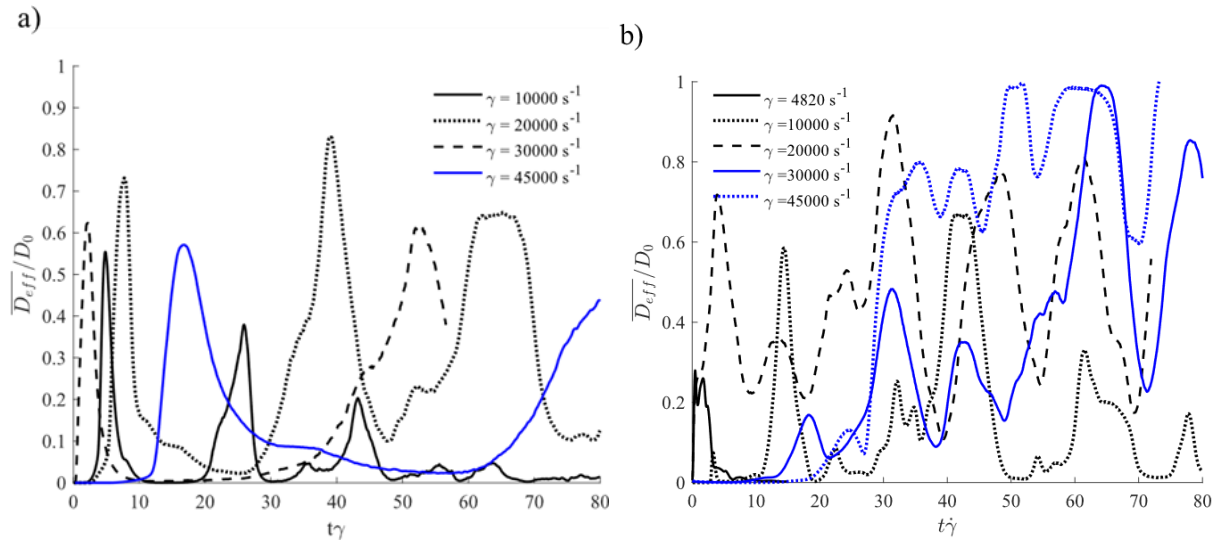


**Figure 43: Membrane-average diffusion coefficient in the a) single and b) multicell case.**

The time average of the membrane-averaged area strains and hemoglobin diffusion coefficients are shown in Table 8 for the single and two-cell cases at shear rates ranging between 4820 and 45,000 s<sup>-1</sup>. There is a significant increase in both time and membrane-averaged and membrane-maximum area strain, as well as the time and membrane-averaged effective diffusion coefficient. As before, the average is taken as the longest integer multiple of the period of the lowest frequency mode found in each simulation.

In general, by 45,000 s<sup>-1</sup>, as might be expected when area strain is very close to rupture, the effective diffusion coefficient approaches the theoretical maximum, 1. It is also interesting to note that at the shear rate of 4820 s<sup>-1</sup> there is significant hemoglobin diffusion whereas in the single-cell case this value was on the order of 10<sup>-3</sup>, indicating that red blood cell collisions lower the threshold of sublethal hemolysis.

**Table 8: Time and membrane averaged values of area strain and effective transmembrane hemoglobin diffusion coefficients for one and two cells in a Couette shear flow.**

$N_{cells}$	$\dot{\gamma}$ [s <sup>-1</sup> ]	$\bar{\epsilon}_A$	$\bar{\epsilon}_{A,max}$	$\bar{D}_{eff}/D_0$
<i>1</i>	<i>4820</i>	<i>0.0160</i>	<i>0.0721</i>	<i>3.88·10<sup>-4</sup></i>
<i>2</i>	<i>4820</i>	<i>0.0471</i>	<i>0.1376</i>	<i>0.045</i>
<i>1</i>	<i>10000</i>	<i>0.0320</i>	<i>0.1090</i>	<i>0.0429</i>
<i>2</i>	<i>10000</i>	<i>0.0559</i>	<i>0.1516</i>	<i>0.1636</i>
<i>1</i>	<i>20000</i>	<i>0.06474</i>	<i>0.1395</i>	<i>0.2734</i>
<i>2</i>	<i>20000</i>	<i>0.0843</i>	<i>0.2059</i>	<i>0.4685</i>
<i>1</i>	<i>30000</i>	<i>0.06175</i>	<i>0.1125</i>	<i>0.3305</i>
<i>2</i>	<i>30000</i>	<i>0.0919</i>	<i>0.1726</i>	<i>0.3986</i>
<i>1</i>	<i>45000</i>	<i>0.08494</i>	<i>0.139</i>	<i>0.4582</i>
<i>2</i>	<i>45000</i>	<i>0.136</i>	<i>0.204</i>	<i>0.7628</i>

In Figure 44, the erf function surface fit is repeated for the two-cell cases, and it is found that the correlation between the diffusion data and the erf surface between membrane-averaged and maximum area strain is improved. This can be attributed to several factors, including that a better sampling of the oscillations is obtained, and because the red blood cells have far less local deformation due to shear instability, such as wrinkling. This also further supports the idea that the distribution of the nanopore parameters with average and maximum area strain is

normal. This is not necessarily surprising as the pore model includes an erf threshold function. Yet it is interesting to observe that either strain distribution induced by collisions, is normal or close to normal (or the difference does not have a significant effect) and thus the end distribution still results in the erf function behaviour. This observation highlights the importance of considering collision dynamics and their impact on red blood cell strain distribution, and consequently transmembrane hemoglobin diffusion and sublethal hemolysis. Having a better understanding of the mechanical strains experienced by the red blood cells at various dynamic conditions also is an important step in developing constitutive models for RBC damage.

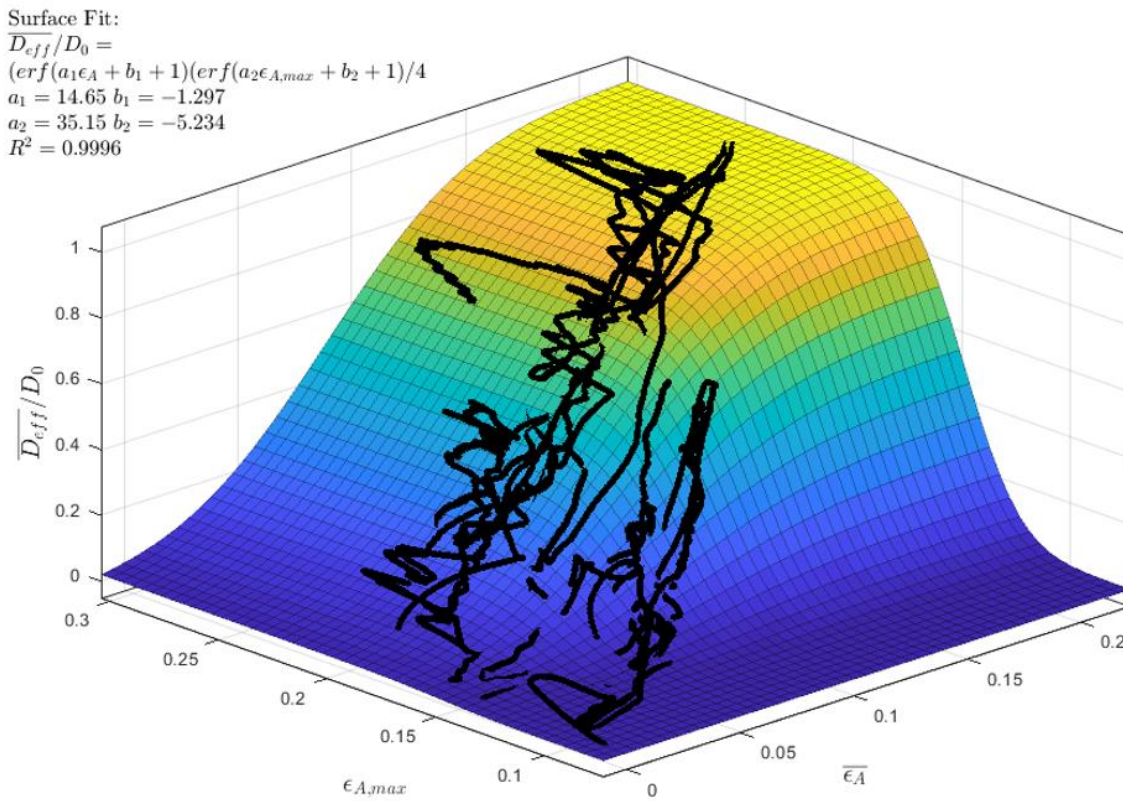


**Figure 44:** Fitting of effective transmembrane hemoglobin diffusion coefficient with membrane-averaged area strain and membrane-maximum area strain to an erf surface.

#### 4.1.4 Effect of Viscoelasticity

In this section, the effect of membrane viscoelasticity on the dynamics of red blood cell collisions and their subsequent impact on area strain and transmembrane hemoglobin diffusion coefficient are examined. As the viscoelastic response time in single-cell cases requires prohibitively long simulation times, the focus will be on the relatively short timescales of collisions in the presence of 2 and 4 cells, corresponding to 6% and 12.1% hematocrit levels. The viscoelastic properties of the membrane are modelled by applying a Newtonian viscosity



multiplied by the membrane boundary indicator function, as detailed in Section 0, wherein the viscosity inside of the membrane is set to  $0.3 \text{ } [\mu\text{Pa s m}]$ . By analyzing the dynamics of collisions between two cells with realistic membrane viscosities in Figure 45, the influence of viscoelasticity on red blood cell behaviour and hemolysis is ascertained.

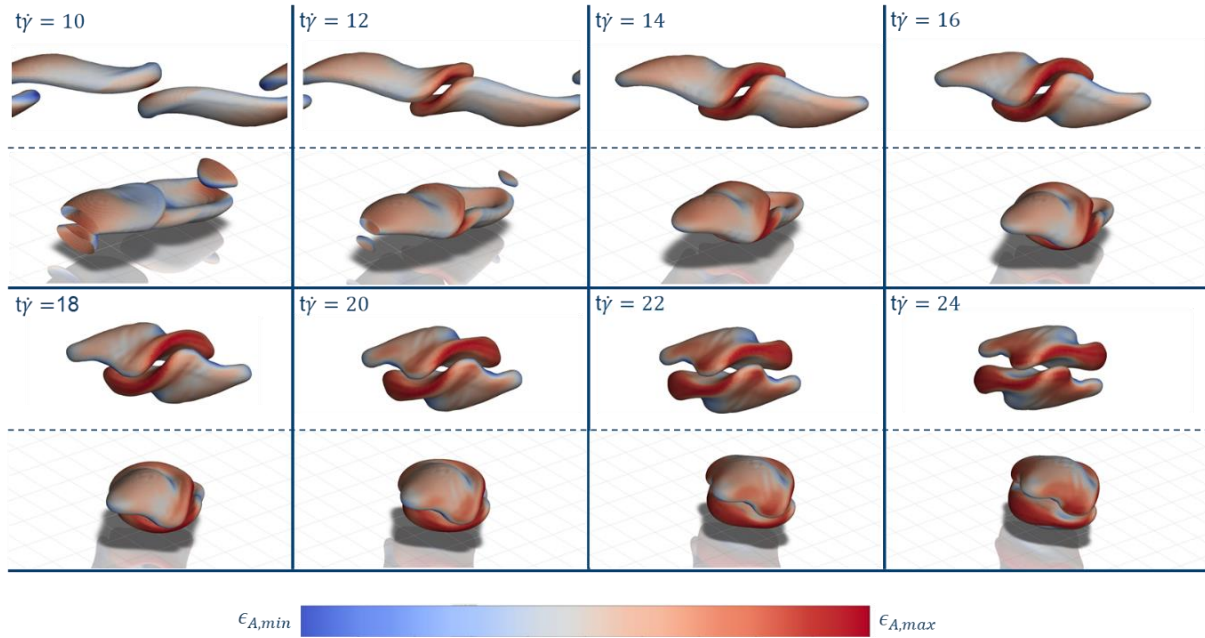


**Figure 45: Illustration of glancing collision between red blood cells wherein viscosity inside of the boundary indicator function where the structural model is set to  $0.3 \text{ } [\mu\text{Pa s m}]$ .**

In Figure 47, it is observed that the dynamics of red blood cell collisions and the shape of the red blood cells are significantly different when viscoelasticity is incorporated into the red blood cell membrane. The inclusion of membrane viscosity, which is on average two orders of magnitude higher than that of the nearby plasma or cytoplasm, adds considerable stiffness to the membrane on the timescale of the collision. This effect is partially due to the high shear rate ( $20,000 \text{ s}^{-1}$ ), which results in a relatively large velocity difference between the two oncoming cells. This effect may be less pronounced at lower shear rates; however, given that the timescale of RBC recovery is  $0.1 - 0.2 \text{ s}$ , the ratio of time between collisions to recovery time is not significantly different for the higher shear cases and thus this would not be significantly different.

Indeed, Figure 46 shows that during the collision, there is a much slower response of the membranes due to the proximity of the other RBC. Deformation seems to occur locally only for the portions of the RBC that are near the other RBC, and the response of the rest of the membrane is delayed because the relatively low membrane stiffness is quite insufficient to transmit the stress. The interaction appears as if a rigid structure is deforming plastically due

to a rapid impact. Consequently, there is little recoil from the collision, and the cells appear to stick together.

The increased stiffness causes the spacing between the membranes to decrease, and in the regions where there is near contact, the spacing is much smaller than in the non-viscoelastic case. Because of this, significant shear is applied to the red blood cells, and they begin to rotate around one another due to their collision. Following the collision, the two cells rotate together and do not separate for the duration of the simulation. It is unclear whether this is a consequence of some numerical defect of the Eulerian structural membrane model, but it is considered unlikely because despite the close proximity of the cells, there are at least two grid cells between the RBCs where  $B_s$  is close to  $I$ .

Figure 46 and Figure 47 below presents the membrane-averaged, -maximum, and -minimum strains experienced by the membrane with 2 and 4 cells, as well as membrane-averaged effective diffusion coefficients. One of the main observations is that there is little difference between viscoelastic and non-viscoelastic 2 and 4 cell cases in terms of average strain, which will be discussed in the next section. The 2-cell viscoelastic case was terminated early because the colliding red blood cells would, in the absence of other cells forcing them out of their locked position, continue spinning together in an almost solid-body rotation motion. In general, the initial strain experienced by the blood cells is quite similar, and the time average of area strain is comparable for both two and four cells. When comparing the four-cell viscoelastic case with its non-viscoelastic counterpart, it is evident that the strains experienced by each are indeed very similar, but the peaks of the 4-cell non-viscoelastic case are higher during collisions.

This is a somewhat counter-intuitive result as it was expected that the smaller spacing and more localized impact zone would result in more damage to the red blood cells. It appears, however, that in fact the viscosity of the membrane is so great and at high shear rates has such a large effect that it absorbs the impact and moderates the effect of the collision. Maximum strains are found also to be nearly identical between the 4-cell viscoelastic and 4-cell non-viscoelastic cases. The two-cell viscoelastic case in which the cells collide and roll together, appears to experience very high area strains during the head-on collision, indicating that the increased rigidity of the viscoelastic membrane during collisions seems to cause locally increased stresses during head on collisions, but not during glancing collisions which were experienced in the 4-cell case. Nevertheless however, in general it is found that viscoelasticity while apparently having a large impact on the dynamics of the cells, does not appear to have a strong impact on

the mean strain experienced by red blood cells during collisions, though more data is necessary to verify this concretely. If true, this is fortuitous as modelling viscoelasticity adds substantial complexity to membrane modelling.

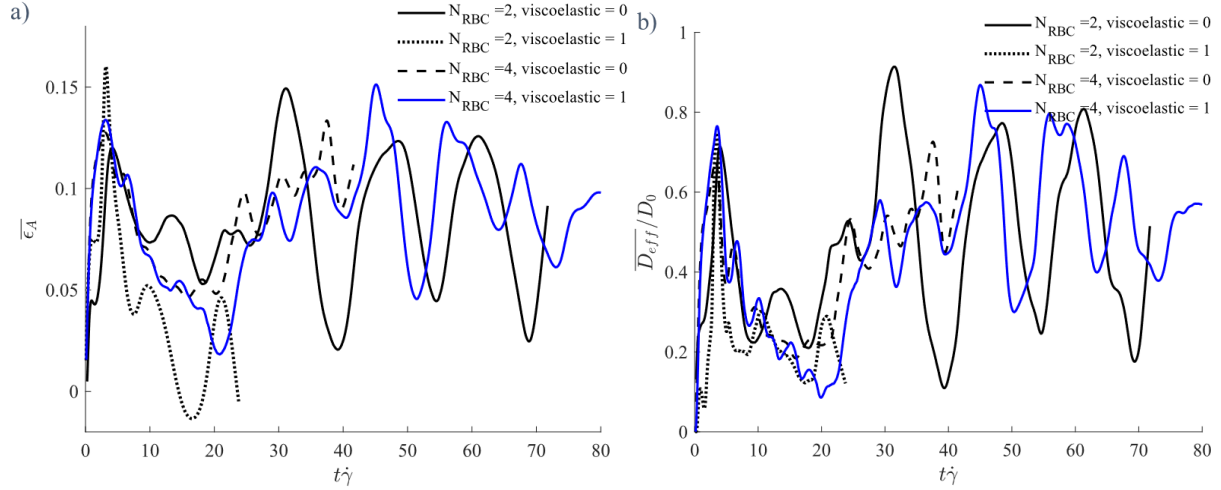


**Figure 46: Comparison of a) membrane-averaged area strain and b) the effective transmembrane diffusion coefficient during collisions at 20 000 s<sup>-1</sup> in the viscoelastic and non-viscoelastic cases for 2 and 4 cells.**

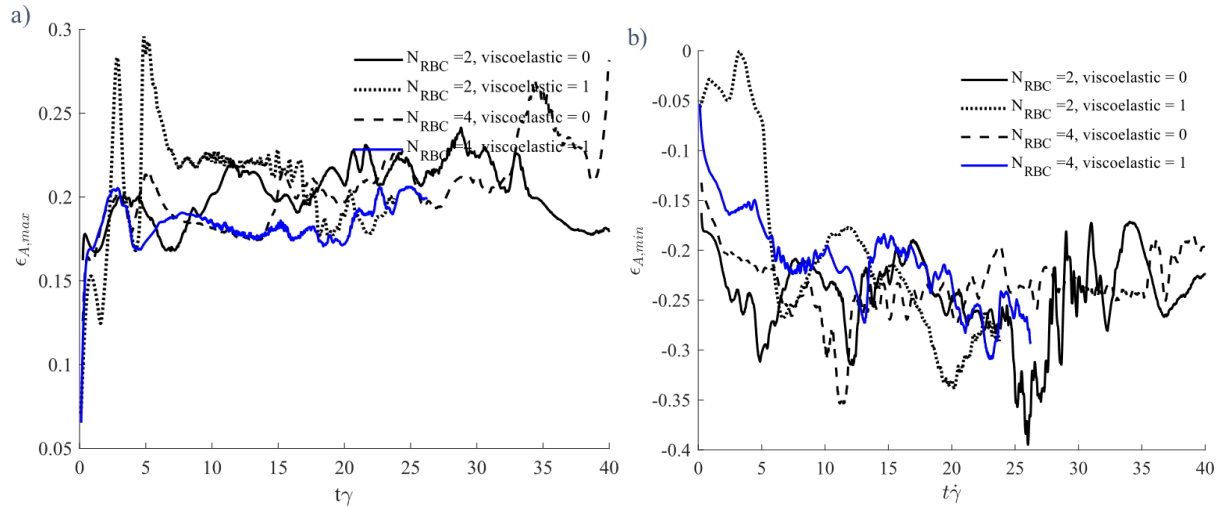


**Figure 47: Comparison of a) membrane-maximum and b) membrane-minimum area strain during collisions at 20 000 s<sup>-1</sup> in the viscoelastic and non-viscoelastic cases for 2 and 4 cells.**

#### 4.1.5 Effect of Hematocrit on Area strain and Sublethal Hemolysis at Constant Shear Rate

This section describes the results of the multicell simulations in which the shear rate is kept constant, but the number of cells is increased causing an increase in the hematocrit and decrease in the average intercellular spacing. Hematocrit is varied between 3% and 36%, corresponding to the 1 to 12 cell simulations.



Figure 48 shows a sample of the dynamics of red blood cell collisions over a timescale representing the time it takes a red blood cell to pass through the domain 2.4 times. The dynamics are completely different compared to the single cell case. The shape of the red blood cells is generally constrained by the presence of nearby red blood cells, resulting in an elongated ellipsoid shape. As discussed, there are two general types of collisions: glancing and head-on collisions. Glancing collisions, visualized in the previous sections, do not cause a contraction in length, but the hydrodynamic lubrication forces can cause substantial shear on the red blood cell membrane, leading to localized maxima and minima in area strain. This results in an overall increased peak area strain, as seen in Figure 48.

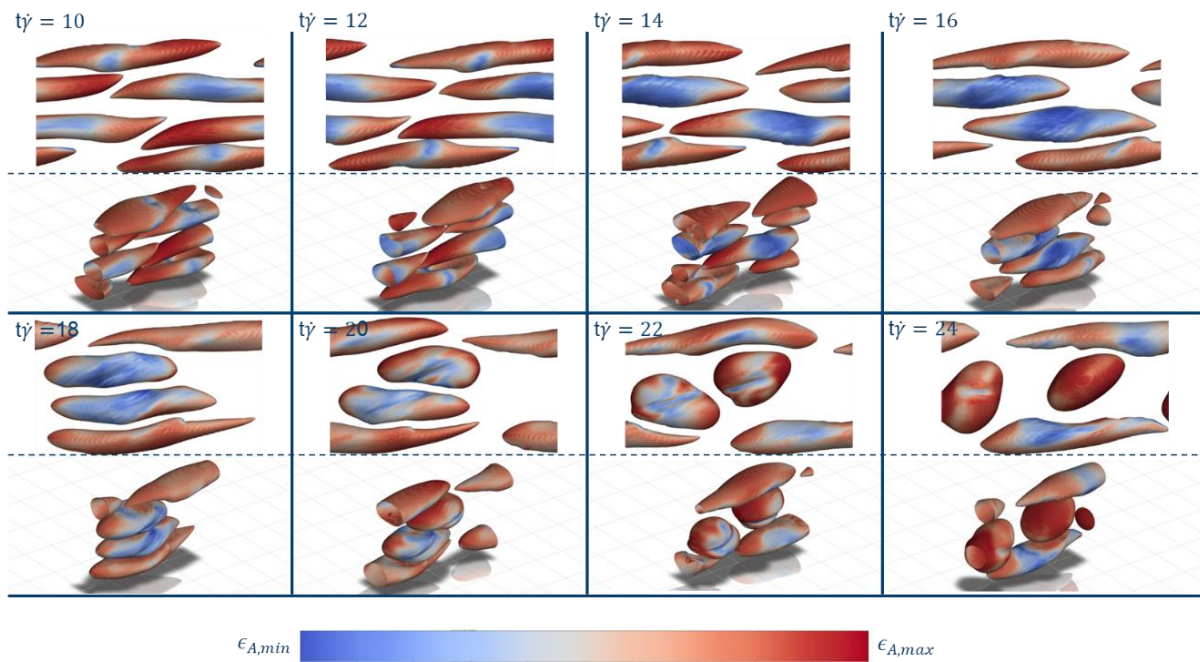


**Figure 48: Visualization of head on collisions in the 4-cell case ( $Hct = 12.1\%$ ) causing contraction in length and rotation in the 4-cell case at  $20\,000\,s^{-1}$  shear rate. Collision begins at  $t\dot{\gamma} = 16$ .**

Head-on collisions, as seen in Figure 48, cause red blood cells to contract in length due to the high shear experienced by the closely packed blood cells. The contraction results in higher overall area strain and a degree of wrinkling. The greater degree of shear mutually imposed on the RBCs causes them to spin around each other.

**Figure 49 presents the time-traces of membrane-averaged area strain at a shear rate of  $20,000 \text{ s}^{-1}$ , with varying numbers of red blood cells in the domain, and**

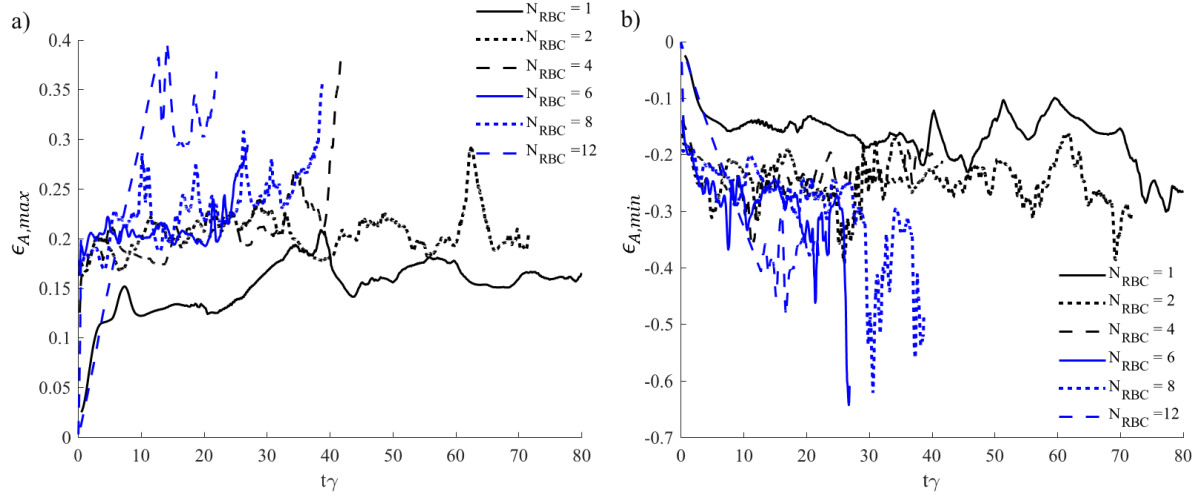
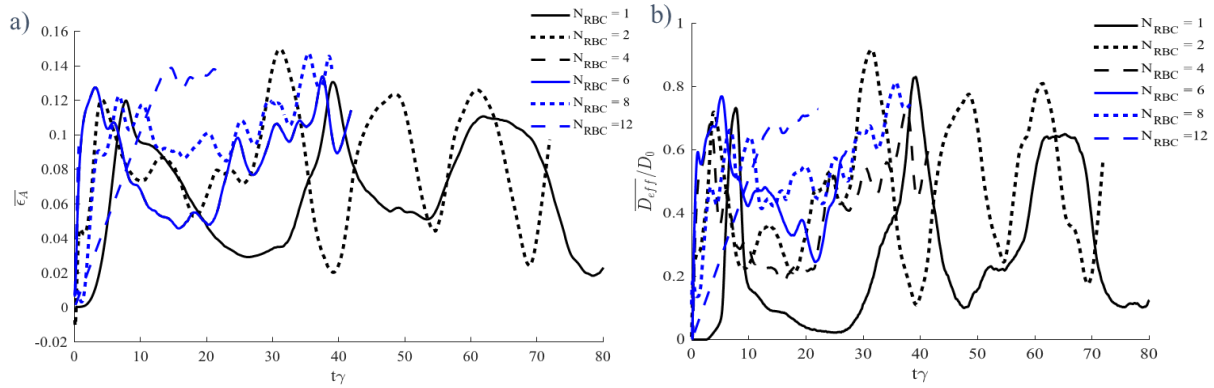


Figure 50 presents the membrane-maximum and membrane-minimum time-traces. The data reveals a distinct relationship between the average area strain observed and the number of cells. As the number of cells increases, more collisions occur, leading to shorter oscillation periods in the membrane-averaged area strain. Although the average area strain increases with the number of cells, it is challenging to determine this conclusively due to the ongoing increase in the time-traces for all cell counts above two, indicating that a steady period was not reached during the simulation. Nevertheless, there is a consistent increase in the trend of area strain between 6, 8, and 12 red blood cells which is consecutively increasing, the consistent increase suggesting that increased hematocrit induces more collisions, which induce greater area strain. The effect seems to saturate, with diminishing increase after 8 cells (24% Hct). Interestingly, while the average area strain is higher with increasing numbers of RBCs, the trend towards increasing hemoglobin diffusion rate is not as apparent. This may be attributed to the greatly increasing stiffness of the membrane mechanical model, which limits area strain to approximately 23-25%. The time and membrane-averaged hemoglobin diffusion coefficient display a similar pattern to the time and membrane-averaged membrane strain. The diffusion coefficient is found to increase with hematocrit until saturation at approximately 0.7, a value that mirrors the sublethal hemoglobin diffusion coefficient observed at rupture shear for the two-cell case. This observed relationship further supports the notion that red blood cell collisions at high shear rates lead to increased membrane area strain and hemoglobin diffusion. Table 9 presents the time averaged values of membrane area strain and the time averaged values of effective hemoglobin diffusion. As noted earlier, the average area strain generally increases with the number of cells, reaching saturation at around 14%. This saturation threshold aligns with the time averaged maximum strain observed in the single cell cases at high shear rates, as

shown in Figure 34. It is however not possible to draw a concrete conclusion, given that the membrane-averaged strain in the higher cell-number cases does not reach a statistical steady state within the timeframe of the simulations. Despite this difficulty, the distinct increase in membrane strain in higher cell-number cases, along with the findings from previous sections, suggests that at high shear rates, red blood cell collisions result in an overall higher degree of membrane area strain.



**Figure 49:** Time variation of membrane-averaged area strain and diffusion coefficient with number of cells. Effective hematocrit is between 3 and 36%, computed as the ratio of cytoplasmic to total volume.

The time and membrane-averaged hemoglobin diffusion coefficient display a similar pattern to the time and membrane-averaged membrane strain. The diffusion coefficient is found to increase with hematocrit until saturation at approximately 0.7, a value that mirrors the sublethal hemoglobin diffusion coefficient observed at rupture shear for the two-cell case. This observed relationship further supports the notion that red blood cell collisions at high shear rates lead to increased membrane area strain and hemoglobin diffusion.

**Table 9:** Comparison of time and membrane-averaged area strain and effective transmembrane hemoglobin diffusion coefficients with increasing hematocrit

$N_{cells}$	Hematocrit	$\bar{\epsilon}_A$	$\bar{\epsilon}_{A,max}$	$\bar{D}_{eff}/D_0$
1	3.02	0.0647	0.1395	0.273
2	6.0	0.0843	0.2059	0.469
4	12.1	0.0844	0.2110	0.407
6	18.1	0.0777	0.2129	0.435
8	24.1	0.1343	0.2845	0.752
12	36.2	0.1379	0.3324	0.733

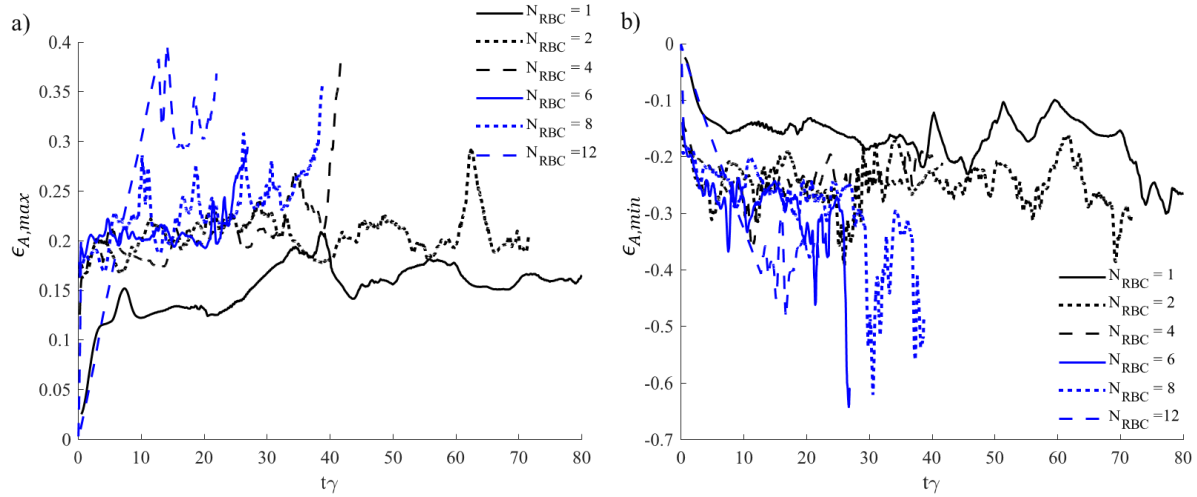


**Figure 50:** Time variation of a) membrane-maximum and b) membrane-minimum area strain with between 1 and 12 cells in the domain, which corresponds to effective hematocrit of 3% and 36%.

#### 4.1.6 Summary of Findings and Contributions

The deformation of red blood cells in a Couette shear flow was simulated using a fully Eulerian method for fluid-structure interaction modelling. The hyperelastic Yeoh model utilized by Mills et al.<sup>207</sup> was extended to attempt to enforce area elasticity and constrain area strains to approximately 6.4% at a rupture shear rate of  $45,000 \text{ s}^{-1}$  for a single cell in a Couette shear flow, as well as to prevent a stretch past  $19 \mu\text{m}$  (the streamwise length of the periodic domain) at rupture shear rate of  $45,000 \text{ s}^{-1}$ . The study focused on examining the effects and interactions of red blood cell collisions, shear rate, and viscoelasticity on the area strain experienced by the red blood cell membrane.

The simulations showed that in a Couette shear flow, red blood cells transition from a tumbling motion to tank treading between a shear rate range of approximately  $1,000$  to  $5,000 \text{ s}^{-1}$ . During this transition, the dynamics become complex with both tumbling and tank treading occurring simultaneously. In the single-cell case, below shear rates of  $5,000 \text{ s}^{-1}$ , the strain experienced on the membrane is generally insufficient to cause sublethal hemolysis, as the effective transmembrane hemoglobin diffusion coefficient is  $< 0.001$ . In single cell cases, oscillations in shape parameter length and area strain occur independently of the shear rate.

The study also made several new contributions concerning the effects of viscoelasticity, hematocrit, and collisions. In multicell cases, it appears that cell collisions significantly influence the response of the area strain. when shear rate is varied, it results in a much higher area strain and transmembrane hemoglobin diffusion when compared to single-cell cases. Viscoelasticity seems to dampen the effect of glancing collisions, as well as the membrane's

response to shear, though when area strains are averaged in time and over the membrane, there was not a significant difference between the viscoelastic cases and the non-viscoelastic cases. It was found that the average area strain increases with increased hematocrit and collision frequency, with a saturation point at approximately 14%, which was driven by the material model it is uncertain if this maximum area strain corresponds to an actual local maximum area strain experienced by the red blood cell. The maximum strain remains relatively constant across all cases near the saturation point of approximately 23-25%. The diffusion coefficient generally increases with area strain, saturating at approximately 70% in the most extreme cases of mechanoporation. Notably, the diffusion coefficients at varying strains in the case of two-cell collisions correlated very well with an erf surface fit. This may suggest that pore parameters, pore distributions, and strains are normally distributed. It may also be caused by the fact that the modelled probability density function of pore formation with respect to strain is also normal. The latter is believed to be more likely, though in this case it is noted that the overall area strain distribution is either uniform itself, or also normal. Finally, in multicell cases, it was found that transmembrane hemoglobin diffusion begins to occur at a lower shear rate, with small but significant hemoglobin diffusion occurring at  $4820 \text{ s}^{-1}$ .

## 4.2 Simulation of the Effect of Hemolysis on Thrombosis

### 4.2.1 Fitting Embolization Rate from Experiment

The embolization rates were obtained by solving equation 3-83, obtaining the steady-state platelet distributions at each radial location, followed by an optimization procedure that varied the parameters in question to minimize the sum squared distance to the experimental data of Navitsky et al.<sup>353</sup>. The modified-Goodman model was fit for different values of  $\kappa$  in Equation 3-81, resulting in varying values for  $k_{emb}$  and  $\tau_{emb,W}$ , shown in Figure 51. Fits for the power law model and fitting values for  $\tau_{emb,W}$  and  $\kappa$  in Equation 3-76 are depicted in another Figure 52. The steady state, adhered, platelet concentration at the center of the disk,  $r = 0$ , is solely a function of the adhesion coefficient, allowing the determination of the deposition rate,  $k_{a_{dep,W}}$ , in isolation of the other parameters. This value is thereby consistent across all fits. For PUU,  $k_{a_{dep,W}}$  was calculated to be  $7.93 \cdot 10^{-8} \text{ [m/s]}$ , making it one of the most biocompatible materials available.

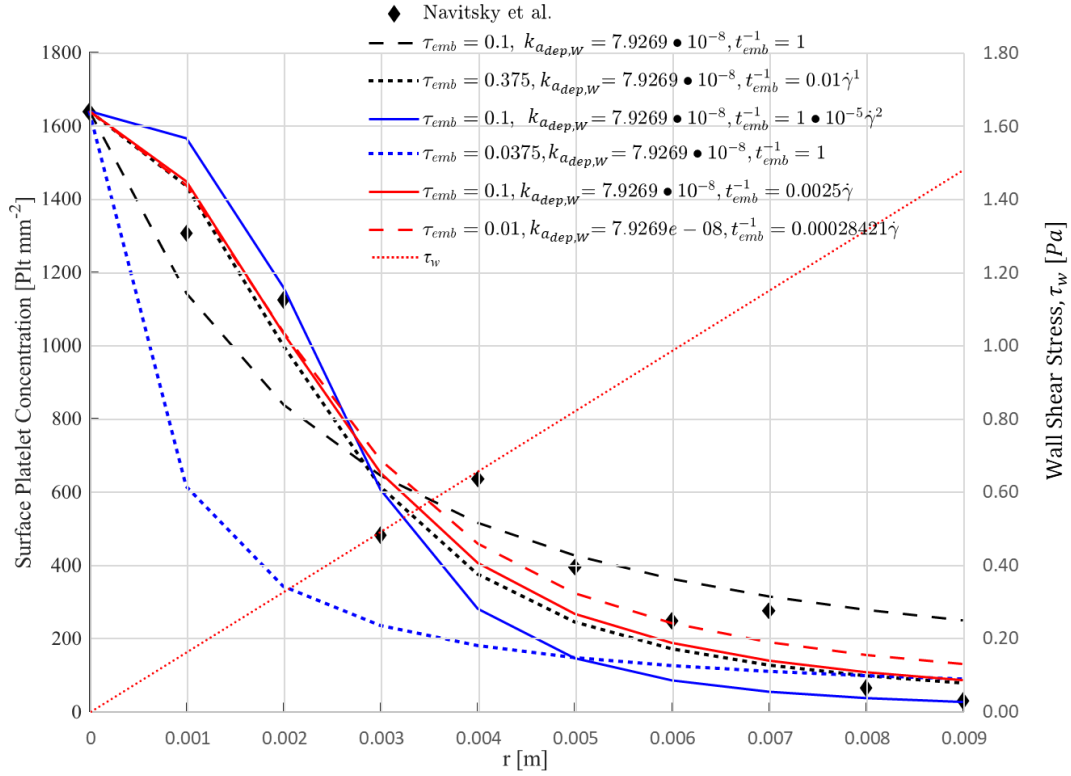


**Figure 51: Fitting of embolization rate and threshold stress in modified-Goodman model using experimental data from Navitsky et al<sup>353</sup>.**

Notably, the model with  $k = 0$  did not fit the surface embolization data effectively. It either underpredicted surface platelet concentrations at lower shear stress or overpredicted, necessitating the need for dependence on shear rate. The most accurate fit was achieved with  $\kappa = 1$ . A value of  $\tau_{emb,W}=0.01$  [Pa] was chosen to align with Goodman et al.<sup>325</sup>, yielding  $k_{emb} = 0.00028421$ . For  $\tau_{emb,P}$ , similar values to those of Wu et al.<sup>339</sup> and Rojano et al.<sup>18</sup> were selected. Given that Wu, found that  $\tau_{emb,W} = 3.0$  [Pa] led to excessive growth, the value from Rojano et al.<sup>18</sup> was chosen, resulting in  $\tau_{emb,P}=0.9$  Pa. Selecting these values, it is found that in non-physiological flows such as in MCS, where shear rate in thrombogenic areas can reach up to  $40,000 \text{ s}^{-1}$ , the characteristic embolization time is  $t_{emb} = (k_{emb}\dot{\gamma})^{-1} = 0.43 \text{ [s]}$ . In the present study, shear rate varies between 0 and 50,000, due to the variation in rotor speed and complexity of the flow. This is in line with the value that both Wu<sup>339</sup> and Rojano.<sup>18</sup> use, whereas in Goodman's case, where  $\dot{\gamma} = 654 \text{ [s}^{-1}\text{]}$ ,  $t_{emb} = 5.25 \text{ s}$ , within the range of possible values specified by Goodman. Generally, shear rate is a proxy of shear stress. As this is a computational study and this data is available, it is more illustrative in the case of thrombosis to consider shear stress directly.



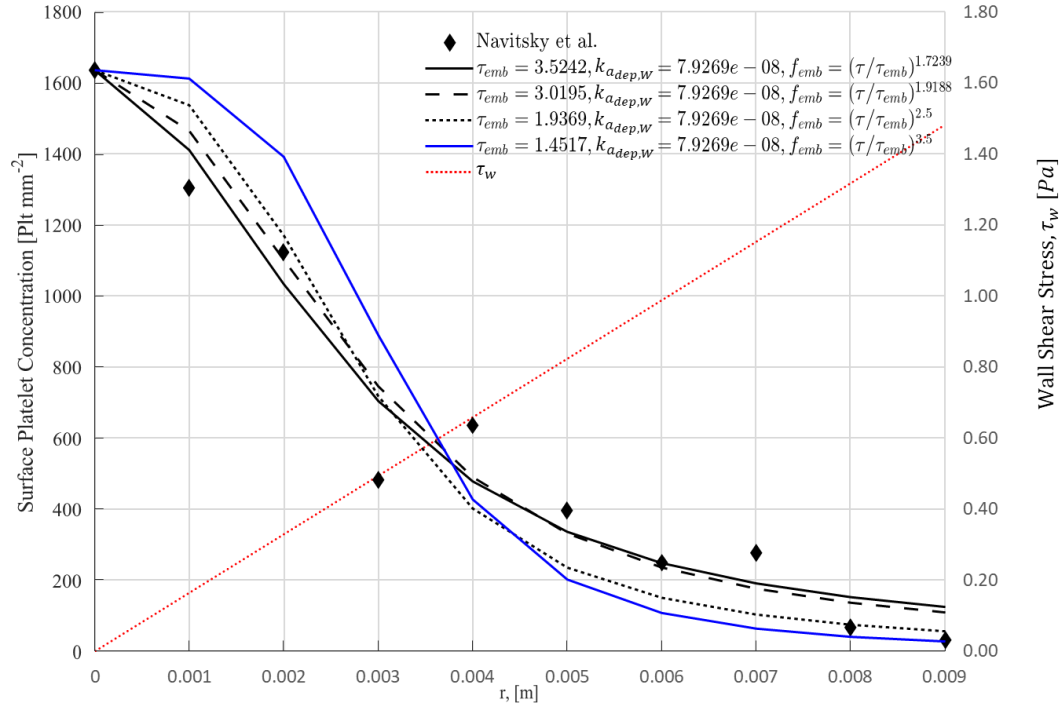


**Figure 52: Fitting of embolization rate and threshold stress in power law model using experimental data from Navitsky et al<sup>353</sup>.**

Notably, the same surface platelet distribution could be achieved through different values of  $k_{emb}$  and  $\tau_{emb}$ . This overparameterization of the embolization scheme was also noted by Goodman et al.<sup>325</sup>, who compensate for a high critical embolization stress with a low embolization rate. This collinearity of these two parameters with respect to embolization rate explains why there is such a discrepancy in the literature between characteristic embolization rate,  $k_{emb}$ , and surface embolization stresses,  $\tau_{emb,W}$ .

The power law model, as presented in Figure 52, offers a relatively good fit for platelet concentration at different radii on the spinning disk, with the added advantage of fewer parameters. In the first two fits shown, both  $\kappa$  and  $\tau_{emb}$ . Despite different values, these fits remarkably produce similar platelet distributions, illustrating that in general a value of  $\tau_{emb}$  can be chosen for a given  $\kappa$  to yield very similar platelet distributions. This shows a similar over-parameterization problem as the modified-Goodman embolization model, and that either the embolization stress or exponent can be chosen somewhat arbitrarily. Selecting a higher power, however, led to increased platelet concentration at lower shear stresses at the inner half of the ring. Conversely, a lower power led to decreased platelet concentration at higher shear on the disk's outer rim. Considering it was beneficial to allocate more weight to points with higher radius, a power of  $\kappa=2.5$  was chosen, subsequently yielding  $\tau_{emb,W}=1.9369$ . The Platelet-Platelet embolization stress, having no reference from literature, was set based on the

Platelet-Platelet relative to surface embolization rate of the modified-Goodman scheme in the power law model. Accordingly,  $\tau_{emb,P} = 2.40 \tau_{emb,W}$ . The factor of  $2.40^{-2.5}$  represents the average value of the ratio of the surface and platelet-platelet embolization rates for  $\tau < 50 \text{ Pa}$ , of the modified-Goodman scheme with  $\tau_{emb,W} = 0.01$  and  $\tau_{emb,P} = 0.9$ . This approach led to the successful reproduction of thrombus formation patterns as observed experimentally by Taylor et al<sup>342</sup>, which are discussed in detail in the following section.

#### 4.2.2 Verification and Validation of Thrombosis Simulations

##### Grid Convergence Analysis for Thrombosis Formation in an LVAD

Grid convergence analysis is conducted on both the validation case and the open-hub LVAD case, each presenting similar grid spacings. For the validation case, both coarse and fine meshes were depicted, and the wall shear stress distribution was assessed. Figure 53 illustrates the shear stress distribution for both the fine and coarse grids in the validation simulation. Notably, no significant change was observed in the wall shear stress distribution between these two cases. Additionally, an adaptive grid refinement approach was employed, wherein the grid at the grid interface was refined (the platelet volume fraction gradient was utilized as a criterion with a normalized refinement criterion of 0.01). It was established that adaptive grid refinement levels exceeding one did not lead to an appreciable change in either the growth rate or the shear stress distribution on the thrombus.

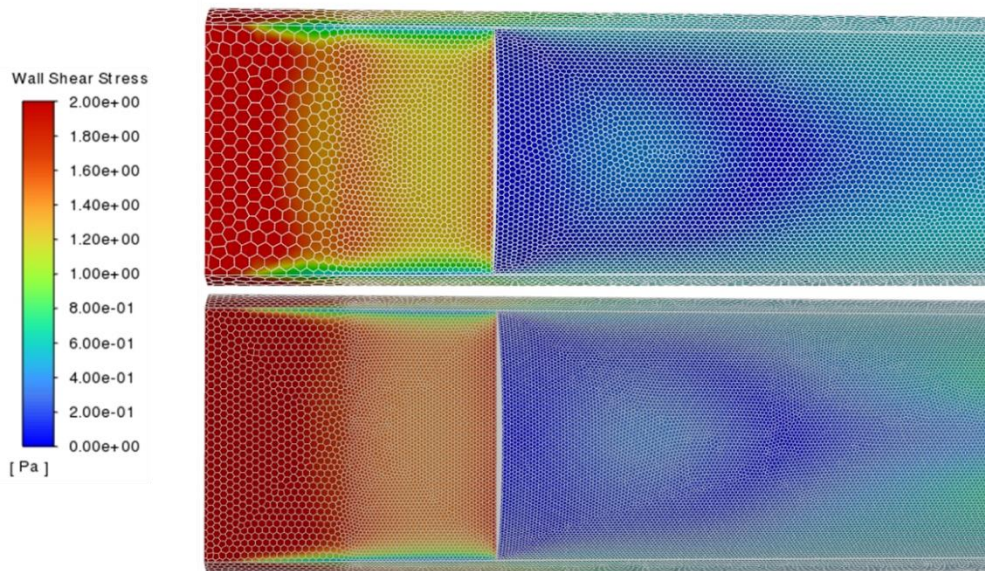


**Figure 53: Steady-state wall shear stress distributions in backwards-facing step validation case with fine (top) and coarse (bottom) polyhedral element computational grids in the area of interest where thrombus forms immediately downstream from the step.**



The process of grid refinement in the case of the LVAD is comparatively complex due to the numerous intricate features and flow phenomena that may be present. Grid convergence was addressed by studying the maximum and average shear stress on all wall surfaces, maximum hemolysis index in the domain, and total hemolysis index at the outlet, while adjusting the maximum grid spacing, the minimum grid spacing, and the number of inflation layers. The parameters of the proximity and curvature refinements remained unchanged as they scaled with the maximum and minimum grid spacing. The outcomes of these steady-state simulations are depicted in Figure 54, conducted at a rotor speed of 3000 RPM.

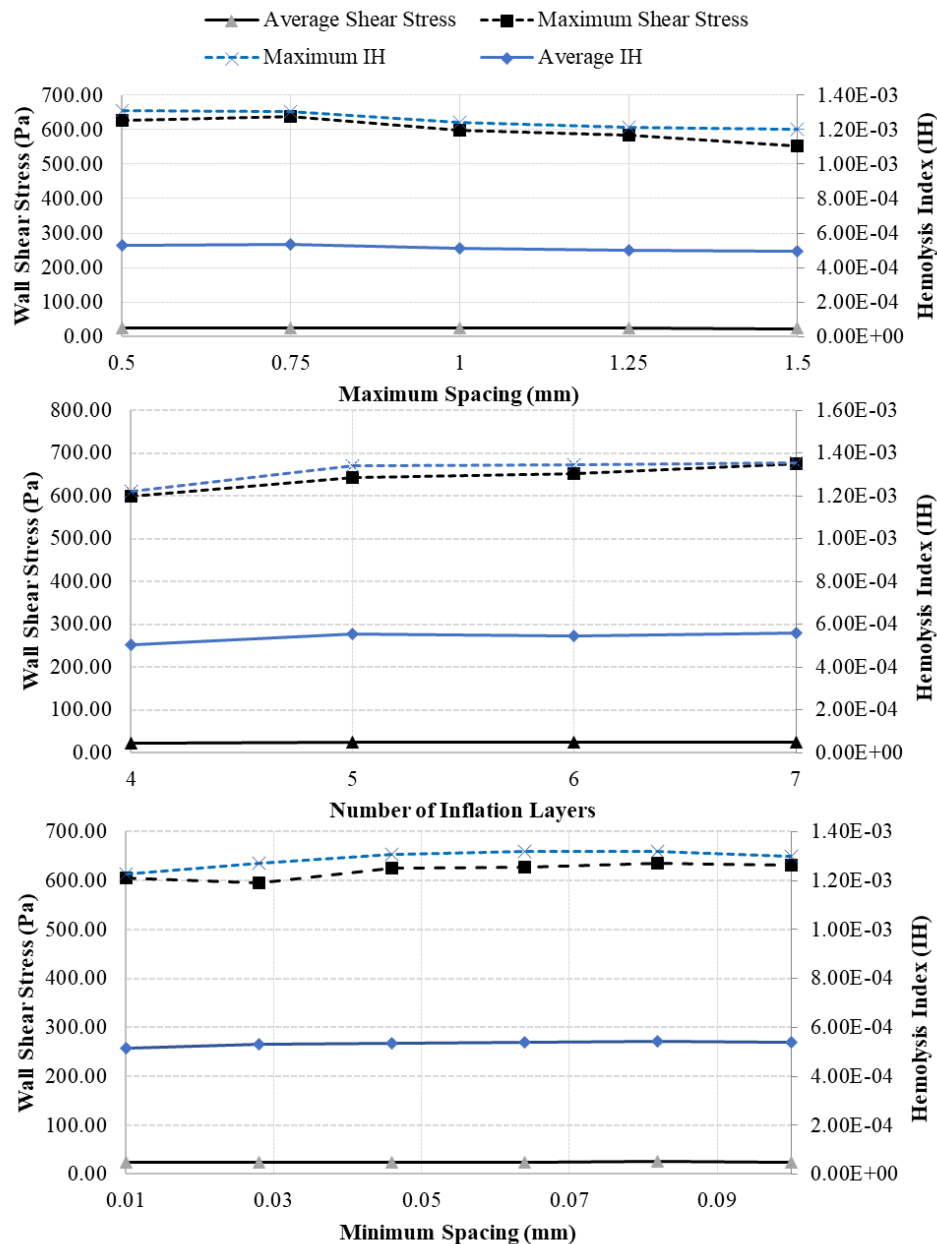


**Figure 54: Variation of maximum and wall-averaged wall shear stress and volume maximum and volume averaged hemolysis index with maximum grid spacing, number of inflation layers, and minimum grid spacing.**

As one might expect, the maximum wall shear stress, and maximum hemolysis index on surfaces, are most sensitive to the maximum grid spacing. This indicates that adequate grid spacing away from the walls must be ensured to effectively resolve detached vortex structures. Maximum shear stress, and maximum hemolysis index, vary by less than 10% at a maximum grid spacing, minimum spacing, and number of inflation layers of 0.75, 0.03, and 7, respectively. Therefore, values of 0.75, 0.05, and 5 are used for the maximum and minimum spacing, and the number of inflation layers, respectively.

A sensitivity analysis was also performed to examine the effect of hemolysis time scaling factors and platelet adhesion time scaling factors, carried out on the LVAD simulations. Figure 68 and Figure 69 in Appendix A demonstrates the effect on the overall thrombus growth rate between a case with a hemolysis and platelet adhesion time acceleration factor of 25, and another with 100. It was determined that the thrombus growth rate between the cases is identical, implying that the simulation is not sensitive to the time acceleration factors used to accelerate the vWF conversion process, hemolysis, and thrombosis adhesion processes.

#### Validation Over Backwards-Facing Step

The validation of our computational method against experimental data on thrombus formation was based on studies by Taylor et al.<sup>342</sup> and Yang et al.<sup>384</sup>. In these studies, a thrombus forms downstream from a backward-facing step at low Reynolds number in a circular channel flow. Taylor et al.<sup>342</sup> used Bovine blood for their experiment, while Yang et al.<sup>384</sup>, provide data for both bovine and human blood. Both studies utilized MRI imaging of the thrombus in their experimental setup to determine the thrombus' length, volume, and height. Additionally, they provide visuals showing the temporal variation of the boundary the thrombus, extracted from the MRI imaging.

There exists a significant discrepancy between the data from Yang et al.<sup>384</sup> and Taylor et al.<sup>342</sup>, with the viscosity of human blood measured by Yang being notably higher at 4.4 [cP]. Thus, to combine the datasets, a normalization procedure was required. Yang normalized their data by the length of the separation region, which is challenging to define in our case and furthermore not provided by Taylor. Therefore, considering the length of the separation zone is generally proportional to velocity and inversely proportional to viscosity, the Reynolds number was chosen as a normalization scale for both length and time. The length and time scales used for normalization were consequently defined as  $L_{Re} = \nu/U$  and  $t_{Re} = \nu/U^2$ . The normalized length equates to the Reynolds number based on the length of the thrombus. The

time-evolution of the length of the thrombus in the simulations is compared with both Taylor and Yang, as shown in Figure 55 and Figure 56. Post-normalization, the length values reported by Taylor and Yang show good agreement, suggesting the Reynolds length and time scales are appropriate for normalization. Taylor provides data for longer durations, but their data shows more scatter, particularly after 30 minutes ( $t/t_{Re} = 20.0 \cdot 10^6$ ).

The simulations in the present study generally agree with the experimental data; however, there is a noticeable discrepancy, especially during the initial growth phase. A top-view comparison of the simulations with the data of Taylor is provided in Figure 55. Taylor's data is preferred for visual comparison due to the longer time-frame reported. During the initial growth phases, the thrombus does not grow in the same way in simulations as observed in the MRI data. In the present study, platelets gradually accumulate over a large surface area all at once, rather than rapidly growing outwards from the vertical step face.

Furthermore, in the simulations, length, initially calculated as  $\max(\phi_{Pad}x)$ , rapidly grows as the near-wall elements start to fill and then saturates; the sigmoid shape reflects the increase in volume fraction at the peak more than a gradual growth. Due to uncertainties in the measurement procedure and the volume fraction interval used to create the contour in the MRI images, it is more appropriate to use the average length, computed as 3 times the distance of the centroid from the step (i.e.; volume fraction weighted average streamwise distance). This relationship corresponds to measuring the length by idealizing the thrombus as a rectangular pyramid and de-emphasizes the near-wall elements of the thrombus. This is furthermore somewhat more congruent with the experimental measurement scheme because the minimum size of the near-wall elements is in general approximately 1/5 the finest theoretical spatial accuracy of the MRI. By employing this method, our simulation results show better agreement with the experimental data.

Subsequently, the thrombus grows uniformly as it moves past the initial wake region, though once it begins to experience increasing shear outside of the wake growth slows.

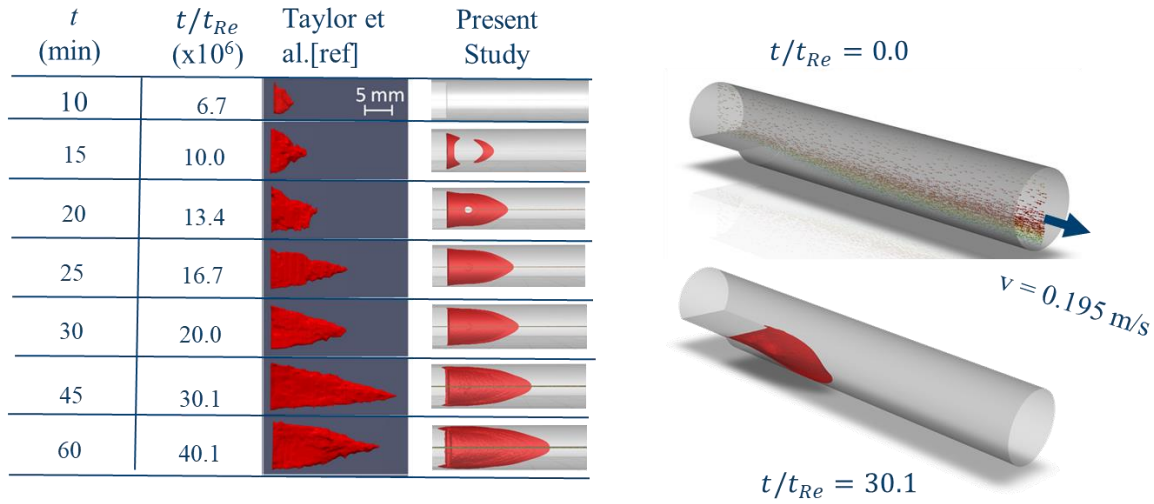


**Figure 55: Top-view of thrombus formed downstream from a backward-facing step in a 10mm diameter tube (modified-Goodman model), visualized as isosurfaces of platelet volume fraction,  $\phi_{pad} = 0.1$ , to the MRI imaging experiments from Taylor et al.<sup>342</sup> using bovine blood.**

Broadly speaking, both the power-law and modified-Goodman embolization schemes provide nearly identical results in our simulations. However, the power-law scheme demonstrates a slightly better fit to the data by delaying the onset of thrombus growth. This subtle difference underscores the efficacy of the power-law scheme in capturing the nuanced dynamics of thrombus formation. The simulations reveal that the platelet growth rate is profoundly influenced by the formulation of the embolization regime, as small variations in the embolization scheme had a very large effect on the thrombus growth rate. Therefore, the selection and calibration of the embolization regime should be performed with meticulous care to ensure the reliability of the simulation results.

The discrepancies between the current study's results and experimental findings may arise from differences in the actual and simulated shear stress distribution. These differences can be attributed to several factors. Firstly, turbulence is not modelled in these simulations (as the Reynolds number of the flow is quite low  $\sim 570$ ), causing the separation region to be longer than it should be. This is because the flow regime is a classical laminar free-shear layer (or separation bubble) flow, where the much more unstable separated shear layer rapidly transitions to turbulence and reattaches. The result would be a much shorter low-shear separation region and thus a lower initial thrombus length. As there is not a turbulence model, this is not accounted for, but indeed even if turbulence is modelled, the inadequacies of current turbulence models for blood leave doubts as to whether this could be captured. The extended separation region results in low shear regions away from the step, and thus the thrombus pattern

that is observed in the simulations. Moreover, the inlet region might not be sufficiently long to allow the flow to adequately develop, leading to a longer wake region ( $Re_L = 567$ ), which may affect the dynamics of thrombus formation. Furthermore, in the simulations, the fluid was modelled as a Newtonian fluid with a viscosity of 3.5 [cP]; this was a limitation as the shear rate where the thrombus grows is well within the non-Newtonian regime.

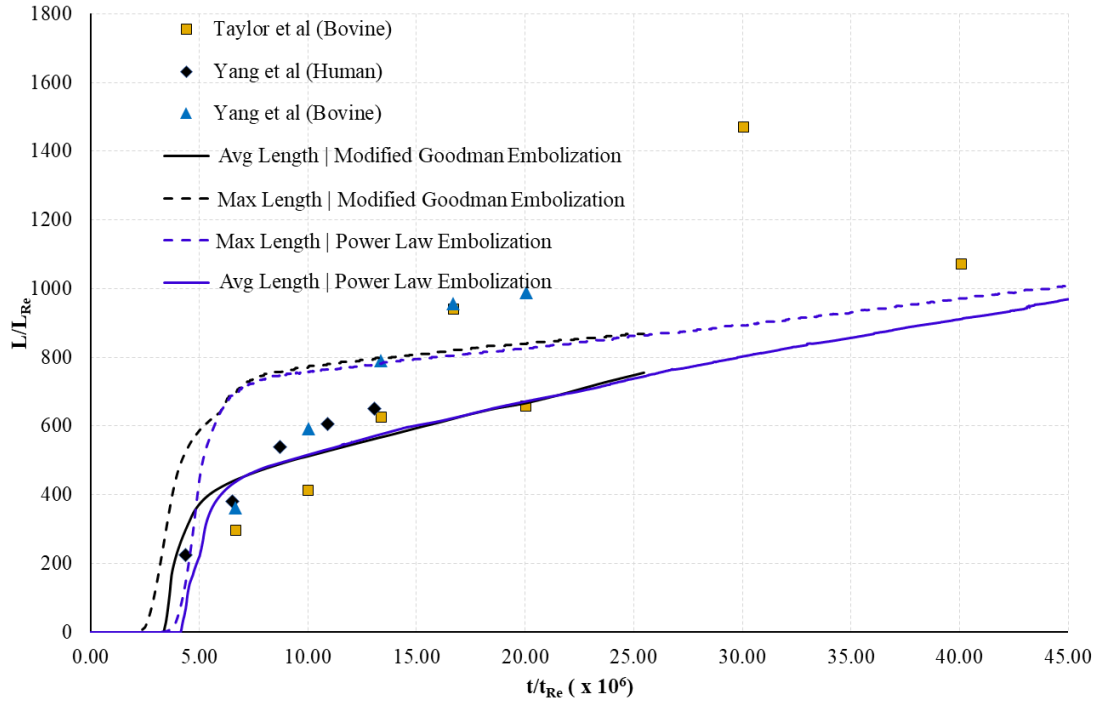


**Figure 56: Quantitative comparison of thrombus length formed downstream from a backward-facing step with Yang et al.<sup>384</sup> and Taylor et al.<sup>342</sup>. Average Length is computed as  $3 \int x \phi_{P_{ad}} dV / \int \phi_{P_{ad}} dV$ .**

All these hemodynamic factors could contribute to an overall lower wall shear stress in the wake region immediately downstream from the step. Further studies could focus on refining the model to address these aspects to better capture the complex interplay of factors that affect thrombus formation.

#### 4.2.3 Simulation of Hemolysis and Thrombosis

To examine the influence of hemolysis on thrombus formation within an LVAD, Computational Fluid Dynamics (CFD) simulations were conducted using the thrombosis model on an open-hub LVAD geometry, as outlined in Section 2.5. Simulations were generally carried out at three rotor speeds, corresponding to the minimum and maximum rotor speeds needed to yield 80-120 mm Hg of outflow pressure. The baseline geometry, optimized by Bao<sup>410</sup>, was devised to enhance hemolysis and pressure. For this study, a variant geometry was selected that produced sublethal hemolysis levels at the lower rotor speed and lethal hemolysis levels at the

higher rotor speed. Initially, the hemodynamics were scrutinized to understand the general characteristics of the flow. Following this, the hemolysis and von-Willebrand Factor adhesion were assessed. For clarity and ease of interpretation, time is usually depicted in terms of thrombus time, which is 100 times faster than flow time and 4 times faster than hemolysis time.

The flow dynamics attain a statistical steady state after approximately 0.1s of flow simulation time. The thrombosis and hemolysis model is then activated only post this duration in all LVAD cases. This approach aids numerical convergence as the high shear stresses during the initial transient phase of the simulation might instigate excessive and nonphysical hemolysis and platelet activation. The analysis was conducted after 15 minutes of thrombus time (10 s of flow simulation time). The inflow rate remains constant for all cases at 4.5 L/min.

#### Hemodynamics in an Open-Hub LVAD

Figure 57 displays the distribution of velocity magnitude as a flood plot image of a plane bisecting the LVAD through its central axis at the three different rotor speeds after 15 minutes of thrombus growth.

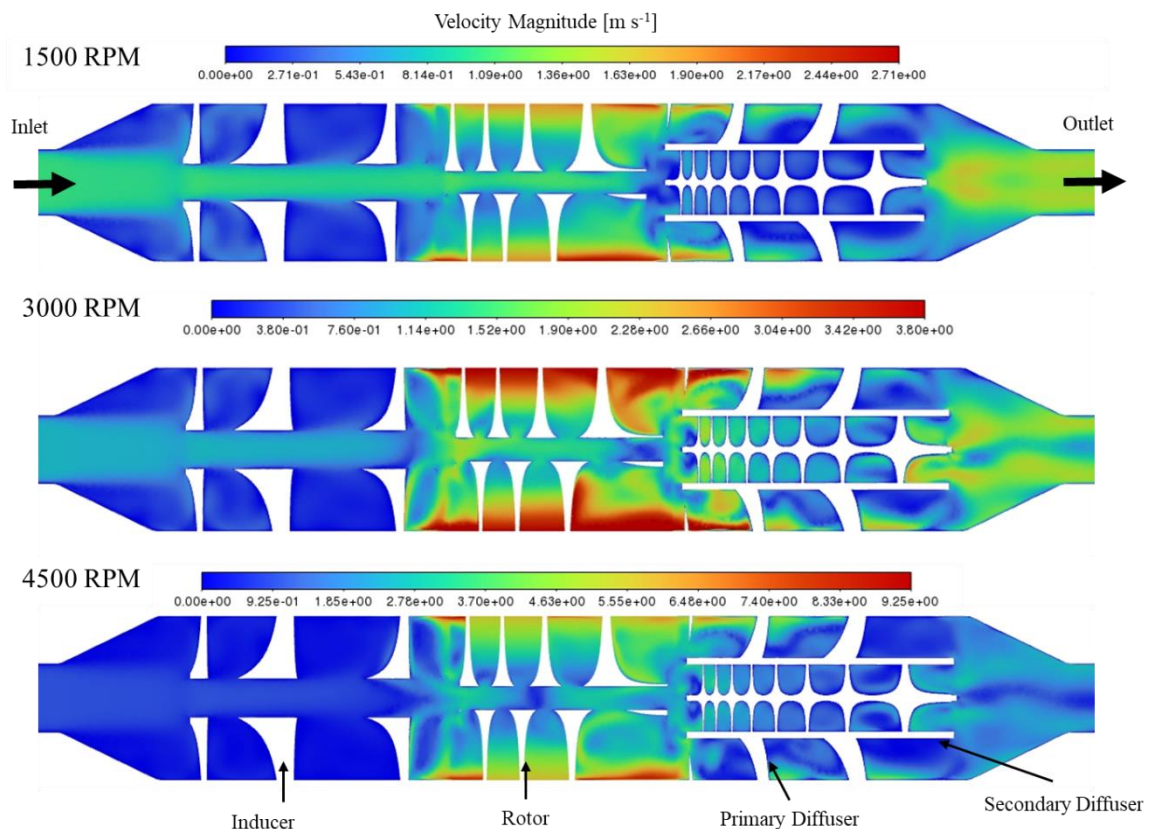


**Figure 57: Flood plots of velocity magnitude at three characteristic rotor speeds of the open-hub LVAD. Velocity magnitude is scaled with peak global velocity in the domain. Images are extracted from transient simulation data after quasi-steady state is reached (10 s flow-time).**

The visualization of velocity magnitude, as portrayed in Figure 57, offers insights into the spread of flow structures and wake regions. The flood plot legend is scaled according to the domain's peak velocity magnitude, thus highlighting areas of maximum velocity, and consequently, maximum shear. Predictably, the maximum velocity is detected at the rotor edge, where the rotor tangential velocity is highest, especially near the junction of the rotor and diffuser, where the axial velocity is likewise at its peak. In terms of hemolysis, it is instructive to identify high shear regions, which correlate with areas demonstrating the largest velocity magnitude gradients. These regions, as depicted in Figure 58, are found at the diffuser inlet, the rotor walls, and downstream from the open hub in the inducer where a free shear layer forms. A particularly high degree of shear and, consequently, hemolysis, is expected inside the secondary diffuser inlet owing to the small dimensions of the channels.

When examining thrombosis, it is beneficial to broadly examine flow regions characterized by low momentum. Such low momentum regions (represented in deep blue) are generally located downstream from bluff bodies, inside vortex cores, and in sharp corners. Such low momentum regions are observable at all three rotor speeds, most notably downstream from the inlet where two large flow separation regions emerge on either side of the inflow jet due to the abrupt divergence angle of the inducer from the inflow.

The open hub LVAD, by design, allows inflow to pass unrestricted through the core region, which typically reduces the momentum at the periphery of the inducer. This creates low momentum stagnation regions inside of the inducer. Such low momentum regions are also found in abundance inside the secondary diffuser, contrasting with the primary diffuser, which suffers from a degree of reverse flow. In all cases, downstream from the diffuser, a substantial vortex exists at the outlet (represented as a filament of low momentum in its core and high momentum towards the outlet walls), induced by an inefficient de-swirling process in the diffuser.

Recirculation regions, such as those found downstream from the inflow jet, are critical as they correspond to areas of high recirculation time, where blood cells can become trapped for long times on the order of 0.1s. Consequently, hemolysis can occur due to prolonged exposure of entrained blood to lower, but substantial shear stress.

Figure 58 illustrates the distribution of shear stress on the LVAD walls at 3000 RPM and the distribution of von-Mises stress through a plane bisecting the LVAD's central axis. The shear stress distribution, depicted in Figure 58, utilizes exponential scale contour plots to effectively



capture the broad range of shear stresses experienced within the LVAD. Peak stress (full domain peak is 775 [Pa]) typically occurs on surfaces interacting with high momentum fluid, such as the impeller outlet, and the primary and secondary diffuser inlets. These are the major sources of hemolytic activity. Regions with low momentum, such as vortex cores, can result in stagnation points on a surface, leading to very low shear stress. These flow stagnation zones naturally accumulate extracellular hemoglobin, platelets, and thrombo-agonists. Corners and wakes also characteristically present low shear stress due to the constraint of flow in two directions and the consequent stagnation points that occur.

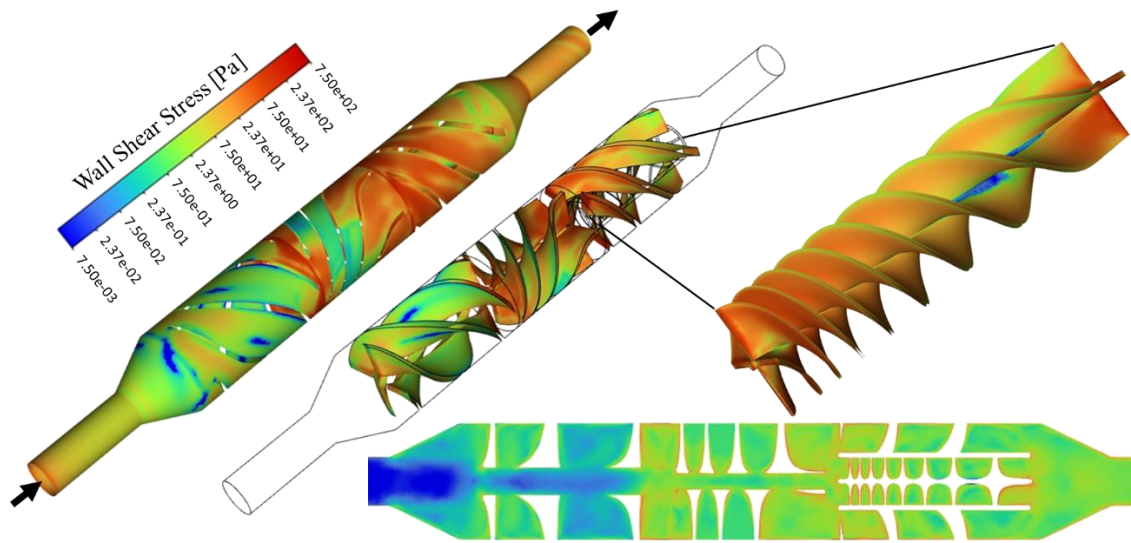


**Figure 58:** Flood plots of shear stress on the LVAD surfaces, and of von-mises stress on a plane passing through the LVAD central axis, at 15 minutes thrombus time at 3000 RPM. A logarithmic scale is used to illustrate the huge variation of shear stresses experienced.

#### Hemolysis in an Open-Hub LVAD

Figure 59 illustrates the mass-average value of the hemolysis index (IH) at the LVAD outlet. It ranges from a sub-hemolytic level at 1500 RPM (0.3%) to 5.2% at 4500 RPM. Hemolysis converges quite swiftly within the first few minutes of thrombus growth, as the hemolysis equation is sped up by the same factor that accelerates the  $vWF$  and  $vWF_{ha}$  equations.

This is more representative of reality, as the hemolytic convergence time is considerably quicker than the hyper-adhesive  $vWF$  convergence time, as shown in Figure 61, which is in turn slower than the thrombus convergence time. This was intentionally designed to ensure that the faster equations reach an equilibrium state relative to the slower equations.



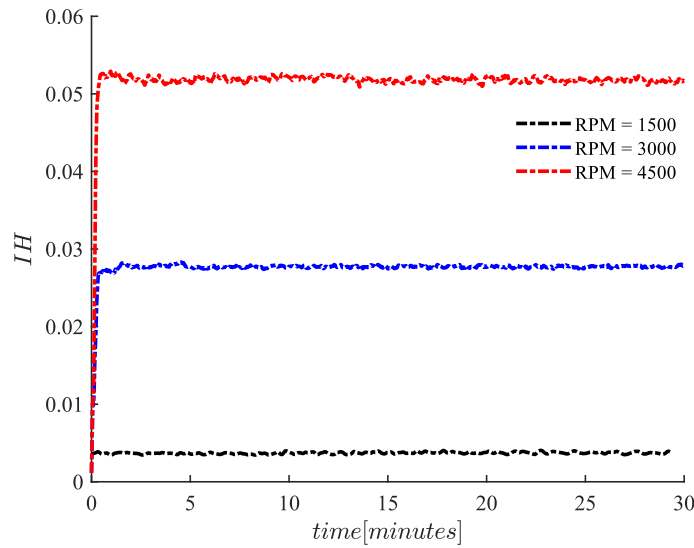


**Figure 59: Variation of mass-flow averaged Index of hemolysis at the LVAD outlet at various rotor speeds with thrombus time.**

The distribution of hemolysis index in the domain is shown for the 3000 RPM case in Figure 60, as flood plots on a plane passing through the central axis of the LVAD. From Figure 60, it is observed that the highest concentrations of the hemolysis index occur directly downstream of the impeller. These high-concentration areas are usually found in regions with low momentum (that generally correspond to vortex cores), which allowing for the accumulation of hemolysis through convective entrainment. Specific areas like the secondary diffuser and downstream wakes from the inducer present local peaks. Additionally, stagnation zones near the impeller's walls also show local IH peaks. As a mechanical dose formulation for hemolysis index, which only necessitates a single equation, diffusion is essentially not modelled for plasma free hemoglobin. As hemolysis is related to the mechanical dose by,  $IH = D^\alpha$ , the diffusion coefficient of hemoglobin is not easily translated to diffusion of mechanical dose.

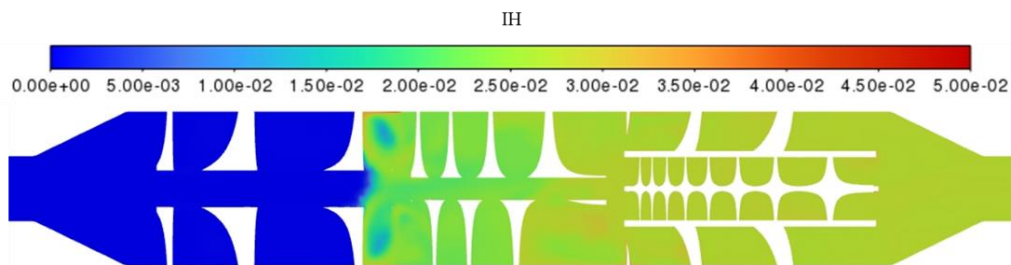


**Figure 60: Flood plot of hemolysis index at 3000 RPM after 15 minutes of thrombus time.**

#### Conversion of vWF Into Hyper-Adhesive Von-Willebrand Factor

The time-variation of maximum hyper-adhesive vWF concentration and the corresponding maximum platelet hyperadhesion factor,  $k_{\text{hemo}}$ , reach a general steady state by approximately 15 minutes. Peak  $vWF_{\text{ha}}$  concentrations reach approximately 54% of the initial vWF

concentration of  $3.7 \cdot 10^7$  [nmol m<sup>-3</sup>]. This is sufficient to lead to a very high local hyperadhesion factor of 6.2. This is somewhat misleading however, as the domain peak of maximum  $vWF_{ha}$ , occurs inside of the thrombus, and it is unclear if this preceded thrombus formation and facilitated its development, or merely occurred inside of the thrombus due to the flow sheltering effect that thrombus generally have on blood constituents.

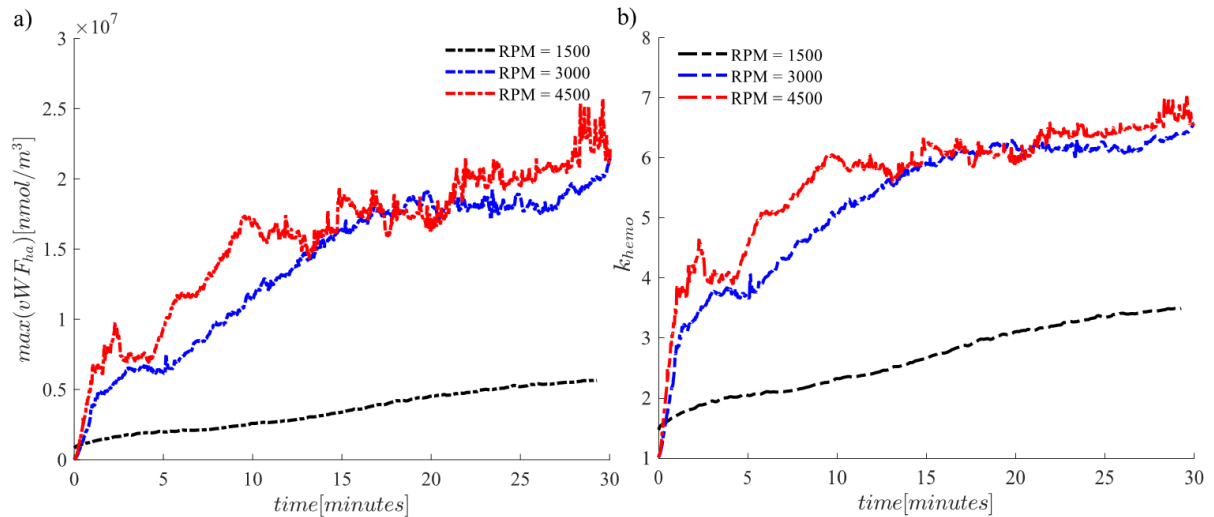


**Figure 61: Variation of a) Maximum value of hyper-adhesive vWF ( $vWF_{ha}$ ) and b) Maximum platelet hyperadhesion factor in the domain with thrombus time.**

The distribution of hyper-adhesive vWF is shown in Figure 62. Accumulation of hyper-adhesive vWF is interesting because, due to the very long production time of vWF and the relatively short time it takes a fluid packet to enter and leave the LVAD (generally on the order of 1-10 ms), it is mainly possible for significant vWF to be fully converted inside of a stagnation or recirculation zone, where there is little fluid velocity and thus low outward flux. Accumulation of  $vWF_{ha}$  also occurs inside of thrombus, where in fact the domain peak values of  $vWF_{ha}$  are found, as shown in Figure 62 at the surface in the inset.

As noted, there is a kind of paradox where thrombus formation aids in facilitating hyperadhesion by slowing down the flow locally, allowing the long pFHb-vWF reaction to proceed to completion, but the effect of hemolysis has a relatively limited effect on the initiation of thrombus. For instance, the local platelet hyperadhesion factor is shown on the surfaces of the LVAD at 15 minutes thrombus time at 3000 RPM in Figure 64.

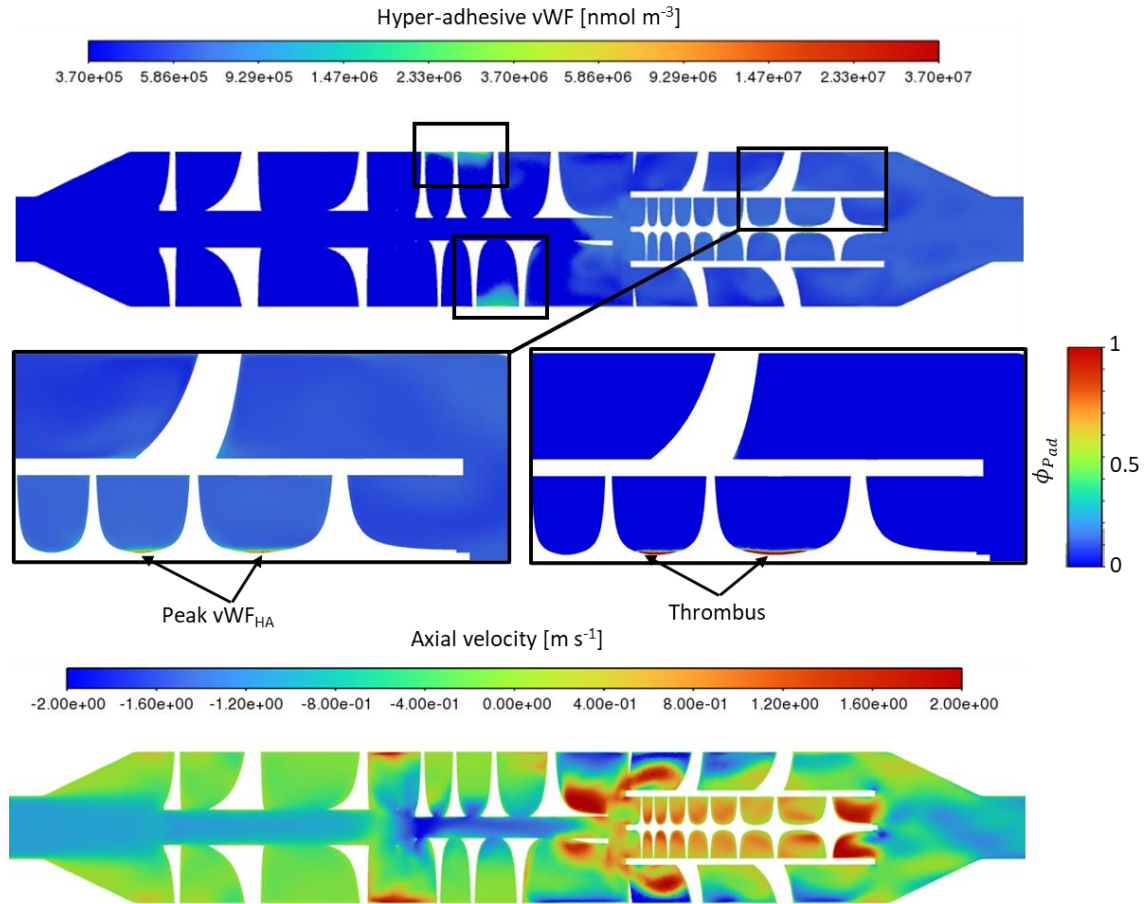


**Figure 62:** Flood plots in a plane bisecting the central axis of the open-hub LVAD at 3000 RPM of (top) hyper-adhesive vWF, (middle-right) platelet volume fraction, and (bottom) axial velocity at 15 minutes thrombus time, illustrating the spatial distribution of  $vWF_{ha}$ . Peak values of  $vWF_{ha}$  are indicated by the black boxes.

The peak hemolysis index and likewise  $k_{hemo}$  was found inside of the secondary diffuser at the core, but appreciable platelet hyperadhesion multiplying the platelet adhesion rate by a factor of 2 is found on non-thrombogenic regions such as the impeller surface and at the outer edges of the impeller blades, where no thrombus is present due to the relatively high shear in the impeller region. In these regions, it is possible, however that if rotor speed increased and there is more hemolysis, and the hemolytic fluid containing extracellular hemoglobin passed over a wake region, a confluence of high hemolysis and stagnation zones would allow the hyper-adhesive effect of extracellular hemoglobin to induce thrombogenesis in locations where it was not previously possible.

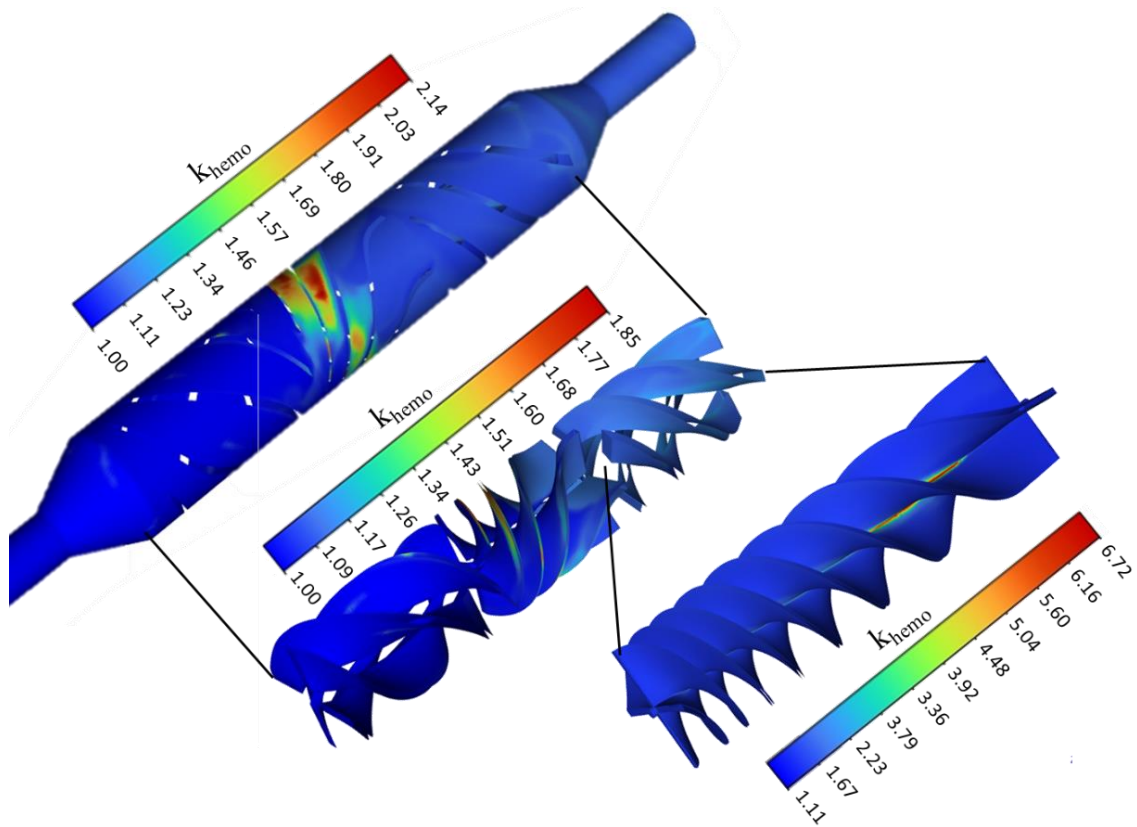


**Figure 63: Flood plots of platelet hemolysis induced hyperadhesion factor,  $k_{Hemo}$ , at 3000 RPM at 15 minutes thrombus time, indicating the spatial distribution of the local effect of hemolysis on LVAD walls.**

#### Examining the Effect of Hemolysis on Thrombosis in an Open-Hub LVAD

Figure 64 shows the variation of thrombus volume over time in the LVAD at three different rotor speeds, and either the effect of ADP released during hemolysis, vWF hyperadhesion, both or neither. Unsurprisingly, thrombus formation in LVADs is most significantly influenced by the speed of the rotor. As rotor speed increases, the rate of thrombus growth decreases due to increased shear stress in the impeller and downstream inducer and the consequent increase in platelet embolization rates. Higher wall shear stress in general are considered as conditions less favorable for thrombus formation. Interestingly, at lower rotor speeds, specifically at 1500 RPM, adenosine diphosphate (ADP) release plays a significant role in initiating thrombus growth. Evidently, the lower shear stress at this speed amplifies the impact of ADP on platelet activation, and a relatively low hemolysis index can trigger thrombus growth slightly earlier, around one minute earlier than in other conditions. Despite this, the overall rate of thrombus growth does not significantly differ as the effect of hyperadhesion is muted. Conversely, at higher rotor speeds (3000 and 4500 RPM), the initiation time of thrombus remains constant, but there is a noticeable increase in the overall growth rate. Compared to non-hemolytic cases, there is a 10.7% and 12% growth rate increase at 3000 and 4500 RPM, respectively.

Interestingly, at 3000 RPM, ADP release has a negligible impact, but it contributes to 4% of the growth rate increase at 4500 RPM. The primary factor driving the increased growth rate at these higher speeds is hyperadhesion. Therefore, at these elevated rotational speeds, the relationship between hemolysis and thrombus formation becomes more complex, hinting at the intricacy of balancing rotor speed and hemolytic effects to manage thrombus formation.

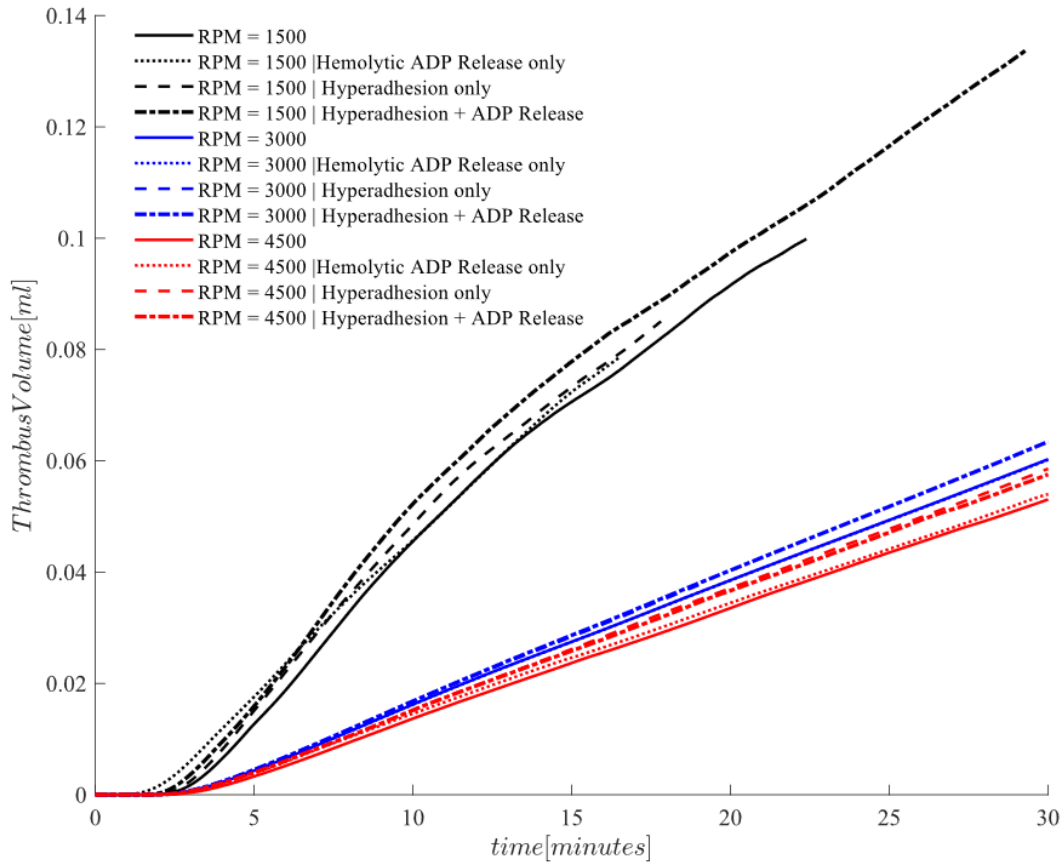


**Figure 64:** Variation of total thrombus volume in the LVAD over the domain at three rotor speeds, without hemolysis modelling (solid), with hemolysis modelling where  $k_{Hemo}$  is set to 1 (dotted), with hemolysis modelling where no ADP is released during hemolysis (dashed), and where both interactions are modelled (dash-dot).

At 15 minutes of thrombus time, Figure 65 illustrates substantial thrombus formation in the LVAD, especially prominent at lower rotational speeds. The baseline geometry of the LVAD inherently exhibits a high degree of thrombogenicity. As the RPM increases, thrombus formation in the rotor and diffuser regions is significantly reduced, though it persists in the inducer region. Again, areas of thrombus formation generally align with the regions of low shear stress demonstrated in previous analysis, underscoring the relationship between shear stress distribution and thrombus formation in the LVAD.



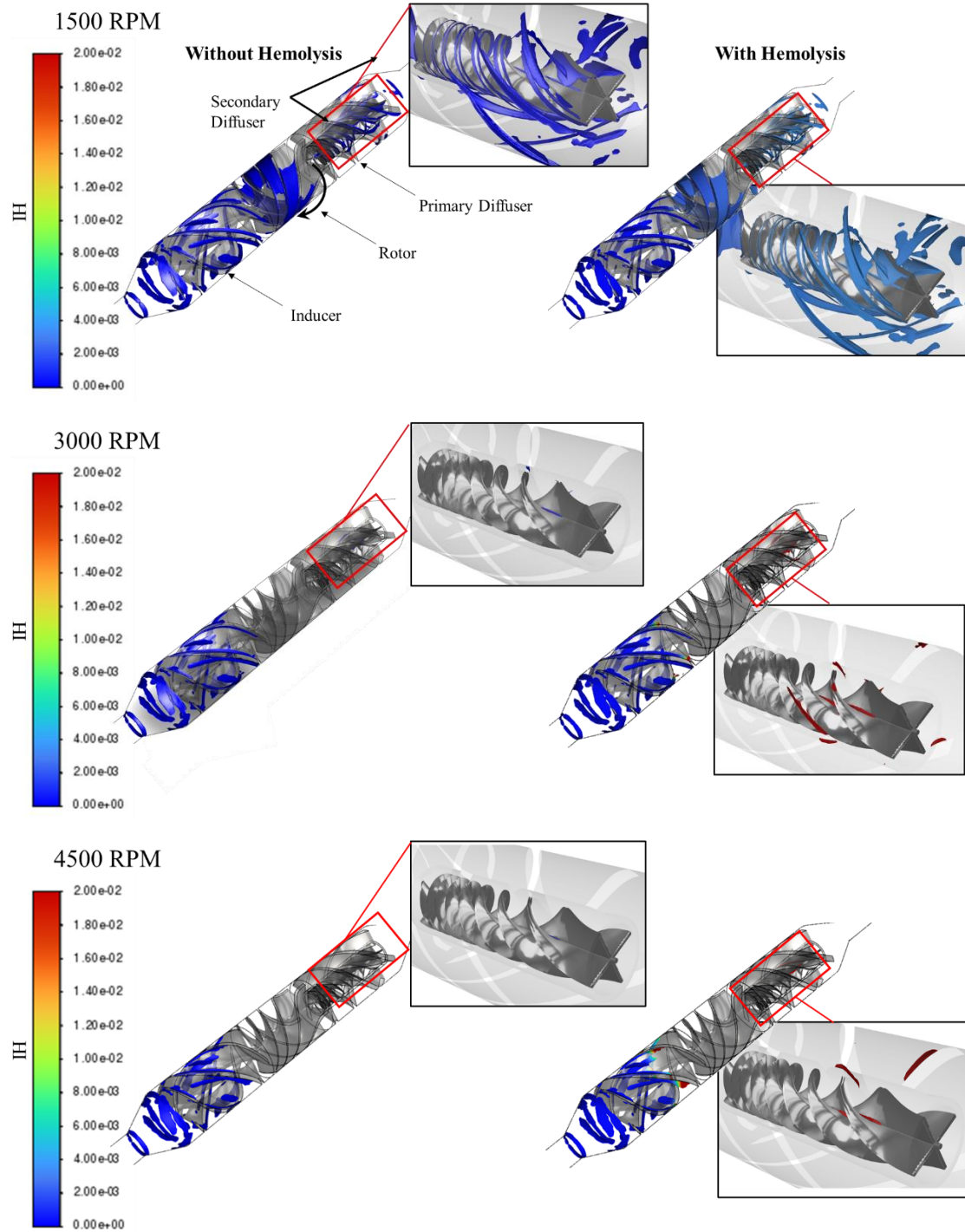


**Figure 65: Illustration of Thrombus (Isosurfaces of deposited platelet volume fraction,  $\phi_{pad} = 0.1$ ) at three rotor speeds extracted at 15 minutes thrombus time, illustrating the effect of hemolysis at various RPM. Isosurfaces are colored by index of hemolysis to indicate thrombus where hemolysis has a large effect (Cases without hemolysis  $IH = 0$  as it is not simulated).**

The transient nature of the flow within the LVAD means that the locations of low-shear regions, where thrombus formation is most likely, can shift. This could potentially limit thrombus development. Additionally, these simulations used a frozen rotor approximation, and in reality,

the shear stress field would likely be even more transient due to rotor movement, which would further reduce thrombus formation. Visualizations of thrombus, represented by isosurfaces of platelet volume fraction,  $\phi_{pad} = 0.1$ , are color-coded by hemolysis index to distinguish thrombus influenced by hemolysis (red) from those that are not (blue).

Non-hemolytic thrombus formation appears in all cases at the corners and in the recirculation region downstream from the inlet separation region. However, higher shear in the impeller and diffuser regions effectively embolizes non-hemolytic thrombus in those areas. Increased hemolysis levels seem to foster the formation of smaller thrombus in the diffuser region, including in some places where thrombus had not previously grown. This suggests that significant upstream hemolysis could potentially instigate thrombus formation in high-shear areas.

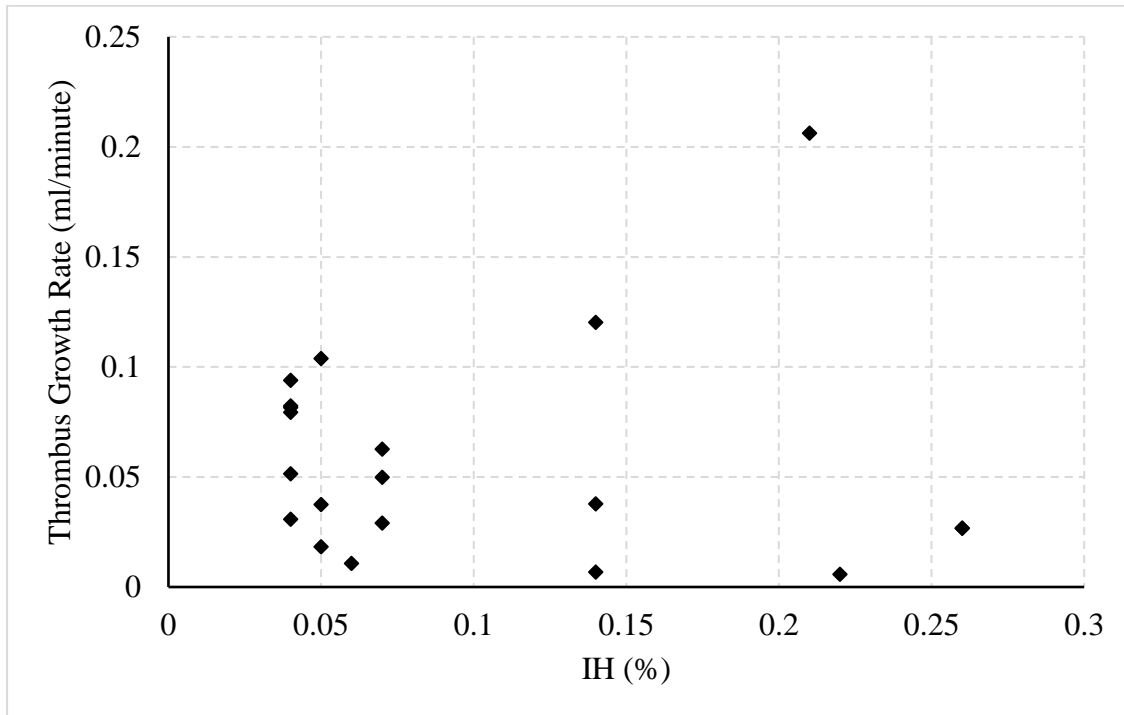
#### 4.2.4 Designing Blood-Wetted Devices to Minimize Thrombosis

##### Parametric Design Study of LVAD Geometry and Operation to Minimize Hemolysis

To elucidate the effects of an LVAD's geometric and operational parameters on thrombus growth rates and hemolysis, as well as their interplay, an automated geometry generation and CFD post-processing tool, CAESSES, was used to carry out a preliminary design optimization. This process led to the generation of 30 distinct geometric variants, each tested at 1500, 3000, and 4500 rpm. The design parameters, 16 selected from the total of 72 that fully defined the LVAD geometry, were varied using the SOBOL algorithm. This algorithm facilitates random sampling in an N-dimensional space uniformly without favoring the centroid region. Hemolysis was modelled for each variant, with simulations running for 10 minutes of thrombus development time. Out of the 30 generated variants, 10 were excluded due to diverse reasons including numerical divergence before reaching the 10-minute thrombus time, inadequate mesh quality (below the minimum specified quality of 0.15 in Ansys Fluent solver), or issues arising during the meshing step such as excessively small gaps or geometric self-intersections.

The maximum thrombus growth rate and hemolysis index among the three speeds for each variant are presented in Figure 66. Overall, the wide design space sampled and the limited number of points made it challenging to establish a definitive trend between hemolysis index and thrombus growth rate. Interestingly, however, it was found that many geometries could be highly thrombogenic but not hemolytic, and vice versa, and others exhibited cases of both, likely due to the inverse effect of shear stress. Often, however, better performing geometries

experienced both hemolysis and thrombosis. For the purpose of this study, the focus was predominantly on thrombogenicity rather than performance.



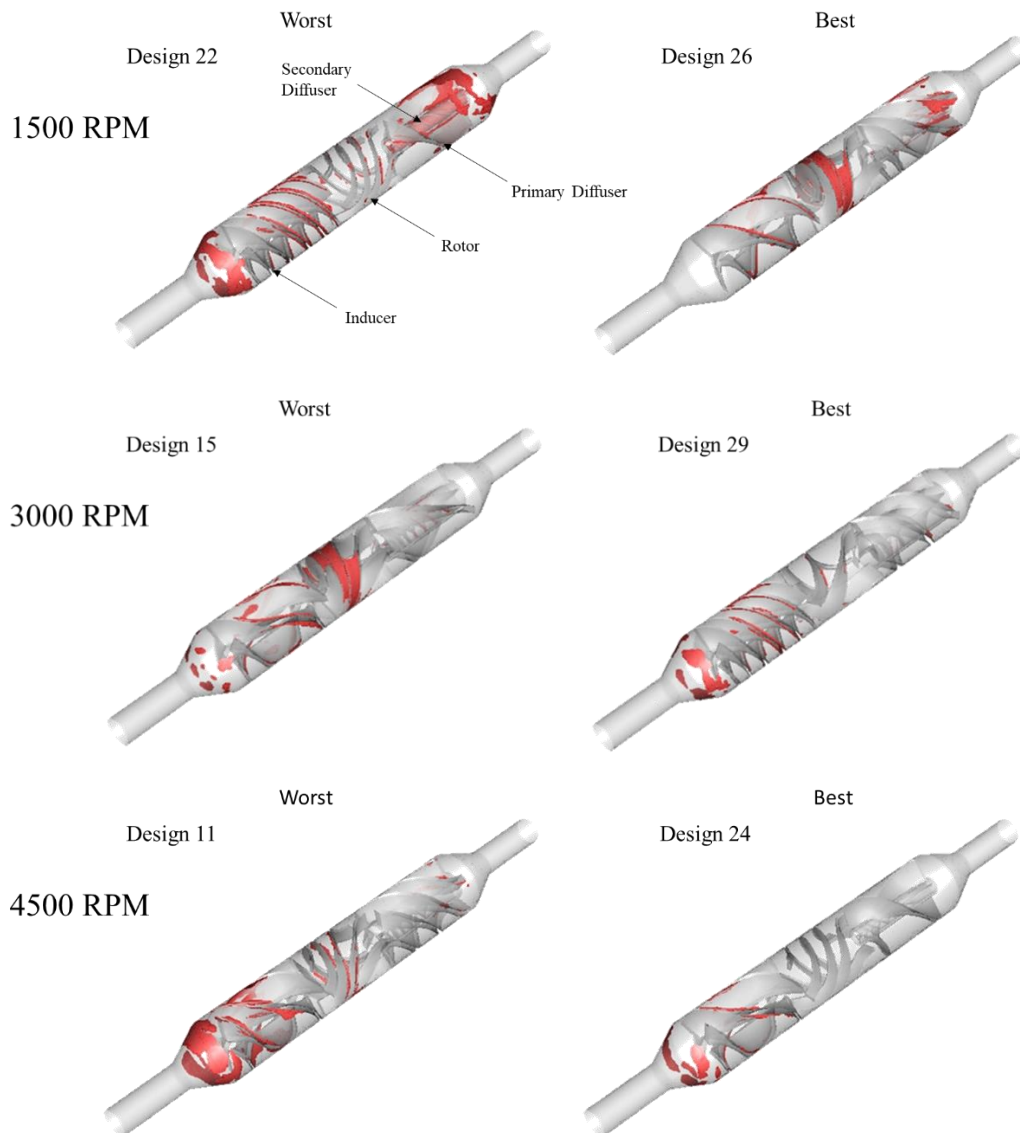
**Figure 66: Design of experiments illustrating the effect of hemolysis on thrombus growth rate. Each dot is a unique (and random) geometric configuration at 3000 RPM, overall 30 unique geometries are simulated, 10 experienced numerical instability, leaving 20 points.**

Figure 67 presents a comparison of the best and worst cases across three rotor speeds, shedding light on how various design elements impact thrombogenic risk. Key insights include a general trend indicating that higher blade area, increased blade count, are associated with heightened thrombogenic risk. For lower rotor speeds, determining a design with minimum thrombogenic potential proved challenging due to inherent limitations; any stagnation zone can catalyze thrombosis. Interestingly, the thrombus formation at the inlet induced by the flow separation region was effectively mitigated by expanding the inner hub diameter of the inducer and reducing the blade count. This adjustment caused the inflow jet to spread more evenly, thus reducing flow separation.

As a rule of thumb, enlarged blade surface area tends to heighten both hemolysis and thrombosis, albeit at the cost of increased pressure output. Many thrombi observed in the inducer were situated at the corners, a challenge potentially resolvable by the introduction of corner fillets to the blades. In a notable instance, as seen in the worst-case scenario at 1500



RPM, an overly small secondary diffuser became highly thrombogenic due to excessive flow constriction creating stagnation zones.



**Figure 67: Effect of geometric opetimizaition to reduce thrombogenesis at three rotor speeds at 10 minutes thrombus time. Thrombus regions are indicated in red.**

A sensitivity analysis was undertaken to probe the influences of LVAD's geometric and operational parameters on thrombus growth rates, which is summarized in Table 10. Note that graphical illustrations of design parameters can be found in Bao<sup>410</sup>. This was accomplished by constructing a least-squares fit of an N-dimensional plane to the data, enabling the computation of the thrombus growth rate gradient relative to the parameters. Each parameter was normalized by its range, allowing the sensitivity to reflect the relative change across the parameter range. A negative sensitivity implies a decrease in thrombus growth rate with an increased parameter value. For instance, rotor speed displayed a negative sensitivity as increasing RPM

correspondingly reduced the thrombus growth rate. The analysis considered several factors including blade divergence, the number of turns, inflow and outflow plane angles, and the number of blades. "Blade divergence" refers to the growing gap between the blades or the increasing blade pitch in the axial direction.

**Table 10: Normalized sensitivity of thrombus growth rate to changes in geometric and operating parameters.**

parameter names			Thrombus Growth Rate	Parameter Values			
			(ml/minute)				
			normalized sensitivity	sensitivity	mean value	max value	min value
Primary Diffuser Blade Divergence			0.097	0.144	0.614	0.881	0.31875
Inducer Blade Divergence			-0.028	-0.0400	0.517	0.687	0.3125
Impeller Blade Divergence			0.197	0.899	0.282	0.487	0.125
Impeller Blade Area (# Turns)			0.70	0.672	0.740	0.456	0.981
Induce Blade Area (# Turns)			0.085	0.0849	0.772	1.038	0.441
Diffuser Blade Area (# Turns)			0.082	0.0949	0.688	0.9125	0.365
Rotor Speed (RPM)			-0.22	-8.95E-05	3000	4500	1500
Primary Diffuser - blade angle with outflow plane			~0	0.0000631	13.5	28.13	1.88
Primary Inflow/outflow tangent weight	Diffuser plane angle	-	-0.263	-1.24	0.143	0.197	0.1
Impeller blade angle with outflow plane			0.0161	0.00158	17.6	32.8	2.19
Primary diffuser – No. blades			0.0431	0.0103	4.10	6	2
Secondary Diffuser – No. blades			-0.073	-0.0197	3.85	6	2
Impeller – No. blades			0.512	0.079	4.50	6	3
Inducer – No. blades			-0.0556	-0.0119	3.75	5	2
Impeller Diameter Ratio			-0.057	-0.218	0.402	0.733	0.108
Secondary Diameter	Diffuser	Outlet	0.349	0.350	0.622	0.788	0.400

Among all factors, it was the impeller's characteristics - its blade divergence, area, and number of blades - that had the most substantial impact on thrombogenicity. The "number of turns" denotes how many times a blade completes a circular path when viewed from the axial direction, which essentially quantifies the normalized blade area. The secondary diffuser tangent weight, indicating the length of the flat region at the diffuser's leading or trailing edge, also played a significant role. As the tangent weight increases, the flow entering the diffuser

slows down more gradually, lessening the hemolysis due to decreased blood stress. Interestingly, an enlarged outlet diameter appears to be thrombogenic, presumably because it enhances the extent of flow separation downstream from the secondary diffuser. On the contrary, reducing the outlet diameter decreases the size and intensity of the secondary streamwise vortex that forms downstream from the outlet, thereby mitigating thrombus formation.

#### **4.2.5 Summary of Findings and Contributions**

The validation of the model provided encouraging results. Existing embolization schemes were modified to rectify discrepancies in the literature on embolization timescales, and two new single-platelet embolization models were proposed: the Power Law model and the modified-Goodman model. The validation study revealed that both models reproduced MRI imaging of thrombus formation downstream from a backward-facing step, relatively accurately up to 30 minutes of flow time. The Power Law model, proved to be slightly more accurate and simpler than the modified-Goodman model when it came to predicting the growth rate of thrombus length.

The investigation on the interactions between hemolysis and thrombosis in left ventricular assist devices (LVADs) has yielded some interesting insights. The results confirm that hemolysis exhibits a mild but notable influence on thrombosis, affecting thrombus formation in distinct ways depending on the rotational speed of the LVAD. Furthermore, the study delves into the mechanisms through which hemolysis influences thrombosis, especially through ADP release and hyperadhesion caused by the interaction between hemoglobin and von Willebrand factor (vWF).

It is found that the effect of ADP release and hyperadhesion, the two primary mechanisms linking hemolysis to thrombosis, depends largely on the rotor speed and level of shear present in the bulk flow. At lower rotor speed, ADP release plays a more significant role, by triggering early platelet activation in low-shear situations, but this effect is reduced at higher rotor speed. Conversely, at lower rotor speed, the decreased level of hemolysis, limits the degree of hyperadhesive vWF produced, whereas at higher rotor speed, speeds growth of pre-existing thrombus significantly, and also helps facilitate growth of thrombus in areas where it would not otherwise occur. Although hemolysis was found to incite thrombosis, via the mechanism of hyperadhesion, because the reaction occurs over a relatively long period of time, stagnation zones are required to shelter the reaction so that it can run to completion. Hyperadhesion, was

thus most significant inside of thrombi, but was generally limited outside of thrombi to accelerating platelet adhesion rate to a factor of 2 inside stagnation zones in the rotor region. The effect of hyperadhesion thus depends on the hydrodynamic efficiency inside of the LVAD, the level of turbulent diffusion that facilitate entrainment of hemoglobin into low-momentum regions, and the presence of low-momentum fluid regions. This reinforces the notion that hemolysis has a nuanced impact on thrombosis mediated by particularities of the LVAD geometry and design, and the presence of stagnation zones as well as low-shear regions.

Overall, at lower rotor speed, hemolysis seemed to precipitate the earlier onset of thrombogenesis, whereas at higher rotor speed it induced an approximately 10%-12% increase in thrombus growth rate. Although it was not examined whether the occurrence of thrombosis in turn heightened the effects of hemolysis, it is logical that the prevalence of this effect in small fluid channels results in significant hemolytic effects as the flow becomes constricted, creating a feedback loop that exacerbates both processes. This phenomenon showcases the intricate relationship between the effects, and thus the complexities in predicting the effect and disentangling the mechanisms.

Finally, a simple stochastic optimization method is used to improve the design of the LVAD and offer some basic design guidance. The results illustrate the crucial role of geometric and operational parameters, highlighting that impeller features, such as its blade divergence, area, number of blades, and diffuser tangent weight, have the most substantial impact on thrombogenicity. With this understanding, LVADs can be optimally designed to help reduce the risk of thrombosis, enhancing their safety.

In summary, the study offers a comprehensive exploration into the complex relationship between hemolysis and thrombosis. Our findings illustrate the significant impact of hemolysis on thrombus formation, the complex interplay with rotor speed, the existence of a feedback loop between hemolysis and thrombosis, and the necessity for accurate modelling to further our understanding of these dynamics.

## Chapter 5: Discussion

---

The following discussion is structured in two major segments. The first segment focuses on the cellular scale studies and sheds light on the pivotal role of red blood cell mechanics in membrane strain. It delves into how modelling of sublethal hemolysis can be enhanced and how hemolysis modelling, in general, should be approached. The findings of these studies will be interpreted in the context of existing knowledge and will be assessed for their validity based on initial expectations. Recommendations for future studies that could add depth and detail to the current understanding will also be put forth. In the second segment, the discussion will pivot to the results of the thrombosis-hemolysis interaction studies. The intricate mechanisms of hemolysis and thrombosis will be examined, and the relationship between the impact of ADP release and hyperadhesion will be disentangled. A sensitivity analysis will be conducted to understand the impact of various factors and to devise strategies for minimizing thrombus interaction. Recognizing the limitations of the current study is essential to refine future research in this area, so these will also be discussed. The conclusion will detail potential directions for future work in this field.

### 5.1 Effect of Collisions on Hemolysis

The following sections discuss the results obtained on the effect of RBC collisions on membrane area strain and transmembrane hemoglobin diffusion. The sections first discuss the single cellular mechanics, then go on to discuss the effect of shear rate on the effects of collisions on area strain transmembrane hemoglobin diffusion, and then touch on the effect of viscoelasticity. Finally the limitations of the study are discussed in depth, and future work is proposed.

#### 5.1.1 Dispersed Cellular Mechanics in a Couette Shear Flow

##### Material Modelling

The material modelling utilized in this study was a modification of the hyperelastic Yeoh model, originally proposed by Mills et al.<sup>207</sup>. This modified model included the integration of area inextensibility, as suggested by Skalak<sup>200</sup>, and the addition of high-order polynomial terms to the energy function as a function of both first and second deformation invariants, reflecting both linear and area strain.

These modifications were necessitated by the limitations of previous material models, which were unable to effectively constrain the indefinite extension of the red blood cell at higher shear rates. There is a physical rationale for such modifications, as it can be expected that at extreme uni-axial strains, the spectrin mesh fibres become aligned with the stress direction, thereby maximizing stiffness even if area strain is negligible or compressive. The Yeoh model of Mills, which is derived from experiments where red blood cells are stretched at forces approximately an order of magnitude lower than those experienced by red blood cells near the rupture shear rates, consequently does provide sufficient stiffness. Conversely, simply increasing stiffness without adding higher order terms produces substantially lower length measurements compared to those found experimentally by Mills et al.<sup>207</sup>, at lower shear rates. Additionally, following McKean<sup>9</sup>, coefficients were selected to attempt to achieve a membrane-averaged area strain of 6.4% at a shear rate of  $45,000 \text{ s}^{-1}$  in single-cell instances. Care was taken to ensure that the contribution of these high-order terms at the strain levels experienced by the RBC during the stretch (approximately 10-20% of linear and area strain) was less than 10% of the original model.

Simulation results generated with this modified model were found to align with the experimental data obtained in Mills' study, falling within their experimental error margins. This was anticipated, as efforts were made to minimize the influence of the newly added high-order terms on lower shear rates and Mills' optical tweezers experiments - the basis for the original Yeoh model fitting - were used for reference. The low order coefficients ( $\mu_0$ ,  $C_3$ ) from Mills et al.'s original formulation were retained, resulting in a model that exhibited greater stiffness, and it proved challenging to eliminate completely the influence of high-order terms at lower shear rates. This was also due to the preference for using volumetric invariants over surface invariants for these terms, and maintaining a polynomial form, also in keeping with Mills' original Yeoh formulation.

#### RBC Membrane Rupture

The hyperelastic model deployed in this study could be considered as an area incompressible and stiffened adaptation of Mills' material model, effectively constraining the membrane-averaged area strain to approximately 8% at a shear rate of  $45,000 \text{ s}^{-1}$ . Furthermore, the maximum area strain was limited to approximately 23-25%, though in extreme cases this can reach peaks of 30-40%. This limit is convenient, as it was noted by Li et al.<sup>212</sup>, that this is a theoretical limit strain limit at which actin and spectrin begin to dissociate. As was noted, this was not exactly by design but was a byproduct of the increasing stiffness sufficiently, to

reconcile the two experimental observations that on average strain at rupture occurred at 6.4%, and that rupture has been observed to start at in shear rates of  $42,000 - 45,000 \text{ s}^{-1}$ . It might also be however that RBC membrane rupture begins when average area strain is approximately 6.4%, which given the loading, length of the RBC, and membrane model results in a maximum strain of 23-25% in a shear flow. This is of course conjecture, however, because global area strain rupture criteria are obtained from micropipette aspiration and RBC spherizing experiments, which is an entirely different loading scenario than a shear flow and would produce far different stress distributions. Furthermore, the 7<sup>th</sup> order Yeoh hyperelastic model employed here requires RBC membrane strain data or, at minimum, shape deformation data at higher strains to validate. It is however notable, that whatever mathematical form the membrane model takes, the membrane model must produce similar stiffness at lower and peak strain rates to what was used in this work to reproduce the RBC shape of the optical tweezer experiments and to prevent extreme stretching.

#### Single Cell Dynamics in Shear Flow

The study observed that within a Couette shear flow, red blood cells transitioned from a tumbling motion to a tank-treading behaviour. This transition phase was initiated at approximately  $1000 \text{ s}^{-1}$ , reaching culmination around  $5000 \text{ s}^{-1}$ . The intermediary phase was characterized by complex dynamics that encompassed elements of both tumbling and tank-treading motions. This observation aligns well with the findings documented in the existing literature, which find the transition begins at approximately  $1000 \text{ s}^{-1}$ . The transition ratio was found to be higher due to the increased stiffness of the modelled material. Further complexities were noted in the tumbling motion. Predicting strain during the tumbling and complex tumbling phases was challenging due to the heavy dynamic nature of the membrane, which exhibited significant wrinkling and complex dynamics. Consequently, there is a large degree of scatter in average and peak area strains found at low shear rates. The wrinkling in the red blood cell membrane was provoked by rapid contractions of the RBC membrane. Several triggers were identified as causing these rapid contractions, including collisions, sudden changes in flow conditions (acceleration), as well as during complex tumbling phenomenon. During the complex tumbling phase, the red blood cell alternately stretched and rotated, leading to contractions and consequent wrinkling when one extended end was rotated into the opposing flow stream.

When the red blood cell membrane was engaged in a mix of tank-treading and tumbling, tank-treading dynamics helped to prevent wrinkling, however. This was due to the transient nature

of the tank-treading membrane, which does not permit persistent local concentrations of strain to form. Furthermore, the rate of change in local membrane curvature was largely defined by the rotation speed of the membrane, which was primarily in tension due to the membrane's inertia and centrifugal stress induced by rotation, analogous to a high-speed bicycle chain.

Relatedly, it was observed that the length of the red blood cell in the tank-treading phase was significantly shorter than the length attained during full tensile stretching. A multitude of factors contributed to this difference. Firstly, the dynamic nature of tank-treading, with constant membrane movement and bending, led to additional dynamic portions of the stress. This dynamic tension was most pronounced at the sites of maximum curvature, where the rate of strain change was most severe, as seen in Figure 32 and Figure 33. In addition, the strain did not have sufficient time to fully extend due to the additional tension forces required to counterbalance the centrifugal forces from the membrane's inertia. Furthermore, the build-up of pressure inside of the cell caused linear extensions to evolve into area extensions, further reducing wrinkling. The rotation speed of the membrane positively influenced these factors—the higher the rotation speed, the greater the internal pressure, the less the wrinkling. This unique interplay of factors was also responsible for the observed increase in nanopore formation and average diameter during the tank-treading phase, which naturally, are related to the local area strain.

#### *Steady Oscillations in Membrane Area Strain and Shape*

Investigations into the behaviour of a single red blood cell in various conditions revealed that oscillations in shape parameters and area strain are intrinsic features, independent of the shear rate. Instead, these fluctuations are more associated with the membrane's elasticity. This implies that the linear extension, which can be conceptualized as a spring-mass-damper system, possesses an inherent oscillatory mode.

As shear rates intensified, especially during the complex tumbling states, a weakened correlation was noted between the shape parameter and area strain. This observation can be attributed to the limitations of the shape parameter, which measures the length to diameter aspect ratio but doesn't account for non-area conserving shape changes, frequent occurrences in the complex tumbling phases. In general, complex flow conditions hindered the prediction of average area strain directly from the shape parameter. Therefore, more research is needed to



formulate constitutive models representing these phenomena by analyzing the single-cell mechanics under a variety of shear conditions.

These findings align with those by Nakamura et al.,<sup>245</sup> wherein better correspondence between the shape parameter and membrane strain was observed during extension phases than contraction. Interestingly, both average and maximum area strains are higher during tank-treading than during tumbling or axial stretching. This may result from the tensioning mechanism inherent to tank-treading, an underdeveloped initial transient phase causing peak axial stretch, or the induced internal pressure from stretching, which forces the non-stretched sides outward.

However, these observations could also be an artifact of the material model that might be overly stiff to uni-axial strain due to the higher powers added to the material model. Lastly, the study found that the absolute value of compressive (minimum) strain generally falls below tensile (maximum) strain, potentially due to internal cellular pressure pushing the membrane outward or the tension induced by the centrifugal force required to maintain the tank-treading membrane's integrity, creating a positive bias.

#### Effect on Transmembrane Hemoglobin Diffusion

The study found specific trends in the rate of hemoglobin diffusion in single-cell dynamics. By utilizing the probability of pore formation data from Koshiyama and Wada<sup>270</sup> and setting a critical strain for pore formation and a minimum radius for diffusion, the mathematical formulation established a sort of threshold for sublethal hemolysis. The findings suggest that shear rates below  $5000 \text{ s}^{-1}$  generally don't exert sufficient strain on the red blood cell membrane to trigger sublethal hemolysis. This claim is supported by the effective transmembrane hemoglobin diffusion coefficient remaining less than  $10^{-3}$  at these lower shear rates. Peak diffusion rate occurs at regions of high area strain, which are predominantly located at the tips of axially stretched red blood cells, or within the regions of highest curvature of tank-treading red blood cells, typically at the ends.

#### Possible Influence of Viscoelasticity

The integration of viscoelasticity into the single-cell simulation cases could have a variety of implications. These potential effects can be extrapolated from the findings in the two-cell cases presented in this study. Firstly, viscoelasticity was found to dampen shape oscillations in two-cell cases. If applied to single-cell cases, this might lead to less dramatic shape changes during the simulation. The cell's shape would respond slower, particularly in high-shear scenarios,

adding an apparent stiffness that could reduce membrane wrinkling and possibly induce a more solid-body response. Viscoelasticity could also affect the transition from tumbling to tank treading in single-cell cases, potentially causing the shift to occur at higher shear rates, indicating that the membrane material model is substantially stiffer than real red blood cells. This implies that the red blood cell (RBC) material model may be overly stiff. In the presence of viscoelasticity, it would be plausible to reduce the stiffness of the RBC model, as the increased membrane stiffness wouldn't be required to limit the cell's stretch, and indeed could be a requisite feature to capture the red blood cell shape at high shear rates. This is particularly the case as during tank-treading rotation rate is linked to shear rate, and thus strain experienced at a Lagrangian point on the moving membrane oscillates with this frequency. This means that the membrane viscosity will contribute to the apparent stiffness of the membrane, possibly decreasing the need for the increased stiffness of the elastic model. This lack of accommodation for viscoelasticity is a limitation in these simulations. Another possible impact of viscoelasticity relates to hemolysis. As seen in the two-cell cases, viscoelasticity affected the hemoglobin diffusion rates, and similar effects might be anticipated in single-cell scenarios. By potentially dampening extreme strains, viscoelasticity could influence the onset and progression rate of sublethal hemolysis. Moreover, viscoelasticity appeared to redistribute stresses around the cell in multi-cell cases, lessening peak stress points. This effect could potentially occur in single-cell cases as well, possibly diminishing instances of high local stresses and distributing them more evenly. Additionally, viscoelastic properties could delay or smooth out the area strain peaks experienced by the single-cell cases. However, it remains uncertain whether the classical concept of viscoelasticity holds for cellular mechanics. The viscoelasticity of cells considered a highly stiff component, is mechanistically related to the breakage and reforming of spectrin-actin bonds on the RBC cytoskeleton. The current understanding of cellular viscoelasticity is predominantly derived from low-frequency measurements, blurring the line between viscoelastic and viscoplastic behaviour in cells. There's a lack of high-frequency cellular mechanics studies or cellular collision studies, making it difficult to understand whether cell membranes exhibit true viscoelasticity. The validity of the approach used in this study, setting membrane viscosity to an experimentally determined value, is thus uncertain when it comes to accurately representing the cellular viscoelastic response.

### Possible Effect of Bending

In the model utilized, bending moments were not incorporated due to the need to reduce the computational time of the simulations, which could potentially influence the strain distribution and shape of the red blood cell. If a bending modulus were introduced and proven to be sufficiently stiff, the amount of membrane wrinkling might be significantly reduced. However, there were reasons for omitting bending moments from the model. For instance, the inclusion of area stiffness - the surface tension force component of area inextensibility - resulted in a bending-moment-like response. This response is proportional to the product of the area strain and surface curvature. In practice, it was found that the force resulting from this response was greater than the bending moment generated by the bending model. Therefore, it was concluded that modelling membrane bending added little value. Hence, it was not anticipated that including membrane bending in the model would significantly alter the mechanics observed in these simulations, and early simulation results revealed that indeed this was true. The conclusions drawn from the study should thus remain largely unaffected by this modelling choice.

## **5.1.2 Effect of Collisions on the Red Blood Cell Membrane and Sublethal Hemolysis**

### Red Blood Cell Dynamic Response and Shape Under Collisions

In the exploration of red blood cell (RBC) behaviour under collisions, the findings indicated that the dynamics of the RBC membrane response were heavily impacted by these interactions, especially at high shear rates. The fluctuations in area strain seemed to be largely governed by collision frequency as opposed to the membrane's elastic response to shear. This was particularly evident as the local peaks in mean area strain correlated closely with collision events, for instance, the congruence between a local peak in area strain in Figure 41 and a collision event in Figure 40.

The immediate aftermath of these collisions witnessed an elastic response as the cells endeavoured to regain their former state. Furthermore, area strains tended to stabilize more rapidly in the wake of collisions. An impact on the RBC length was also observed, with the cells appearing shorter and more ellipsoid post-collision. This change could be attributed to the increased shear stress exerted on the membrane during the collision, causing it to contract. At elevated shear rates, the cells, despite the lack of viscoelastic modelling, often lacked sufficient recovery time between collisions to revert to their original shape.

Interestingly, the degree of wrinkling was generally mitigated in collision instances, a phenomenon suspected to be a result of the increase in internal pressure of the RBCs due to frequent collisions.

These observations carry significant implications for constitutive strain-based hemolysis modelling approaches, such as those put forth by past and future attempts to model hemolysis from a strain-based or constitutive approach. These models generally postulate an ellipsoidal RBC shape in a shear flow. Given that more intricate aspects of membrane mechanics, like wrinkling, seem to be suppressed by collisions, the RBC shape is more ellipsoidal, indicating that a droplet or ellipsoidal approximation of shape is more valid than in single-cell cases where complex dynamics emerge.

#### Types of Collisions

Investigation into collision types revealed two distinct dynamic collision regimes: glancing and head-on collisions. These were exemplified in Figure 40 and Figure 48, respectively. The distinguishing factors between these types of collisions were the mean intercellular spacing and consequently, the extent of shear or stress exerted on the cell during the collision.

Glancing collisions typically occurred in dispersed flows, where the trajectory of red blood cells (RBCs) was not hindered by a wall or the presence of other cells. In contrast, head-on collisions were more common when the RBCs were forced into close proximity due to the presence of other cells, which in turn, induced greater mutual shear. This induced shear resulted in a significant contraction in RBC length and a near return to a spherical shape. There was a substantial torque applied to the RBCs during the collision, leading them to spin about one another and collide with other cells, causing disorderliness. Such observations though qualitative, serve as a vital foundation for constitutive modelling, allowing for physically realistic assumptions to simplify modelling.

Collision types also appeared to influence the membrane strain experienced. Glancing collisions often resulted in localized increases in area strain, while head-on collisions led to significant overall area strain due to high shear stress. Glancing collisions were more likely when RBCs were not heavily constrained, which was typical in low hematocrit situations. Under these conditions, the spacing between RBCs remained minimal, with inadequate shear applied to significantly alter the RBC's direction or shape. Conversely, head-on collisions were characterized by a significant contraction in RBC length due to substantial normal or shear

stress. This phenomenon could occur if RBCs were forced near each other by a solid boundary or the presence of nearby RBCs, resulting in a significant buildup of area strain.

#### *Effect of Varying Shear rate on Area Strain in Simple Two-cell Collisions*

Investigations into the effect of varying shear rates on area strain in simple two-cell collisions presented some interesting results. At lower shear rates, collisions had a substantial effect, almost doubling the effective strain experienced by the membrane at  $10,000 \text{ s}^{-1}$ , though this effect lessened as the shear rate increased. It was observed that cell-to-cell collisions played a significant role in dictating the membrane area strain response. These collisions tended to overshadow the natural elastic response of the RBC membrane to shear stress in the surrounding fluid. Average area strain fluctuations had a narrower amplitude, but the average was much higher.

Although not directly shown, the outsized influence of collisions at lower shear rates suggested that tumbling was likely suppressed by collisions. For example, in the low shear rate case at  $4,820 \text{ s}^{-1}$ , the complex tumbling behaviour was attenuated. More simulations are required to validate this conclusion. At high shear rates, RBC collisions resulted in a higher degree of membrane area strain on average. The maximum strain was not significantly affected, owing to the increased stiffness of the membrane hyperelastic model at area strains nearing 23%. Collisions skewed the strain distribution to be on average higher. Therefore, a possible modelling approach might consider collisions as an apparent time-varying stress on the membrane, akin to turbulent stress.

Data from Table 8 showed that the average strain was consistently higher in the two-cell colliding case, indicating a substantial effect from collisions. Notably, at  $30,000 \text{ s}^{-1}$  and  $45,000 \text{ s}^{-1}$ , the average membrane strain for single-cell cases was approximately 50% higher, indicating that even at higher shear, the real membrane strain experienced by RBCs was significantly higher than previously expected if collisions are considered. The 6.4% area strain rupture criterion often cited in the literature, is obtained from quasi-steady-state spherical rupture of cells sucked into a micropipette and is somewhat arbitrary. Given that the load induced by collisions was exceptionally high frequency, an upper boundary of 42% area strain might be more appropriate to consider the increased stress when considering RBC collisions. As few studies measure the area strain during a dynamic rupture event, however, it is uncertain what the actual rupture area strain should be. There is thus a clear need to better understand how ultimate strain rupture criteria should be translated into material modelling. The lack of

appropriate material modelling at high shear rates likely explained why RBC membrane mechanics simulations were seldom attempted near rupture. Therefore, the stiffness of the RBC at higher strains needed to be refined and better validated against data from RBC rupture events under a variety of loads. Interestingly, the average area strain appeared to saturate near 14%. The reasons for this were unclear. Nonetheless, in extreme cases, the significant effect of collisions on average area strain and hemoglobin diffusion rate highlighted the need to include this phenomenon in constitutive modelling approaches for sublethal hemolysis.

#### Diffusion Coefficient

Findings from the study revealed that the transmembrane hemoglobin diffusion coefficient, associated with the potential for sublethal hemolysis in the absence of cell rupture, also increased relative to single-cell cases. This diffusion coefficient eventually plateaued at about 70-74%, corresponding to almost complete membrane poration. It is worth noting that in this study, the pore radius was effectively limited to approximately 90 nm by the pore formation model of Tolpekina et al.<sup>268</sup>, where the maximum patch size for pore formation was set to 100 nm.

Modelling the strain behaviour during the dynamics of complex tumbling presented significant challenges. Generally, there was a correlation between maximum and average area strain at rupture of 14% and 8.4%, respectively, in the single-cell cases, and 20% and 8.4% in the two-cell cases. If we conceptualize the stress distribution on the RBC membrane as a probability density function, it was observed that increasing shear rate effectively shifted the average of this distribution by skewing it towards the hyperelastic stiffening limit. At this stage, material stiffness significantly increased, limiting area strain to the 23-25% limit and thereby constraining the increase in average area strain.

A key difference between the present work and previous studies, such as those by Sohrabi and Liu<sup>10</sup>, is in the mechanoporation model employed. In this study, the thermodynamic scaling procedure suggested by Tolpekina et al.<sup>268</sup> was used to scale up their original model, which was fit from molecular dynamics data conducted on a very small patch of membrane with sides measuring 16 nm. A square patch of 100nm was selected based on the physical argument that the nominal length of RBC spectrin fibres was 80-100 nm. This was done because it was assumed that the actin connections from the membrane to the cytoskeleton would act as reinforcements to the membrane and present a similar radius-limiting effect as the boundary conditions of CGMD simulations. The resulting pore distribution corresponded relatively well

(Figure 17) with molecular dynamics simulations of much larger bilipid membrane patches that included the spectrin cytoskeleton by Razizadeh et al<sup>83</sup>.

Conversely, Sohrabi and Liu<sup>10</sup> did not apply a thermodynamic scaling procedure, incorrectly applying Tolpekina's poration model<sup>268</sup> to their numerical membrane elements, which were significantly larger. In their model, pore formation began at 80% area strain and culminated at 120% area strain, puzzlingly the area strains computed from their multiscale analysis of an RBC in an LVAD flow were in this range without rupturing the membrane. The argument that the area strains could reach these levels while the average remained at the 6% rupture threshold is generally contradicted by the findings in this study which show that the area strain generally cannot exceed 23% without excessive elongation of the membrane.

The complex behaviour of the system resulted in a poor correlation between area strain and average hemoglobin diffusion rate. However, fits from Figure 33, Figure 37, and Figure 38 can be used to construct a pseudo-empirical model for transmembrane hemoglobin diffusion. Notably, the findings of the present study suggest that correlations for transmembrane hemoglobin diffusion rate should include both minimum and maximum area strain, as well as membrane averaged area strain to better capture variations in the RBC shape. It was furthermore interesting to find that the effective diffusion coefficient fit an erf function surface of average area strain and maximum area strain quite well, with an  $R^2 = 0.94$  (from Figure 38). This is likely due to the modelling approach, as the inclusion of an erf function to model the probability of pore formation probability naturally casts pore property data into a similar format.

#### *Effect of Hematocrit at High Constant Shear Rate on Area Strain and Transmembrane Hemoglobin Diffusion*

The hematocrit level, which defines the proportion of blood volume occupied by RBCs, was found to play a crucial role in determining area strain. As illustrated in Table 10, increased hematocrit corresponded to progressively higher average strains and a more rapid increase in membrane strain. This effect can be qualitatively explained by several factors.

As hematocrit increases, the frequency of collisions also increases, leading to a corresponding rise in the average membrane area strain. Additionally, higher hematocrit levels reduce intercellular spacing, forcing cells into closer proximity and making their paths more constrained by the presence of other cells. Consequently, the average shear stress on cells

resulting from collisions also increases as cells pass over each other in closer proximity. Consequently, the proportion of head-on collisions is increased, as is overall collision severity.

The impact of hematocrit on hemolysis has been contentious in the literature, however, which was one of the motivations for this study. Previous studies have found the effect of hematocrit on hemolysis to be small or insignificant. These results can be reconciled with the present work in several ways. For instance, the study by Leverett et al.<sup>4</sup>, which found little to no effect of hematocrit on hemolysis, was done in conditions where it is difficult to completely isolate the interaction of cells, and spatial variations of hematocrit could not be accounted for, particularly as the shear rate is only completely uniform in their case in a small portion of their apparatus. The effect of hematocrit in their study was evaluated at a constant shear rate of approximately  $100,000 \text{ s}^{-1}$ , at which point the cell membrane is likely to experience lysis regardless of the effect of collisions. Indeed, in the present study, it was found that collisions had the most pronounced effect at lower shear rates whereas at higher shear rates near rupture, the effect was increasingly less pronounced. This is again logical, as the relative increase in collision rate declines as the shear rate decreases, and thus at high shear rates cells would likely experience similar levels of stress regardless of the hematocrit level. Rather, it was found that the more significant effect of collisions is to facilitate rupture or increase sublethal hemolysis at lower shear rates. The other key difference between the present study and that of Leverett et al.<sup>4</sup>, however, is that in the present study, it is possible to completely isolate the cells from one another by excluding all other cells from the computational domain, thus ensuring that no collisions happen and observing the membrane area strain.

Finally, in this study, the membrane strain is measured and rupture is assumed as a consequence of that, whereas in the study of Leverett, hemolysis is measured directly; due to the viscoelastic nature of the membrane, it does not necessarily follow that increased instantaneous membrane area strain will lead to increased rupture. With regards to these points, it is not necessarily that the effect of collisions will increase hemolysis rate at high rupture, but rather that lysis and sublethal hemolysis will begin to occur at lower shear rates with increased hematocrit due to increased frequency of collisions. Thus, a more appropriate experimental investigation on the effect of hematocrit would be to vary hematocrit and shear rate independently and examine the effect of hematocrit at different shear rates, which, appears to not have been done at the time of writing.



It remains difficult, however, to make a definitive conclusion regarding the effect of hematocrit on membrane area strain from the data in this study, primarily due to the need for more simulation time to allow the average values of area stress to reach a steady-state in the simulations. It is possible that despite the tendency of area strain to increase earlier and more rapidly in high hematocrit cases, they will reach an equilibrium state near the same area strain. That said, it's clear from the number of cases observed that collisions have a strong effect on membrane area strain. More analysis is however required to verify and quantify the effect of hematocrit on area strain, particularly at high shear rates.

In general, it was found that red blood cell collisions lower the threshold for sublethal hemolysis. The onset of sublethal hemolysis occurs at a shear rate of approximately  $1000 \text{ s}^{-1}$  in colliding cases and  $4820 \text{ s}^{-1}$  in non-colliding cases. This is not surprising as the collision event leads to a short-term localized increase of membrane area strain near the collision site. It is indeed generally difficult to attain the high level of strain required to cause sublethal hemolysis without collision events. Furthermore, the experimentally observed threshold of sublethal hemolysis occurs approximately at  $1000 \text{ s}^{-1}$ , which is more consistent with the colliding cases.

#### Effect of Viscoelasticity

The simulation incorporated viscoelasticity using a Kelvin-Voigt damper model, effectively applying a Newtonian viscosity, equivalent to the membrane viscosity of  $0.3 \text{ } [\mu\text{Pa} \cdot \text{s} \cdot \text{m}]$  computed by Mills et al.<sup>207</sup>. Two simulations were conducted where membrane viscosity was set to the lower range of physiologically measured values to examine the effect of viscoelasticity on collisions with two and four RBCs at  $20,000 \text{ s}^{-1}$ . In general, incorporating viscoelasticity appeared to dampen the amplitude of the area strain oscillations observed during collisions, whereas the mean of oscillations in the time-trace of membrane averaged area strain were generally similar. In the two-cell collision case, cells came into far closer proximity, however, and began to rotate about each-other rather than glancing, as was observed more frequently in the non-viscoelastic cases, because the high viscosity prevented the membrane from reacting quickly enough to allow a uniform lubricating film to form between the cells. This means that the onset of head-on collisions and the likelihood of generating disorderly motions on the order of the RBC scale is much higher in the presence of viscoelastic membrane collisions. Furthermore, as shear rate was rather high, the deformability of the cell membrane appeared to be highly attenuated. On average, however, particularly in the 4-cell case, time averaged area strain was found to be similar despite the attenuated peaks. More data is however needed to verify this, as these simulations like the high hematocrit simulations suffered from

numerical instability and simulation time was relatively short due to this. The numerical instability arose from the very small lubricating films due to the increased membrane stiffness during collision, which when lower than the mesh spacing would cause stress to be computed from the gradient of two red blood cell membranes. This was another reason why viscoelastic simulations were difficult to simulate as finally it was necessary to use up to four adaptive grid refinement levels to ensure numerical stability, significantly increasing simulation time.

#### *Implications of Collision Mechanics for Turbulence in Blood*

The findings from this study preliminarily indicate that the dynamics which occur due to head-on collisions between red blood cells (RBCs) may contribute to a form of microscale turbulence within blood flow as RBC collisions are shown to generate microscale disorderly motion.

This phenomenon generally transpires during 'head-on' collisions where RBCs are in close enough proximity or are sufficiently constrained to generate significant shear stress to generate angular momentum. Given that RBCs are typically exhibiting a tank-treading motion while in flow, the shear stress between these cells becomes even more pronounced. Within confined conditions, the generated shear stress becomes significant enough to perturb the path of the RBCs. As a result, the RBCs spin together due to mutually induced moments, eventually colliding with other cells and further disturbing the flow. This sequence essentially represents a small-scale conversion of energy from mean flow to fluctuation energy or, in other words, the production of turbulence kinetic energy at a length scale equal to the RBC diameter.

In the absence of nearby cells or walls, RBCs are generally kept from colliding by lubrication forces, however. These forces can minimize the shear experienced by the RBCs such that their path is not disturbed. Nevertheless, at higher hematocrit levels, the pressure exerted by surrounding cells and the higher inertia at high shear rates tend to force the cells into closer proximity, which would result in the observed disorderliness. It is still unknown, however, whether this phenomenon will persist if the computational domain size is increased, and the flow consequently becomes less constrained. It is important to note that this effect can also be dissipative, as it tends to break up the high shear rate vortical entities larger than the red blood cell. For example, in a vortex flow on the order of our computational domain (roughly the order of the Kolmogorov scale in an LVAD), the kinetic energy of the larger eddy is effectively converted by the collisions into rotational motion on the order of (twice) the RBC diameter. In the context of classical isotropic turbulence theory, the Kolmogorov scale,  $\eta$ , is the length scale at which viscous forces dominate inertia and turbulence kinetic energy is converted into heat.

This scale is traditionally computed as the ratio of  $\eta = \left(\frac{\nu^3}{\epsilon}\right)^{1/4}$ , where  $\nu$  is kinematic viscosity and  $\epsilon$  is the turbulence dissipation rate at that location. Using such classical turbulence modelling techniques, it is found to be an order of magnitude larger than the diameter of a red blood cell. The current findings support the hypothesis of Antiga and Steinman<sup>194</sup> and suggest that the smallest scale of turbulence should indeed be (on the order of) the red blood cell diameter, or rather the inter-cellular spacing. This means that at the very least, there should be an increase in the production of turbulence dissipation rate to account for the effect of collision so that the Kolmogorov scale is closer to the red blood cell diameter. This consequently results in a decrease in turbulence kinetic energy production in blood, resulting in lower overall turbulence viscosity, which is likewise more in line with the lower effective shear stress experienced by red blood cells in shear flow. This perspective is further corroborated by the observation of non-Kolmogorov turbulent decay (that is, the energy of eddies decays with eddy length at a greater rate than the classical  $-5/3$  exponent found in hydrodynamic flows), as documented in physiological carotid arterial flows of health patients in-vivo<sup>192,193</sup>.

### 5.1.3 Study Limitations and Validity of the Computational Method

Overall, this study is confronted by a range of limitations that restrict the conclusions to more qualitative understandings. The study encountered limitations primarily revolving around time constraints, computational cost, numerical diffusion, inability to validate membrane strain or mechanoporation parameters, flow over-constraint due to small domain size, and investigation of the effect of hematocrit under constant shear rate.

A notable hindrance in examining the long-term behaviour or responses of red blood cells under shear flow, particularly in multicellular scenarios, came from time constraints. The employed simulation method does not allow for membrane contact, which is calculated from the membrane volume fraction gradient using a high-order method. When two cell membranes come close enough for the gradient of the deformation tensor to be computed in the same finite-volume grid cell from different RBC membranes, the immense resulting force induces a non-physical behaviour on the membrane, leading to solver divergence. To avoid this, cell spacing had to be kept considerably smaller than intercellular spacing; this was achieved using adaptive grid refinement. This issue was particularly prominent in stiff membrane cases, such as the viscoelastic cases. As the number of cells and hematocrit levels increased, the risk of contact events also rose, leading to shorter simulation times and preventing a comprehensive examination of high-momentum or stiff-membrane cellular collisions.

Despite using a semi-implicit method for the deformation transport equations, the multiphase stability criteria were far more stringent, necessitating a convective Courant number at the volume fraction interface of less than one. This effectively meant with regards to simulation time-step that the methodology was effectively explicit, leading to prolonged simulation times and considerable computational costs given the limited available computational resources (two 64vcpu server nodes). Moreover, during the validation process, each simulation had to be run multiple times due to adjustments in material properties, grid refinement, stability parameters, etc., further limiting the study's scope.

The necessity of small timesteps, induced by the stringent multiphase stability criteria and the structural model itself, also led to numerical diffusion in the equations transporting the left-Cauchy deformation tensor. This resulted in strain being underpredicted, strain accumulating in unexpected locations, and convective-diffusive numerical instability. Therefore, simulation time was confined to approximately  $t\dot{\gamma} < 200$  to keep values of the deformation tensor outside the cellular membrane below 2% of the mean membrane value.

Another significant challenge in cellular modelling is the impossibility of directly measuring strain on the RBC membrane experimentally. Instead, measurements are done indirectly using proxies such as RBC shape parameters. Using this approach, while it is possible to determine overall average strain, it can yield a multitude of strain distributions due to a corresponding multitude of membrane structural models. Moreover, in general it is difficult from these approaches to compute the area strain, particularly in a dynamically stretched red blood cell.

Insufficient data is also available on mechanoporation parameters, with the best information being obtained from molecular dynamics simulations, which are often not validated. Despite some reassurance in the ability to bridge parameters across different molecular dynamics studies, it remains questionable whether the mechanics and distribution from electroporation and mechanoporation are the same.

The study was also limited by the constraining effect of no-slip walls at the upper and lower boundaries of the computational domain, which were necessary to achieve a uniform Couette shear flow. Although the domain size was generally increased to maintain a cell-free layer, as was noted, the effect of the walls is acknowledged to influence cell dynamics. Therefore, it is uncertain whether the level of cellular constraint observed in the study, particularly in head-on collisions really occurs. Indeed, using streamwise periodicity resulted in the use of a zero-pressure-gradient flow, and indeed the absence of any spanwise non-uniformity means that the

study is effectively subject to the same limitations as a lubrication flow between two infinitely long and wide plates, and therefore the study has the same limitations.

Finally, the findings of an overall increase in membrane strain and transmembrane hemoglobin diffusion within high hematocrit cases may not translate at all shear rates, as the engagement of different physics emerge given higher cell momentum and collision pressure.

#### **5.1.4 Future Work**

The current study presents various opportunities for future research in understanding of cell collision effects on membrane area strain when modelling hemolysis, and the turbulent behaviour of blood flow.

The key insight from this study suggests that the current constitutive approaches to modelling hemolysis, relying on single-cell approximations, fail to accurately predict the strain experienced by red blood cells in multi-cell situations. Hence, more robust models are needed that incorporate the influences of cell collisions as well as deformation by shear. Such a model could include a term analogous to turbulent kinetic energy, contributing additional shear stress on the RBC membrane, necessitating the interplay between collision pressure and nominal lubrication gap between cells to be considered. Moreover, the viscoelasticity effect, which seems to dampen collision-induced area strain oscillations, needs further exploration. Longer simulations at elevated shear rates with many cells would provide validation of whether the effect of hematocrit indeed reaches a steady-state at a higher value relative to two cell or single cell simulations. Simulations at high hematocrits and shear rates could also reveal whether shear rate increases have consistent impacts at both low and high hematocrits, a question not thoroughly examined in this study. Furthermore, it is necessary to examine how changing shear rate or streamline curvature affects red blood cell membrane mechanics or turbulence, in the presence of collisions.

This study has initiated an investigation into the collision impact on sublethal hemolysis and its effect on transmembrane hemoglobin diffusion coefficients. However, the application of these results to improve sublethal hemolysis modelling is an ongoing process that needs further investigation. Specifically, constitutive modelling of the increased strain on red blood cell membranes needs to be developed and incorporated into existing constitutive modelling frameworks.

Furthermore, experimental validation would greatly enhance this study, which is primarily simulation-based, especially concerning the constitutive modelling of RBC membrane structural mechanics. It would be prudent for example, to follow Yazdani et al.<sup>388</sup> and use dielectrophoresis to measure cell deformation in flowing blood plasma. At the least, it is necessary to have optical tweezer measurements at extreme forces close to and surpassing the RBC rupture criteria, and at different loading rates to validate the material model at higher shear rates.

Finally, the study uncovered the potential of red blood cell collisions to contribute to turbulence kinetic energy production and increase dissipation through lubrication mechanics during collisions. More comprehensive studies are needed to quantify turbulence characteristics in larger or fully periodic domains. Moreover, there is a clear need to develop correction terms to existing two-equation turbulence models to account for the increased dissipation due to collisions. Furthermore, given that turbulent fluctuations on the scale of the red blood cell membrane may be induced by the dynamics of RBC cell collisions. The smallest length scale should be considered as twice the red blood cell diameter for turbulence kinetic energy dissipation production, like what was proposed by Antiga and Steinman<sup>194</sup>.

## **5.2 Modelling Thrombosis and Effect of Hemolysis on Thrombosis**

The discussion delves into the relationship between hemolysis and thrombosis and analyzes the major findings of the study. The vital role of embolization mechanics in thrombosis prediction are highlighted, providing insights into the complex processes that govern these phenomena. Moreover, it demonstrates the impact of hemolysis on the thrombosis model. The discussion is then turned to practical applications, offering strategies for designing Left Ventricular Assist Devices (LVADs) to minimize thrombosis risks, which are informed by the improved understanding of the interplay between hemolysis and thrombosis. The last section acknowledges the limitations of the study and proposes avenues for further research and model refinement to enhance thrombosis prediction accuracy.

### **5.2.1 Embolization Mechanics and Effect of Shear Rate on Embolization**

To help reduce the risk of thromboembolic complications in LVAD users, embolization formulations were developed and validated in this study. These formulations' precision is crucial given the life-threatening implications of thrombosis, the critical role that embolization plays in thrombosis, and the noted ambiguity in the thrombus modelling literature regarding platelet embolization, which necessitated the development of novel embolization formulations.

To assess the formulations used in this study, a dual-faceted approach was adopted. The first step entailed testing the formulation against empirical data provided by Navitsky et al.<sup>353</sup>, to which embolization models were fit. The spinning disk experiment of Navitsky within a closed volume of platelets proved to be useful due to its predictable flow mechanics and relatively uniform distribution of activated platelets across the disk's surface. In the thrombosis model, the balance between adhesion and embolization rates determines the steady-state value of platelet concentration. A nonlinear, reduced ODE model was solved numerically, and the dataset was beneficial as it allowed the computation of the adhesion coefficient independently of the embolization model. The platelet distribution was anticipated by a simplified version of the thrombosis model, enabling an effective computation of adhesion and embolization coefficients. The second step applied the formulation to simulate thrombus length patterns downstream from a backward-facing step in a small circular channel. In comparison to Navitsky, the adhesion coefficient was found to be two orders of magnitude larger than theirs due to differences in the approach to platelet adhesion and embolization. The study of Navitsky set the maximum surface concentration of platelets to the experimentally determined value while embolization occurred at a constant rate. Consequently, the adhesion and embolization rates could be chosen somewhat arbitrarily in their case as given enough time the platelet concentration always approached the experimental value, which Navitsky acknowledged as a limitation of their study. Conversely, in the present study as the platelet concentration is determined by the balance of adhesion and embolization rate, and constants associated with adhesion and embolization were determined from the steady-state platelet concentration on the surface.

The embolization formulation proposed by Goodman et al.<sup>325</sup> proved inadequate in describing the accurate platelet distribution on the spinning disk, either overpredicting embolization at low stress or underpredicting it at higher stress. Thus, it was necessary to incorporate the variation of the characteristic embolization timescale with shear rate. Both models presented in this study, while effective, were found to be over-parameterized, leading to similar platelet distributions despite variation in key parameters.

To compare with in-vitro thrombus MRI imaging studies by Taylor et al.<sup>342</sup> and Yang et al.<sup>384</sup>, length was chosen as a validation metric. Height and volume growth over time were excluded from the comparison as height saturated to step height too quickly and volume is in general dictated by the platelet-platelet embolization rate, which is considered to be far more ambiguous than the platelet-surface embolization rate due to the lack of data available for

fitting. The data showed that the overall average length, well predicted the overall trend and growth presented by Taylor et al.<sup>342</sup> and Yang et al.<sup>384</sup> In examining the thrombus growth patterns, discrepancies were noted, however, between simulations and experimental results. Growth occurred more suddenly and uniformly in simulations, while experiments showed a more gradual spreading outwards from the vertical step face. This was attributed to potential inadequacies in the representation of shear stress distribution due to the low Reynolds number in the simulation, which was modelled as laminar, as well as potential deficiencies in non-Newtonian blood modelling. Subsequent inclusion of these however did not significantly improve prediction accuracy.

Two embolization models were examined in the study: the power law model and the modified-Goodman model, to improve the fitting of the embolization model to Navitsky's data. Despite being fit from data from an entirely different experiment type, both models demonstrated robust alignment with data of Taylor et al.<sup>342</sup> and Yang et al.<sup>384</sup>, indicating that the model was relatively robust. This extra step of cross-validation is one of the key values of this analysis as it helps ensure that the modelling scheme is transferable to different flow regimes, and furthermore material types.

### **5.2.2 Effect of Hemolysis on Thrombosis**

Hemodynamic phenomena play a significant role in thrombogenesis and necessitate an understanding of stagnation zones and low/high shear stress regions to understand how thrombosis can be avoided in blood exposed biomedical devices. Low shear stress on surfaces, combined with adequate activated platelet concentration supplied by an upstream high shear stress region, allows continuous platelet accumulation until surface saturation. The emergence of thrombosis at these low shear or stagnation points has been corroborated by studies such as Wu et al.<sup>339</sup>. Additionally, the process depends upon the presence of high shear regions upstream and low-shear downstream, which are found in the non-physiological flow within LVADs, as illustrated in Figure 57 and Figure 58. This complex dependence on shear stress confounds the prediction of thrombosis. High shear stress regions facilitate maximum platelet activation, predominantly within the turbine and inducer regions. Stagnation zones provide critical shelter to slower, long timescale chemical reactions from convective effects, enabling the accumulation of significant chemical concentrations of activated platelets, agonists, and most critically, hyper-adhesive von-Willebrand factor. The mechanism of entrainment of the products of these high shear stress processes, play an instrumental role in thrombosis and the effect of hemolysis.



Stagnation zones and low shear regions, which are largely a feature of the open-hub LVAD that was selected for analysis in this study, are highly important. These regions are generated by several hemodynamic phenomena in an LVAD, such as the generation of free shear layers downstream from a sharp geometric change (such as a backward-facing step), inside vortex cores or at the center of high swirl regions, and in locations of adverse pressure gradients. These phenomena can be seen in the outlet of the LVAD (Figure 57), where rapid flow direction changes at the interface of the impeller and diffuser can lead to separation and stagnation zones. While these zones can be difficult to eliminate, strategies such as inducing a higher degree of flow unsteadiness can be used to break up or relocate these zones, hence preventing the formation of consistent low-shear areas where platelets can accumulate.

The geometry of LVADs can be an influential factor in thrombogenesis. The design chosen for analysis in this study was intentionally sub-optimal to highlight the effect of hemolysis on thrombosis and the geometric optimization process. Flow unsteadiness introduced through varying rotor speeds can disrupt stagnation zones, though this may not in fact eliminate thrombosis. The persistence of thrombosis in the face of strategies such as rotor pulsation may be due to the accumulation of vWF in these zones over approximately two-three minutes, which is sufficiently rapid that accumulation of significant concentration of  $vWF_{ha}$  is possible as the periods of high convection are insufficient to remove the accumulation. In addition, given that  $vWF_{ha}$  is primarily converted in the flow rather than on cells, the accumulating zone of  $vWF_{ha}$  would simply shift with the moving vortex core. It is thus necessary to further examine the effect of flow transience in the presence of hemolysis-induced hyperadhesion.

Hemolysis, in the context of Left Ventricular Assist Devices (LVADs), converges rapidly compared to vWF conversion to  $vWF_{ha}$  and platelet accumulation. This was one reason why the hemolysis equation had the same time-scale factor as the vWF conversion, as to realistically model this process, the hemolysis equation should be in an equilibrium state relative to the vWF conversion. Hemolysis values within the LVAD fall in line with hemolysis indices expected in MCS devices, with typical extracellular hemoglobin levels between 0.01-1%. Hemolysis mostly occurs in very high shear regions or where blood residence time is high such as in stagnation zones. Notably, diffusion is not modelled for hemoglobin due to the absence of a clear relationship between hemoglobin and mechanical dose in the context of diffusion rate.

Hemolysis plays a multifaceted role in thrombogenesis within LVADs, with effects varying according to the level of hemolysis and environmental conditions. At low shear stress and low rotational speeds, hemolysis contributes to thrombogenesis through the release of ADP, a potent platelet activation agent, which is found in large quantities in red blood cells. Indeed, the concentration is so high that even at low hemolytic levels, this ADP release was found to trigger coagulation earlier than the reference case by activating nearly all platelets in the domain. However, at high shear stresses, where most platelets are already activated by shear stress, the effect of ADP release is far less pronounced.

In high rotational speed environments, where significant hemolysis occurs, hemoglobin binds to vWF, converting it into a hyper-adhesive form. This conversion process requires high shear for extracellular hemoglobin production and sufficient time for vWF to vWF<sub>ha</sub> conversion, conditions usually met in the wake or stagnation regions of LVADs. In these zones, vWF<sub>ha</sub> accumulates due to slow convection of the reaction products out of the zone. The highest concentrations of vWF<sub>ha</sub> is thus generally found within the thrombi themselves. However, the overall effect of hemolysis in the open-hub LVAD used in this study is relatively contained, mainly confined to the rotor's stagnation zones downstream from the impeller. It is however noted, that the magnitude of this effect is largely dependant on the rate of conversion of vWF to vWF<sub>ha</sub>. This is found because in regions where the conversion is allowed to progress to completion, the adhesion rate is increased by a factor of 5. Given that the conversion rate of vWF to vWF<sub>ha</sub>, is determined from a single study conducted at relatively shear stress, it is possible that there is a high degree of error in this. Furthermore, an incredibly simplistic treatment is used in this study, where platelet adhesion rate is simply scaled by a single factor. This factor was in turn computed from the average of the increased adhesion rates measured in the presence of collagen extracellular matrix (all fibres) and fibrinogen, which were 2, 5 and 9, respectively.

ADP release during hemolysis on the other hand, can activate most platelets in a volume, and though hemolytic ADP release can bypass the thrombin-inhibitory feedback mechanism of heparin, these effects remained relatively minor. This was partially due to the fact that the degree of thrombosis in the LVAD was already relatively high in the studied geometry, as it was selected for its high thrombogenicity in the first place. Nevertheless, Hb-induced hyperadhesion increases the growth rate by approximately 10-12%, and was found to induce thrombosis in surfaces that experienced a relatively high degree of shear, where it would not have occurred otherwise.

Notably, however, his study neglects several key factors, such as Hb-induced hyperadhesion's effect on reducing platelet embolization rate, the interaction between Hb and anticoagulation, and the shielding of vWF<sub>ha</sub> from cleavage at high shear by the ADAMS-13 protein. These mechanisms are likely to enhance the effect of hemolysis on thrombosis substantially, and a full understanding of these mechanisms is crucial to comprehend the complete impact of hemolysis on thrombosis at high shear. Despite this, it is evident that hemolysis should be considered when modelling thrombosis, and that the interaction of hemolysis with thrombosis, particularly in the context of anticoagulation, necessitates additional experimental studies of thrombosis with whole blood.

### 5.2.3 Minimizing Thrombosis in Blood-Wetted Devices and MCS

The study provides some comprehensive insight into the mechanisms of thrombosis and strategies for its minimization in blood-exposed medical devices, particularly focusing on Left Ventricular Assist Devices (LVADs). Minimization of thrombosis in MCS in general involves the consideration and optimization of various hemodynamic factors. A small design of experiments study was executed to examine the sensitivity of various design and operational parameters to thrombogenesis. The simulations were carried out for 10 minutes of thrombus growth, while the hemodynamics were allowed to reach a statistically steady state prior to initializing thrombus growth. The rate of thrombus growth at the end of this period is utilized to assess thrombogenicity. This is somewhat problematic as in general the Platelet-Platelet adhesion and embolization rates are not as well validated as surface adhesion and embolization. Notably, however, in the context of the LVAD, the thrombi expanded generally more in area rather than in height due to relatively high shear stress present in the device.

One of the fundamental challenges with LVAD design is managing rotor speed to balance shear stress. Excessive shear stress can trigger hemolysis, while too little can lead to flow stagnation. In general, low shear areas and stagnation zones are prone to thrombosis, and help entrainment of extracellular hemoglobin and facilitate the long-term vWF-Hb reaction, which plays a mild yet noticeable role in promoting thrombosis in LVADs. This can prove challenging because these parameters are often at odds with the task of improving performance of the LVAD.

Interestingly, rotor speed was not the most impactful determinant of thrombogenicity. Instead, impeller characteristics such as the number of blades and blade area played a significant role. An increase in blade area and number of blades, which generally have similar effect, amplifies both hemolysis and thrombosis and extends the total corner length. Thrombus in

general grow in corners as this is a common site of stagnant flow, and thus these parameters lead to enhanced thrombus growth area. The study also found that enlarging the impeller hub diameter could reduce thrombus formation. Increasing the open-hub diameter results in more low axial flow through the core and improves momentum transfer towards the outer radius of the impeller, which reduced the degree of flow separation experienced within the impeller itself.

Impeller blade divergence, which refers to the rate of increase of the gap between impeller blades as the blades are swept in the streamwise direction, also had a thrombogenic effect. Increased divergence can recover static pressure from kinetic energy as it acts like an extra diffuser within the impeller. This however imposes a strong adverse pressure gradient as static pressure increases, which seems to create flow separation zones within the impeller and leads to thrombosis despite the high shear in this region.

Furthermore, it was discovered that a larger outlet diameter tends to increase thrombogenicity, possibly due to an increase in flow separation downstream from the secondary diffuser. Conversely, reducing the outlet diameter diminishes the wake size and intensity of the secondary streamwise vortex that forms downstream from the outlet (visible as a low velocity region at the center near the outlet in Figure 57). Reducing outlet diameter increases the axial flow in the outlet and helps reduce angular velocity, thereby reducing the strength of the axial vortex and minimizing thrombosis downstream from the secondary diffuser. On another note, an excessively small secondary diffuser creates stagnant flow and promotes thrombosis due to the increased resistance in the secondary diffuser and the consequent tendency of the flow path to bypass it. Despite these findings, the study did not find a strong, definitive relationship between hemolysis and thrombosis. In most cases, hemolysis and thrombosis seemed to occur separately, likely because thrombosis tends to happen at low to moderate shear, whereas hemolysis takes place at moderate to high shear.

The moderate shear range seems to induce an increase in both hemolysis and thrombosis, however. This range coincides with the operating conditions of many blood pumps, however, that aim to reduce shear to minimize hemolysis but cannot do so completely due to the necessity to generate sufficient pressure to assist cardiac function. Therefore it is likely that in the context of MCS devices that are optimized to reduce hemolysis, the effect of hemolysis will have a paradoxically larger impact in producing thrombus.

#### 5.2.4 Limitations of the Computational Method and Study

In general, the present study was relatively well validated experimentally compared to other thrombosis modelling efforts and included a relatively thorough grid convergence study. A particular strength of the present study is that model coefficients are fit from one data set and cross validated against another data, which is seldom done in other such studies. This additional validation step is important to establish that the thrombus modelling scheme was robust over a wide variety of flows, and remarkably was able to reproduce experimentally measured thrombus length and growth over time despite changing material types.

Despite this and the comprehensive insights gained, however, the study acknowledges several gaps in the validation approach that present both challenges for future work and opportunities for model improvement. For instance, while the experiment succeeded in validating thrombus growth downstream from a backward-facing step, it is unclear whether it can accurately predict thrombus formation sites. The backward-facing step case generally guarantees thrombus formation due to the presence of a complete stagnation point, which guarantees thrombus formation and is thus a very basic validation point. Therefore, to make the model more robust, it is necessary to validate it against a more stringent validation case where shear stress is low but not zero, and scrutinize the model's proficiency in predicting thrombus locations. Additionally, this study majorly focuses on modelling the effect of hemolysis on thrombosis, but this aspect remains unvalidated as flow conditions and shear stresses in the backward-facing step case are insufficient to cause appreciable hemolysis. Future studies should measure thrombus growth at higher speeds in a similar experimental channel. Validation of the hemolysis model itself would be useful as hemolysis, and in particular stress-based models have notoriously high error and tend to severely underpredict the degree of hemolysis in the sublethal regime. Nevertheless, as it was desired to gauge the degree to which several ranges of hemolysis affect thrombosis, the accuracy of the hemolysis model is in fact not material to the results. In general however, validating the model developed here of the interaction between hemolysis and thrombosis is challenging, as it is challenging to separate the two phenomena *in vitro* due to the extreme complexity of blood chemistry. For example, attempting to introduce agents that bind to hemoglobin to prevent it from binding to vWF will affect vWF and heparin as well. A possible validation approach would be to reproduce the immersed spinning disk experiments of Navitsky et al.<sup>353</sup>, but then to introduce varying concentrations of hemoglobin into the PRP solution and allowing it to sufficiently mix prior to beginning blood shearing.

Such a step was planned, but hindered due to the difficulty in finding an appropriate lab space to conduct validation experiments with whole blood.

Furthermore, certain modelling limitations should be carefully reconsidered. The assumption of blood as a Newtonian fluid, commonly applied in vascular hemodynamics simulations, may not be appropriate for thrombus formation studies as thrombus form typically at low stress, which are precisely the regime where the Newtonian viscosity assumption is basically invalid.

Similarly, flow in the backwards-facing step validation case was also modelled as Newtonian and laminar, which though initially making sense, given the above arguments is flawed because it underpredicts shear stress in low-shear regions where stress thrombus form. Indeed, as was noted, the separated shear layer in a hydrodynamic flow would normally transition to turbulence and reattach. It is also noted that very little experimental evidence examines the turbulent characteristics of separated flows. Although it can be difficult to visualize blood flow, it is relatively trivial to visualize the separation length through dye visualization, and 4D flow MRI or laser-doppler velocimetry can be used to examine the surface characteristics in clear experimental chambers.

Moreover, as has been noted, the usage of a  $k-\omega$  model for turbulence modelling in blood might not produce accurate turbulence kinetic energy and dissipation rate distributions found in real blood. In this regard, turbulent shear stress is known to overpredict hemolysis, yet fluctuating component of stress is also found to underpredict platelet activation using conventional models. It is furthermore unclear whether turbulent or laminar stress should be used in embolization terms or platelet activation terms. Presently however, no appropriate alternative model exists. For this reason, the study computed hemolysis using the laminar component of the von-mises stress. Furthermore, sublethal hemolysis, which is neglected in the model, is crucial as the power law formulation of hemolysis is known to underpredict hemolysis in the sublethal regime, and it was shown that sublethal hemolytic levels could aide thrombosis by activating platelets in low-shear conditions. Additionally, the model sets hemoglobin diffusion to zero, and while turbulent diffusion is ostensibly present, its accuracy in reflecting reality is unclear.

Furthermore, the shear stress activation of platelets is based on Hellums<sup>324,326</sup> data and fitting, which included short time-scale activation data is flawed, since Hellums' data predicts the onset of platelet activation based on stress, and not the level of platelet activation itself. The data of Hellums also does not consider the self-activation of platelets via thrombin. More recent

models, like those of Sheriff et al.<sup>329</sup>, should be considered for future work. Nonetheless, these models don't account for platelet activation at short timescales that correspond to the range of residence times found in MCS. Considering the knowledge that high frequency stresses' impact on platelet activation, it was deemed appropriate to use Hellum's data, following the methodology of Wu et al.<sup>339</sup> and Rojano et al.<sup>18</sup>, aiming to capture platelet activation at short time scales effectively. In general, the implications of changing the platelet activation parameters in relation to the current model warrant further investigation, though as shear levels are already high, platelet activation already occurs relatively early in the domain. The model is also quite sensitivity to several other key parameters, notably the platelet adhesion rate, and the embolization parameters, which have an outsized impact on thrombogenicity.

Thus, while our computational method achieved a degree of overall agreement with experimental data and underwent validation and verification processes, in consideration of the limitations inherent in modelling blood flow the results can be considered with a grain of salt. Future work can focus on refining the computational model by incorporating more accurate representations of the flow behaviour and blood rheology to further enhance the validity of the results.

### **5.2.5 Future Work**

In light of the above, the current study leaves many questions unanswered and paves the way for several avenues of future work. These are broadly categorized into efforts to improve model accuracy and scope, the need for better model validation, and further investigation of physical effects found in the course of the present study.

While the current embolization model provides a basis for understanding platelet dynamics, several enhancements could refine the model further. It's important to clarify the material dependency of embolization and frame constitutive models accordingly. The processes of surface immobilization of adhesion mediators like collagen, fibrinogen, and von Willebrand factor, which are instrumental in platelet adhesion, remain ambiguous, as does their incorporation into continuum models. Yet, the process of immobilization itself is central to material biocompatibility. Clarifying these could further our ability to predict and improve device hemocompatibility by enabling a deeper understanding of how to select or even design materials that do not immobilize adhesion mediator proteins. Similarly, more comprehensive continuum models of adhesion processes are needed that incorporate the full spectrum of mediating proteins, along with their associated active shear rates would help establish more

robust methods of predicting adhesion. The process of embolization involves the reverse of these processes, protein breakage and dissociation, which are viscoelastic and time-dependent. Adopting a more fundamental approach, that takes a stochastic view of microscale mechanics such as the method proposed in Fogelson's classical 1992 paper<sup>347</sup> could help develop robust embolization formulations. Even developing empirical relationships for adhesion and embolization that have physical grounding, however, would go a long way to enhance continuum modelling of thrombosis. Despite our vast knowledge on platelet function, it is still unclear how such formulations would look, due to the complexity and scope of the processes involved. Furthermore, as large, stabilized clots tend to embolize as units rather than platelet-by-platelet, clot structural mechanics and whole clot embolization must be better understood to truly predict the risk of thromboembolic events to patients in a patient-specific manner. Finally, improved platelet activation modelling necessitates more data and modelling tools that captures the effect of high-frequency loading conditions such as those induced by turbulent fluctuations or the rapid hemodynamic fluctuations inherent in MCS.

Like other works, this study also ignores the effect of red blood cells in clot growth, electing to model white clot growth rather than the weaker, softer, and potentially more dangerous red blood clots. Incorporation of red blood cells into thrombosis modelling is a necessary step that must be taken in order to give such models any real predictive value in vivo.

The necessary acceleration of several of the ADR equations in this work to make the computations more tractable, is also somewhat dubious. In this study, due to the absence of significant nonlinearities between fast and slow processes, it was possible to not include a more comprehensive bridging treatment of the temporal scales. As the complexity of the modelling increases, however, multiscale mixing techniques, such as multi timestep and flux splitting become more necessary. Such schemes account for the interaction between fluctuating portions of fast equations and the slow terms and improve accuracy while further reducing computational time.

Additionally, a sensitivity analysis should be conducted on model parameters such as the characteristic platelet activation time and vWF conversion time which could aid in refining the model's predictions. The current neglect of the coagulation cascade, particularly the impact of endothelial cells on thrombosis, is also a critical flaw in the model. As long-term implants undergo reendothelialization, it's imperative to consider the endothelium in the modelling process. Additionally, to predict thrombotic events within the vasculature better, especially



considering atherosclerotic profiles of an artery, incorporating the extrinsic coagulation cascade is essential. In general, more refined hemolysis modelling, particularly in the sublethal hemolytic regime, would improve the understanding of the effect of hemolysis on thrombosis. In addition, it would be useful to examine the effect of hemolysis on thrombosis more thoroughly in low-shear environments like cannulae, catheters, or stents, to gauge whether the importance of ADP release during sublethal hemolysis has a significant effect on thrombosis.

Lastly, a robust model also requires extensive in-vitro validation data for both hemolysis and thrombosis across various flow regimes with whole blood. As noted, a better understanding is needed on the impact of material biocompatibility and surface roughness on platelet adhesion and embolization, as to date, no comprehensive review has been done on the thrombogenicity of various materials and this information is generally very difficult to find. Moreover, validating the model against data sets involving thrombosis formation over less simplified and not inherently thrombogenic geometries could help assess the model's predictive accuracy. This is doubly true in the present study, in which the hemolytic interaction with thrombosis is not thoroughly validated.

Given that thrombosis occurs readily in low shear areas where fibrin-mediated adhesion becomes important, understanding fibrin polymerization and clot stabilization becomes paramount, especially for predicting thrombus detachment. Finally, as discussed, the effect of anticoagulants like heparin on the adhesion rate, particularly under the influence of extracellular hemoglobin, needs to be considered for a more comprehensive understanding of the impact of hemolysis on thrombosis.

Thus, while insightful, the present modelling approach leaves substantial room for improvement. Implementing these suggested enhancements could pave the way for a more comprehensive and predictive model, thereby enabling a more accurate understanding and prediction of blood damage phenomena.

## Chapter 6: Conclusions

---

In the course of this work, two computational studies were performed. The first focused on examining the impact of red blood cell (RBC) collisions, viscoelasticity, and hematocrit on the strain accumulated on the RBC membrane, as well as the diffusion of transmembrane hemoglobin. The second study modelled and examined the effect of hemolysis, specifically the hemolytic release of ADP and hemolysis induced hyperadhesion, on thrombus development in an open-hub LVAD.

To achieve the objective of the first study, a novel formulation of the Yeoh hyperelastic membrane model was established that integrated area inextensibility into the formulation proposed by previous work. This model was enhanced with higher-order terms to create an increased stiffening effect on the membrane under high shear rates to prevent excessive extension. Validation against experimental data derived from optical tweezer studies showed that the model reproduced the force-displacement curves shown in experiment at lower shear rates. Constraints applied to the area strain in single-cell cases resulted in approximately 6-8% membrane-averaged area strain near known rupture shear rates. Simultaneously, the required stiffening restricted maximum area strain to around 23-25%.

The study's findings revealed that RBC collisions indeed had a significant impact on membrane area strain, in some instances, increasing membrane-averaged area strain by up to a factor of two. The overall dynamics and strain experienced by the RBC membrane in a shear flow appeared in fact to be largely driven by these collisions. This relative effect was amplified at lower shear rates yet persisted at higher shear rates. Moreover, elevating the hematocrit, at a constant shear rate of  $20,000 \text{ s}^{-1}$ , seemed to intensify the area strain developed on the membrane. The influence on transmembrane hemoglobin diffusion was noticeable and proportional to the rise in area strain. These findings are in general contradiction to the commonly accepted knowledge that collisions between RBCs do not influence hemolysis or the development of area strain. Finally, the study observed that under sufficient packing, collisions could generate turbulent kinetic energy at the length scale of the red blood cell diameter. The findings support Antiga and Steinman's hypothesis that the Kolmogorov scale should be on par with the diameter of the red blood cell, and calls for further work into this phenomenon.

The second investigation undertaken as part of this study aimed to model and examine the impact of hemolysis on thrombus growth within an open-hub LVAD. Two mechanisms of interaction were considered: the release of ADP during hemolysis and the effect of extracellular hemoglobin-induced hyperadhesion. In addition, the research probed the effect of varying LVAD geometry and operating parameters on thrombosis.

The computational method was validated against in-vitro MRI imaging experiments performed on thrombus growing downstream from a backwards-facing step in a small cylindrical channel flow and found adequate agreement with the thrombus length predicted over time. A new constitutive relationship for single-platelet embolization rates was proposed, which enhanced the model's ability to predict experimental platelet distribution concentrations.

Overall, the study found that hemolysis exerted a modest but noteworthy effect on thrombus growth in the LVAD, with the impact varying based on rotor speed and shear level. At lower rotor speeds, where shear-stress-based activation of platelets was less prevalent, the release of ADP during hemolysis had a more pronounced effect, potentially triggering earlier onset of thrombosis. Meanwhile, hyperadhesion had a dominant role in high shear rate cases. In these scenarios, a significant release of hemoglobin led to an increased conversion of von Willebrand factor to its hyper-adhesive form, which enhanced the local rate of thrombus growth in affected areas by up to a factor of 6. Due to the long reaction time of the vWF conversion process, however, the impact of hemolysis was contingent upon the presence of stagnation zones. Hyperadhesion was found to mostly accelerate the growth of existing thrombus, within which the hyperadhesion reaction had sufficient time to reach completion. It was however, found to increase the local adhesion rate outside of formed thrombi by up to a factor of 2, enabling thrombus formation in regions where it was not found in the non-hemolytic case.

In conclusion, the study's principal objectives – to determine the effect of red blood cell collisions on the development of area strain, and to quantify the influence of hemolysis on thrombosis – were met. The study discovered a profound influence of collisions on the strain experienced by red blood cells and transmembrane hemoglobin diffusion rate. Furthermore, it was found that hemolysis indeed affected thrombosis over a wide range of rotor speeds. Although the effect was relatively mild given the pre-existing thrombogenicity in the LVAD, the mechanisms of ADP release and hemoglobin-induced hyperadhesion were both identified as significant factors that affect thrombogenesis.

## References

---

1. Toyoda Y, Sloane Guy T, Kashem A. Present status and future perspectives of heart transplantation. *Circulation Journal*. 2013;77(5):1097-1110. doi:10.1253/circj.CJ-13-0296
2. Kirklin JK, Naftel DC, Pagani FD, et al. Sixth INTERMACS annual report: A 10,000-patient database. *Journal of Heart and Lung Transplantation*. 2014;33(6):555-564. doi:10.1016/j.healun.2014.04.010
3. Bartoli CR, Zhang D, Kang J, et al. Clinical and In Vitro Evidence That Subclinical Hemolysis Contributes to LVAD Thrombosis. *Annals of Thoracic Surgery*. 2018;105(3):807-814. doi:10.1016/j.athoracsur.2017.05.060
4. L. B. Leverett, J. D. Hellums, C. P. Alfrey ad ECL. Red blood cell damage by shear stress. *Journal of Biophysics*. 1972;12:257-273. <https://www.ncbi.nlm.nih.gov/pmc/articles/PMC1484094/pdf/biophysj00725-0044.pdf>
5. Vercaemst L. Hemolysis in cardiac surgery patients undergoing cardiopulmonary bypass: A review in search of a treatment algorithm. *Journal of Extra-Corporeal Technology*. 2008;40(4):257-267.
6. Giersiepen M, Wurzingler LJ, Opitz R, Reul H. Estimation of shear stress-related blood damage in heart valve prostheses - in vitro comparison of 25 aortic valves. *International Journal of Artificial Organs*. 1990;13(5):300-306. doi:10.1177/039139889001300507
7. Arora D, Behr M, Pasquali M. A tensor-based measure for estimating blood damage. *Artif Organs*. 2004;28(11):1002-1015. doi:10.1111/j.1525-1594.2004.00072.x
8. Vitale, F., Nam, J., Turchetti, L., Behr, M., Raphael, R., Annesini, M. C., & Pasquali M. A Multiscale, Biophysical Model of Flow-Induced Red Blood Cell Damage. *AIChE Journal*. 2014;60(4):1509-1516. doi:10.1002/aic
9. Mckean A. *Development of a New Hemolysis Model with Sublethal Hemoglobin Release*. Master's. McGill University; 2020.
10. Sohrabi S, Liu Y. A Cellular Model of Shear-Induced Hemolysis. *Artif Organs*. 2017;41(9):E80-E91. doi:10.1111/aor.12832

11. Nikfar M, Razizadeh M, Zhang J, Paul R, Wu ZJ, Liu Y. Prediction of mechanical hemolysis in medical devices via a Lagrangian strain-based multiscale model. *Artif Organs*. 2020;44(8):E348-E368. doi:10.1111/aor.13663
12. Nikfar M, Razizadeh M, Paul R, Liu Y. Multiscale modeling of hemolysis during microfiltration. *Microfluid Nanofluidics*. 2020;24(5):1-13. doi:10.1007/s10404-020-02337-3
13. May-Newman K, Vu V, Herold B. Modeling the link between left ventricular flow and thromboembolic risk using lagrangian coherent structures. *Fluids*. 2016;1(4). doi:10.3390/fluids1040038
14. Hosseinipour M, Gupta R, Bonnell M, Elahinia M. Rotary mechanical circulatory support systems. *J Rehabil Assist Technol Eng*. 2017;4:205566831772599. doi:10.1177/2055668317725994
15. Wu WT, Yang F, Wu J, Aubry N, Massoudi M, Antaki JF. High fidelity computational simulation of thrombus formation in Thoratec HeartMate II continuous flow ventricular assist device. *Sci Rep*. 2016;6. doi:10.1038/srep38025
16. Tobin N, Manning KB. Large-Eddy Simulations of Flow in the FDA Benchmark Nozzle Geometry to Predict Hemolysis. *Cardiovasc Eng Technol*. 2020;11(3):254-267. doi:10.1007/s13239-020-00461-3
17. Li Y, Wang H, Xi Y, et al. A New Mathematical Numerical Model to Evaluate the Risk of Thrombosis in Three Clinical Ventricular Assist Devices. *Bioengineering*. 2022;9(6). doi:10.3390/bioengineering9060235
18. Rojano RM, Lai A, Zhussupbekov M, Burgreen GW, Cook K, Antaki JF. A fibrin enhanced thrombosis model for medical devices operating at low shear regimes or large surface areas. *PLoS Comput Biol*. 2022;18(10). doi:10.1371/journal.pcbi.1010277
19. Paffenbarger RSJ, Kampert JB, Lee IM, et al. The New England Journal of Medicine Downloaded from nejm.org at MONASH UNIVERSITY LIBRARY on May 1, 2014. For personal use only. No other uses without permission. From the NEJM Archive. Copyright © 2009 Massachusetts Medical Society. All rights reserved. *Med Sci Sports Exerc*. 1994;314(7):605-613.

20. Russell SD, Teuteberg J. Clinical Trial Results in Mechanical Circulatory Support. *Mechanical Circulatory Support: A Companion to Braunwald's Heart Disease*. Published online January 1, 2020;175-188. doi:10.1016/B978-0-323-56699-5.00015-2
21. Frazier OH, Rose EA, Macmanus Q, et al. Multicenter clinical evaluation of the HeartMate 1000 IP left ventricular assist device. *Ann Thorac Surg*. 1992;53(6). doi:10.1016/0003-4975(92)90393-I
22. Frazier OH, Rose EA, Dz MC, et al. Multicenter clinical evaluation of the HeartMate vented electric left ventricular assist system in patients awaiting heart transplantation. *Journal of Thoracic and Cardiovascular Surgery*. 2001;122(6). doi:10.1067/mtc.2001.118274
23. Hunt SA, Rose EA. The REMATCH trial: Long-term use of a left ventricular assist device for end-stage heart failure. *Rev Port Cardiol*. 2001;20(12).
24. Jorde UP, Kushwaha SS, Tatroles AJ, et al. Results of the destination therapy post-food and drug administration approval study with a continuous flow left ventricular assist device: A prospective study using the INTERMACS registry (interagency registry for mechanically assisted circulatory support). *J Am Coll Cardiol*. 2014;63(17). doi:10.1016/j.jacc.2014.01.053
25. Kirklin JK, Naftel DC, Pagani FD, et al. Pump thrombosis in the Thoratec HeartMate II device: An update analysis of the INTERMACS Registry. *Journal of Heart and Lung Transplantation*. 2015;34(12). doi:10.1016/j.healun.2015.10.024
26. Miller LW, Pagani FD, Russell SD, et al. Use of a Continuous-Flow Device in Patients Awaiting Heart Transplantation. *New England Journal of Medicine*. 2007;357(9). doi:10.1056/nejmoa067758
27. Frazier OH, Myers TJ, Gregoric ID, et al. Initial clinical experience with the Jarvik 2000 implantable axial-flow left ventricular assist system. *Circulation*. 2002;105(24). doi:10.1161/01.CIR.0000018167.47314.AF
28. Moazami N, Steffen RJ, Naka Y, et al. Lessons learned from the first fully magnetically levitated centrifugal LVAD trial in the United States: The duraheart trial. *Annals of Thoracic Surgery*. 2014;98(2). doi:10.1016/j.athoracsur.2014.04.048

29. Rogers JG, Pagani FD, Tatroles AJ, et al. Intrapericardial Left Ventricular Assist Device for Advanced Heart Failure. *New England Journal of Medicine*. 2017;376(5). doi:10.1056/nejmoa1602954
30. Krabatsch T, Netuka I, Schmitto JD, et al. Heartmate 3 fully magnetically levitated left ventricular assist device for the treatment of advanced heart failure -1 year results from the Ce mark trial. *J Cardiothorac Surg*. 2017;12(1):1-8. doi:10.1186/s13019-017-0587-3
31. Gustafsson F, Shaw S, Lavee J, et al. Six-month outcomes after treatment of advanced heart failure with a full magnetically levitated continuous flow left ventricular assist device: Report from the ELEVATE registry. *Eur Heart J*. 2018;39(37). doi:10.1093/eurheartj/ehy513
32. Neal JR, Quintana E, Pike RB, Hoyer JD, Joyce LD, Scheers G. Using daily plasma-free hemoglobin levels for diagnosis of critical pump thrombus in patients undergoing ECMO or VAD support. *Journal of Extra-Corporeal Technology*. 2015;47(2):103-108.
33. Kormos RL, Cowger J, Pagani FD, et al. The Society of Thoracic Surgeons Intermacs Database Annual Report: Evolving Indications, Outcomes, and Scientific Partnerships. *Annals of Thoracic Surgery*. 2019;107(2):341-353. doi:10.1016/j.athoracsur.2018.11.011
34. Mehra MR, Naka Y, Uriel N, et al. A Fully Magnetically Levitated Circulatory Pump for Advanced Heart Failure. *New England Journal of Medicine*. 2017;376(5). doi:10.1056/nejmoa1610426
35. Berger S, Salzman EW. Thromboembolic complication of prosthetic devices. *Prog Hemost Thromb*. 1974;2(0).
36. Suter SP. Flow induced trauma to blood cells. *Circ Res*. 1977;41(1). doi:10.1161/01.RES.41.1.2
37. Maraj R, Jacobs LE, Ioli A, Kotler MN. Evaluation of hemolysis in patients with prosthetic heart valves. *Clin Cardiol*. 1998;21(6). doi:10.1002/clc.4960210604
38. Ismeno G, Renzulli A, Carozza A, et al. Intravascular hemolysis after mitral and aortic valve replacement with different types of mechanical prostheses. *Int J Cardiol*. 1999;69(2). doi:10.1016/S0167-5273(99)00024-8

39. Minneci PC, Deans KJ, Zhi H, et al. Hemolysis-associated endothelial dysfunction mediated by accelerated NO inactivation by decompartmentalized oxyhemoglobin. *Journal of Clinical Investigation*. 2005;115(12):3409-3417. doi:10.1172/JCI25040
40. De Graaf JC, Banga JD, Moncada S, Palmer RMJ, De Groot PG, Sixma JJ. Nitric oxide functions as an inhibitor of platelet adhesion under flow conditions. *Circulation*. 1992;85(6):2284-2290. doi:10.1161/01.CIR.85.6.2284
41. Badiye AP, Hernandez GA, Novoa I, Chaparro S V. Incidence of hemolysis in patients with cardiogenic shock treated with impella percutaneous left ventricular assist device. *ASAIO Journal*. 2016;62(1). doi:10.1097/MAT.0000000000000290
42. Ravichandran AK, Parker J, Novak E, et al. Hemolysis in left ventricular assist device: A retrospective analysis of outcomes. *Journal of Heart and Lung Transplantation*. 2014;33(1). doi:10.1016/j.healun.2013.08.019
43. Levin AP, Saeed O, Willey JZ, et al. Watchful waiting in continuous-flow left ventricular assist device patients with ongoing hemolysis is associated with an increased risk for cerebrovascular accident or death. *Circ Heart Fail*. 2016;9(5). doi:10.1161/CIRCHEARTFAILURE.115.002896
44. John R, Holley CT, Eckman P, et al. A Decade of Experience With Continuous-Flow Left Ventricular Assist Devices. *Semin Thorac Cardiovasc Surg*. 2016;28(2):363-375. doi:10.1053/j.semtcvs.2016.05.013
45. Tchanchaleishvili V, Sagebin F, Ross RE, Hallinan W, Schwarz KQ, Massey HT. Evaluation and treatment of pump thrombosis and hemolysis. *Ann Cardiothorac Surg*. 2014;3(5).
46. Uriel N, Colombo PC, Cleveland JC, et al. Hemocompatibility-related outcomes in the MOMENTUM 3 trial at 6 months: A randomized controlled study of a fully magnetically levitated pump in advanced heart failure. *Circulation*. 2017;135(21). doi:10.1161/CIRCULATIONAHA.117.028303
47. Bartoli CR, Hennessy-Strahs S, Gohean J, et al. A Novel Toroidal-Flow Left Ventricular Assist Device Minimizes Blood Trauma: Implications of Improved Ventricular Assist Device Hemocompatibility. *Annals of Thoracic Surgery*. 2019;107(6). doi:10.1016/j.athoracsur.2018.11.053



48. Bavaria JE, Desai ND, Cheung A, et al. The St Jude medical trifecta aortic pericardial valve: Results from a global, multicenter, prospective clinical study. *Journal of Thoracic and Cardiovascular Surgery*. 2014;147(2). doi:10.1016/j.jtcvs.2012.12.087
49. Concistrè G, Chiaramonti F, Bianchi G, et al. Aortic Valve Replacement With Perceval Bioprosthesis: Single-Center Experience With 617 Implants. *Annals of Thoracic Surgery*. 2018;105(1). doi:10.1016/j.athoracsur.2017.05.080
50. Hwang HY, Choi JW, Kim HK, Kim KH, Kim KB, Ahn H. Paravalvular leak after mitral valve replacement: 20-year follow-up. *Annals of Thoracic Surgery*. 2015;100(4). doi:10.1016/j.athoracsur.2015.03.104
51. Mecozzi G, Milano AD, De Carlo M, et al. Intravascular hemolysis in patients with new-generation prosthetic heart valves: A prospective study. *Journal of Thoracic and Cardiovascular Surgery*. 2002;123(3). doi:10.1067/mtc.2002.120337
52. Shapira Y, Vaturi M, Sagie A. Hemolysis associated with prosthetic heart valves: A review. *Cardiol Rev*. 2009;17(3). doi:10.1097/CRD.0b013e31819f1a83
53. Feldman D, Pamboukian S V., Teuteberg JJ, et al. The 2013 International Society for Heart and Lung Transplantation Guidelines for mechanical circulatory support: Executive summary. *Journal of Heart and Lung Transplantation*. 2013;32(2). doi:10.1016/j.healun.2012.09.013
54. van Leer B, Powell KG. Introduction to Computational Fluid Dynamics. In: *Encyclopedia of Aerospace Engineering*. ; 2010:34. doi:10.1002/9780470686652.eae048
55. Harter K, Levine M, Henderson SO. Anticoagulation drug therapy: A review. *Western Journal of Emergency Medicine*. 2015;16(1):11-17. doi:10.5811/westjem.2014.12.22933
56. Kirklin JK, Naftel DC, Kormos RL, et al. Interagency Registry for Mechanically Assisted Circulatory Support (INTERMACS) analysis of pump thrombosis in the HeartMate II left ventricular assist device. *Journal of Heart and Lung Transplantation*. 2014;33(1).

57. Starling RC, Moazami N, Silvestry SC, et al. Unexpected Abrupt Increase in Left Ventricular Assist Device Thrombosis. *New England Journal of Medicine*. 2014;370(1). doi:10.1056/nejmoa1313385
58. Stevenson LW. The urgent priority for transplantation is to trim the waiting list. *Journal of Heart and Lung Transplantation*. 2013;32(9). doi:10.1016/j.healun.2013.06.018
59. Najjar SS, Slaughter MS, Pagani FD, et al. An analysis of pump thrombus events in patients in the HeartWare ADVANCE bridge to transplant and continued access protocol trial. *Journal of Heart and Lung Transplantation*. 2014;33(1). doi:10.1016/j.healun.2013.12.001
60. Tuncer ON, Kemaloğlu C, Erbasan O, Gölbaşı, Türkay C, Bayezid. Outcomes and Readmissions After Continuous Flow Left Ventricular Assist Device: Heartmate II Versus Heartware Ventricular Assist Device. *Transplant Proc*. 2016;48(6):2157-2161. doi:10.1016/j.transproceed.2016.03.056
61. Cornwell WK, Ambardekar A V., Tran T, et al. Stroke Incidence and Impact of Continuous-Flow Left Ventricular Assist Devices on Cerebrovascular Physiology. *Stroke*. 2019;50(2):542-548. doi:10.1161/STROKEAHA.118.022967
62. Netuka I, Sood P, Pya Y, et al. Fully Magnetically Levitated Left Ventricular Assist System for Treating Advanced HF A Multicenter Study. *J Am Coll Cardiol*. 2015;66(23). doi:10.1016/j.jacc.2015.09.083
63. Draper K V., Huang RJ, Gerson LB. GI bleeding in patients with continuous-flow left ventricular assist devices: A systematic review and meta-analysis. *Gastrointest Endosc*. 2014;80(3). doi:10.1016/j.gie.2014.03.040
64. Crow S, John R, Boyle A, et al. Gastrointestinal bleeding rates in recipients of nonpulsatile and pulsatile left ventricular assist devices. *Journal of Thoracic and Cardiovascular Surgery*. 2009;137(1). doi:10.1016/j.jtcvs.2008.07.032
65. Hayes HM, Dembo LG, Larbalestier R, O'Driscoll G. Management options to treat gastrointestinal bleeding in patients supported on rotary left ventricular assist devices: A single-center experience. *Artif Organs*. 2010;34(9). doi:10.1111/j.1525-1594.2010.01084.x

66. Kushnir VM, Sharma S, Ewald GA, et al. Evaluation of GI bleeding after implantation of left ventricular assist device. *Gastrointest Endosc.* 2012;75(5). doi:10.1016/j.gie.2011.12.014
67. Stern DR, Kazam J, Edwards P, et al. Increased incidence of gastrointestinal bleeding following implantation of the heartmate II LVAD. *J Card Surg.* 2010;25(3). doi:10.1111/j.1540-8191.2010.01025.x
68. Healy AH, McKellar SH, Drakos SG, Koliopoulou A, Stehlik J, Selzman CH. Physiologic effects of continuous-flow left ventricular assist devices. *Journal of Surgical Research.* 2016;202(2). doi:10.1016/j.jss.2016.01.015
69. Letsou G V., Shah N, Gregoric ID, Myers TJ, Delgado R, Frazier OH. Gastrointestinal bleeding from arteriovenous malformations in patients supported by the Jarvik 2000 axial-flow left ventricular assist device. *Journal of Heart and Lung Transplantation.* 2005;24(1). doi:10.1016/j.healun.2003.10.018
70. Crow S, Chen D, Milano C, et al. Acquired von Willebrand syndrome in continuous-flow ventricular assist device recipients. *Annals of Thoracic Surgery.* 2010;90(4). doi:10.1016/j.athoracsur.2010.04.099
71. Gurvits GE, Fradkov E. Bleeding with the artificial heart: Gastrointestinal hemorrhage in CF-LVAD patients. *World J Gastroenterol.* 2017;23(22). doi:10.3748/wjg.v23.i22.3945
72. Starke RD, Ferraro F, Paschalaki KE, et al. Endothelial von Willebrand factor regulates angiogenesis. *Blood.* 2011;117(3). doi:10.1182/blood-2010-01-264507
73. Nascimbene A, Neelamegham S, Frazier OH, Moake JL, Dong JF. Acquired von Willebrand syndrome associated with left ventricular assist device. *Blood.* 2016;127(25). doi:10.1182/blood-2015-10-636480
74. Wu T, Lin J, Cruz MA, Dong JF, Zhu C. Force-induced cleavage of single VWFA1A2A3 tridomains by ADAMTS-13. *Blood.* 2010;115(2). doi:10.1182/blood-2009-03-210369
75. Tsai HM, Sussman II, Nagel RL. Shear stress enhances the proteolysis of von Willebrand factor in normal plasma. *Blood.* 1994;83(8). doi:10.1182/blood.v83.8.2171.bloodjournal8382171

76. Auton M, Sowa KE, Smith SM, Sedláč E, Vijayan KV, Cruz MA. Destabilization of the A1 domain in von Willebrand factor dissociates the A1A2A3 tri-domain and provokes spontaneous binding to glycoprotein Iba and platelet activation under shear stress. *Journal of Biological Chemistry*. 2010;285(30). doi:10.1074/jbc.M110.103358
77. Kroll MH, Hellums JD, McIntire L V., Schafer AI, Moake JL. Platelets and shear stress. *Blood*. 1996;88(5):1525-1541. doi:10.1182/blood.v88.5.1525.bloodjournal8851525
78. Wijeratne SS, Botello E, Yeh HC, et al. Mechanical activation of a multimeric adhesive protein through domain conformational change. *Phys Rev Lett*. 2013;110(10). doi:10.1103/PhysRevLett.110.108102
79. Ikeda Y, Handa M, Kawano K, et al. The role of von Willebrand factor and fibrinogen in platelet aggregation under varying shear stress. *Journal of Clinical Investigation*. 1991;87(4). doi:10.1172/JCI115124
80. Moake JL, Turner NA, Stathopoulos NA, Nolasco L, Hellums JD. Shear-induced platelet aggregation can be mediated by vWF released from platelets, as well as by exogenous large or unusually large vWF multimers, requires adenosine diphosphate, and is resistant to aspirin. *Blood*. 1988;71(5). doi:10.1182/blood.v71.5.1366.bloodjournal7151366
81. Sarosiek K, Bogar L, Conn MI, O'Hare B, Hirose H, Cavarocchi NC. An old problem with a new therapy: Gastrointestinal bleeding in ventricular assist device patients and deep overtube-assisted enteroscopy. *ASAIO Journal*. 2013;59(4). doi:10.1097/MAT.0b013e318299fed3
82. Federici AB, Rand JH, Bucciarelli P, et al. Acquired von Willebrand syndrome: Data from an international registry. *Thromb Haemost*. 2000;84(2). doi:10.1055/s-0037-1614018
83. Razizadeh M, Nikfar M, Paul R, Liu Y. Coarse-Grained Modeling of Pore Dynamics on the Red Blood Cell Membrane under Large Deformations. *Biophys J*. 2020;119(3):471-482. doi:10.1016/j.bpj.2020.06.016
84. Konstam MA, Kiernan MS, Bernstein D, et al. Evaluation and Management of Right-Sided Heart Failure: A Scientific Statement From the American Heart Association. *Circulation*. 2018;137(20):e578-e622. doi:10.1161/CIR.0000000000000560

85. Farrar DJ, Compton PG, Hershon JJ, Fonger JD, Hill JD. Right heart interaction with the mechanically assisted left heart. *World J Surg.* 1985;9(1). doi:10.1007/BF01656260
86. Houston BA, Shah KB, Mehra MR, Tedford RJ. A new “twist” on right heart failure with left ventricular assist systems. *Journal of Heart and Lung Transplantation.* 2017;36(7). doi:10.1016/j.healun.2017.03.014
87. Dang NC, Topkara VK, Mercando M, et al. Right heart failure after left ventricular assist device implantation in patients with chronic congestive heart failure. *Journal of Heart and Lung Transplantation.* 2006;25(1). doi:10.1016/j.healun.2005.07.008
88. Kormos RL, Teuteberg JJ, Pagani FD, et al. Right ventricular failure in patients with the HeartMate II continuous-flow left ventricular assist device: Incidence, risk factors, and effect on outcomes. *Journal of Thoracic and Cardiovascular Surgery.* 2010;139(5). doi:10.1016/j.jtcvs.2009.11.020
89. Atluri P, Goldstone AB, Fairman AS, et al. Predicting right ventricular failure in the modern, continuous flow left ventricular assist device era. In: *Annals of Thoracic Surgery.* Vol 96. ; 2013. doi:10.1016/j.athoracsur.2013.03.099
90. Fitzpatrick JR, Frederick JR, Hsu VM, et al. Risk Score Derived from Pre-operative Data Analysis Predicts the Need for Biventricular Mechanical Circulatory Support. *Journal of Heart and Lung Transplantation.* 2008;27(12). doi:10.1016/j.healun.2008.09.006
91. Pronschinske KB, Qiu S, Wu C, et al. Neutrophil gelatinase-associated lipocalin and cystatin C for The prediction of clinical events in patients with advanced heart failure and after ventricular assist device placement. *Journal of Heart and Lung Transplantation.* 2014;33(12). doi:10.1016/j.healun.2014.06.007
92. Lampert BC, Teuteberg JJ. Right ventricular failure after left ventricular assist devices. *Journal of Heart and Lung Transplantation.* 2015;34(9). doi:10.1016/j.healun.2015.06.015
93. Takeda K, Takayama H, Colombo PC, et al. Incidence and clinical significance of late right heart failure during continuous-flow left ventricular assist device support. *Journal of Heart and Lung Transplantation.* 2015;34(8). doi:10.1016/j.healun.2015.03.011

94. Krishan K, Nair A, Pinney S, Adams DH, Anyanwu AC. Liberal use of tricuspid-valve annuloplasty during left-ventricular assist device implantation. *European Journal of Cardio-thoracic Surgery*. 2012;41(1). doi:10.1016/j.ejcts.2011.05.047
95. Drakos SG, Janicki L, Horne BD, et al. Risk Factors Predictive of Right Ventricular Failure After Left Ventricular Assist Device Implantation. *American Journal of Cardiology*. 2010;105(7). doi:10.1016/j.amjcard.2009.11.026
96. Puwanant S, Hamilton KK, Klodell CT, et al. Tricuspid Annular Motion as a Predictor of Severe Right Ventricular Failure After Left Ventricular Assist Device Implantation. *Journal of Heart and Lung Transplantation*. 2008;27(10). doi:10.1016/j.healun.2008.07.022
97. Vivo RP, Cordero-Reyes AM, Qamar U, et al. Increased right-to-left ventricle diameter ratio is a strong predictor of right ventricular failure after left ventricular assist device. *Journal of Heart and Lung Transplantation*. 2013;32(8). doi:10.1016/j.healun.2013.05.016
98. Kato TS, Farr M, Schulze PC, et al. Usefulness of two-dimensional echocardiographic parameters of the left side of the heart to predict right ventricular failure after left ventricular assist device implantation. *American Journal of Cardiology*. 2012;109(2). doi:10.1016/j.amjcard.2011.08.040
99. Grant ADM, Smedira NG, Starling RC, Marwick TH. Independent and incremental role of quantitative right ventricular evaluation for the prediction of right ventricular failure after left ventricular assist device implantation. *J Am Coll Cardiol*. 2012;60(6). doi:10.1016/j.jacc.2012.02.073
100. Potapov E V., Stepanenko A, Dandel M, et al. Tricuspid Incompetence and Geometry of the Right Ventricle as Predictors of Right Ventricular Function After Implantation of a Left Ventricular Assist Device. *Journal of Heart and Lung Transplantation*. 2008;27(12). doi:10.1016/j.healun.2008.08.012
101. Smedira NG, Hoercher KJ, Lima B, et al. Unplanned hospital readmissions after heartmate II implantation. Frequency, risk factors, and impact on resource use and survival. *JACC Heart Fail*. 2013;1(1). doi:10.1016/j.jchf.2012.11.001

102. Topkara VK, Kondareddy S, Malik F, et al. Infectious complications in patients with left ventricular assist device: Etiology and outcomes in the continuous-flow era. *Annals of Thoracic Surgery*. 2010;90(4). doi:10.1016/j.athoracsur.2010.04.093
103. Akhter SA, Badami A, Murray M, et al. Hospital readmissions after continuous-flow left ventricular assist device implantation: Incidence, causes, and cost analysis. *Annals of Thoracic Surgery*. 2015;100(3). doi:10.1016/j.athoracsur.2015.03.010
104. Olmsted RZ, Critsinelis A, Kurihara C, et al. Severe LVAD-related infections requiring surgical treatment: Incidence, predictors, effect on survival, and impact of device selection. *J Card Surg*. 2019;34(2). doi:10.1111/jocs.13987
105. O'Horo JC, Saleh OMA, Stulak JM, Wilhelm MP, Baddour LM, Sohail MR. Left ventricular assist device infections: A systematic review. *ASAIO Journal*. 2018;64(3). doi:10.1097/MAT.0000000000000684
106. Imamura T, Kinugawa K, Nitta D, et al. Readmission due to driveline infection can be predicted by new score by using serum albumin and body mass index during long-term left ventricular assist device support. *Journal of Artificial Organs*. 2015;18(2). doi:10.1007/s10047-015-0816-2
107. Forest SJ, Friedmann P, Goldstein DJ. Bacteremia after Implantation of Continuous Flow Devices: Associated Factors and Long-Term Outcomes. *The Journal of Heart and Lung Transplantation*. 2013;32(4). doi:10.1016/j.healun.2013.01.738
108. Aggarwal A, Gupta A, Kumar S, et al. Are blood stream infections associated with an increased risk of hemorrhagic stroke in patients with a left ventricular assist device? *ASAIO Journal*. 2012;58(5). doi:10.1097/MAT.0b013e318260c6a6
109. Aldeiri M, Alvarez P, Cordero-Reyes AM, et al. Pseudomonas Aeruginosa Bacteremia in Patients Supported with a Left Ventricular Assist Device Is Associated with an Increased Risk of Hemorrhagic Stroke. *J Card Fail*. 2013;19(8). doi:10.1016/j.cardfail.2013.06.248
110. Clarke A, Pulikottil-Jacob R, Connock M, et al. Cost-effectiveness of left ventricular assist devices (LVADs) for patients with advanced heart failure: Analysis of the British NHS bridge to transplant (BTT) program. *Int J Cardiol*. 2014;171(3). doi:10.1016/j.ijcard.2013.12.015

111. Teuteberg JJ, Ewald GA, Adamson RM, et al. Risk assessment for continuous flow left ventricular assist devices: Does the destination therapy risk score work?: An analysis of over 1,000 patients. *J Am Coll Cardiol*. 2012;60(1). doi:10.1016/j.jacc.2012.02.032
112. Ogawa D, Kobayashi S, Yamazaki K, et al. Mathematical evaluation of cardiac beat synchronization control used for a rotary blood pump. *Journal of Artificial Organs*. 2019;22(4). doi:10.1007/s10047-019-01117-3
113. Slaughter MS, Myers TJ. Transcutaneous energy transmission for mechanical circulatory support systems: History, current status, and future prospects. *J Card Surg*. 2010;25(4). doi:10.1111/j.1540-8191.2010.01074.x
114. Knecht O, Bosshard R, Kolar JW. High-Efficiency Transcutaneous Energy Transfer for Implantable Mechanical Heart Support Systems. *IEEE Trans Power Electron*. 2015;30(11). doi:10.1109/TPEL.2015.2396194
115. Au SLC, McCormick D, Lever N, Budgett D. Thermal evaluation of a hermetic transcutaneous energy transfer system to power mechanical circulatory support devices in destination therapy. *Artif Organs*. 2020;44(9). doi:10.1111/aor.13679
116. Escalona O, Waterman N, McLaughlin J, McEneaney D. Pulsed transmission waveform to mitigate tissue thermal effects in transcutaneous wireless energy supply systems for high-power rated medical implants. In: *IFMBE Proceedings*. Vol 68. ; 2018. doi:10.1007/978-981-10-9038-7\_175
117. García-Villalba M, Rossini L, Gonzalo A, et al. Demonstration of Patient-Specific Simulations to Assess Left Atrial Appendage Thrombogenesis Risk. *Front Physiol*. 2021;12. doi:10.3389/fphys.2021.596596
118. Skodvin TØ, Evju Ø, Helland CA, Isaksen JG. Rupture prediction of intracranial aneurysms: A nationwide matched case-control study of hemodynamics at the time of diagnosis. In: *Journal of Neurosurgery*. Vol 129. ; 2018. doi:10.3171/2017.5.JNS17195
119. Korkmaz E, Kleinloog R, Verweij BH, et al. Comparative ultrastructural and stereological analyses of unruptured and ruptured saccular intracranial aneurysms. *J Neuropathol Exp Neurol*. 2017;76(10). doi:10.1093/jnen/nlx075



120. Janiga G, Daróczy L, Berg P, Thévenin D, Skalej M, Beuing O. An automatic CFD-based flow diverter optimization principle for patient-specific intracranial aneurysms. *J Biomech.* 2015;48(14). doi:10.1016/j.jbiomech.2015.09.039
121. Ma D, Dumont TM, Kosukegawa H, et al. High fidelity virtual stenting (HiFiVS) for intracranial aneurysm flow diversion: In vitro and in silico. *Ann Biomed Eng.* 2013;41(10). doi:10.1007/s10439-013-0808-4
122. Saxer T, Zumbuehl A, Müller B. The use of shear stress for targeted drug delivery. *Cardiovasc Res.* 2013;99(2). doi:10.1093/cvr/cvt102
123. Tarbell JM, Simon SI, Curry FRE. Mechanosensing at the vascular interface. *Annu Rev Biomed Eng.* 2014;16. doi:10.1146/annurev-bioeng-071813-104908
124. Turitto VT, Weiss HJ. Red blood cells: Their dual role in thrombus formation. *Science (1979).* 1980;207(4430):541-543. doi:10.1126/science.7352265
125. Isaksen JG, Bazilevs Y, Kvamsdal T, et al. Determination of wall tension in cerebral artery aneurysms by numerical simulation. *Stroke.* 2008;39(12). doi:10.1161/STROKEAHA.107.503698
126. Brooks DE, Goodwin JW, Seaman G V. Interactions among erythrocytes under shear. *J Appl Physiol.* 1970;28(2). doi:10.1152/jappl.1970.28.2.172
127. Turitto VT, Goldsmith HL. Rheology, transport, and thrombosis in the circulation. *Vascular Medicine: A Textbook of Vascular Medicine New York: Little, Brown & Co.* Published online 1996:141-184.
128. de Haan M, Zavodszky G, Azizi V, Hoekstra AG. Numerical investigation of the effects of red blood cell cytoplasmic viscosity contrasts on single cell and bulk transport behaviour. *Applied Sciences (Switzerland).* 2018;8(9). doi:10.3390/app8091616
129. Evans E, Fung YC. Improved measurements of the erythrocyte geometry. *Microvasc Res.* 1972;4(4):335-347. doi:10.1016/0026-2862(72)90069-6
130. Omori T, Ishikawa T, Barthès-Biesel D, Salsac A V., Imai Y, Yamaguchi T. Tension of red blood cell membrane in simple shear flow. *Phys Rev E Stat Nonlin Soft Matter Phys.* 2012;86(5). doi:10.1103/PhysRevE.86.056321

131. Takizawa K, Bazilevs Y, Tezduyar TE. Space-Time and ALE-VMS Techniques for Patient-Specific Cardiovascular Fluid-Structure Interaction Modeling. *Archives of Computational Methods in Engineering*. 2012;19(2):171-225. doi:10.1007/s11831-012-9071-3
132. Farhat C, Lakshminarayan VK. An ALE formulation of embedded boundary methods for tracking boundary layers in turbulent fluid-structure interaction problems. *J Comput Phys*. 2014;263:53-70. doi:10.1016/j.jcp.2014.01.018
133. Keller SR, Skalak R. Motion of a tank-treading ellipsoidal particle in a shear flow. *J Fluid Mech*. 1982;120:27-47. doi:10.1017/S0022112082002651
134. Fedosov DA, Caswell B, Karniadakis GE. A multiscale red blood cell model with accurate mechanics, rheology, dynamics. *Biophys J*. 2010;98(10):2215-2225. doi:10.1016/j.bpj.2010.02.002
135. Fogelson AL, Guy RD. Immersed-boundary-type models of intravascular platelet aggregation. *Comput Methods Appl Mech Eng*. 2008;197(25-28):2087-2104. doi:10.1016/j.cma.2007.06.030
136. Zhao H, Isfahani AHG, Olson LN, Freund JB. A spectral boundary integral method for flowing blood cells. *J Comput Phys*. 2010;229(10):3726-3744. doi:10.1016/j.jcp.2010.01.024
137. Qi QM, Shaqfeh ESG. Theory to predict particle migration and margination in the pressure-driven channel flow of blood. *Phys Rev Fluids*. 2017;2(9). doi:10.1103/PhysRevFluids.2.093102
138. Vahidkhah K, Diamond SL, Bagchi P. Platelet dynamics in three-dimensional simulation of whole blood. *Biophys J*. 2014;106(11):2529-2540. doi:10.1016/j.bpj.2014.04.028
139. Vahidkhah K, Diamond SL, Bagchi P. Hydrodynamic interaction between a platelet and an erythrocyte: Effect of erythrocyte deformability, dynamics, and wall proximity. *J Biomech Eng*. 2013;135(5):051002. doi:10.1115/1.4023522
140. Rosti ME, Brandt L, Mitra D. Rheology of suspensions of viscoelastic spheres: Deformability as an effective volume fraction. *Phys Rev Fluids*. 2018;3(1). doi:10.1103/PhysRevFluids.3.012301

141. Hall IM. The displacement effect of a sphere in a two-dimensional shear flow. *J Fluid Mech.* 1956;1(2). doi:10.1017/S002211205600010X
142. Saffmn PG. The lift on a small sphere in a slow shear flow - Corrigendum. *J Fluid Mech.* 1968;31(3). doi:10.1017/S0022112068999990
143. Legendre D, Magnaudet J. A note on the lift force on a spherical bubble or drop in a low-Reynolds-number shear flow. *Physics of Fluids.* 1997;9(11). doi:10.1063/1.869466
144. Hibiki T, Ishii M. Lift force in bubbly flow systems. *Chem Eng Sci.* 2007;62(22). doi:10.1016/j.ces.2007.07.034
145. Kaoui B, Ristow GH, Cantat I, Misbah C, Zimmermann W. Lateral migration of a two-dimensional vesicle in unbounded Poiseuille flow. *Phys Rev E Stat Nonlin Soft Matter Phys.* 2008;77(2). doi:10.1103/PhysRevE.77.021903
146. Tomiyama A. Drag and lift and virtual mass forces acting on a single bubble. *3rd International Symposium on Two-phase Flow Modelling and Experimentation.* 2004;(September).
147. Tomiyama A, Tamai H, Zun I, Hosokawa S. Transverse migration of single bubbles in simple shear flows. *Chem Eng Sci.* 2002;57(11). doi:10.1016/S0009-2509(02)00085-4
148. Zhang J, Zhang H, Zhang L, Zhang J. Large Scale Multiphase Flow Numerical Simulation of Individualized Thoracic Aortic Dissection. In: Atlantis Press; 2018. doi:10.2991/iwmecs-18.2018.120
149. Yilmaz F, Gundogdu MY. Analysis of conventional drag and lift models for multiphase CFD modeling of blood flow. *Korea-Australia Rheology Journal.* 2009;21(3):161-173.
150. Sugiyama K, Ii S, Shimizu K, Noda S, Takagi S. A Full Eulerian Method for Fluid-structure Interaction Problems. *Procedia IUTAM.* 2017;20:159-166. doi:10.1016/j.piutam.2017.03.022
151. Ii S, Gong X, Sugiyama K, Wu J, Huang H, Takagi S. A full Eulerian fluid-membrane coupling method with a smoothed volume-of-fluid approach. *Commun Comput Phys.* 2012;12(2):544-576. doi:10.4208/cicp.141210.110811s

152. Takagi S, Sugiyama K, Ii S, Matsumoto Y. A review of full eulerian methods for fluid structure interaction problems. *Journal of Applied Mechanics, Transactions ASME*. 2012;79(1):010911. doi:10.1115/1.4005184
153. Begent N, Born GVR. Growth rate in vivo of platelet thrombi, produced by Iontophoresis of ADP, as a function of mean blood flow velocity. *Nature*. 1970;227(5261). doi:10.1038/227926a0
154. Tokarev AA, Butylin AA, Ataullakhanov FI. Platelet adhesion from shear blood flow is controlled by near-wall rebounding collisions with erythrocytes. *Biophys J*. 2011;100(4). doi:10.1016/j.bpj.2010.12.3740
155. Fogelson AL, Hussain YH, Leiderman K. Blood clot formation under flow: The importance of factor XI depends strongly on platelet count. *Biophys J*. 2012;102(1):10-18. doi:10.1016/j.bpj.2011.10.048
156. Somer T, Meiselman HJ. Disorders of blood viscosity. *Ann Med*. 1993;25(1):31-39. doi:10.3109/07853899309147854
157. Lowe GDO, Lee AJ, Rumley A, Price JF, Fowkes FGR. Blood viscosity and risk of cardiovascular events: The Edinburgh Artery Study. *Br J Haematol*. 1997;96(1):168-173. doi:10.1046/j.1365-2141.1997.8532481.x
158. Lee K, Danilina A V., Kinnunen M, Priezzhev A V., Meglinski I. Probing the Red Blood Cells Aggregating Force With Optical Tweezers. *IEEE Journal of Selected Topics in Quantum Electronics*. 2016;22(3):365-370. doi:10.1109/JSTQE.2015.2477396
159. Bäumlér H, Neu B, Donath E, Kiesewetter H. Basic phenomena of red blood cell rouleaux formation. In: *Biorheology*. Vol 36. ; 1999:439-442.
160. Crowley TA, Pizziconi V. Isolation of plasma from whole blood using planar microfilters for lab-on-a-chip applications. *Lab Chip*. 2005;5(9). doi:10.1039/b502930a
161. Pries AR, Neuhaus D, Gaehtgens P. Blood viscosity in tube flow: Dependence on diameter and hematocrit. *Am J Physiol Heart Circ Physiol*. 1992;263(6 32-6). doi:10.1152/ajpheart.1992.263.6.h1770
162. Robertson AM, Sequeira A, Kameneva M V. Hemorheology. In: *Hemodynamical Flows*. Birkhäuser Basel; 2008:63-120. doi:10.1007/978-3-7643-7806-6\_2

163. Choi SJ, Schowalter WR. Rheological properties of nondilute suspensions of deformable particles. *Physics of Fluids*. 1975;18(4). doi:10.1063/1.861167
164. Zydney AL, Oliver JD, Colton CK. A constitutive equation for the viscosity of stored red cell suspensions: Effect of hematocrit, shear rate, and suspending phase. *J Rheol (N Y N Y)*. 1991;35(8). doi:10.1122/1.550249
165. Long DS, Smith ML, Pries AR, Ley K, Damiano ER. Microviscometry reveals reduced blood viscosity and altered shear rate and shear stress profiles in microvessels after hemodilution. *Proc Natl Acad Sci U S A*. 2004;101(27). doi:10.1073/pnas.0402937101
166. Fung Y cheng. *Biomechanics: Mechanical Properties of Living Tissues*. Springer Science & Business Media; 2013.
167. Chan WY, Ding Y, Tu JY. Modeling of non-Newtonian blood flow through a stenosed artery incorporating fluid-structure interaction. *ANZIAM Journal*. 2007;47. doi:10.21914/anziamj.v47i0.1059
168. Johnston BM, Johnston PR, Corney S, Kilpatrick D. Erratum to “Non-Newtonian blood flow in human right coronary arteries: Transient simulations”. [Journal of Biomechanics 39 (2006) 1116-1128] (DOI:10.1016/j.jbiomech.2005.01.034). *J Biomech*. 2006;39(11). doi:10.1016/j.jbiomech.2006.05.001
169. Cho YI, Kensey KR. Effects of the non-Newtonian viscosity of blood on flows in a diseased arterial vessel. Part 1: Steady flows. *Biorheology*. 1991;28(3-4). doi:10.3233/BIR-1991-283-415
170. Sia SF, Zhao X, Yu Y, Zhang Y. Multiphase particle-in-cell simulation in severe internal carotid artery stenosis. *Powder Technol*. 2019;358:62-67. doi:10.1016/j.powtec.2018.07.091
171. Fuat Yilmaz and Mehmet Yasar Gundogdu. Acritical -review-on blood flow in large arteries. *Korea Australia Rheology Journal*. 2008;20(4):197-211.
172. Beris AN, Horner JS, Jariwala S, Armstrong MJ, Wagner NJ. Recent advances in blood rheology: A review. *Soft Matter*. 2021;17(47):10591-10613. doi:10.1039/d1sm01212f

173. Johnston BM, Johnston PR, Corney S, Kilpatrick D. Non-Newtonian blood flow in human right coronary arteries: Steady state simulations. *J Biomech.* 2004;37(5):709-720. doi:10.1016/j.jbiomech.2003.09.016
174. Ballyk PD, Steinman DA, Ethier CR. Simulation of non-newtonian blood flow in an end-to-side anastomosis. *Biorheology.* 1994;31(5). doi:10.3233/BIR-1994-31505
175. Bird RB, Armstrong RC, Hassager O. Dynamics of polymeric liquids. Vol. 1: Fluid mechanics. Published online 1987.
176. Easthope PL, Brooks DE. A comparison of rheological constitutive functions for whole human blood. *Biorheology.* 1980;17(3).
177. Apostolidis AJ, Beris AN, Dhurjati PS. Introducing CFD through a cardiovascular application in a fluid mechanics course. *Chem Eng Educ.* 2014;48(3):175-184.
178. Thurston GB, Henderson NM, Jeng M. Effects of erythrocytapheresis transfusion on the viscoelasticity of sickle cell blood. *Clin Hemorheol Microcirc.* 2004;30(2).
179. Yeleswarapu KK. *Evaluation of Continuum Models for Characterizing the Constitutive Behavior of Blood.* 1996.
180. Good BC, Deutsch S, Manning KB. Hemodynamics in a Pediatric Ascending Aorta Using a Viscoelastic Pediatric Blood Model. *Ann Biomed Eng.* 2016;44(4):1019-1035. doi:10.1007/s10439-015-1370-z
181. Pinto SIS, Romano E, António CC, Sousa LC, Castro CF. The impact of non-linear viscoelastic property of blood in right coronary arteries hemodynamics — A numerical implementation. *Int J Non Linear Mech.* 2020;123(October 2019):103477. doi:10.1016/j.ijnonlinmec.2020.103477
182. Anderson JD, Degrez G, Dick E, Grundmann R. *Computational Fluid Dynamics: An Introduction.* Springer Science & Business Media; 2013.
183. Anderson J. *Computational Fluid Dynamics: The Basics with Applications.* 1995. McGrawhill Inc. Published online 1995.
184. Issa RI. Solution of the implicitly discretised fluid flow equations by operator-splitting. *J Comput Phys.* 1986;62(1). doi:10.1016/0021-9991(86)90099-9
185. Ansys Inc. Solver theory guide, Ansys Inc. 2013;Release 15:249.

186. Menter FR, Kuntz M, Langtry R. Ten Years of Industrial Experience with the SST Turbulence Model Turbulence heat and mass transfer. *CfdSpbstuRu*. 2003;4(July 2014).
187. Saqr KM, Rashad S, Tupin S, et al. What does computational fluid dynamics tell us about intracranial aneurysms? A meta-analysis and critical review. *Journal of Cerebral Blood Flow and Metabolism*. 2020;40(5). doi:10.1177/0271678X19854640
188. Nouar C, Bottaro A, Brancher JP. Delaying transition to turbulence in channel flow: Revisiting the stability of shear-thinning fluids. *J Fluid Mech*. 2007;592:177-194. doi:10.1017/S0022112007008439
189. Schüle CY, Affeld K, Kossatz M, Paschereit CO, Kertzscher U. Turbulence measurements in an axial rotary blood pump with laser doppler velocimetry. *International Journal of Artificial Organs*. 2017;40(3). doi:10.5301/ijao.5000571
190. Zhang R, Zhang Y. Experimental analysis of pulsatile flow characteristics in prosthetic aortic valve models with stenosis. *Med Eng Phys*. 2020;79. doi:10.1016/j.medengphy.2020.03.004
191. Saqr KM, Tupin S, Rashad S, et al. Origins of Chaos and Turbulence in Blood Flow: Revisiting the Principles of Hemodynamics. *arXiv preprint*. 2020;arXiv:2002.03857. doi:10.13140/RG.2.2.25108.86402
192. Saqr KM, Kano K, Rashad S, et al. Non-Kolmogorov turbulence in carotid artery stenosis and the impact of carotid stenting on near-wall turbulence. *AIP Adv*. 2022;12(1). doi:10.1063/5.0076271
193. Xu D, Avila M. The effect of pulsation frequency on transition in pulsatile pipe flow. *J Fluid Mech*. 2018;857. doi:10.1017/jfm.2018.789
194. Antiga L, Steinman DA. Rethinking turbulence in blood. *Biorheology*. 2009;46(2):77-81. doi:10.3233/BIR-2009-0538
195. Thurston GB. Rheological parameters for the viscosity viscoelasticity and thixotropy of blood. *Biorheology*. 1979;16(3). doi:10.3233/BIR-1979-16303
196. M. Faghieh M, Sharp MK. Characterization of erythrocyte membrane tension for hemolysis prediction in complex flows. *Biomech Model Mechanobiol*. 2018;17(3):827-842. doi:10.1007/s10237-017-0995-2

197. Lux SE. Anatomy of the red cell membrane skeleton: unanswered questions. Published online 2016. doi:10.1182/blood-2014-12
198. Hansen JC, Skalak R, Chien S, Hoger A. An elastic network model based on the structure of the red blood cell membrane skeleton. *Biophys J*. 1996;70(1):146-166. doi:10.1016/S0006-3495(96)79556-5
199. Fischer TM, Haest CW, Stöhr-Liesen M, Schmid-Schönbein H, Skalak R. The stress-free shape of the red blood cell membrane. *Biophys J*. 1981;34(3):409-422. doi:10.1016/S0006-3495(81)84859-X
200. Skalak, R., Tozeren, A., Zarda RP, Chien S. Strain Energy Function of Red Blood Cell Membranes. *Biophys J*. 1973;13(3):245-264.
201. Ju M, Ye SS, Namgung B, et al. A review of numerical methods for red blood cell flow simulation. *Comput Methods Biomech Biomed Engin*. 2015;18(2):130-140. doi:10.1080/10255842.2013.783574
202. Sugiyama K, Ii S, Takeuchi S, Takagi S, Matsumoto Y. A full Eulerian finite difference approach for solving fluid-structure coupling problems. *J Comput Phys*. 2011;230(3):596-627. doi:10.1016/j.jcp.2010.09.032
203. Pozrikidis C. Axisymmetric motion of a file of red blood cells through capillaries. *Physics of Fluids*. 2005;17(3). doi:10.1063/1.1830484
204. Freund JB. The flow of red blood cells through a narrow spleen-like slit. *Physics of Fluids*. 2013;25(11). doi:10.1063/1.4819341
205. Freund JB, Orescanin MM. Cellular flow in a small blood vessel. *J Fluid Mech*. 2011;671:466-490. doi:10.1017/S0022112010005835
206. Dao M, Lim CT, Suresh S. Mechanics of the human red blood cell deformed by optical tweezers. *J Mech Phys Solids*. 2003;51(11-12):2259-2280. doi:10.1016/j.jmps.2003.09.019
207. Mills JP, Qie L, Dao M, Lim CT, Suresh S. Nonlinear elastic and viscoelastic deformation of the human red blood cell with optical tweezers. *Mech Chem Biosyst*. 2004;1(3):169-180.



208. Hansen JC, Skalak R, Chien S, Hoger A. Influence of network topology on the elasticity of the red blood cell membrane skeleton. *Biophys J.* 1997;72(5):2369-2381. doi:10.1016/S0006-3495(97)78882-9
209. Li J, Dao M, Lim CT, Suresh S. Spectrin-level modeling of the cytoskeleton and optical tweezers stretching of the erythrocyte. *Biophys J.* 2005;88(5):3707-3719. doi:10.1529/biophysj.104.047332
210. Dao M, Li J, Suresh S. Molecularly based analysis of deformation of spectrin network and human erythrocyte. *Materials Science and Engineering C.* 2006;26(8):1232-1244. doi:10.1016/j.msec.2005.08.020
211. Takeuchi M, Miyamoto H, Sako Y, Komizu H, Kusumi A. Structure of the erythrocyte membrane skeleton as observed by atomic force microscopy. *Biophys J.* 1998;74(5):2171-2183. doi:10.1016/S0006-3495(98)77926-3
212. Li J, Lykotrafitis G, Dao M, Suresh S. Cytoskeletal dynamics of human erythrocyte. *Proc Natl Acad Sci U S A.* 2007;104(12):4937-4942. doi:10.1073/pnas.0700257104
213. An X, Christine Lecomte M, Chasis JA, Mohandas N, Gratzer W. Shear-response of the spectrin dimer-tetramer equilibrium in the red blood cell membrane. *Journal of Biological Chemistry.* 2002;277(35):31796-31800. doi:10.1074/jbc.M204567200
214. Dimitrakopoulos P. Analysis of the variation in the determination of the shear modulus of the erythrocyte membrane: Effects of the constitutive law and membrane modeling. *Phys Rev E Stat Nonlin Soft Matter Phys.* 2012;85(4):1-10. doi:10.1103/PhysRevE.85.041917
215. Feng Z, Waugh RE, Peng Z. Constitutive Model of Erythrocyte Membranes with Distributions of Spectrin Orientations and Lengths. *Biophys J.* 2020;119(11):2190-2204. doi:10.1016/j.bpj.2020.10.025
216. Discher DE, Boal DH, Boey SK. Simulations of the erythrocyte cytoskeleton at large deformation. II. Micropipette aspiration. *Biophys J.* 1998;75(3):1584-1597. doi:10.1016/S0006-3495(98)74076-7
217. Boey SK, Boal DH, Discher DE. Simulations of the erythrocyte cytoskeleton at large deformation. I. Microscopic models. *Biophys J.* 1998;75(3):1573-1583. doi:10.1016/S0006-3495(98)74075-5

218. Piontek MC, Lira RB, Roos WH. Active probing of the mechanical properties of biological and synthetic vesicles. *Biochim Biophys Acta Gen Subj*. 2021;1865(4):129486. doi:10.1016/j.bbagen.2019.129486
219. Lim CT, Dao M, Suresh S, Sow CH, Chew KT. Large deformation of living cells using laser traps. *Acta Mater*. 2004;52(7):1837-1845. doi:10.1016/j.actamat.2003.12.028
220. Chien S, Sung KL, Skalak R, Usami S, Tözeren A. Theoretical and experimental studies on viscoelastic properties of erythrocyte membrane. *Biophys J*. 1978;24(2):463-487. doi:10.1016/S0006-3495(78)85395-8
221. Hochmuth RM. Erythrocyte Membrane Elasticity and Viscosity. *Annual Reviews of Physiology*. 1987;49:209-219. doi:10.1212/wnl.31.10.1371
222. Rand RP. Mechanical Properties of the Red Cell Membrane: II. Viscoelastic Breakdown of the Membrane. *Biophys J*. 1964;4(4):303-316. doi:10.1016/S0006-3495(64)86784-9
223. Evans EA, Hochmuth RM. Membrane viscoelasticity. *Biophys J*. 1976;16(1):1-11. doi:10.1016/S0006-3495(76)85658-5
224. Hochmuth RM, Worthy PR, Evans EA. Red cell extensional recovery and the determination of membrane viscosity. *Biophys J*. 1979;26(1):101-114. doi:10.1016/S0006-3495(79)85238-8
225. Gómez F, Silva LS, Araújo GRDS, et al. Effect of cell geometry in the evaluation of erythrocyte viscoelastic properties. *Phys Rev E*. 2020;101(6):1-12. doi:10.1103/PhysRevE.101.062403
226. Suter SP, Mehrjardi MH. Deformation and fragmentation of human red blood cells in turbulent shear flow. *Biophys J*. 1975;15(1):1-10. doi:10.1016/S0006-3495(75)85787-0
227. Sharp MK, Mohammad SF. Scaling of hemolysis in needles and catheters. *Ann Biomed Eng*. 1998;26(5):788-797. doi:10.1114/1.65
228. Xu Z, Wang C, Xue S, He F, Hao P, Zhang X. The erythrocyte destruction mechanism in non-physiological shear mechanical hemolysis The erythrocyte destruction mechanism in non-physiological shear mechanical hemolysis. *PHysics of Fluids*. 2022;34(111901). doi:10.1063/5.0112967

229. Yeleswarapu KK, Antaki JF, Kameneva M V., Rajagopal KR. A Mathematical Model for Shear-Induced Hemolysis. *Artif Organs*. 1995;19(7):576-582. doi:10.1111/j.1525-1594.1995.tb02384.x
230. Rand RP, Burton AC. Area and volume changes in hemolysis of single erythrocytes. *J Cell Comp Physiol*. 1963;61:245-253. doi:10.1002/jcp.1030610306
231. Evans EA, Waugh R, Melnik L. Elastic area compressibility modulus of red cell membrane. *Biophys J*. 1976;16(6):585-595. doi:10.1016/S0006-3495(76)85713-X
232. Li F, Chan CU, Ohl CD. Yield strength of human erythrocyte membranes to impulsive stretching. *Biophys J*. 2013;105(4):872-879. doi:10.1016/j.bpj.2013.06.045
233. Yu H, Engel S, Janiga G, Thévenin D. A Review of Hemolysis Prediction Models for Computational Fluid Dynamics. *Artif Organs*. 2017;41(7):603-621. doi:10.1111/aor.12871
234. Faghieh MM, Sharp MK. *Modeling and Prediction of Flow-Induced Hemolysis: A Review*. Vol 18. Springer Berlin Heidelberg; 2019. doi:10.1007/s10237-019-01137-1
235. Ding J, Niu S, Chen Z, Zhang T, Griffith BP, Wu ZJ. Shear-Induced Hemolysis: Species Differences. *Artif Organs*. 2015;39(9):795-802. doi:10.1111/aor.12459
236. Yu H, Engel S, Janiga G, Thévenin D. A Review of Hemolysis Prediction Models for Computational Fluid Dynamics. *Artif Organs*. 2017;41(7):603-621. doi:10.1111/aor.12871
237. Ding J, Niu S, Chen Z, Zhang T, Griffith BP, Wu ZJ. Shear-Induced Hemolysis: Species Differences. *Artif Organs*. 2015;39(9):795-802. doi:10.1111/aor.12459
238. Heuser G, Opitz R. A Couette viscometer for short time shearing of blood. *Biorheology*. 1980;17(1-2):17-24. doi:10.3233/bir-1980-171-205
239. Grigioni M, Daniele C, Morbiducci U, D'Avenio G, Di Benedetto G, Barbaro V. The power-law mathematical model for blood damage prediction: Analytical developments and physical inconsistencies. *Artif Organs*. 2004;28(5):467-475. doi:10.1111/j.1525-1594.2004.00015.x
240. Arwatz G, Smits AJ. A viscoelastic model of shear-induced hemolysis in laminar flow. *Biorheology*. 2013;50(1-2):45-55. doi:10.3233/BIR-130626

241. Zimmer R, Steegers A, Paul R, Affeld K, Reul H. Velocities, shear stresses and blood damage potential of the leakage jets of the Medtronic Parallel(TM) bileaflet valve. *International Journal of Artificial Organs*. 2000;23(1):41-48. doi:10.1177/039139880002300107
242. Chan CHH, Pieper IL, Robinson CR, Friedmann Y, Kanamarlapudi V, Thornton CA. Shear Stress-Induced Total Blood Trauma in Multiple Species. *Artif Organs*. 2017;41(10):934-947. doi:10.1111/aor.12932
243. Grigioni M, Morbiducci U, D'Avenio G, Di Benedetto G, Del Gaudio C. A novel formulation for blood trauma prediction by a modified power-law mathematical model. *Biomech Model Mechanobiol*. 2005;4(4):249-260. doi:10.1007/s10237-005-0005-y
244. Faghieh MM, Keith Sharp M. Extending the Power-Law Hemolysis Model to Complex Flows. *J Biomech Eng*. 2016;138(12). doi:10.1115/1.4034786
245. Nakamura M, Sadao; B, Wada S. Analysis of Red Blood Cell Deformation under Fast Shear Flow for Better Estimation of Hemolysis Masanori. *Int J Numer Method Biomed Eng*. 2014;30(August 2013):42-54. doi:10.1002/cnm
246. Ezzeldin HM, de Tullio MD, Vanella M, Solares SD, Balaras E. A Strain-Based Model for Mechanical Hemolysis Based on a Coarse-Grained Red Blood Cell Model. *Ann Biomed Eng*. 2015;43(6):1398-1409. doi:10.1007/s10439-015-1273-z
247. Tran-Son-Tay R, Suter SP, Zahalak GI, Rao PR. Membrane stress and internal pressure in a red blood cell freely suspended in a shear flow. *Biophys J*. 1987;51(6):915-924. doi:10.1016/S0006-3495(87)83419-7
248. Richardson E. Applications of a theoretical model for haemolysis in shear flow. *Biorheology*. 1975;12(1). doi:10.3233/BIR-1975-12105
249. Rand RP, Burton AC. Mechanical Properties of the Red Cell Membrane: I. Membrane Stiffness and Intracellular Pressure. *Biophys J*. 1964;4(2):115-135. doi:10.1016/S0006-3495(64)86773-4
250. Chen Y, Sharp MK. A Strain-Based Flow-Induced Hemolysis Prediction Model Calibrated by In Vitro Erythrocyte Deformation Measurements. *Artif Organs*. 2011;35(2):145-156. doi:10.1111/j.1525-1594.2010.01050.x

251. Fung YC. *Biomechanics: Mechanical Properties of Living Tissues*. 2nd Editio. Springer; 1993.
252. Arora D, Behrb M, Coronado-Matuttic O, Pasqualic M. Estimation of hemolysis in centrifugal blood pumps using morphology tensor approach. *3rd MIT Conference on Computational Fluid and Solid Mechanics*. 2005;(713):578-582.
253. Dhruv Arora, Behr M, Pasquali M. Hemolysis estimation in a centrifugal blood pump using a tensor-based measure. *Artif Organs*. 2006;30(11):892. doi:10.1111/j.1525-1594.2006.00318.x
254. Barthas-Biesel D, Rallison JM. The Time-Dependent Deformation Of A Capsule Freely Suspended In A Linear Shear Flow. *J Fluid Mech*. 1981;113:251-267. doi:10.1017/S0022112081003480
255. Maffettone PL, Minale M. Equation of change for ellipsoidal drops in viscous flow. *J Nonnewton Fluid Mech*. 1998;78(2-3):227-241. doi:10.1016/S0377-0257(98)00065-2
256. Razizadeh M, Nikfar M, Paul R, Liu Y. Coarse-Grained Modeling of Pore Dynamics on the Red Blood Cell Membrane under Large Deformations. *Biophys J*. 2020;119(3):471-482. doi:10.1016/j.bpj.2020.06.016
257. Jones SA. A relationship between reynolds stresses and viscous dissipation: Implications to red cell damage. *Ann Biomed Eng*. 1995;23(1):21-28. doi:10.1007/BF02368297
258. Quinlan NJ, Dooley PN. Models of flow-induced loading on blood cells in laminar and turbulent flow, with application to cardiovascular device flow. *Ann Biomed Eng*. 2007;35(8):1347-1356. doi:10.1007/s10439-007-9308-8
259. Kishi T, Matsumoto T, Toh S. Non-Kolmogorov scaling for two-particle relative velocity in two-dimensional inverse energy-cascade turbulence. *Phys Rev Fluids*. 2020;5(5). doi:10.1103/PhysRevFluids.5.054601
260. Ge L, Dasi LP, Sotiropoulos F, Yoganathan AP. Characterization of hemodynamic forces induced by mechanical heart valves: Reynolds vs. viscous stresses. *Ann Biomed Eng*. 2008;36(2):276-297. doi:10.1007/s10439-007-9411-x

261. Quinlan N. Mechanical Loading of Blood Cells in Turbulent Flow. *Computational biomechanics for medicine*. 2014;9781493907(February 2014):1-13. doi:10.1007/978-1-4939-0745-8
262. Hund SJ, Antaki JF, Massoudi M. On the representation of turbulent stresses for computing blood damage. *Int J Eng Sci*. 2010;48(11):1325-1331. doi:10.1016/j.ijengsci.2010.09.003
263. Wu P, Groß-Hardt S, Boehning F, Hsu PL. An energy-dissipation-based power-law formulation for estimating hemolysis. *Biomech Model Mechanobiol*. 2020;19(2):591-602. doi:10.1007/s10237-019-01232-3
264. Fok FP, Schuboth H. Studies on Various Factors Influencing Mechanical Haemolysis of Human Erythrocytes. *Br J Haematol*. 1960;6(4). doi:10.1111/j.1365-2141.1960.tb06253.x
265. Mizuguchi K, Damm GA, Aber GS, et al. Does Hematocrit Affect In Vitro Hemolysis Test Results? Preliminary Study with Baylor/NASA Prototype Axial Flow Pump. *Artif Organs*. 1994;18(9):650-656. doi:10.1111/j.1525-1594.1994.tb03394.x
266. Hughes J, McNaughton J, Andrews J, et al. Infusion pump-mediated mechanical hemolysis in pediatric patients. *Ann Clin Lab Sci*. 2015;45(2):140-147.
267. Omori T, Ishikawa T, Imai Y, Yamaguchi T. Membrane tension of red blood cells pairwise interacting in simple shear flow. *J Biomech*. 2013;46(3):548-553. doi:10.1016/j.jbiomech.2012.09.017
268. Tolpekina T V., Den Otter WK, Briels WJ. Simulations of stable pores in membranes: System size dependence and line tension. *Journal of Chemical Physics*. 2004;121(16):8014-8020. doi:10.1063/1.1796254
269. Koshiyama K, Yano T, Kodama T. Self-organization of a stable pore structure in a phospholipid bilayer. *Phys Rev Lett*. 2010;105(1):1-4. doi:10.1103/PhysRevLett.105.018105
270. Koshiyama K, Wada S. Molecular dynamics simulations of pore formation dynamics during the rupture process of a phospholipid bilayer caused by high-speed equibiaxial stretching. *J Biomech*. 2011;44(11):2053-2058. doi:10.1016/j.jbiomech.2011.05.014

271. Evans E, Heinrich V, Ludwig F, Rawicz W. Dynamic tension spectroscopy and strength of biomembranes. *Biophys J.* 2003;85(4):2342-2350. doi:10.1016/S0006-3495(03)74658-X
272. Tolpekina T V., Den Otter WK, Briels WJ. Nucleation free energy of pore formation in an amphiphilic bilayer studied by molecular dynamics simulations. *Journal of Chemical Physics.* 2004;121(23):12060-12066. doi:10.1063/1.1815296
273. Zhang L, Zhang Z, Negahban M, Jérusalem A. Molecular dynamics simulation of cell membrane pore sealing. *Extreme Mech Lett.* 2019;27:83-93. doi:10.1016/j.eml.2019.01.008
274. Needham D, Hochmuth RM. Electro-mechanical permeabilization of lipid vesicles. Role of membrane tension and compressibility. *Biophys J.* 1989;55(5):1001-1009. doi:10.1016/S0006-3495(89)82898-X
275. Riveros-Moreno V, Wittenberg JB. The self-diffusion coefficients of myoglobin and hemoglobin in concentrated solutions. *Journal of Biological Chemistry.* 1972;247(3):895-901. doi:10.1016/s0021-9258(19)45691-3
276. Longeville S, Stingaciu LR. Hemoglobin diffusion and the dynamics of oxygen capture by red blood cells. *Sci Rep.* 2017;7(1):1-10. doi:10.1038/s41598-017-09146-9
277. Bouwer ST, Hoofd L, Kreuzer F. Diffusion coefficients of oxygen and hemoglobin measured by facilitated oxygen diffusion through hemoglobin solutions. *Biochimica et Biophysica Acta - Protein Structure and Molecular Enzymology.* 1997;1338(1). doi:10.1016/S0167-4838(96)00197-5
278. Davidson MG, Deen WM. Hindered Diffusion of Water-Soluble Macromolecules in Membranes. *Macromolecules.* 1988;21(12):3474-3481. doi:10.1021/ma00190a022
279. Yu H, Engel S, Janiga G, Thévenin D. A Review of Hemolysis Prediction Models for Computational Fluid Dynamics. *Artif Organs.* 2017;41(7):603-621. doi:10.1111/aor.12871
280. Garon A, Farinas MI. Fast three-dimensional numerical hemolysis approximation. *Artif Organs.* 2004;28(11). doi:10.1111/j.1525-1594.2004.00026.x

281. Lacasse D, Garon A, Pelletier D. Mechanical hemolysis in blood flow: User-independent predictions with the solution of a partial differential equation. *Comput Methods Biomech Biomed Engin.* 2007;10(1). doi:10.1080/10255840600985535
282. Salazar FA, Rojas-Solórzano LR, Antaki JF. Numerical study of turbulence models in the computation of blood flow in cannulas. In: *2008 Proceedings of the ASME Fluids Engineering Division Summer Conference, FEDSM 2008*. Vol 1. ; 2009. doi:10.1115/FEDSM2008-55266
283. Farinas MI, Garon A, Lacasse D, N'dri D. Asymptotically consistent numerical approximation of hemolysis. *J Biomech Eng.* 2006;128(5). doi:10.1115/1.2241663
284. De Bartolo C, Nigro A, Fragomeni G, et al. Numerical and experimental flow analysis of the Wang-Zwische double-lumen cannula. *ASAIO Journal.* 2011;57(4). doi:10.1097/MAT.0b013e31821c08bc
285. Avcı M, O'rear EA, Foster KM, Papavassiliou D V. Sublethal Damage to Erythrocytes during Blood Flow. *Fluids.* 2022;7(2):1-16. doi:10.3390/fluids7020066
286. Belyaev A V., Dunster JL, Gibbins JM, Pantelev MA, Volpert V. Modeling thrombosis in silico: Frontiers, challenges, unresolved problems and milestones. *Phys Life Rev.* 2018;26-27:57-95. doi:10.1016/j.plrev.2018.02.005
287. Diamond SL. Systems Analysis of Thrombus Formation. *Circ Res.* 2016;118(9):1348-1362. doi:10.1161/CIRCRESAHA.115.306824
288. Orfeo T, Butenas S, Brummel-Ziedins KE, Mann KG. The tissue factor requirement in blood coagulation. *Journal of Biological Chemistry.* 2005;280(52):42887-42896. doi:10.1074/jbc.M505506200
289. Da Q, Teruya M, Guchhait P, Teruya J, Olson JS, Cruz MA. Free hemoglobin increases von Willebrand factor-mediated platelet adhesion in vitro: Implications for circulatory devices. *Blood.* 2015;126(20):2338-2341. doi:10.1182/blood-2015-05-648030
290. Orfeo T, Brummel-Ziedins KE, Gissel M, Butenas S, Mann KG. The nature of the stable blood clot procoagulant activities. *Journal of Biological Chemistry.* 2008;283(15):9776-9786. doi:10.1074/jbc.M707435200



291. Stalker TJ, Traxler EA, Wu J, et al. Hierarchical organization in the hemostatic response and its relationship to the platelet-signaling network Key Points. Published online 2013. doi:10.1182/blood-2012
292. Fogelson AL, Tania N. Coagulation under flow: The influence of flow-mediated transport on the initiation and inhibition of coagulation. *Pathophysiol Haemost Thromb*. 2006;34(2-3):91-108. doi:10.1159/000089930
293. Fogelson AL, Neeves KB. Fluid mechanics of blood clot formation. *Annu Rev Fluid Mech*. 2015;47(1):377-403. doi:10.1146/annurev-fluid-010814-014513
294. Tosenberger A, Ataullakhanov F, Bessonov N, Panteleev M, Tokarev A, Volpert V. Modelling of platelet–fibrin clot formation in flow with a DPD–PDE method. *J Math Biol*. 2016;72(3):649-681. doi:10.1007/s00285-015-0891-2
295. Krasotkina Y V, Sinauridze EI, Ataullakhanov FI. *Spatiotemporal Dynamics of Fibrin Formation and Spreading of Active Thrombin Entering Non-Recalcified Plasma by Diffusion*. www.elsevier.com/locate/bba
296. Guria K, Guria GT. Spatial aspects of blood coagulation: Two decades of research on the self-sustained traveling wave of thrombin. *Thromb Res*. 2015;135(3):423-433. doi:10.1016/j.thromres.2014.12.014
297. Coller BS. Historical perspective and future directions in platelet research. *Journal of Thrombosis and Haemostasis*. 2011;9(1 S):374-395. doi:10.1111/j.1538-7836.2011.04356.x
298. Spyropoulos AC. Platelets in Thrombotic and Non-thrombotic Disorders: Pathophysiology, Pharmacology, and Therapeutics. *Chest*. 2003;124(3):1182-1183. doi:10.1378/chest.124.3.1182
299. Gailani D, Renné T. Intrinsic pathway of coagulation and arterial thrombosis. *Arterioscler Thromb Vasc Biol*. 2007;27(12):2507-2513. doi:10.1161/ATVBAHA.107.155952
300. Gailani D, Renné T. The intrinsic pathway of coagulation: A target for treating thromboembolic disease? *Journal of Thrombosis and Haemostasis*. 2007;5(6):1106-1112. doi:10.1111/j.1538-7836.2007.02446.x

301. Renné T, Gailani D. Role of factor XII in hemostasis and thrombosis: Clinical implications. *Expert Rev Cardiovasc Ther.* 2007;5(4):733-741.  
doi:10.1586/14779072.5.4.733
302. Hockin MF, Jones KC, Everse SJ, Mann KG. A model for the stoichiometric regulation of blood coagulation. *Journal of Biological Chemistry.* 2002;277(21):18322-18333.  
doi:10.1074/jbc.M201173200
303. Tokarev AA, Butylin AA, Ermakova EA, Shnol EE, Panasenkov GP, Ataulakhanov FI. Finite platelet size could be responsible for platelet margination effect. *Biophys J.* 2011;101(8). doi:10.1016/j.bpj.2011.08.031
304. Závodszy G, Van Rooij B, Czaja B, Azizi V, De Kanter D, Hoekstra AG. Red blood cell and platelet diffusivity and margination in the presence of cross-stream gradients in blood flows. *Physics of Fluids.* 2019;31(3). doi:10.1063/1.5085881
305. Chen H, Angerer JI, Napoleone M, et al. Hematocrit and flow rate regulate the adhesion of platelets to von Willebrand factor. *Biomechanics.* 2013;7(6).  
doi:10.1063/1.4833975
306. Davì G, Patrono C. *Mechanisms of Disease Platelet Activation and Atherothrombosis.* www.nejm.org
307. Zucker MB, Nachmias VT. Platelet Activation. *Arteriosclerosis.* 2008;(February 1985):2-18.
308. Allen RD, Zacharski LR, Widirstky ST, Rosenstein R, Zaitlin LM, Burgess DR. *Transformation and Motility of Human Platelets: Details of the Shape Change and Release Reaction Observed by Optical and Electron Microscopy.* Vol 83.; 1979.  
<http://rupress.org/jcb/article-pdf/83/1/126/1073948/126.pdf>
309. Zhu S, Travers RJ, Morrissey JH, Diamond SL. FXIa and platelet polyphosphate as therapeutic targets during human blood clotting on collagen/tissue factor surfaces under flow. *Blood.* 2015;126(12):1494-1502. doi:10.1182/blood-2015-04-641472
310. Del Principe D, Ruggieri A, Pietraforte D, et al. The relevance of estrogen/estrogen receptor system on the gender difference in cardiovascular risk. *Int J Cardiol.* 2015;187(1):291-298. doi:10.1016/j.ijcard.2015.03.145

311. Connolly TM, Limbird LE. *Removal of Extraplatelet Na Eliminates Indomethacin-Sensitive Secretion from Human Platelets Stimulated by Epinephrine, ADP, and Thrombin*. Vol 80.; 1983. <https://www.pnas.org>
312. Li N, Wallén NH, Ladjevardi M, Hjemdahl P. Effects of serotonin on platelet activation in whole blood. *Blood coagulation & fibrinolysis*. 1997;8(8):517-524.
313. Brown CH, Leverett LB, Lewis CW, Alfrey CP, Hellums JD. Morphological, biochemical, and functional changes in human platelets subjected to shear stress. *J Lab Clin Med*. 1975;86(3).
314. Weiss HJ, Turitto VT, Baumgartner HR. Effect of shear rate on platelet interaction with subendothelium in citrated and native blood. I. Shear rate-dependent decrease of adhesion in von Willebrand's disease and the Bernard-Soulier syndrome. *J Lab Clin Med*. 1978;92(5).
315. Weiss HJ, Baumgartner HR, Tschopp TB, Turitto VT, Cohen D. Correction by factor VIII of the impaired platelet adhesion to subendothelium in von Willebrand disease. *Blood*. 1978;51(2). doi:10.1182/blood.v51.2.267.bloodjournal512267
316. Moake JL, Turner NA, Stathopoulos NA, Nolasco LH, Hellums JD. Involvement of large plasma von Willebrand Factor (vWF) multimers and unusually large vWF forms derived from endothelial cells in shear stress-induced platelet aggregation. *Journal of Clinical Investigation*. 1986;78(6). doi:10.1172/JCI112736
317. Jackson SP, Nesbitt WS, Westein E. Dynamics of platelet thrombus formation. *Journal of Thrombosis and Haemostasis*. 2009;7(SUPPL. 1):17-20. doi:10.1111/j.1538-7836.2009.03401.x
318. Razi MS, Hameed W, Habib SS, Aslam M, Ashraf R. Synergism between collagen - Adenosine diphosphate and collagen - Epinephrine in platelets' aggregation: Different dose response relationships. *J Pak Med Assoc*. 2009;59(6):368-371.
319. Nylander S, Mattsson C, Ramström S, Lindahl TL. Synergistic action between inhibition of P2Y<sub>12</sub>/P2Y<sub>1</sub> and P2Y<sub>12</sub>/thrombin in ADP- and thrombin-induced human platelet activation. *Br J Pharmacol*. 2004;142(8):1325-1331. doi:10.1038/sj.bjp.0705885

320. Sorensen EN, Burgreen GW, Wagner WR, Antaki JF. Computational Simulation of Platelet Deposition and Activation: I. Model Development and Properties. *Ann Biomed Eng.* 1999;27(4):436-448. doi:10.1114/1.200
321. Frojmovic MM, Mooney RF, Wong T. Dynamics of platelet glycoprotein IIb-IIIa receptor expression and fibrinogen binding. I. Quantal activation of platelet subpopulations varies with adenosine diphosphate concentration. *Biophys J.* 1994;67(5):2060-2068. doi:10.1016/S0006-3495(94)80689-7
322. Chatterjee MS. Systems Biology of Blood Coagulation and Platelet Activation. *ProQuest Dissertations and Theses.* Published online 2011:208.
323. Yin W, Gallocher S, Pinchuk L, Schoepfoerster RT, Jesty J, Bluestein D. Flow-induced platelet activation in a St. Jude mechanical heart valve, a trileaflet polymeric heart valve, and a St. Jude tissue valve. *Artif Organs.* 2005;29(10). doi:10.1111/j.1525-1594.2005.29109.x
324. J. D. HellumsD. M. PetersonN. A. StathopoulosJ. L. MoakeT. D. Giorgio. *Studies on the Mechanisms of Shear-Induced Platelet Activation.* Vol 110.; 1987.
325. Goodman PD, Barlow ET, Crapo PM, Mohammad SF, Solen KA. Computational model of device-induced thrombosis and thromboembolism. *Ann Biomed Eng.* 2005;33(6):780-797. doi:10.1007/s10439-005-2951-z
326. Hellums JD. 1993 Whitaker lecture: Biorheology in thrombosis research. *Ann Biomed Eng.* 1994;22(5):445-455. doi:10.1007/BF02367081
327. Jesty J, Bluestein D. Acetylated prothrombin as a substrate in the measurement of the procoagulant activity of platelets: Elimination of the feedback activation of platelets by thrombin. *Anal Biochem.* 1999;272(1):64-70. doi:10.1006/abio.1999.4148
328. Jesty J, Bluestein D. Assay of the activation state of platelets. *Anal Biochem.* 1999;272(1):64-70. <http://www.google.com/patents/WO2001005948A1?cl=en>
329. Sheriff J, Soares JS, Xenos M, Jesty J, Bluestein D. Evaluation of shear-induced platelet activation models under constant and dynamic shear stress loading conditions relevant to devices. *Ann Biomed Eng.* 2013;41(6):1279-1296. doi:10.1007/s10439-013-0758-x

330. Soares JS, Sheriff J, Bluestein D. A novel mathematical model of activation and sensitization of platelets subjected to dynamic stress histories. *Biomech Model Mechanobiol.* 2013;12(6):1127-1141. doi:10.1007/s10237-013-0469-0
331. Consolo F, Sheriff J, Gorla S, et al. High Frequency Components of Hemodynamic Shear Stress Profiles are a Major Determinant of Shear-Mediated Platelet Activation in Therapeutic Blood Recirculating Devices. *Sci Rep.* 2017;7(1). doi:10.1038/s41598-017-05130-5
332. Walton BL, Lehmann M, Skorzewski T, et al. Elevated hematocrit enhances platelet accumulation following vascular injury. *Blood.* 2017;129(18):2537-2546. doi:10.1182/blood-2016-10-746479
333. Passos A, Sherwood JM, Kaliviotis E, Agrawal R, Pavesio C, Balabani S. The effect of deformability on the microscale flow behavior of red blood cell suspensions. *Physics of Fluids.* 2019;31(9). doi:10.1063/1.5111189
334. Zydney AL, Colton CK. A Concentration Polarization Model for the Filtrate Flux in Cross-Flow Microfiltration of Particulate Suspensions. *Chem Eng Commun.* 1986;47(1-3):1-21. doi:10.1080/00986448608911751
335. Hund SJ, Antaki JF. An extended convection diffusion model for red blood cell-enhanced transport of thrombocytes and leukocytes. *Phys Med Biol.* 2009;54(20):6415-6435. doi:10.1088/0031-9155/54/20/024
336. Phillips RJ, Armstrong RC, Brown RA, Graham AL, Abbott JR. A constitutive equation for concentrated suspensions that accounts for shear-induced particle migration. *Physics of Fluids A.* 1992;4(1):30-40. doi:10.1063/1.858498
337. Wu WT, Aubry N, Massoudi M, Antaki JF. Transport of platelets induced by red blood cells based on mixture theory. 2017;118:16-27.  
<https://arxiv.org/ftp/arxiv/papers/1703/1703.00611.pdf>
338. Jackson SP. The growing complexity of platelet aggregation. *Blood.* 2007;109(12). doi:10.1182/blood-2006-12-027698
339. Wu WT, Jamiolkowski MA, Wagner WR, Aubry N, Massoudi M, Antaki JF. Multi-Constituent Simulation of Thrombus Deposition. *Sci Rep.* 2017;7. doi:10.1038/srep42720

340. Leiderman K, Fogelson AL. Grow with the flow: A spatial-temporal model of platelet deposition and blood coagulation under flow. *Mathematical Medicine and Biology*. 2011;28(1):47-84. doi:10.1093/imammb/dqq005
341. Bark DL, Ku DN. Platelet transport rates and binding kinetics at high shear over a thrombus. *Biophys J*. 2013;105(2):502-511. doi:10.1016/j.bpj.2013.05.049
342. Taylor JO, Witmer KP, Neuberger T, et al. In vitro quantification of time dependent thrombus size using magnetic resonance imaging and computational simulations of thrombus surface shear stresses. *J Biomech Eng*. 2014;136(7):1-11. doi:10.1115/1.4027613
343. Evans E, Berk D, Leung A. Detachment of agglutinin-bonded red blood cells. I. Forces to rupture molecular-point attachments. *Biophys J*. 1991;59(4):838-848. doi:10.1016/S0006-3495(91)82296-2
344. Evans E, Ritchie K. Dynamic strength of molecular adhesion bonds. *Biophys J*. 1997;72(4):1541-1555. doi:10.1016/S0006-3495(97)78802-7
345. Fogelsonl A, Yu H, Kuharsky3 A. *Computational Modeling of Blood Clotting: Coagulation and Three-Dimensional Platelet Aggregation.*; 2003.
346. Du J, Aspray E, Fogelson A. Computational investigation of platelet thrombus mechanics and stability in stenotic channels. *J Biomech*. 2021;122:110398. doi:10.1016/j.jbiomech.2021.110398
347. Fogelson AL. Continuum models of platelet aggregation: Formulation and mechanical properties. *SIAM J Appl Math*. 1992;52(4):1089-1110. doi:10.1137/0152064
348. Stefan Samra. *Numerical Implementation of a Continuum Platelet Aggregation Model*. Thesis. The Pennsylvania State University; 2011.
349. Taylor JO, Meyer RS, Deutsch S, Manning KB. Development of a computational model for macroscopic predictions of device-induced thrombosis. *Biomech Model Mechanobiol*. 2016;15(6):1713-1731. doi:10.1007/s10237-016-0793-2
350. Basmadjian D. the Hemodynamic and Embolizing Forces Acting on Thrombi-Ii . the Effect of Pulsatile Blood. *J Biomech*. 1986;19(10):837-845.

351. Basmadjian D. The hemodynamic forces acting on thrombi, from incipient attachment of single cells to maturity and embolization. *J Biomech.* 1984;17(4):287-298. doi:10.1016/0021-9290(84)90139-8
352. Basmadjian D. Embolization: Critical thrombus height, shear rates, and pulsatility. Patency of blood vessels. *J Biomed Mater Res.* 1989;23(11):1315-1326. doi:10.1002/jbm.820231108
353. Navitsky MA, Taylor JO, Smith AB, et al. Platelet adhesion to polyurethane urea under pulsatile flow conditions. *Artif Organs.* 2014;38(12):1046-1053. doi:10.1111/aor.12296
354. Conor James Flannery. *Thrombus Formation Under High Shear in Arterial Stenotic Flow.* 2005.
355. Ageno W, Gallus AS, Wittkowsky A, Crowther M, Hylek EM, Palareti G. Oral anticoagulant therapy - Antithrombotic therapy and prevention of thrombosis, 9th ed: American College of Chest Physicians evidence-based clinical practice guidelines. *Chest.* 2012;141(2 SUPPL.). doi:10.1378/chest.11-2292
356. Sobel M, McNeill PM, Carlson PL, et al. Heparin inhibition of von Willebrand factor-dependent platelet function in vitro and in vivo. *Journal of Clinical Investigation.* 1991;87(5):1787-1793. doi:10.1172/JCI115198
357. Sixma JJ, Chiphorst ME, Verweij CL, Pannekoek H. Effect of deletion of the A1 domain of von Willebrand factor on its binding to heparin, collagen and platelets in the presence of ristocetin. *Eur J Biochem.* 1991;196(2):369-375. doi:10.1111/j.1432-1033.1991.tb15826.x
358. Douketis JD. Pharmacologic properties of the new oral anticoagulants: a clinician-oriented review with a focus on perioperative management. *Curr Pharm Des.* 2010;16(31). doi:10.2174/138161210793563338
359. Metharom P, Berndt MC, Baker RI, Andrews RK. Current state and novel approaches of antiplatelet therapy. *Arterioscler Thromb Vasc Biol.* 2015;35(6):1327-1338. doi:10.1161/ATVBAHA.114.303413
360. Griffith MJ, Carolina N. Kinetics of the Heparin-enhanced Antithrombin III / Thrombin Reaction. *J Biol Chem.* 1982;257(13):7360-7365.

361. Griffith MJ. Kinetics of the heparin-enhanced antithrombin III/thrombin reaction. Evidence for a template model for the mechanism of action of heparin. *Journal of Biological Chemistry*. 1982;257(13):7360-7365. doi:10.1016/s0021-9258(18)34385-0
362. Griffith MJ. The heparin-enhanced antithrombin III/thrombin reaction is saturable with respect to both thrombin and antithrombin III. *Journal of Biological Chemistry*. 1982;257(23):13899-13902. doi:10.1016/s0021-9258(19)45315-5
363. Helms CC, Marvel M, Zhao W, et al. Mechanisms of hemolysis-associated platelet activation. *Journal of Thrombosis and Haemostasis*. 2013;11(12):2148-2154. doi:10.1111/jth.12422
364. Omar HR, Mirsaeidi M, Socias S, et al. Plasma free hemoglobin is an independent predictor of mortality among patients on extracorporeal membrane oxygenation support. *PLoS One*. 2015;10(4). doi:10.1371/journal.pone.0124034
365. Zhou Z, Han H, Cruz MA, López JA, Dong JF, Guchhait P. Haemoglobin blocks von Willebrand factor proteolysis by ADAMTS-13: A mechanism associated with sickle cell disease. *Thromb Haemost*. 2009;101(6):1070-1077. doi:10.1160/TH08-10-0677
366. Zhou Z, Behymer M, Guchhait P. Role of extracellular hemoglobin in thrombosis and vascular occlusion in patients with sickle cell anemia. *Anemia*. 2011;2011. doi:10.1155/2011/918916
367. Ruggeri ZM. Platelet adhesion under flow. *Microcirculation*. 2009;16(1):58-83. doi:10.1080/10739680802651477
368. Cholette JM, Pietropaoli AP, Henrichs KF, et al. Elevated free hemoglobin and decreased haptoglobin levels are associated with adverse clinical outcomes, unfavorable physiologic measures, and altered inflammatory markers in pediatric cardiac surgery patients. *Transfusion (Paris)*. 2018;58(7):1631-1639. doi:10.1111/trf.14601
369. Dufour N, Radjou A, Thuong M. Hemolysis and plasma free hemoglobin during extracorporeal membrane oxygenation support: From clinical implications to laboratory details. *ASAIO Journal*. Published online 2020:239-246. doi:10.1097/MAT.0000000000000974



370. Chamchoi A, Srihirun S, Paiboonsukwong K, et al. Hemoglobin-bound platelets correlate with the increased platelet activity in hemoglobin E/ $\beta$ -thalassemia. *Int J Lab Hematol*. 2020;42(5):518-525. doi:10.1111/ijlh.13260
371. Manning KB, Nicoud F, Shea SM. Mathematical and computational modeling of device-induced thrombosis. *Curr Opin Biomed Eng*. 2021;20. doi:10.1016/j.cobme.2021.100349
372. Gong X, Sugiyama K, Takagi S, Matsumoto Y. The deformation behavior of multiple red blood cells in a capillary vessel. *J Biomech Eng*. 2009;131(7):1-5. doi:10.1115/1.3127255
373. Du J, Aspray E, Fogelson A. Computational investigation of platelet thrombus mechanics and stability in stenotic channels. *J Biomech*. 2021;122:110398. doi:10.1016/j.jbiomech.2021.110398
374. Du J, Kim D, Alhawael G, Ku DN, Fogelson AL. Clot Permeability, Agonist Transport, and Platelet Binding Kinetics in Arterial Thrombosis. *Biophys J*. 2020;119(10):2102-2115. doi:10.1016/j.bpj.2020.08.041
375. Kuharsky AL, Fogelson AL. Surface-mediated control of blood coagulation: The role of binding site densities and platelet deposition. *Biophys J*. 2001;80(3):1050-1074. doi:10.1016/S0006-3495(01)76085-7
376. Wang Y, Luo K, Qiao Y, Fan J. An integrated fluid-chemical model toward modeling the thrombus formation in an idealized model of aortic dissection. *Comput Biol Med*. 2021;136. doi:10.1016/j.compbiomed.2021.104709
377. Xu Z, Chen N, Kamocka MM, Rosen ED, Alber M. A multiscale model of thrombus development. *J R Soc Interface*. 2008;5(24):705-722. doi:10.1098/rsif.2007.1202
378. Sorensen EN, Burgreen GW, Wagner WR, Antaki JF. Computational Simulation of Platelet Deposition and Activation: II. Results for Poiseuille Flow over Collagen. *Ann Biomed Eng*. 1999;27(4):449-458. doi:10.1114/1.201
379. Erik Nathaniel Sorensen. *COMPUTATIONAL SIMULATION OF PLATELET TRANSPORT, ACTIVATION, AND DEPOSITION*. 2002.

380. Bark D. *Mechanistic Numerical Study of Thrombus Growth*. Masters. Georgie Institute of Technology; 2007.
381. Wu WT. Theoretical and Computational Studies on Thrombus Formation and Multiphase Characteristics of Blood Flow. *Mechanical Engineering*. 2015;Ph.D.(2011).
382. Yang L, Neuberger T, Manning KB. In vitro real-time magnetic resonance imaging for quantification of thrombosis. *Magnetic Resonance Materials in Physics, Biology and Medicine*. 2021;34(2):285-295. doi:10.1007/s10334-020-00872-2
383. Yang L. *NUMERICAL AND MAGNETIC RESONANCE IMAGING STUDIES FOR DEVICE-INDUCED THROMBOSIS A Dissertation in Bioengineering.*; 2020.
384. Yang L, Tobin N, Manning KB. Refining a numerical model for device-induced thrombosis and investigating the effects of non-Newtonian blood models. *J Biomech*. 2021;120. doi:10.1016/j.jbiomech.2021.110393
385. Tobin N, Manning KB. Toward modeling thrombosis and thromboembolism in laminar and turbulent flow regimes. *Int J Numer Method Biomed Eng*. 2022;38(10). doi:10.1002/cnm.3638
386. Belyaev A V., Pantelev MA, Ataulakhanov FI. Threshold of Microvascular Occlusion: Injury Size Defines the Thrombosis Scenario. *Biophys J*. 2015;109(2):450-456. doi:10.1016/j.bpj.2015.06.019
387. Murallidharan JS, Payne SJ. Thrombus growth modelling and stenosis prediction in the cerebral microvasculature. *J Theor Biol*. 2019;478:1-13. doi:10.1016/j.jtbi.2019.06.013
388. Yazdani A, Zhang P, Sheriff J, Slepian MJ, Deng Y, Bluestein D. *Multiscale Modeling of Blood Flow-Mediated Platelet Thrombosis.*; 2020. doi:10.1007/978-3-319-44680-6\_69
389. Zheng X, Yazdani A, Li H, Humphrey JD, Karniadakis GE. A three-dimensional phase-field model for multiscale modeling of thrombus biomechanics in blood vessels. *PLoS Comput Biol*. 2020;16(4). doi:10.1371/journal.pcbi.1007709
390. Flamm MH, Diamond SL. Multiscale systems biology and physics of thrombosis under flow. *Ann Biomed Eng*. 2012;40(11):2355-2364. doi:10.1007/s10439-012-0557-9

391. Flamm MH, Colace T V., Chatterjee MS, et al. Multiscale prediction of patient-specific platelet function under flow. *Blood*. 2012;120(1):190-198. doi:10.1182/blood-2011-10-388140
392. Shankar KN, Zhang Y, Sinno T, Diamond SL. A three-dimensional multiscale model for the prediction of thrombus growth under flow with single-platelet resolution. *PLoS Comput Biol*. 2022;18(1). doi:10.1371/journal.pcbi.1009850
393. Ha H, Kvitting JPE, Dyverfeldt P, Ebbers T. 4D Flow MRI quantification of blood flow patterns, turbulence and pressure drop in normal and stenotic prosthetic heart valves. *Magn Reson Imaging*. 2019;55:118-127. doi:10.1016/j.mri.2018.09.024
394. Pozrikidis C. Effect of membrane bending stiffness on the deformation of capsules in simple shear flow. *J Fluid Mech*. 2001;440:269-291.
395. Gong X, Sugiyama K, Takagi S, Matsumoto Y. The deformation behavior of multiple red blood cells in a capillary vessel. *J Biomech Eng*. 2009;131(7):1-5. doi:10.1115/1.3127255
396. Sugiyama K, Ii S, Shimizu K, Noda S, Takagi S. A Full Eulerian Method for Fluid-structure Interaction Problems. *Procedia IUTAM*. 2017;20:159-166. doi:10.1016/j.piutam.2017.03.022
397. Wang X, Gong X, Sugiyama K, Takagi S, Huang H. An immersed boundary method for mass transfer through porous biomembranes under large deformations. *J Comput Phys*. 2020;413:109444. doi:10.1016/j.jcp.2020.109444
398. Tomaiuolo G, Simeone M, Martinelli V, Rotoli B, Guido S. Red blood cell deformation in microconfined flow. *Soft Matter*. 2009;5(19):3736-3740. doi:10.1039/b904584h
399. Ansys F. Solver theory guide, Ansys Inc. 2013;Release 15:249.
400. Casassa EF. Equilibrium distribution of flexible polymer chains between a macroscopic solution phase and small voids. *J Polym Sci B*. 1967;5(9):773-778. doi:10.1002/pol.1967.110050907
401. Razizadeh M. *Supra Coarse-Grained Modeling of Biological Membranes*. Lehigh University; 2021.

402. Koshiyama K, Wada S. Molecular dynamics simulations of pore formation dynamics during the rupture process of a phospholipid bilayer caused by high-speed equibiaxial stretching. *J Biomech.* 2011;44(11):2053-2058. doi:10.1016/j.jbiomech.2011.05.014
403. Johnson G, Massoudi M, Rajagopal KR. Flow of a fluid-solid mixture between flat plates. *Chem Eng Sci.* 1991;46(7):1713-1723. doi:10.1016/0009-2509(91)87018-8
404. Wu WT, Aubry N, Massoudi M. On the coefficients of the interaction forces in a two-phase flow of a fluid infused with particles. *Int J Non Linear Mech.* 2014;59:76-82. doi:10.1016/j.ijnonlinmec.2013.11.006
405. Baumgartner HR. *The Role of Blood Flow in Platelet Adhesion, Fibrin Deposition, and Formation of Mural Thrombi.* Vol 5.; 1973.
406. Grunenwald LE. the Effects of Hematocrit and Rotation Time on Platelet Adhesion To a Polyurethane Urea Surface. 2013;(May):1-95.
407. Taylor JO, Yang L, Deutsch S, Manning KB. Development of a platelet adhesion transport equation for a computational thrombosis model. *J Biomech.* 2017;50:114-120. doi:10.1016/j.jbiomech.2016.11.012
408. James P, Rydz N. *Structure, Biology, and Genetics of von Willebrand Factor.* Seventh Ed. Elsevier Inc.; 2017. doi:10.1016/B978-0-323-35762-3.00138-4
409. Kaza N, Ojaghi A, Robles FE. Hemoglobin quantification in red blood cells via dry mass mapping based on UV absorption. *J Biomed Opt.* 2021;26(08):1-10. doi:10.1117/1.jbo.26.8.086501
410. Bao Y. *Optimization and Computational Fluid Dynamics (CFD) Analysis of a Novel Left Ventricular Assist Device (LVAD) Configuration.* McGill University (Canada); 2022.
411. Rowlands GW, Pagani FD, Antaki JF. Classification of the Frequency, Severity, and Propagation of Thrombi in the HeartMate II Left Ventricular Assist Device. *ASAIO Journal.* 2020;Publish Ah:1-8. doi:10.1097/mat.0000000000001151

## Appendix A: Timescale Sensitivity Analysis of Thrombosis Acceleration

---

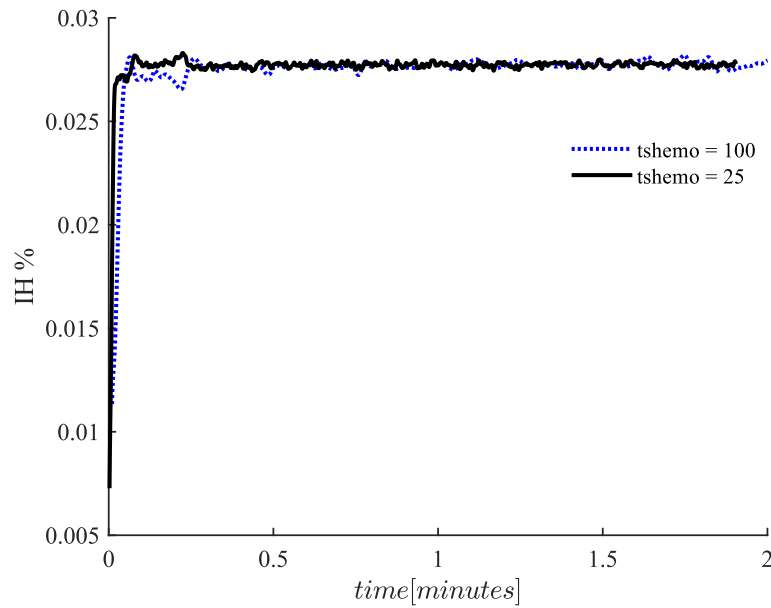


**Figure 68:** Comparison of hemolysis index at outlet in the open-hub LVAD where hemolysis equations are sped up by a factor of 25 and 100. Time is given in minutes hemolysis time.

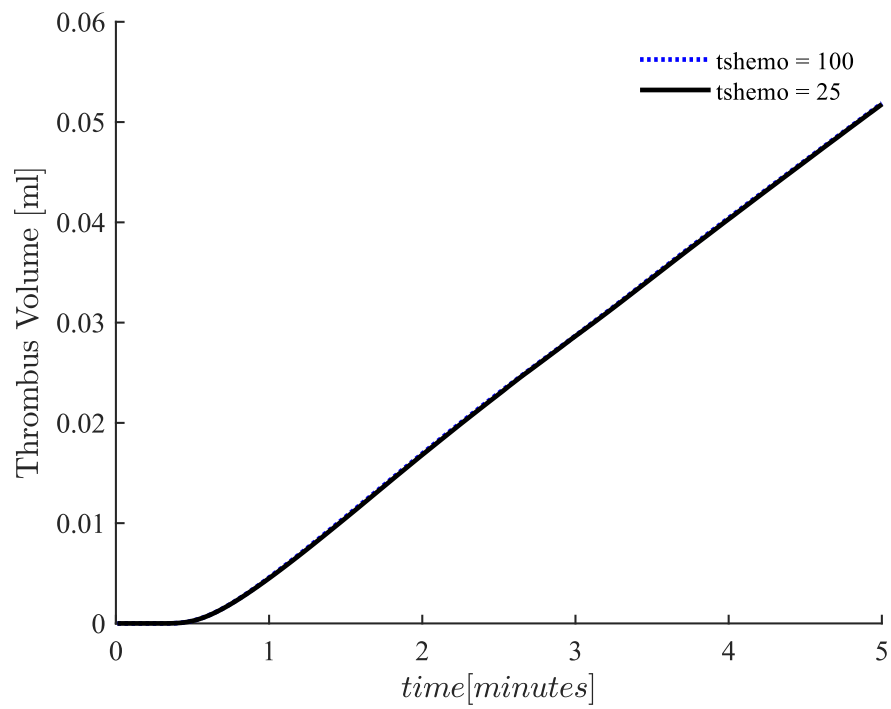


**Figure 69:** Comparison of thrombus volume in the open-hub LVAD where hemolysis equations. Time is given in minutes thrombus time.

## Appendix B: Parameters for Six Best LVADs

Design	22	26	15	29	11	24
Primary Diffuser Blade Area	0.4531	0.584375	0.365625	<b>0.671875</b>	0.51875	<b>0.75938</b>
Primary Diffuser Blade Divergence	0.8063	0.84375	0.58125	<b>0.31875</b>	0.4125	<b>0.69375</b>
Impeller Blade Divergence	0.4401	0.800523	0.840565	<b>0.880607</b>	0.900628	<b>0.32002</b>
Impeller Blade Area	-0.681	-0.94375	-0.75625	<b>-0.56875</b>	-0.6625	<b>-0.7938</b>
Inducer Blade Area	0.997	0.791162	0.585287	<b>1.03821</b>	0.688225	<b>0.62646</b>
Inducer blade Divergence	0.4875	0.5625	0.4375	<b>0.6125</b>	0.625	<b>0.6625</b>
RPM	1500	1500	3000	<b>3000</b>	4500	<b>4500</b>
Primary Diffuser - blade angle with outflow plane	4.6875	6.5625	23.4375	<b>17.8125</b>	1.875	<b>14.0625</b>
Primary Diffuser - Inflow / Outflow Tangent Weight	0.178	0.122	0.141	<b>0.134</b>	0.194	<b>0.197</b>
Impeller - Acceleration parameter	0.413	0.138	0.263	<b>0.488</b>	0.425	<b>0.238</b>
Impeller - blade angle with outflow plane	7.7	18.6	29.5	<b>5.5</b>	24.1	<b>27.3</b>
Primary Diffuser No. Blades	2	5	3	<b>3</b>	5	<b>2</b>
Secondary Diffuser No. Blades	3	4	4	<b>2</b>	3	<b>3</b>
Impeller No. Blades	5	4	5	<b>3</b>	5	<b>4</b>
Inducer No. Blades	5	3	4	<b>5</b>	4	<b>4</b>
Impeller ID Ratio	0.73	0.42	0.25	<b>0.35</b>	0.51	<b>0.56</b>
Diffuser ID Ratio	0.29	0.39	0.49	<b>0.60</b>	0.44	<b>0.25</b>
Secondary Diffuser outlet D	0.59	0.41	0.54	<b>0.76</b>	0.58	<b>0.71</b>
Thrombus Vol. (ml)	0.179	0.097	0.100	<b>0.021</b>	0.067	<b>0.017</b>
Growth Rate (ml/h)	0.680	0.257	0.313	<b>0.089</b>	0.315	<b>0.057</b>
IH	0.04	0.04	0.05	<b>0.06</b>	0.14	<b>0.14</b>

